Inaugural dissertation

for

obtaining the doctoral degree

of the

Combined Faculty of Mathematics, Engineering and Natural Sciences

of the

Ruprecht - Karls - University

Heidelberg

Presented by

M.Sc. Dan Zhang

born in: Guizhou, China

Oral examination: 2022.07.07

Opposite polarity programs regulate asymmetric subsidiary cell divisions in grasses

Referees: **Prof. Dr. Karin Schumacher**

Prof. Dr. Michael Raissig

Abstract

Stomata, breathing pores located on leaf epidermal made up of paired guard cells surrounding a central pore, are identified in most aerial tissues of plants. They can regulate the entry of photosynthetic CO_2 and loss of water vapor. Grasses show particularly intriguing differences in stomatal development programs compared to the dicots in multiple ways. A four-celled stomatal complex presents a unique morphology in grasses termed graminoid, a pair of center dumbbell-shaped guard cells (GCs) recruiting specialized support cells called subsidiary cells (SCs), which develop in parallel rows with specific cell identity. These SCs serve as supporters of GCs in the molecular and mechanical perspectives, to facilitate stomatal movement in response to environmental signals. Production of SCs involves subsidiary mother cells (SMCs) establishment, polarization, and SCs division. The molecular genetic regulation of stomatal development process has been extensively studied in the dicot *Arabidopsis thaliana*. Yet, this process in grasses still required more exploration, especially the formation of SCs.

In my thesis work, I have examined the comparative transcriptomics (wild-type (WT) vs. mutant (*bdmute*)), focusing mainly on novel genes involved in SC divisions. My studies are performed using the forage grass *Brachypodium distachyon*, a recently developed, genetically tractable model species related to wheat. First, I describe mutations in the candidate gene *BdPOLAR* from transcriptomics, and *BdPAN1*, whose known orthologue was described as a polarity regulator during SC formation in maize. Although both mutants display SC defects, quantification analysis suggests they work together to regulate SC divisions. Subsequently, I identify that BdPOLAR localizes in the SMCs periphery while mainly being absent at the sites of guard mother cells (GMCs), which is a novel, distal polarity domain, and BdPAN1 polarized at the GMC/SMC interface; thus, two polarity proteins build up an opposing, almost reciprocal polarity pattern. Further, comparative imaging and polarity index data suggest *BdMUTE* and *BdPAN1* are required for the expression and polarization of BdPOLAR, respectively. Moreover, *BdPOLAR* and *BdPAN1* display different

functions to promote SC polarizations. *BdPAN1* is responsible for pre-mitotic nuclear polarization, which resembles its orthologue in maize. Strikingly, *BdPOLAR* acquires novel functions that specify SMC division plane orientation and control SMC division capacity. In addition, leaf-level gas exchange measurement discovered that correct SC formation is required for sufficient graminoid stomatal functionality. Finally, I describe the polarity role of *BdPOLAR* homologue gene, *BdPOLAR-LIKE*, report that link between *BdPOLAR* and (Brassinosteroid) BR signaling/biosynthesis in *Brachypodium,* and discuss prospects for using time-lapse imaging to gain insight into SMC polarity.

Zusammenfassung

Stomata, Atmungsporen in der Blatt-Epidermis, bestehen aus einem Paar von Schließzellen um eine zentrale Pore und können sich in den meisten oberirdischen Pflanzengeweben befinden. Sie regulieren die Aufnahme von CO_2 für Photosynthese und den Verlust von Wasser über Ausdünstungen. Gräser weisen im Vergleich zu Dikotyledonen spezielle Unterschiede in der stomatalen Entwicklung auf. Hier präsentieren vierzellige stomatale Komplexe eine einzigartige Morphologie, die als graminoid bezeichnet wird. In Zellreihen bestimmter Zellidentität gibt es jeweils ein Paar von zentralen, hantelförmigen Schließzellen (guard cells, GCs), die spezialisierte Hilfszellen, sogenannte Nebenzellen (subsidiary cells, SCs), aus parallel verlaufenden Zelllinien rekrutieren. Diese SCs dienen als Unterstützer der GCs bei den molekularen und mechanischen Vorgängen, die die stomatale Bewegung als Reaktion auf Umwelteinflüsse vereinfachen. Die Entstehung von SCs involviert die Einrichtung von Nebenzellen-Mutterzellen (subsidiary mother cells, SMCs), Polarisierung und Teilung in SCs. Die molekulargenetische Regulierung des stomatalen Entwicklungsprozesses wurde in der dikotyledonen Pflanze *Arabidopsis thaliana* bereits ausführlich untersucht. In Graspflanzen hingegen besteht hier noch weiterer Forschungsbedarf, vor allem bei der Entstehung der SCs.

Im Zuge der Arbeit für meine Dissertation habe ich Transkriptome von Wildtyppflanzen (WT) und Mutanten (*bdmute*) verglichen und meinen Fokus auf neue Gene gelegt, die in der Teilung von SCs eine Rolle spielen. Meine Untersuchungen hierbei habe ich an der Gras-Futterpflanze *Brachypodium distachyon* durchgeführt, ein kürzlich etablierter Modellorganismus, der mit Weizen verwandt ist. Zuerst beschreibe ich Mutationen im Kandidatengen *BdPOLAR* aus meinem Transkriptom-Datensatz und *BdPAN1*, dessen bekanntes Ortholog in Mais als Polaritätsregulator in der Formierung von SCs beschrieben wurde. Beide Mutanten zeigen SC-Defekte und quantitative Analyse weist darauf hin, dass die Gene zusammenarbeiten, um die Teilung von SCs zu kontrollieren. Nachfolgend identifiziere ich die Lokalisierung von *BdPOLAR* in der Peripherie von SMCs mit hauptsächlicher Abwesenheit an der

Grenze zu Schließzellen-Mutterzellen (guard mother cells, GMCs), womit hier eine neue, distale Polaritätsdomäne besteht; und *BdPAN1* polarisiert an dieser Verbindungsstelle von GMC/SMC. Demnach bilden diese beiden Polaritätsproteine ein gegensätzliches, nahezu reziprokes Polaritätsmuster. Des Weiteren deuten Vergleiche von Mikroskopiebildern und Auswertung mittels Polaritätsindex darauf hin, dass *BdMUTE* und *BdPAN1* für die Expression und Polarisierung von *BdPOLAR* benötigt werden. Zusätzlich zeigen *BdPOLAR* und *BdPAN1* verschiedene Wege, wie sie die Polarisierung von SCs vorantreiben. *BdPAN1* ist für die prä-mitotische nukleare Polarisierung, ähnlich wie auch das Mais-Ortholog, zuständig. Bemerkenswert für *BdPOLAR* ist, dass das Gen eine neuartige Funktion aufweist, die für die Orientierung der SMC-Teilungsebene und die Teilungsfähigkeit der SMC wichtig ist. Außerdem zeigen Gasaustauschmessungen auf Blattebene, dass die korrekte Formierung der SCs notwendig ist für eine ausreichende Funktionalität der graminoiden Stomata. Zum Schluss beschreibe ich die Polaritätsrolle des *BdPOLAR*-Homologs *BdPOLAR-LIKE*, berichte über die Verbindung zwischen *BdPOLAR* und Brassinosteroid (BR) Signalwegen/ Biosynthese in *Brachypodium* und diskutiere mögliche Aussichten bezüglich der Nutzung von Time-lapse Imaging, um damit weitere Einblicke in die Polarität von SMC zu gewinnen.

Acknowledgments

Upon the completion of this thesis, I am grateful to those who have offered me encouragement and support during my PhD study. Reviews around four years of study life, feeling is quite deep, rich harvest. In this lovely and beautiful city of Heidelberg, I have been truly fortunate to be a part of the Raissig lab, Centre for Organismal Studies community.

First and foremost, I am extremely grateful to my supervisors, Prof. Dr. Michael Raissig for his continuous support, and patience during my Ph.D. study, and a big thank-you goes also to Dr. Heike Lindner for her countless help on tissue culture and invaluable advice for my study. Michael and Heike, they build up a warm, friendly, and passionate lab environment where I had a lot of happy time. They have seen me grow up to a significant extent. They have shown great enthusiasm, intelligence, and scientific insight during work, and also behaved their positive attitudes with life, expressed sincere concern for people around, which inspire me a lot.

I would particularly like to thank Tiago Daniel Gomes Nunes, the colleague of my whole Ph.D. life as well as my dear friend. He saw me through the many ups and downs of my Ph.D. and always supported and encouraged me. He always helped me with experimental difficulties and stand up behind me when I face tough life issues. His kindness and sense of humor meant I felt warm and happy inside and outside of lab. Our friendship made my time in Heidelberg so much fun.

I would also like to especially thank many members of the Raissig lab who have overlapped with me during my Ph.D. time, for their uncountable help in my studies and life living abroad. Thank you to Barbara Jesenofsky, who worked on tissue culture with Heike, producing many brilliant and precious transgenic reporter and CRISPR lines; Thank you to Inés Hidalgo Prados, who worked on polarity index part of my project; Thank you to Roxane Spiegelhalder, who sincerely helped me on work and life issues; Thank you to Xin for her encouragement and sympathetic ear during my thesis writing; Thank you to Lea

Berg, who gave me a lot of help and also actively organized lab activities, making me feel very happy when I joined in; Thanks as well to rotation students who have been contributed in my experiments, including Deniz Bak, Rashmi Tandon, Irem Polat, Kim Janssen, and Nika Gorsek.

I would also like to especially thank my co-authors of the Bergmann Lab. Thank you to Prof. Dr. Dominique Bergmann, who has given me helpful discussion and supervision in my research; To Emily Abrash, who invested a lot of time and effort in characterizing *bdpan1-1* and analyzing of *BdPAN1* reporter expression and protein localization; To Juliana de Lima Matos and Akhila Bettadapur for their help in the original screen that identified the *bdpan1-1* mutant; To Laura R. Lee for her support in RNA-seq data analysis; A special thank-you as well to Dr. John Vogel, who has generously provided M3 generation of an EMS mutagenesis and genomic resources.

A big thank-you goes also to my committee members, Prof. Dr. Karin Schumacher, Prof. Dr. Thomas Greb, and Prof. Dr. Sabine Müller, who have always taken the time to offer me advice on science. Thanks as well to members from COS and HBIGS, who have been helped me a lot during my Ph.D. including Ines Steins, Dr. Rolf Lutz, and Martina Galvan. Thank you in particular to Dr. Upendo Lupanda and Dr. Zaida María Andrés González, who has helped me a lot with cloning issues. Thank you to Michael Schilbach, who has intently and carefully taken care of our plants. My deepest gratitude goes also to the many labs I've interacted with over the years, especially the Lohmann, Greb, Schumacher, Maizel and Wolf Labs in INF230, and Rausch Lab in INF360. Thanks as well to GUSE and Wittbrodt labs for microscopy assistance.

I also want to extend my deepest thanks to the friends who are not involved in my work but have nonetheless supported and encouraged me over the course of my Ph.D. A huge thank-you goes to my friend, Lili, who has been with me through a tough time, as well as happy distractions to rest my mind outside of my study. Thank you so much also to Pengfei Fan, Zoe, Fei Xu, and Rashmi Tandon, who have always encouraged me, and their self-confidence,

enthusiasm, and optimistic attitude towards life also inspired me deeply. A big thank-you as well to my friend, Yali Wei, Chunmiao Zhang, Lixia Yang, and Shiao Zhang, who have always believed in me, and sent me their positive energy from seven thousand kilometers away.

The biggest thank-you of all goes to my parents, whose boundless love and whole-hearted support has kept me optimistic, grounded, and persistent during some of the most challenging periods of my Ph.D. and life.

TABLE OF CONTENTS

List of figures

List of tables

List of supplemental figures

List of abbreviations

Abbreviation	Explanation
ABD2	Actin-binding domain2
ACD	Asymmetric cell division
BAK1	BRI1ASSOCIATED KINASE1

BASL	BREAKING OF ASYMMETRY IN THE STOMATAL LINEAGE
BES1	BRI1-EMSSUPPRESSOR
bHLH	basic helix-loop-helix
BIN2	BRASSINOSTEROID INSENSITIVE 2
BL	Brassinolide
BR	Brassinosteroids
BRI1	BRASSINOSTEROID INSENSITIVE 1
BRK	BRICK
BRX	BREVIS RADIX
BZR1	BRASSINAZOLE-RESISTANT 1
CO_2	Carbon dioxide
CRISPR/Cas9	Clustered regularly interspaced short palindromic repeats / CRISPR-associated Protein9
dag	Days after germination
DCD1	DISCORDIA1
DIC	Differential interference contrast
EMS	Ethyl methane sulfonate
EPF	EPIDERMAL PATTERNING FACTOR
ER	ERECTA
g_{sw}	Stomatal conductance
GC	Guard cell
GIF1	GRF-INTERACTING FACTOR 1
GMC	Guard mother cell
GRF4	GROWTH-REGULATING FACTOR 4
ICE1	Inducer of CBF expression1
LRR-RLK	Leucine-rich repeat receptor-like Ser/Thr kinase
LWR	GMC length-to-width ratio
MAPK	Mitogen-activated protein kinase
MMC	Meristemoid mother cells
MT	Microtubule
MYR	Myristoylation
PAR	Photosynthetic active radiation
PAN1/2	PANGLOSS1/2
PC	Pavement cell
PI	Polarity index
PI	Propidium iodide
PL	Proximity labeling
PM	Plasma membrane

POK1/2	PHRAGMOPLAST ORIENTING KINESIN1 and 2
POLAR	POLAR LOCALIZATION DURING ASYMMETRIC DIVISION AND REDISTRIBUTION
POME	Polarity measurement
PPB	Preprophase band
Ppz	Propiconazole
ROP	Rho GTPases OF PLANTS
SC	Subsidiary cell
SLGC	Stomatal lineage ground cell
SMC	Subsidiary mother cell
SPCH	SPEECHLESS
SCRM2	SCREAM2
TAN1	TANGLED1
TMM	TOO MANY MOUTHS
WUE	Water-use efficiency
YDA	YODA

Introduction

Life on land requires plants to balance global carbon dioxide (CO_2) and water cycles. The critical structure to perform this function are stomata. The term “stoma” represents mouth in Greek. As a “breathing” mouth, stomata are adjustable epidermal pores on plant leaves that control the entry of photosynthetic CO_2 and the loss of water vapor. Approximately 20% of the atmospheric CO_2 was reported to go through stomata and is subsequently absorbed annually (Hetherington and Woodward 2003). Furthermore, each year the double amount of atmospheric water goes through stomata via transpiration, which occupies an estimated 50% of total terrestrial evaporation (Hetherington and Woodward 2003, Jasechko, Sharp et al. 2013). Regulation of stomatal development and adjustment of pore aperture is important in optimizing water use efficiency and drought tolerance of plants. Due to the following benefits, stomata have emerged as an excellent system for understanding asymmetric cell division, cellular differentiation, signaling networks, and responses to hormones and environmental cues. Firstly, stomatal architecture and distribution exhibit species-distinct patterns and normally remands multi-step developmental procedures; Secondly, stomata are highly achievable and simple to observe on the leaf surface. Most current knowledge about stomatal function and development is primarily from studies in the dicot *Arabidopsis thaliana.* Grasses display variations in stomatal development and patterning that probably successfully adapted to their living environments. Although crops are essential players in providing the majority of human food sources, we still know remarkably little about their stomata. With annually rising global temperatures and limited water sources, untangling the mystery behind stomatal formation and performance in grasses could create “climate-ready crops” with superior drought tolerance.

1. Stomatal Cell Lineage

In *Arabidopsis*, in addition to petals and stamen filaments, stomata exist in the epidermis of all organs aboveground (Sessions, Nemhauser et al. 1997, Geisler, Yang et al. 1998, Pillitteri, Bogenschutz et al. 2008). Even though different plant

organs appear diverse stomata distributions, the stomatal pattern faithfully sticks to the one-cell spacing rule – the minimal patterning rule for stomata, in which stomata are separated by at least one pavement cell and do not contact directly each other. This one-cell pattern allows stomata to improve the gas exchange efficiency and prevent unnecessary water consumption. Stomatal development in *Arabidopsis* proceeds by a dedicated and specialized epidermal lineage through a series of cell divisions and successive cell-fate transitions. Initially, a subset of protodermal cells became meristemoid mother cells (MMC), the earliest precursor cell in the cell lineage. Then, through an "entry" asymmetric division, MMC generates two daughter cells with different cell sizes and cell destiny: the smaller meristemoid cell may continue several times self-renewing via asymmetric amplifying division or undergo a morphological transition into a guard mother cell (GMC); the larger stomatal lineage ground cell (SLGC) can terminally differentiate into a lobed pavement cell (PC) alternatively, perform an asymmetric spacing division to produce a satellite meristemoid, which is always placed away from the existing stomata or precursor cell. As the last precursor cell in the lineage, a GMC will divide symmetrically to yield two guard cells (GC) of a stoma (Fig. 1A, Fig.2A). Both entry divisions occur in meristemoids, and spacing divisions in SLGCs create new meristemoids and consequently directly increase the stomatal number. Amplifying divisions also increase the number of SLGC, which contains the ability to differentiate into a pavement cell. Thus, most of the epidermal cells in a leaf are derived from the stomatal lineage (Geisler, Nadeau et al. 2000).

The stomatal development in grasses is different from that of the dicots in multiple ways. Most remarkably, a four-celled stomatal complex presents a unique and typical morphology in grasses termed graminoid, consisting of a pair center dumbbell-shaped GCs flanked by two subsidiary cells (SCs), which develop in parallel rows with specific cell identity. On the contrary, dicots form kidney-shaped GCs, and stomata are distributed nonrandomly across the epidermis within a less order pattern. In nascent grass leaves, stomatal cell lineage follows the trail of the young, undifferentiated cells at the bottom and the mature, differentiated cells moving upwards as the leaf expands (Stebbins

and Shah 1960, Liu, Ohashi-Ito et al. 2009). This linear stomatal cell file is initiated from the leaf base. A potential stomatal precursor cell proliferates in a specialized file (stage1), dividing asymmetrically to produce a small GMC and a large daughter cell that terminally becomes a GC and a pavement cell, respectively (stage2). Sequentially, the GMC recruits its lateral companion cells transiting into subsidiary mother cells (SMCs) (stage3). Along with GMC expansion, SMCs convert into SCs through asymmetric divisions (stage4). The symmetric division of the GMC generates two immature GCs (stage5). Finally, GCs and SCs expand and differentiate, building up graminoid morphology (stage6) (Fig. 1B). These SCs supporter GCs in the molecular and mechanical perspectives to facilitate stomatal movement in response to environmental signals (Nunes, Zhang et al. 2020). Furthermore, this graminoid morphology is believed to increase the drought tolerance of grasses under dry climates (Chen, Chen et al. 2017). In one Pooidae species, *Brachypodium distachyon* (*Brachypodium*), it has been reported that mutant stomata failed to recruit SCs displayed faint responsiveness to changing light conditions, and closed slowly in darkness (Raissig, Matos et al. 2017). Studies from some agriculturally critical grasses, such as rice (*Oryza Sativa*), barley (*Hordeum Vulgare*), and maize (*Zea mays*), have described that the four-celled stomatal complex is essential in improving plant yield (Chen, Chen et al. 2017).

2. The Making of Stomata

In the light of numerous discoveries in *Arabidopsis* and studies in grasses, the genetic control of stomatal development is getting clear. Researchers have identified some early-acting genes responsible for stomata initiation and spacing, and late-acting genes participate in cell transitions and differentiation. The former comprises signaling peptides and their cognate receptors to mediate cell-cell communication, accompany by kinase cascades. Basic helix-loop-helix (bHLH) proteins are known to define cellular identity and polarity proteins associated with asymmetric divisions. The latter one consists of additional bHLH proteins that play roles within GCs specification, differentiation, and stomatal morphogenesis. Meanwhile, some cell cycle regulators regulate division.

2.1 Basic Helix-Loop-Helix (bHLH) proteins

Genome and functional analysis indicate many ancestral land plants employ the same core transcription factors (TFs) to direct stomatal development (MacAlister and Bergmann 2011, Chater, Caine et al. 2016, Raissig, Abrash et al. 2016, Ortega, de Marcos et al. 2019, Wu, Chen et al. 2019). Most of these TFs belong to the basic bHLH family, an ancient group that acts as the critical player for cellular identity in both plants and animals (Rhodes and Konieczny 1989, Weintraub, Davis et al. 1991). The over-cell identity and behavior in stomatal lineage also require the precise control of bHLH family TFs at specific time points. According to sequences in the bHLH domains and other domains or motifs, bHLHs are divided into several subgroups (Pires and Dolan 2010). *Arabidopsis* encodes for 158 bHLH proteins that are classified into 26 subfamilies. Five core bHLH family TFs have been demonstrated as positive regulators of stomatal development (Ohashi-Ito and Bergmann 2006, MacAlister, Ohashi-Ito et al. 2007, Pillitteri, Sloan et al. 2007, Kanaoka, Pillitteri et al. 2008). In particular, the subgroup Ia bHLHs, AtSPEECHLESS (AtSPCH), AtMUTE, and AtFAMA act sequentially to initiate "entry" asymmetric division of precursor cells, commit to stomatal fate and differentiate of GCs, respectively (Fig. 2A) (Ohashi-Ito and Bergmann 2006, MacAlister, Ohashi-Ito et al. 2007, Pillitteri, Sloan et al. 2007). Despite the share conserved motifs outside the bHLH region and appearing highly similar, their functions are unparalleled and incapable of replacing one another (MacAlister, Ohashi-Ito et al. 2007, MacAlister and Bergmann 2011). Throughout stomatal development, two additional IIIb group members, AtICE1 and AtSCREAM2 (AtSCRM2), work redundantly to coordinate the activities of AtSPCH, AtMUTE, and AtFAMA through heterodimerization (Fig. 2A) (Kanaoka, Pillitteri et al. 2008).

Leaf primordia arise from the shoot apical meristem, and the epidermis is specified simultaneously. At the earliest stomatal lineage fate, although the molecular mechanism activating the transition from protodermal cell to MMC is unknown, stomatal initiation and subsequent self-renew occur in meristemoids require the activity of AtSPCH. *AtSPCH* is broadly expressed in the MMCs of

young leaf and is restricted to the meristemoid that allows them to continue asymmetric division. *spch* mutant cannot initiate stomatal lineages and generate epidermis owns pavement cells solely. Other stomatal lineage markers cannot be detected in *spch* mutant. By contrast, *AtSPCH* overexpression causes excessive "entry" asymmetric division and epidermis with numerous small dividing cells (MacAlister, Ohashi-Ito et al. 2007). Thus, AtSPCH serves as a master regulator to promote asymmetric division that initiates, amplifies, and spaces future stomata in the epidermis. Along the expression of *AtSPCH* dies away in meristemoids, the bHLH protein AtMUTE emerges to terminate asymmetric division and specify the GMC fate. *mute* meristemoids get stuck in excessive self-renewing asymmetric division stage and break down during the transition from a meristemoid to a GMC. When *AtMUTE* is overexpressed, it results in an epidermis composed solely of stomata (Pillitteri, Sloan et al. 2007). The final transition from a GMC to a GC requires *AtFAMA*. This specific stage involves two separable events: symmetric cell division of the GMC and acquisition of the GC identity. *AtFAMA* represses GMC cell division ability and promotes GC transition (Ohashi-Ito and Bergmann 2006). Thus, *AtFAMA* loss of function mutants undergoes extra symmetric division, leading to the production of abnormally elongated GMCs with many short columns. At each of the cell-state transition stages, AtSPCH, AtMUTE, and AtFAMA heterodimerize with broadly expressed AtICE1 and AtSCRM2 to promote stomatal lineage transitions (Kanaoka, Pillitteri et al. 2008). Loss of single and double AtICE1 and AtSCRM2 terminates the stomatal lineage, resulting in phenotypes that resemble *spch*, *mute*, and *fama* mutants. For example, the *ice1scrm2* double mutant produces *spch* like phenotype. SCRM was initially named inducer of CBF expression 1 (ICE1) and identified as involved in chilling and freezing tolerance in *Arabidopsis* (Chinnusamy, Ohta et al. 2003). Notably, SCRM was reported as a gain-of-function mutation (*scrm-D*), which converts all epidermal cells into stomatal guard cells similar to an *AtMUTE* overexpression phenotype (Kanaoka, Pillitteri et al. 2008). Therefore, SCRM acts as an organizing node to unite the environmental cues and stomatal developmental process (Hetherington and Woodward 2003, Dong and Bergmann 2010).

The above paragraphs introduce three paralogous bHLH TFs AtSPCH, AtMUTE, and AtFAMA function as molecular switches to control distinct sequential stages during stomatal development in *Arabidopsis*. Despite the diversities in stomatal ontogeny, morphology, development, and leaf organization between monocots and dicots, based on comparative sequence analysis, functionally orthologous grass genes *SPCH*, *MUTE*, and *FAMA* have been investigated that required for stomatal development in grasses (Liu, Ohashi-Ito et al. 2009, Raissig, Abrash et al. 2016, Raissig, Matos et al. 2017, Wu, Chen et al. 2019).

Notably, compared to the single *SPCH* of the dicots *Arabidopsis*, a grass-specific *SPCH* duplication event has been revealed through protein sequences analysis. This discovery is surprising because grasses cannot achieve self-renewing that is mediated by a single *AtSPCH* in *Arabidopsis*. For example, rice and *Brachypodium* have two *SPCH* duplications, as well as potential three duplications of *SPCH* in maize (Liu, Ohashi-Ito et al. 2009, McKown and Bergmann 2020). In contrast to *OsSPCH1*, *OsSPCH2* is more similar to *AtSPCH* in the gene sequence. Furthermore, *OsSPCH2* and maize *SPCH* orthologs display conserved N-terminal domains, in which the transcriptional activation domain is located. Consistent with this finding, overexpression of *OsSPCH2* leads to more cell division in the pavement cells but not *OsSPCH1*(Liu, Ohashi-Ito et al. 2009). This indicates at least *OsSPCH2* is required to promote the early phase of rice stomatal development. More recently, in *Brachypodium*, it was described that *BdSPCH2* showed a stronger translational signal than *BdSPCH1* within the stomatal lineage. Moreover, the CRISPR/Cas9 targeting *bdspch2* single mutant exhibited an 80% reduction in stomatal density compared to a 20% reduction in *bdspch1* single mutant. While only null *bdspch1 bdspch2* double allele produced stomata less phenotype, this suggests that *BdSPCH1* and *BdSPCH2* act partially redundant for establishing stomatal lineage fate, but *BdSPCH2* occupies a dominant role (Raissig, Abrash et al. 2016). In addition, due to the missing degradation-associated PEST domain that is associated with phosphorylation regulatory in BdSPCH1 and

BdSPCH2, BdSPCH1/2 can be accumulated and result in ectopic stomatal lineage phenotypes in their overexpression assays. In contrast, no such phenotypic class represents when *AtSPCH* is overexpressed. Taken together, SPCH paralogs in grasses function conservatively to determine stomatal fate, but not completely equivalent to *AtSPCH*.

ICE/SCRM also builds the “alternatively wired” grass-specific pathway to regulate stomatal formation. In contrast to the *AtICE1/AtSCRM2* act redundantly through the whole stomatal development event, in *Brachypodium*, the group IIIb proteins BdICE1/BdSCRM2 acquire individual functions with distinct partnerships regulate overlapping stages of stomatal development. *BdICE1* mutation arrests stomatal lineage initiation and produces normal epidermal cells but lacks stomata completely. In the absence of *BdSCRM2*, the mutant still has four-celled complexes, but GCs fail to differentiate into stomata correctly in morphology (Raissig, Abrash et al. 2016). Hereafter, *BdICE1* primarily functions at the start of stomatal development to initiate “entry” asymmetric division, assisting to *BdSPCH1/2*. *BdSCRM2* plays a role later during the differentiation of GMCs, suggesting BdSCRM2 perhaps is the functional binding partner of later bHLHs, such as BdFAMA. This concludes that ICE/SCRM appear to have divergent roles in grass stomatal development. However, the overexpression signal of *BdICE1/SCRM2*, as well as *BdSPCH1/2,* were clearly only detected within stomatal cell lineages, implying that spatial regulation of these genes is essential for the stomatal pattern across the epidermal cell files.

The recruitment of flanking SCs is a universal trait among grass stomatal complexes. These cells have been recognized to support altering aperture size and further improve stomatal physiology (Chen, Chen et al. 2017). Despite their significant role, surprisingly, our knowledge about how SCs are developmentally regulated remains elusive. Again, in *Brachypodium*, a forward genetic screen identified a mutant *sid* fails to produce SCs and instead forms dicot-like two-celled stomata (Raissig, Matos et al. 2017). For the first time, researchers got the opportunity to test the importance of SCs to grass stomatal

physiology. *sid* stomata without SCs cannot respond to changing light conditions as rapidly as wild-type, confirming the critical function of SCs. Through whole-genome sequencing, *sid* plants were discovered that contain 5–base pair (bp) deletion on *Brachypodium* homolog, *BdMUTE* genome. Instead of contributing to terminate asymmetric division in meristemoid cells and define the GMC fate, as the job *AtMUTE* takes in *Arabidopsis*. *BdMUTE* shows signs of playing a role in establishing SMC identity, and some of the BdMUTE proteins travel from GMCs to neighboring SMCs based on expression and localization evidence (Raissig, Matos et al. 2017). *MUTE* orthologues in grasses are necessary for specifying SMC identity. However, *MUTE* appears to diverge its function associated with GMC fate. Despite *BdMUTE* mutants failing to recruit SCs entirely, only 30% of the GMCs represent defects with aberrant misoriented division planes, and plants are still alive (Raissig, Matos et al. 2017). In maize, the ethyl methane sulfonate (EMS) mutagenized line *zmmute* is completely unable to form stomatal complexes with normal GC morphology. By contrast to the longitudinal division orientation of GMCs division in wild-type, loss-of-function of *ZmMUTE* leads to the transverse or diagonal directional division of GMCs, producing elongated GCs with short columns (Wang, Guo et al. 2019), indicating that *ZmMUTE* is critical for specifying GMC identity, similar to *AtMUTE*. F-actin patches are not accumulated obviously at the SMCs/GMCs contact, and nuclei are unpolarized in SMCs from *zmmute* plants, which suggests that *ZmMUTE* also plays a role in determining SMC polarity. Thus, *ZmMUTE* mutation results in GCs division dramatic defects and the loss of SCs, then eventually seedling lethality. The expression pattern of ZmMUTE is observed in early GMCs and then detected in neighboring SMCs, supporting the mobile capability of ZmMUTE protein, as is seen with BdMUTE in *Brachypodium* (Wang, Guo et al. 2019). In rice, CRISPR/Cas9 genome editing line *osmute* fails to terminate the asymmetric division in stomatal precursor cells and convert the cell fate from precursor cells to GMCs, finally producing excessive small arrested precursor cells without SCs in the epidermis. Therefore, OsMUTE combines the ability to promote stomatal precursor cells to GMC conversion as *AtMUTE* and the function on SCs recruitment identical to *BdMUTE*. Some swollen GCs with transverse or

diagonal directional division planes are present in *osmute* mutants, similar to that of *ZmMUTE* mutation in maize (Wu, Chen et al. 2019). According to the comparative overexpression assay between maize and rice, *ZmMUTE* overexpression converts all epidermal cells into stomata resembling *AtMUTE* overexpression. In contrast, ectopic overexpression of *OsMUTE* produces excessive divisions in the epidermis with loads of small cells, which is the similar phenotype showing in the *AtSPCH* overexpression line (Pillitteri, Sloan et al. 2007, Liu, Ohashi-Ito et al. 2009, Wang, Guo et al. 2019), implying that MUTE might employ different ways to achieve SCs formation and determine GMCs fate in grasses.

The coordination between the recruitment of SCs and the differentiation and morphogenesis of GCs at the final step is essential to build a functional four-celled stomatal complex during grass stomatal development. This process may require the function of *AtFAMA* homologs and *FOURLIPS(FLP)* (Wang, Guo et al. 2019). *OsFAMA* and *ZmFAMA* display highly identical to *AtFAMA*. The expression pattern of the *OsFAMA* transcript indicates its consistent role in regulating the late stage of stomatal development as *AtFAMA* (Liu, Ohashi-Ito et al. 2009). The GCs in the *osfama* mutant formed box-shaped instead of a dumbbell-shape, but no extra divisions were observed. This suggests that *OsFAMA* promotes guard cell differentiation but not cell division. Additionally, *OsFAMA* may initiate the SMC to SC fate transition and SMC asymmetric division with partner *OsICE1*. In *Arabidopsis*, *AtMUTE* directly targets *AtFAMA* and *AtFLP*, enabling single symmetric cell division in GMC through their repression on cell-cycle genes expression (Han, Qi et al. 2018). *OsFLP* and *OsFAMA* do not control the times of GMC divisions in rice. Notably, *OsFLP* was identified to maintain the proper direction of GMC symmetric division (Wu, Chen et al. 2019). More interestingly, *SCARECROW* (*SCR*) and *SHORT ROOT* (*SHR*), two genes that were initially been discovered involved in the development of roots and shoots, also participate in stomatal developmental processes in rice. *OsSCR* and *OsSHR* mutants displayed arrested meristemoids, reduced stomatal density, and abnormal SCs, revealing that they can control the initiation of stomatal lineage cells and the recruitment of SCs,

and the transcription level of *OsSCR* is triggered by *OsSPCH* and *OsMUTE* (Wu, Chen et al. 2019).

2.2 Signaling peptide regulates stomatal development

Together with the above bHLH transcription factors, a family of cysteine-rich intracellular signaling peptides regulates plenty of processes in stomatal development. These EPIDERMAL PATTERNING FACTORS (EPFs and EPF-like (EPFLs)) and their associated receptor kinases ERECTA (ER) family are well-specified in *Arabidopsis*. AtEPF1 and AtEPF2 are both released from stomatal lineage cells: *AtEPF2* acts primarily to regulate asymmetric entry divisions in meristemoids (Hara, Yokoo et al. 2009), whereas *AtEPF1* takes following responsibility for enforcing stomatal one-cell spacing rule (Hara, Kajita et al. 2007). The loss-of-function of *AtEPF2* leads to increased stomatal density, and the *atepf1* mutant displays both the increase in stomatal density and stomatal clusters. Taken together, *AtEPF1* and *AtEPF2* serve as negative regulators of stomatal development in *Arabidopsis*. Conversely, the EPF-like peptide, AtEPFL9, also named STOMAGEN, is produced in the mesophyll. STOMAGEN positively triggers stomatal lineage initiation by functioning as a competitor of AtEPF2 for binding receptor complex (Hunt, Bailey et al. 2010, Sugano, Shimada et al. 2010).

The orthologues of patterning factors, *AtEPF1/2*, also have been characterized in grasses. Julie E. Gray's group discovered EPF-overexpressing barley, rice, and wheat plants exhibit significantly reduced stomatal density (Hughes, Hepworth et al. 2017, Caine, Yin et al. 2019, Dunn, Hunt et al. 2019). The ectopically overexpressed *EPF1* created arrested stomatal development, aborted SCs, and aberrantly GMCs formation. Interestingly, *OsEPF2* enables partially rescuing the phenotypes of *AtEPF1* and *AtEPF2* mutants. However, *OsEPF1* can only partially complement the *AtEPF1* mutant but not the *AtEPF2* mutant (Lu, He et al. 2019). Therefore, the functions of *EPF2* are conserved in rice and in *Arabidopsis*. The divergent function of *EPF1* might be due to the missing of successive asymmetric division ability in grasses. The loss-of-function study is more blurred than overexpression analysis regarding the

patterning genes in grasses. Only the genome editing of *OsEPFL9-1* has been described so far. *OsEPFL9-1* displays a higher sequence similarity than *OsEPFL9-2.* Its disruption resulted in an 8-fold reduction in stomatal density (Yin, Biswal et al. 2017), identical to the significantly lower stomatal density observed in *OsEPFL9-1* RNAi plants (Lu, He et al. 2019). Furthermore, overexpression of *OsEPFL9-1* and *OsEPFL9-2* caused distinct organ-specific phenotypes; stomata clusters existed at the rosette of leaves and hypocotyl with *OsEPFL9-1*-overexpressed plant, whereas with *OsEPFL9-2,* excessive stomata were exclusively observed at hypocotyl (Lu, He et al. 2019). This indicates these two *OsEPFL9* equivalents retain similar but different features in their functions. Taken together, EPF/EPFL is a highly conserved peptide in dicots and monocots.

Manipulation of peptide factors is potentially a promising way of crop improvement through altering stomatal density. The significant reductions of stomatal density from *HvEPF1*, *OsEPF1*, and *TaEPF1* overexpression lines triggered improved drought tolerance and higher water use efficiency in barley, rice, and wheat (Hughes, Hepworth et al. 2017, Caine, Yin et al. 2019, Dunn, Hunt et al. 2019), whereas did not impact the grain production. It is mysterious if *EPF* driven modulation performs in parallel to bHLH transcription factors regulation for stomatal density.

2.3 Signaling through receptors and MAPK cascade

Environmental signals have been reported to modulate development via improving or reducing the levels of EPF/L family ligands. Consequently, in *Arabidopsis*, signal transduction went through EPF/L. It was perceived by the ERECTA family (ERf) of leucine-rich repeat (LRR) receptor-like Ser/Thr kinases (RLKs) and the receptor-like kinase, TOO MANY MOUTHS (TMM). TMM is a cell-surface protein expressed in stomatal precursor cells, and it includes extracellular LRRs and a transmembrane domain but lacks a cytoplasmic kinase domain. TMM is involved in a receptor complex to sense positional cues that control the orientation of spacing divisions and inhibit asymmetric divisions to form the stomatal spacing pattern (Geisler, Nadeau et al. 2000). Mutations

in TMM randomized the orientation of asymmetric divisions and produced excess stomata in leaves.

The genetic screen has discovered new mutations in the ER gene to gain more insights into its function. ER signal has been identified to control various aspects of plant development and growth and responses to biotic and abiotic stresses (Lease, Lau et al. 2001). ER enables the regulation of organ shape and inflorescence architecture; the *er* alleles are all recessive and cause diverse organ growth phenotypes throughout the whole plant's life, for example, shorter petioles, inflorescence, pedicel, and fruits than wild-type. This is mainly because of the disruption of ER function to promote cell proliferation during organ development (Lease, Lau et al. 2001). The version of ER missing kinase domain (Δ kinase) caused more severe growth defects phenotype than *er* mutant, indicating that the truncated ER protein presents with dominant-negative effects and redundancy exists in ER signaling pathway (Shpak, Lakeman et al. 2003). The ER's closest paralogous ERECTA-like receptors, ERL1 and ERL2, can partially complement the *er* growth phenotype when triggered by ER promoter. Additionally, although *erl1* and *erl2* mutations do not have any obvious growth phenotype, they exaggerated *er* defects in a different manner, suggesting they participate in ER signaling pathway but with distinct functions (Shpak, Berthiaume et al. 2004). The triple mutant *er erl1 erl2* displayed spacing defects and stomatal clustering patterns. TMM associates with ER-family as a complex work to negatively regulate stomatal cell fate. TMM confers contrasting functions to regulate stomatal pattern in leaves, siliques, and stem organs, and stoichiometric dynamics of epistasis exists among *TMM, ER, ERL1,* and *ERL2.* Thus, these four receptors stay in close proximity to determine stomatal pattern and differentiation (Shpak, McAbee et al. 2005). Although this signaling pathway remains unknown in grasses, orthologs of TMM and two ER families have been identified in *Brachypodium* (Abrash, Anleu Gil et al. 2018). The EPF/L family ligands are perceived by the ER-family and TMM receptor complex in *Arabidopsis*. Sequentially the intracellular signaling is transduced through the downstream mitogen-activated protein (MAP) kinase signaling pathway.

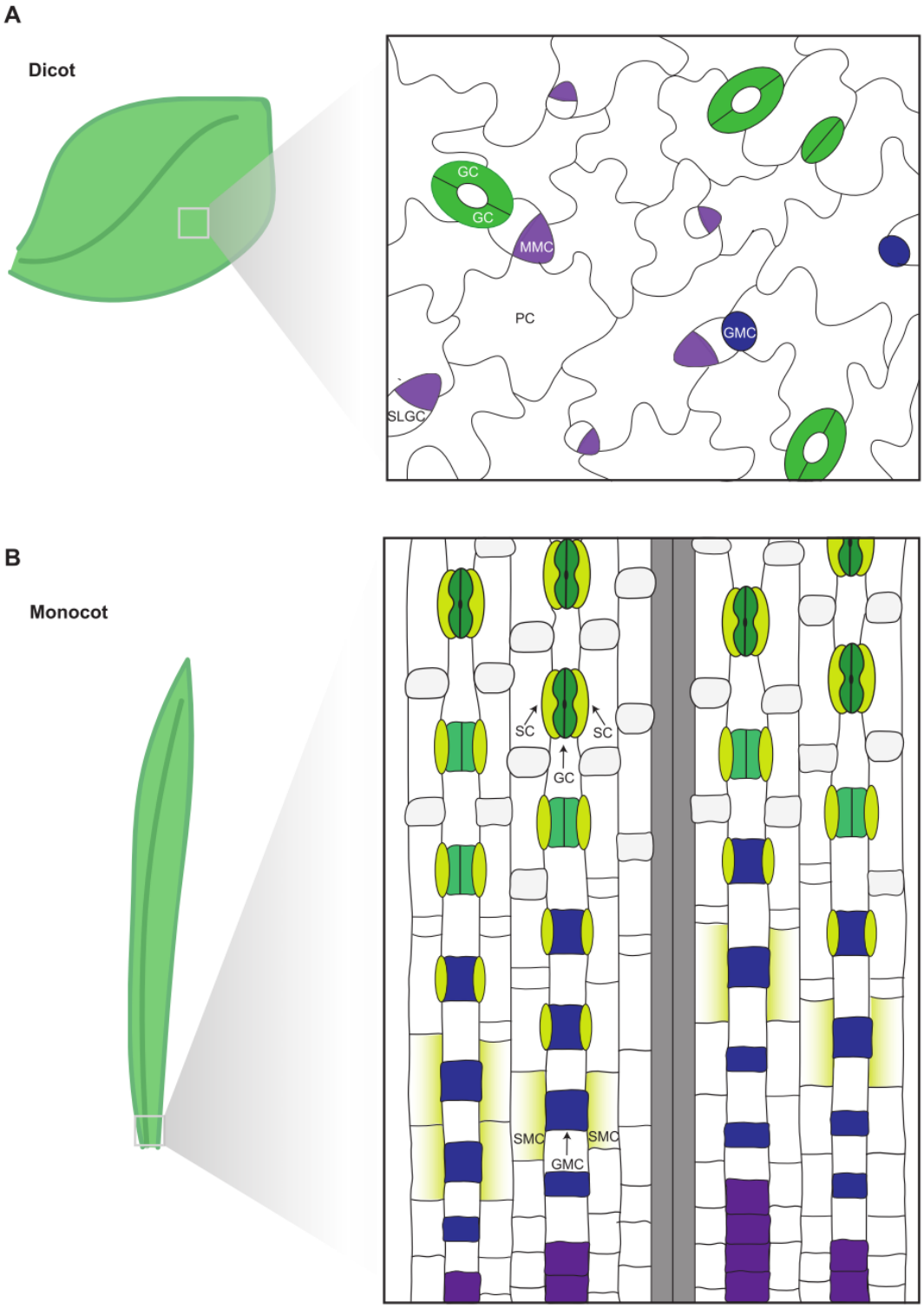

Figure 1. Comparison of stomatal lineage development in dicots and monocots.
(A) Stomatal development in *Arabidopsis*: stomatal meristemoid mother cells (MMCs, purple) generate stomatal lineage ground cells (SLGCs), which will differentiate into pavement cells (PCs), and meristemoids, which eventually transition into guard mother cells (GMCs, blue). GMCs divide to generate the two guard cells (GCs, green). (B) Stomatal development in *Brachypodium distachyon*: in a stomatal file, the smaller cell of an asymmetric division becomes a GMC (blue) and laterally induces subsidiary mother cell

(SMC) fate (yellow). SMCs divide asymmetrically before GMCs divide symmetrically, and the complex matures.

3. Cell Polarity

Living systems build a marvelous spatial network critical for their development and growth. This network is organized by establishing the asymmetric distribution of subcellular domains, known as cell polarity. Polarity can determine the division orientation, cell shape, and different fates in daughter cells at the cell level. At the tissue and organ level, cell polarity can provide spatial information to influent the plane of tissue, the positioning, and patterning of organelles. Compared to yeast and animal cells, the principles and mechanisms studies of cell polarity in plants are more limited. João Jacob Ramalho et. al proposed three distinct polarity categories: localized growth polarity, transient polarity, and axial polarity. Localized growth polarity comprises the extremely polarized tip growth of pollen tubes and root hairs, in which proteins are unevenly distributed in the individual cell. Transient polarity includes stomatal lineage in *Arabidopsis,* where polarization and subsequent oriented ACD occur during a fixed time appear at a leaf section. Axial polarity forms a general and basal body axis independent of cell types within an organ, such as the embryonic axis (Ramalho, Jones et al. 2022).

3.1 Polarity proteins in plant cells

The plant cells behave a variety of polarity required for fundamental growth and patterning during development. For example, the formations of the pollen tube and root hair demand highly polarized tip growth (Guan, Guo et al. 2013, Mendrinna and Persson 2015). The structure of stomatal complexes in dicot and monocot requires tightly mediated lineage determination, multidimensional ACDs, cell-fate transition, and differentiation (Guo, Wang et al. 2021). Polarity is also the key to some specialized cell functions, such as directional uptake of nutrients or efflux and influx of phytohormones, which can be achieved by the polarization of relevant transporters (Yoshinari and Takano 2017). The hallmark of cell polarity is the uneven localization of regulatory molecules in the cell.

Some well-recognized proteins include auxin transporters PIN family, the small GTPase ROPs and the scaffold proteins BASL, POLAR, and BRX family in stomatal development (Muroyama and Bergmann 2019).

Polarized distribution of auxin influences numerous aspects of plant growth and development, including the establishment of the apical-basal axis during embryogenesis in *Arabidopsis* (Friml, Vieten et al. 2003), root hair formation (Benkova, Michniewicz et al. 2003), and aerial organs growth (Gallei, Luschnig et al. 2020). Auxin gradients are established and maintained mainly via the polarization of transporters. PIN-FORMED (PIN) transmembrane carriers facilitate the directional auxin efflux. Its five family members (PIN1, PIN2, PIN3, PIN4, and PIN7) showed polarization at the plasma membrane in a cell-type-specific manner in *Arabidopsis* (Adamowski and Friml 2015). During early embryo development in *Arabidopsis*, PIN1, PIN4, and PIN7 polarized localization guide auxin enrichment towards different areas of the embryo. Consequently, the apical-basal axis and the division patterning are specified (Friml, Vieten et al. 2003). In the root, the polarization of PIN proteins at different cell layers controls designated directional auxin to flow, for example, PIN1 and PIN7 localized to the basal domain in the vasculature drives a root tip–toward auxin flow. On the contrary, the apical localization of PIN2 in the epidermis directs to shoot-toward auxin movement (Blilou, Xu et al. 2005).

Among all eukaryotic organisms, the Rho family of small GTPases are conserved regulators required to establish of cell polarity. Empirical studies indicate that the Rho GTPases OF PLANTS (ROPs) are closely related to the cytoskeleton and vesicular trafficking (Craddock, Lavagi et al. 2012). ROPs are polarized into dispersed plasma membrane domains in tip-growing cells, including pollen tubes and root hairs (Molendijk, Bischoff et al. 2001). Meanwhile, several ROP domains can also coexist in a single cell to promote more complex morphogenetic transformation, for example, the lobe formation in pavement cells and the patterning of the cell wall in xylem cells (Fu, Li et al. 2002, Oda and Fukuda 2012). ROPs cycle between membrane-bound and cytoplasmic locations is spatiotemporally regulated by GTPase activity via

GTPase-activating proteins (GAPs) (Wu, Li et al. 2000), guanine nucleotide exchange factors (GEFs) (Berken, Thomas et al. 2005), and Rho GDP dissociation inhibitors (RhoGDIs) (Bischoff, Vahlkamp et al. 2000). However, the interactors and mechanisms underlying establishing ROP polarized domains rely on plant species and cell type. The commonly used way to maintain ROP self-organization is the combination of positive feedback and inhibitory mechanisms (Muroyama and Bergmann 2019).

3.2 Cell polarity in stomatal development

Although monocots and dicots display different stomatal complex morphologies, 4-celled and 2-celled, respectively, the construction of both types demands extremely regulated ACD that defines cell fates in daughter cells. In the model plant *Arabidopsis*, several polarized proteins associated with stomatal development have been deciphered in past decades. The eudicot-specific protein, BREAKING OF ASYMMETRY IN THE STOMATAL LINEAGE (BASL), was first identified during stomatal ACD and can drive MMC asymmetry (Dong, MacAlister et al. 2009). *basl* mutants produce symmetrically stomatal divisions, causing stomatal clusters and grouped stomatal precursors. Before an ACD, BASL protein accumulates in the MMC nucleus and polarizes in a cortical crescent, which can faithfully predict asymmetric division orientation. BASL is only inherited by the SLGC and maintained for several hours at the membrane after an ACD (Dong, MacAlister et al. 2009). The tomato BASL is also polarized and participates in stomatal asymmetric divisions, but the model of division types diverges between the species (Nir, Amador et al. 2022). The polarized BASL associated with YDA MAPK components, the MAPKKK YODA (YDA) and MAPK 3 and 6, constitute a polarity module at the cortex. The BASL-MAPK positive-feedback loop represents a mechanism that links cell polarity to fate determination during asymmetric cell division in plants (Zhang, Wang et al. 2015). The BREVIS RADIX (BRX) family of proteins were identified as interaction partners of BASL and their cortical position is coincident with BASL except for nuclear localization (Bringmann and Bergmann 2017, Rowe, Dong et al. 2019). Additionally, POLAR LOCALIZATION DURING ASYMMETRIC

DIVISION AND REDISTRIBUTION (POLAR) is another plant-specific protein that involves the stomata lineage and depolarizes in *basl* mutants (Pillitteri, Peterson et al. 2011). POLAR seems not to interact with BASL directly but serves as a stomatal lineage scaffold by recruiting BRASSINOSTEROID INSENSITIVE 2 (BIN2) and other GSK3-like kinases to the cytosol polarity crescent, in which BIN2 suppresses the YDA MAPK signaling module, as a consequence, SPCH accumulates and drives the stomatal ACD (Houbaert, Zhang et al. 2018). BSL1 was reported that colocalize with polarized BASL, and the polarization of BSL1occurs in MMCs at the onset of mitosis when PPB appear (Guo, Park et al. 2021). As a phosphatase protein, BSL1 modulates the placement of BIN2 between the nucleus and cell polarity complex in MMCs via its phosphatase activity (Guo, Park et al. 2021). In addition, BSL1 dephosphorylates and activates YDA, further elevating the MAPK signalling pathway. Thus, BSL1 can promote the transition from MMC cell division to the specification of SLGC cell-fate differentiation (Guo, Park et al. 2021).

In monocots, grass-specific graminoid morphology displays a four-cell stomatal complex consisting of two GCs and two SCs. The formation of such a stomatal complex requires a series of coordinated ACDs. A stomatal precursor cell goes through an ACD to produce a GMC. During GMC elongation, it may release unknown signals to prompt the neighboring cells to transform and acquire SMCs identities (Facette and Smith 2012). The SMCs subsequently divide asymmetrically and vertically to form SCs in contact with GMC, and the GMC then divides symmetrically and longitudinally to generate a pair of GCs. Multiple polarity regulators required for proper SMC asymmetric divisions have been characterized through the genetic and cytological studies in *Zea mays*. ZmBRICK (ZmBRK) family belongs to the SCAR/WAVE regulatory complex and is the earliest known marker of SMC polarity, which polarizes at the GMC/SMC interface (Facette, Park et al. 2015). The SCAR/WAVE regulatory complex may activate the ARP2/3-mediated actin nucleation (Facette, Park et al. 2015). Genetic screens identified the catalytically inactive leucine-rich-repeat receptor-like kinase (LRR-RLKs) ZmPANGLOSS2 (ZmPAN2) and

ZmPAN1, which act cooperatively to promote division asymmetry in SMC, moreover, the polarized accumulation of ZmPAN1 relies on ZmPAN2. Mutations of either gene lead to defective SMC divisions and aberrant SCs formation (Cartwright, Humphries et al. 2009, Zhang, Facette et al. 2012). The ZmPAN1 and ZmPAN2 proteins accumulate asymmetrically at the GMC/SMC interface to promote the formation of actin patches, which seemed to drive the SMC nucleus directionally migrate to the site of SC formation (Humphries, Vejlupkova et al. 2011). ZmPAN1 physically interacts with and induces the polarization of the type I Rho of Plants (ROP) GTPases, ZmROP2, and ZmROP9, to promote asymmetric SMC division (Humphries, Vejlupkova et al. 2011). Conversely, ZmROP2 and ZmROP9 physically interact with and may activate the SCAR/WAVE complex, resulting in Arp2/3-mediated actin polymerization, then actin patches form at a late stage of SMC polarization (Facette, Park et al. 2015).

The preprophase band (PPB) is a highly organized cytoskeletal array forecasting the edging of the future division plane. Therefore the formation of PPB indicates the cell entering mitosis (Livanos and Muller 2019). Before and after SMC ACD, the SMC nucleus migrated against and towards the GMC/SMC interface, respectively (Muroyama, Gong et al. 2020, Guo, Wang et al. 2021). During SMC ACD, the mechanical signal produced by the differential elongation rate between GMCs and SMCs precedes the positions of PPB (Nunes, Zhang et al. 2020). PPB is positioned to guide the phragmoplast extension within the pre-mitotic SMC. Previous work suggested that a monopolar prophase microtubule spindle supports nuclear migration and anchors the SMC nucleus to the polar site and proximal to GMCs (Panteris, Apostolakos et al. 2006). Finally, after a proper PPB is established and the SMC nucleus has migrated to the GMC/ SMC interface, asymmetric SMC division occurs along the PPB, which is functionally promoted by DISCORDIA1 (DCD1) (Gallagher and Smith 1999, Wright, Gallagher et al. 2009). Generally, mutations in all genes implicated in establishing SMC polarity result in mis-specified and abnormally divided SCs to different extents, and these genes act synergistically to promote SMC polarity (Facette and Smith 2012, Facette, Park et al. 2015).

Nuclear migration before asymmetric cell divisions has been observed and studied in multiple cell types of plants, such as pollen tubes, trichomes, and root hair tips (Griffis, Groves et al. 2014). Muroyama et al. identified that nuclear movements correlate with ACD orientation in *Arabidopsis* stomatal lineage cells. Drug treatments and time-lapse imaging discovered that different from the actin-dependent nuclei pre-division movement in most plant systems, pre-division nuclear migration requires the microtubule cytoskeleton in MMCs (Kimata, Higaki et al. 2016, Muroyama, Gong et al. 2020). On the contrary, the post-division nuclear migration is actin-dependent in MMCs. The BASL/BRX polarity crescent is the spatial landmark to orient nuclear migration. Nucleus moves away from the polarity crescent before ACD in MMCs and reorients toward the polarity site in SLGCs after ACD. Instead, nuclear display stochastic motion in *basl* before and after ACD, indicating that polarity crescent formation is essential for both nuclear migrations in the stomatal lineage (Muroyama, Gong et al. 2020). The daughter cells formed with roughly identical sizes due to the random nuclear movements in *basl.* Thus, stomatal clusters were produced because of an inability to orient divisions (Muroyama, Gong et al. 2020). This study provides a broader understanding of how polarity factors and cell mechanics interact. However, SMCs utilize actin for pre-division nuclear migration, which demands the polarity factors ZmBRK1, ZmPAN1, and ZmPAN2 in *Zea mays* (Cartwright, Humphries et al. 2009, Zhang, Facette et al. 2012, Facette, Park et al. 2015).

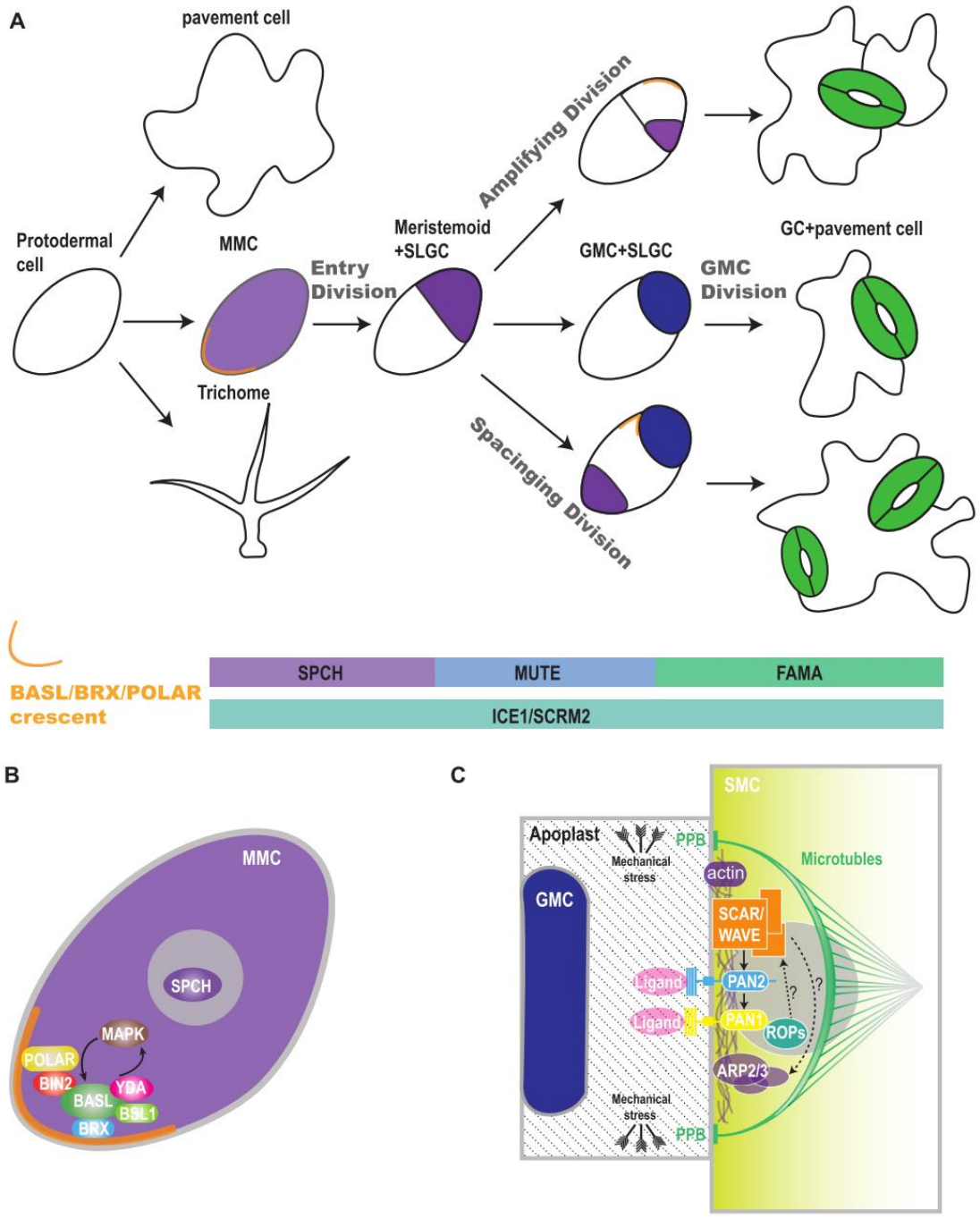

Figure 2. Cell polarity drives asymmetric cell division during stomatal formation in dicots and monocots.

(A) Distinct divisions during stomatal development, and model of bHLH transcription factors control stomatal development in *Arabidopsis*. The protodermal cells enable to become meristemoid mother cell (MMC, light purple), pavement cell, and trichome. MMC initiates the stomatal lineage through an entry asymmetric division to create two daughter cells, a smaller meristemoid (dark purple) and a larger stomatal lineage ground cell (SLGC). The meristemoid can go through a limited number of amplifying divisions to generate new satellite meristemoid but eventually differentiate into a guard mother cell (GMC, blue). The GMC divides symmetrically to form two equally-sized guard cells (GC, green). Alternatively, a meristemoid can differentiate into GMC directly. The SLGC can undergo spacing division to produce a pavement cell and a satellite meristemoid positioned away from an existing stomatal precursor. The bHLH transcription factors SPCH, MUTE, and FAMA together with ICE1/SCRM2 are responsible for the establishment of stomatal lineage, GMC transition,

and GC transition, respectively. (B) In meristemoid of *Arabidopsis*, a polarity domain (orange) defined by BASL (dark green), BRX (blue), and POLAR (yellow) drives asymmetric cell division and differential fate in daughter cells. Polarized POLAR could recruit BIN2 (red) to inhibit the kinase activity of YDA (pink). BSL1 (light green) associates with the BASL polarity complex. Polarized BSL1 inhibits BIN2's function at the PM and activates YDA through its phosphatase activity. Positive feedback between BASL and MAPK (brown) and BIN2 mediation are critical for the calibration of SPCH (purple) expression level, consequently, determine the polarity establishment and fate establishment. (C) Model of SMC polarization in maize. During GMC longitudinal elongation, the different elongation rate between GMC and SMC induced the generation of a mechanical signal, consequently, triggering SMC polarizes SCAR/WAVE complexes (orange) and formation of the preprophase band (PPB, green). Then, SCAR/WAVE promotes the polarization of PANGLOSS2 (PAN2, blue), which polarizes PAN1 (yellow) that then recruits Rho of Plants (ROPs, turquoise). Next, ROPs might then activate SCAR/WAVE complexes, which activate actin-related proteins (ARP) 2/3 complexes (purple) to trigger actin filament accumulation at the GMC/SMC interface earlier than nuclear migration. Nuclei are positioned by a monopolar prophase spindle and cell division occurs simultaneously with the formation of PPB. In addition to the mechanical signal, unidentified ligands (pink) might bind to the PANs to trigger SMC polarization.

4. Stomatal Physiology

The balance of gas exchange between the leaf and atmosphere by stomata governs CO_2 uptake for photosynthetic carbon assimilation (A) and restricts water loss through transpiration. The stomatal pore is surrounded by two specialized GCs, which in some plants are accompanied by SCs. GC movements regulate the size of the stomatal pore through turgor and GC volume adjustment. The increase of turgor in GCs gives rise to stomatal opening, while the decrease of turgor leads to stomatal closure. Stomatal movements are controlled by several environmental factors, such as light, humidity, temperature, and CO_2 concentration. GC continuously senses these environmental abiotic and biotic stimuli and integrates them to change osmotic potential (Kim, Bohmer et al. 2010, Kollist, Nuhkat et al. 2014). The speed of stomatal movement is determined by the ability of GCs to sense environmental information, converse the signal, and cause changes in cell turgor.

Stomatal conductance (g_{sw}) is the quantitative rate of the amount of water vapor that goes through the stomatal pore (in mol sec^{-1} m^{-2}). It has been identified that photosynthetic efficiency was correlated with stomatal conductance when other elements were not limiting (Wong, Cowan et al. 1979). Low stomatal conductance restricts the assimilation rate by limiting CO_2 passing through the stomata and, accordantly, will influence the carbohydrate level of the leaf with

consequences for crop production. Water-use efficiency (WUE) is defined at a range of scales of how much carbon plants gain relative to lost water molecules, has been considered a critical constraint on crop yield. Thus, the trade-off between photosynthesis and transpiration directly influent WUE. Rapid stomatal movement can balance CO_2 influx with transpirational water loss more efficiently and benefit plants under water limitation conditions (Lawson and Vialet-Chabrand 2019). The grasses that contain innovative graminoid morphology have been recognized for fast stomatal responses with improved stomatal kinetics (Franks and Farquhar 2007, Raissig, Matos et al. 2017).

The transport of ions and water through ion pumps, transporters, and channels proteins across the plasma membrane and in the vacuolar membranes changes the osmotic pressure of GCs, thereby regulating stomatal opening and closing (Kollist, Nuhkat et al. 2014). It was reported that SCs not merely play as ion reservoirs but also mechanically accommodate GCs movement by adjusting osmotic potential and turgor pressure contrast to GCs. Consequently, the reciprocity of ion shuffling between the GCs and SCs promotes the responsiveness of grass stomata (Franks and Farquhar 2007, Nunes, Zhang et al. 2020).

5. Brachypodium: A Grass Model for Recent Discovery

As a botanist and author, John Hendley Barnhart put forward the Poaceae concept in 1895 (Barnhart 1895), the most species-rich in the graminid clade (Keller and Feuillet 2000). Poaceae is a large plant family of Monocotyledons flowering plants commonly referred to as grasses, meanwhile is economically crucial for food production for human and domesticated animals, and is increasingly used in manufacture. *Brachypodium distachyon* was proposed as a new model system for the grasses study in 2001 (Draper, Mur et al. 2001). The phylogenetic position of *Brachypodium* is relatively close to cereal crops such as *Triticum Aestivum* (wheat), rice, and maize, and near to most of the important temperate cereals and forage grasses (Draper, Mur et al. 2001). Diploid ecotypes *Brachypodium* displays the smallest genome size in the described several species of Poaceae and contains five pairs of distinctive

chromosomes (Draper, Mur et al. 2001). Furthermore, *Brachypodium* possesses a small stature of around 20 cm height when the plant matures, a rapid life cycle of fewer than 4 months, the ability to self-fertile, simple growth conditions required, and high seed yield (Draper, Mur et al. 2001). In the last two decades, the internet resources for *Brachypodium* research have been becoming broad. The International Brachypodium Initiative described the high-quality genome sequence of *Brachypodium* in 2010, and *Brachypodium* mains one of the smallest grass genome sizes, approximately 272 Mb (International Brachypodium 2010). A large number of DNA libraries and microarrays, extensive collections of T-DNA mutants and mutagenesis populations, a broad-scale gathering of natural accessions and inbred lines, highly developed bioinformatics resources, and efficient transformation methods are boosting the use of *Brachypodium* by a rapidly growing research community (Brkljacic, Grotewold et al. 2011).

6. CRISPR/Cas9 System Applied in Grasses

Rapid, precise, and efficient genome editing technologies are valuable and significant for molecular biosciences. Most genome editing approaches take advantage of sequence-specific nucleases (SSNs) to cause a DNA double-strand break (DSB) within a genome. DSBs can be repaired subsequently by nonhomologous end joining (NHEJ) or homologous recombination (HR) (Kanaar, Hoeijmakers et al. 1998). Through targeted DNA DSBs tie with repair pathways to achieve mutations or modifications at desired genome loci. Currently, SSNs consist of meganucleases (Stoddard 2005), zinc finger nucleases (ZFNs) (Urnov, Rebar et al. 2010), transcription activator-like effector nucleases (TALENs) (Moscou and Bogdanove 2009), and clustered regularly interspaced short palindromic repeats (CRISPR) / CRISPR-associated Protein9 (CRISPR/Cas9) (Jinek, Chylinski et al. 2012, Cong, Ran et al. 2013). Meganucleases, ZFNs, and TALENs, have not been widely applied in the plant research community since they are challenging to construct technically and expensive. Strikingly, CRISPR/Cas9 system mediates RNA-guided DSBs effectively. Cas9 protein, CRISPR RNA, and trans-activating CRISPR RNA are required for DNA cleavage in CRISPR/Cas9. Later, a single guide RNA (gRNA) was created to replace the function of two RNA components,

which significantly simplifies the CRISPR/Cas9 system (Jinek, Chylinski et al. 2012, Cong, Ran et al. 2013). As a result, CRISPR/ Cas9 provides the potential for multiple genome engineering simultaneously (Li, Norville et al. 2013). Yiping Qi lab developed a CRISPR/ Cas9 toolbox for monocots and dicots utilizing Golden Gate and Gateway cloning approaches to assemble different compatible cloning modules (Lowder, Zhang et al. 2015). They use the popular small RNA promoter U6 or U3, fusion transcriptional regulators, and diverse gRNA expression cassettes to establish a multiplex CRISPR/Cas9 genome-editing system, achieving effective genome editing and transcriptional regulation. The function and effectiveness of this toolbox have been successfully verified in tobacco (*Nicotiana benthamiana*), *Arabidopsis*, and rice. The streamlined assembly protocol they offered only takes three steps and can be complemented within 10 days.

Taking advantage of TALENs and the CRISPR/ Cas9 system, Daniel F. Voytas and his group reported a comprehensive toolkit targeting gene knockouts, replacements, and modified transcriptional regulations in many plant species (Čermák, Curtin et al. 2017). This genome editing toolkit provides one set of direct cloning vectors to enable fast cloning to create targeted gene knockouts. The other set of modular vectors was designed to assemble different functional components for multiplex gene engineering demands. Furthermore, they accomplished the simultaneous multiple gRNAs expression via applying Csy-type (CRISPR system yersinia) ribonuclease 4 (Csy4) and tRNA processing enzymes. This was proved with the results that targeted several genes deletions in both dicots and monocots utilizing up to 12 gRNAs.

Most recently, GROWTH-REGULATING FACTOR 4 (GRF4) and its cofactor GRF-INTERACTING FACTOR 1 (GIF1) from wheat has burst on the scene after their chimeric protein GRF–GIF1 was shown to improve the efficiency and speed up regeneration in crops (Debernardi, Tricoli et al. 2020). Technologies combined GRF–GIF1 with CRISPR–Cas9 system facilitates genome editing efficiency. Moreover, transgenic plants were fertile and grew normally.

7. Arabidopsis TANGLED (TAN1) Marks the Division Plane

Plant cells are embedded and restricted within a matrix of cell wall substances. Hence the relative placement of cells is established by the orientation of the division plane at cytokinesis. Consequently, correct positions of division planes, future cell walls during development are essential for the overall organization of plant tissues. Cell walls are determined by consequent formation and placement of three characteristic microtubule arrays: the preprophase band (PPB), a cortical ring of microtubule and actin microfilaments, which assembles in the late interphase, maintains throughout prophase, then disappears during nuclear envelope breakdown; the mitotic spindle forms in metaphase and anaphase; the cytokinetic phragmoplast, arises between the daughter nuclei and guides the new cell wall attachment at the former PPB site during telophase and cytokinesis (Van Damme 2009).

Previous studies implicated that microtubule-binding protein TANGLED1 (TAN1) is mainly involved in determining the orientation of division planes in maize (Smith, Hake et al. 1996, Cleary and Smith 1998, Smith, Gerttula et al. 2001). The *tangled-1* mutation causes misguided phragmoplasts and aberrant cell division. In *Arabidopsis*, the localization and function of the *TANGLED* orthologue (*AtTAN1*) have been investigated. AtTAN1-YFP can colocalize with PPB at the cortical division site, remain the localization after PPB assembly, and persistently during mitosis and cytokinesis. The cortical division site of AtTAN1 demands the participation of microtubule and kinesins PHRAGMOPLAST ORIENTING KINESIN 1 and 2 (POK1, POK2) (Walker, Müller et al. 2007). *AtTAN1* plays a critical role in the guidance of expanding phragmoplasts to the division site forecasted by PPB (Walker, Müller et al. 2007). POK1 and POK2 were identified during a yeast two-hybrid screen for interacting proteins of TAN1, and share sequence homology (Müller, Han et al. 2006). The double mutants *pok1;pok2* have a remarkable resemblance with maize *tan1* mutants, demonstrated by misoriented cell wall in root meristem and embryo morphogenesis, accompanied by misoriented mitotic microtubule arrays (Müller, Han et al. 2006). *POK1* and *POK2* perform their functions

redundantly in the spatial control of cytokinesis by interacting with AtTAN1 (Müller, Han et al. 2006, Walker, Müller et al. 2007).

8. Myristoylation Plays an Essential Role in Membrane Targeting

Myristoylation is one approach to implement protein lipid-modification, which contributes to multiple biological processes, including protein-protein interaction, localization of proteins to organelles or the plasma membrane, influencing protein stability, and so on (Wright, Heal et al. 2010). The process of attaching 14-carbon fatty acid, myristates, to the N-terminal glycine of proteins through an amide bond is known as myristoylation. The myristate transfer process is catalyzed by the ubiquitous eukaryotic enzyme N-myristoyl transferase (NMT), which uses myristoyl-coenzyme A (CoA) as a substrate. The addition of myristoyl-CoA to a protein typically occurs during co-translational after removing the leader methionine residue by methionine aminopeptidase. In addition, post-translationally myristoylation can rarely occur on an internal glycine exposed by caspases in the apoptotic cascade (Udenwobele, Su et al. 2017). Myristoylation was applied to anchor proteins to the cytoplasmic sides. At the N-terminal of myristoylated proteins, (M^1) G^2XXXS^6/T^6, a consistent sequence is pivotal and indispensable for myristoylation (Nalivaeva and Turner 2009).

9. The Roles and Visualizations of Cytoskeleton in Plants

Filaments Actin (F-actin) are dynamic structures and play crucial roles in numerous cellular processes in cell division (Rasmussen, Wright et al. 2013), cytoplasmic streaming (Geitmann and Nebenfuhr 2015), organelle positioning (Takagi 2003), and cell morphogenesis (Hussey, Ketelaar et al. 2006). The establishment of genetic and biochemical approaches and the development of light microscopic methods dramatically facilitated the study of actin dynamics.

Almost two decades ago, microinjection of fluorescent-phalloidin conjugates provided the first glimpses into the dynamics of the F-actin in vivo (Bresnick,

Warren et al. 1990). Phalloidin contains the capacity to bind F-actin specifically and inhibit its depolymerization (Cooper 1987). Fluorescent derivatives of phalloidin have been extensively used to localize actin filaments for light microscopy in fixed or live cells. Alexa Fluor 488-phalloidin has been utilized to observe actin cytoskeleton in rice root cells (Yang, Ren et al. 2011, Zhang, Zhang et al. 2011), as well as in the pollen, root tip, leaf epidermis, and stomatal cells of maize (Vitha, Baluska et al. 1997, Gibbon, Kovar et al. 1999, Cartwright, Humphries et al. 2009, Panteris, Achlati et al. 2018). This approach remains essential for studying actin function in fixed plant cells, offering more benefits than the widely used F-actin reporters in live cells (Collings and Wasteneys 2005, Wilsen, Lovy-Wheeler et al. 2006). However, since phalloidin into living cells will affect actin organization patterns and cell mobility (Cooper 1987), and microinjection is invasive and only has limited use in fixed cells, various fluorescent probes have been identified and become more convenient to be used for F-actin visualization in plant cells.

Initially, fusion proteins actin–GFP were utilized to visualize the localization and dynamics of actin, while this direct binding with tag would undermine its activity (Westphal, Jungbluth et al. 1997, Al-Bassam, Ozer et al. 2002). Additionally, the irrelevant fluorescence emitted by unpolymerized actin–GFP could interfere with the observation of F-actin. To solve these problems, actin side-binding proteins with GFP-tagged were applied for studying the actin cytoskeleton. The C-terminus of mouse talin (mTn) contains 197 amino acids, which produces a highly conserved F-actin binding domain. The expression of mTn attached with GFP can be used to label actin cytoskeleton in a diverse group of living plant cells (Kost, Spielhofer et al. 1998, Xu, Wang et al. 2002). In addition, the actin-binding domain (ABD) from fimbrin has been utilized extensively for imaging F-actin in living plant cells. Fimbrin is a 68kDa polypeptide identified as a prominent component of the microvillus core bundles of microvilli in intestinal epithelial cells. Moreover, it presents in the cell surface of membrane ruffles and microspikes (Bretscher and Weber 1980). In plants, a 76 kDa fimbrin-like polypeptide (AtFim1) was first isolated from *Arabidopsis*. This predicted polypeptide possesses significant similarity with non-plant fimbrins and

contains two tandem repeats, each of which owns a 27 amino acid region characterized as a putative actin-binding domain (ABD) (McCurdy and Kim 1998), which is a hallmark of actin cross-linking proteins families such as fimbrins, α-actinin, dystrophin, β-spectrin and ABP-120 (Dearruda, Watson et al. 1990, Adams, Botstein et al. 1991). The stable transformation of GFP-ABD2, a fusion protein between GFP and the second actin-binding domain (ABD2) of AtFim1 in tobacco BY-2 cells and *Arabidopsis* cell cultures, would enable the visualization of actin microfilaments (MF) and investigate the dynamic actin organization and turnover during time-sequential observations (Sheahan, Staiger et al. 2004, Sano, Higaki et al. 2005).

However, overexpression of endogenous ABD2 has already been suggested to affect actin-myosin interplay, which would disturb the mobility of cellular compounds' actin-associated processes (Holweg 2007). It was described that Lifeact, a first 17-amino-acid peptide of yeast protein Abp140 fused to C-terminal GFP (Lifeact-GFP) could be applied as a universal marker for actin visualization. Furthermore, Lifeact probes did not exert side effects on actin dynamics (Riedl, Crevenna et al. 2008). Lifeact labeled filamentous actin has been developed in different plant species, such as liverwort *Marchantia polymorpha*, moss *Physcomitrella*, *Lilium formosanum*, *Nicotiana tobacum*, and *Arabidopsis* (Era, Tominaga et al. 2009, Vidali, Rounds et al. 2009, Smertenko, Deeks et al. 2010). Lifeact-Venus appears to be a practical approach for studying the actin cytoskeleton in many plant categories.

Microtubules (MTs) are an essential cytoskeleton component that mediates many fundamental cellular processes, including cell division (Rasmussen, Wright et al. 2013), intracellular transport (Geitmann and Nebenfuhr 2015), cell wall formation, and morphogenesis (Paredez, Somerville et al. 2006, Fujita, Himmelspach et al. 2011, Oda and Fukuda 2013) in eukaryotic cells. α-tubulin (TUA) and β-tubulin (TUB) dimers polymerize to form MTs via binding with GTP in a head-to-tail pattern (Wong and Hashimoto 2017). At least six a-tubulin and nine β-tubulin were reported in *Arabidopsis* (Kopczak, Haas et al. 1992, Snustad, Haas et al. 1992). Microtubule-associated proteins (MAPs) regulate

the dynamic stability of MTs by binding tubulin subunits (Drewes, Ebneth et al. 1998, Al-Bassam, Ozer et al. 2002), serving as the cross-bridged with MTs connect with other proteins or other organelles (Hamada 2007). The expression of a recombinant protein, GFP fused to the mammalian microtubule-associated protein 4 (MAP4) would enable visualization of the microtubule arrangements in living epidermal cells (Marc, Granger et al. 1998). Furthermore, MAP4 binds to MTs specifically via the microtubule-binding domain (MBD), a conserved domain between plants and animals, and has been developed as a reporter gene to label microtubules in vivo and in vitro (Hugdahl, Bokros et al. 1993, Marc, Granger et al. 1998).

The visualization of MTs is a strong demand to investigate the connection between MTs and above biological processes. In *Arabidopsis* living cells, the distribution patterns of MTs were observed by visualizing the fluorescence of fusion protein GFP-TUA6 in a stable transformant (Ueda, Matsuyama et al. 1999). To preclude the aberrant right-handed helical growth of petioles and petals in GFP-TUA6 lines, GFP-TUB6 marker lines were generated to trace the dynamic behavior of MTs with drug treatment (Nakamura, Naoi et al. 2004). In *Brachypodium*, we created the MTs marker version employing the chimeric protein in which Turquoise was fused to the N-terminus of BdTUB6 (Bradi2g21340).

10. TurboID-Mediated Proximity Labeling

Protein-protein interactions (PPIs) and protein compartmentalization are essential for almost all cellular processes. A broad number of methods have been established and developed to study the proteins' activity and interaction networks at a cellular level. However, there are intrinsic restrictions corresponding to some traditional methods respectively, for example, Fluorescence resonance energy transfer (FRET) can be used to measure the interaction efficiency between two light-sensitive molecules in spatial-temporal dynamics with extreme sensitivity, but FRET is unable to identify unknown interactors or protein complex. Moreover, one pair fluorophore with less background noise is required for FRET (Sekar and Periasamy 2003);

Bimolecular fluorescence complementation (BiFC) is a powerful method typically used to visualize PPIs directly in living cells, as well as is available for weak interactions and low expression proteins, while BiFC is irreversible and impotent to provide real-time detection (Kerppola 2006); Two-hybrid screens are not available to detect the interactions between high-affinity proteins in vitro, and also give rise to high false-positive rate (Auerbach and Stagljar 2005). Alternatively, Co-immunoprecipitation (Co-IP) is an effective technique that is applied to isolate proteins via direct or indirect interaction to target proteins in a complex, while it is limited to identifying low affinity and transient PPIs and also is not capable of isolating low amounts or insoluble proteins and those expressed in rare tissues or cell types (Lin and Lai 2017).

In response to these weaknesses, enzyme-catalyzed proximity labeling (PL) has emerged to discover interacting or proximal proteins and proteomes of novel biological structures in live cells (Roux, Kim et al. 2012, Han, Li et al. 2018). Biotin ligase-based PL utilized an engineered labeling enzyme biotin ligase targeted to the protein of interest. The addition of substrate biotin initiates the covalently biotinylate interaction with neighboring proteins within a marking radius around 10 nanometers to the labeling enzyme. Subsequently, these labeled proteins can be harvested by affinity purification and analysis through protein mass spectrometry (MS) (Kim and Roux 2016, Branon, Bosch et al. 2018). PL based on BioID, a mutant E. coli biotin ligase (BirA), can be achieved easily and is non-toxic to living samples, and has successfully applied to screen interacting proteins and uncover subcellular compartments (Roux, Kim et al. 2012). The main weakness of BioID, however, is its low catalytic activity, which demands the biotin labeling time can be extended for 24 hours to generate adequate biotinylated proteins (Branon, Bosch et al. 2018). Alice Y. Ting and her group developed two highly active promiscuous ligases, TurboID and miniTurbo, from mutated BirA variants using directed evolution (Branon, Bosch et al. 2018). TurboID enables rapid labeling time (~10 mins), stable performance in various subcellular organelles, and producing larger proteome size along with increasing labeling time. Even though miniTurbo behaves 1.5-2-fold less kinetics than TurboID, it owns more precise temporal control in the

labeling time and provides less background. Additionally, it has a smaller protein size (28 versus 35 kD), which secures the fusion protein transportation and function more than TurboID (Branon, Bosch et al. 2018).

Due to the endogenous biotin expression, unstable biotin absorption efficiency existence and plant culture temperature being lower than the best temperature for enzyme catalysis, some attempts to apply BioID in plant systems have not achieved good results as expected in previous work (Lin, Zhou et al. 2017, Conlan, Stoll et al. 2018, Khan, Youn et al. 2018). Dominique C. Bergmann's lab reported that both TurboID and miniTurbo performed effective PL in stably transformed *Arabidopsis* and transiently transformed *N. benthamiana* leaves. Furthermore, they verified the potential of TurboID to identify protein complexes and proteomes in stomatal cell type by determining new partners and protein compositions for AtFAMA in young guard cells using AtFAMA-TurboID (Mair, Xu et al. 2019). Zhiyong Wang group applied PL-MS of BIN2-TurboID and revealed multiple formerly proven interactors and broad new proximal proteins of BIN2, which established the framework of an extensive GSK3/BIN2 mediated network in *Arabidopsis*. This study demonstrated that TurboID is a powerful approach for mapping signaling networks (Kim, Park et al. 2019). Hence, PL based on expressing the TurboID fusion with interested proteins using cell-type-specific promoters will be widely implemented in plants and turn into a valuable tool for the plant community.

11. Brassinosteroid Signaling Plays a Role During the Stomatal Development

Brassinosteroids (BRs) are steroid phytohormones crucial for plant growth and development. They have participated in multiple developmental and physiological processes in *Arabidopsis*, such as cell division, cell elongation, cell differentiation, fertility, photomorphogenesis, and stress tolerance. Accordingly, mutant plants defective in BR synthesis and signaling pathways displayed obvious phenotypes, including short stature, petite and round-shaped leaves, short petioles, and limited plant fertility (Li and Chory 1997). In *Arabidopsis*, the leaf growth is resolved by expanding individual cells and cell

proliferation. The dwarf leaf phenotype in BRs biosynthetic mutant, *de-etiolated2* (*det2*), was a function of remarkably decreased cell size and cell number, which could be rescued by exogenous BRs treatment (Nakaya, Tsukaya et al. 2002), indicating that BRs facilitate leaf growth by positively regulating both cell expansion and cell proliferation. The loss-of-function BRs insensitive *bri1-116* null mutant displayed reduced root growth and smaller root apical meristems, implying that BRs are essential for proper cell-cycle progression in the root meristem (Gonzalez-Garcia, Vilarrasa-Blasi et al. 2011). Regarding the mechanism BRs associated with cell division, there was evidence supported that BRs promote cell division through upregulating transcription of the *CYCLIND3* (*CYCD3*) (Hu, Bao et al. 2000), which mediates cell division activated by cytokinins (Riou-Khamlichi, Huntley et al. 1999); In Tobacco BY-2 cell suspension, the brassinolide (BL) application induced the increased accumulation of B-type cyclin (*CYM*) and *histone H4* (Miyazawa, Nakajima et al. 2003), whose transcripts level are the hallmarks of M phase and the S phase, respectively (Reichheld, Sonobe et al. 1995, Ito, MarieClaire et al. 1997). Concerning cell differentiation in plant development, BRs play pivotal roles in controlling the differentiation of cells to form leaf shape in the margin (Reinhardt, Hanggi et al. 2007) and determining the time of cell differentiation in the root meristem of *Arabidopsis* (Pavelescu, Vilarrasa-Blasi et al. 2018). Besides the small root meristem that occurs in *bri1 brl1 brl3* triple mutants account for reduced cell elongation, protophloem differentiation is impaired in mutants suggesting BRs signaling guides formative cell divisions and protophloem sieve element differentiation in the *Arabidopsis* root meristem (Kang, Breda et al. 2017).

BRs are perceived extracellularly at the cell surface, where they directly bind to BRASSINOSTEROID INSENSITIVE 1 (BRI1) LRR-RLK family (Li and Chory 1997), thereby triggers the binding of a coreceptor protein is SOMATIC EMBRYOGENESIS RECEPTOR KINASE 3 (SERK3)/ BRI1ASSOCIATED KINASE1 (BAK1) (Nam and Li 2002, Russinova, Borst et al. 2004). The formation of a BRI1-BAK1 heterodimer initiates an intracellular phosphorylation cascade that relays BR signals to the transcription factors BRASSINAZOLE-

RESISTANT 1 (BZR1) (Wang, Nakano et al. 2002) and BRI1-EMSSUPPRESSOR 1 (BES1) (Yin, Wang et al. 2002), which control thousands of BR-regulated gene expression and hence regulate growth and development events in the plant (He, Gendron et al. 2002, Sun, Fan et al. 2010). When BRs are absent, the glycogen synthase kinase3 (GSK3)-like kinase BRASSINOSTEROID INSENSITIVE 2 (BIN2) phosphorylates the homologous transcription factors BZR1 and BES1, thus inhibiting their DNA binding activities by promoting their cytoplasmic retention and degradation via binding to 14-3-3 proteins (Li, Nam et al. 2001, He, Gendron et al. 2002, de Vries 2007). Therefore, BIN2 operates as a negative regulator in the BR signaling pathway (Li, Nam et al. 2001). BIN2 can also phosphorylate the AUXIN RESPONSE FACTORs (ARFs) from their repressor proteins AUXIN/INDOLE-3-ACETIC ACID (AUX/IAA), positively regulating auxin-mediated lateral root development (Cho, Ryu et al. 2014). Furthermore, it was investigated that BIN2 possesses direct interaction with OCTOPUS (OPS), an active master of phloem cell differentiation and vascular patterning in the root meristem (Truernit, Bauby et al. 2012). OPS works as a positive regulator of BR signaling through interacting with BIN2, restraining BIN2 repression on BES1 and BZR1 to promote phloem differentiation (Anne, Azzopardi et al. 2015). *ops* phloem differentiation defects are recovered when BIN2 activity is inhibited (Anne, Azzopardi et al. 2015). BRX is also a positive regulator for optimal root growth, and root protophloem cells constantly fail to differentiate correctly in *brx* mutant (Mouchel, Briggs et al. 2004). The reduced root growth phenotype in *brx* can be rescued with BR application (Mouchel, Osmont et al. 2006). Taken together, these results could reflect the fact that BR signaling takes part in the root protophloem differentiation.

Despite the differences in the number of cotyledons and flowers, arrangement of leaf veins and vascular bundles, stomatal morphology, and other characteristics between monocots and dicots, BR biosynthetic and signaling pathways are conserved mainly between representatives of these two angiosperms. For example, *DWARF4*, encoding the enzyme that catalyzes the final steps of BR biosynthetic in *Arabidopsis*, has been identified in rice

(Sakamoto 2006) and maize (Makarevitch, Thompson et al. 2012). Likewise, the receptor BRI1 has orthologs with the same functions in rice (Yamamuro, Ihara et al. 2000), maize (Kir, Ye et al. 2015), and barley (Chono, Honda et al. 2003), respectively. *OsBZR1* and *ZmBZR1* also perform the same transcription factor functions as *BES1/BZR1* in rice and maize separately (Tong and Chu 2012, Manoli, Trevisan et al. 2018). In *Brachypodium*, both the sequence and function of *BdBRI1* were reported to be conserved. *BdBRI1* RNAi mutants displayed a classical BR insensitive phenotype, and altered the expression of BR-related genes (Feng, Yin et al. 2015). However, the heterologous overexpression of *BdBRI1* could not rescue dwarf phenotypes of *bri1-5* mutant plants, which is a weak allele of *AtBRI1* (Corvalan and Choe 2017). This suggests that a *Brachypodium* version of *BRI1* is incompetent to perform as the BR receptor in *Arabidopsis*, possibly due to the different functions and structures between AtBRI1 and BdBRI1 (Corvalan and Choe 2017). Heterologous expression of the *BIN2* ortholog *BdBIN2* in *Arabidopsis* affected plant height and fertility greatly, implying that *BdBIN2* is capable of working as a negative regulator of the BR signaling pathway in *Brachypodium* (Corvalan and Choe 2017). Moreover, orthologs of enzymes DWARF4, BR6ox2, and CPD involved in BR biosynthesis are under negative feedback regulation in *Brachypodium*, the same as the regulated mechanism of genes located downstream of BR in *Arabidopsis* (Corvalan and Choe 2017). Ultimately, there are similarities and some differences between the BR biosynthesis and signaling pathways in *Arabidopsis* and *Brachypodium* from previous observations.

It was reported that BR could regulate stomatal density. The kinase BIN2 directly controls SPCH activity through phosphorylation. When BR is present, and thereby BIN2 is inhibited, inactivated BIN2 stabilizes SPCH to trigger stomatal development (Gudesblat, Schneider-Pizon et al. 2012). Strikingly and almost simultaneously, BIN2 was characterized as containing the ability to inhibit YDA kinase activity through phosphorylation, promoting stomatal production (Kim, Michniewicz et al. 2012). The above two investigations demonstrate that BRs regulate stomatal development through *BIN2* controls

SPCH activity directly or mediates the MAPK signaling pathways. In addition, Eugenia Russinova identified *AtPOLAR* play as a scaffolding protein to mediate the transient polarization of BIN2 with BASL, and its turnover requires phosphorylation by BIN2 (Houbaert, Zhang et al. 2018). Thus, POLAR-BIN2–BASL polarity module redundantly works with the MAPK signaling pathway to regulate ACDs during stomatal development in *Arabidopsis*.

Results

1. Forward Genetic Screening of NaN Lines

In my PhD study, I want to discover novel players in SMC and SC formation using forward and reverse genetics. Firstly, I screened through the NaN mutant population available in our lab in a forward genetics approach. NaN lines are a whole-genome resequenced mutant population mutagenized by sodium azide. The Brachypodium Project (BRACHYTIL) at INRA research team from France constructed a reference of NaN induced mutant population of 6000 M2 families and provided the phenotype characterization and sequence information on mutant genes.

To identify and evaluate the SC formation related phenotypes among the NaN lines, our student helpers Deniz Bak and Yigit Berkay Gündogmus grew 10 plants per mutant family, harvested the third leaves from each individual line (~18-21 days after germination (dag)), fixed the leaves in 7:1 EtOH: Acetic acid then mounted on Hoyer's solution. I imaged and counted aberrant SCs for fixed leaves on slides under the light microscope. Among my screening work from around 100 NaN lines, NaN99, NaN191, and NaN230 displayed abnormal stomata phenotypes. In particular, NaN99 and NaN191 both showed SC defective phenotypes, and NaN99 showed stronger severe phenotypes compared with NaN191 (Fig. 3). In NaN99, approximately half of SCs were affected, whereas, in NaN191, approximately one-fourth showed a mutant phenotype. NaN230 appeared to have GC morphogenesis defects, with some GCs being completely collapsing while others failed to form a proper dumbbell shape (Fig. 3). Importantly, all these lines were whole-genome resequenced; NaN99, NaN191, and NaN230 have 38, 53, and 135 non-synonymous homozygous mutations, respectively. However, no obvious or previously described candidate is among the lists. This means that I will have to use rough mapping to narrow down the candidates and that all mutants represent novel factors.

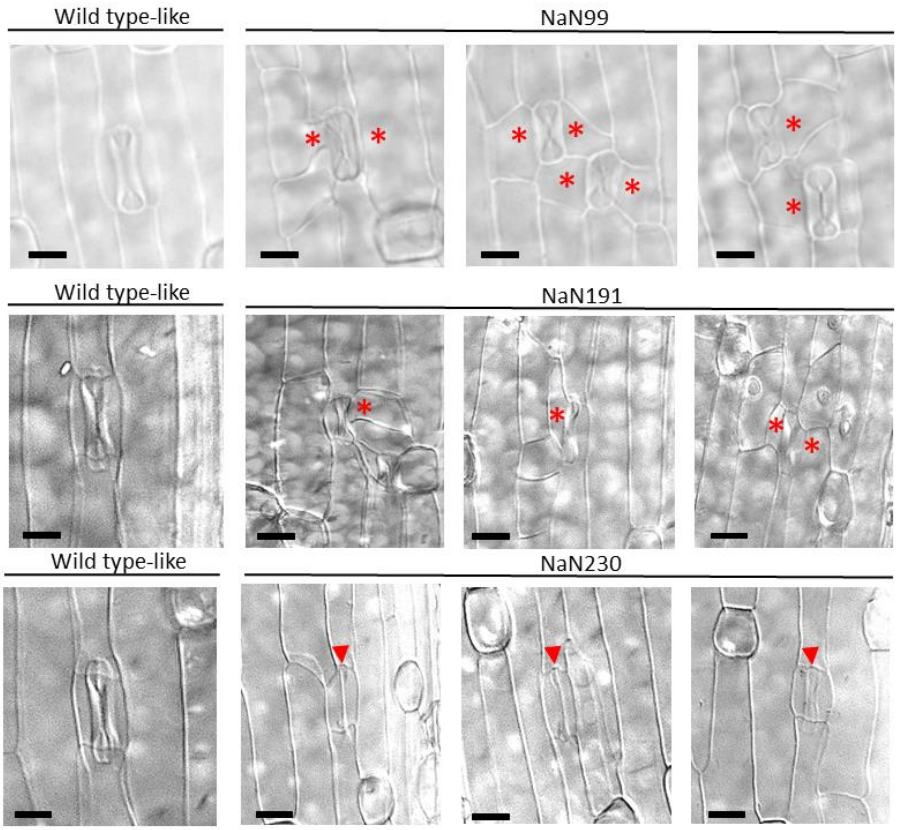

Figure 3. NaN99, NaN191, NaN230 display aberrant stomata phenotypes.
Differential interference contrast (DIC) images of the epidermis in NaN99, NaN191 and NaN230. Red asterisks indicate the defective SCs. Red arrowheads indicate the aberrant GCs. Scale bars, 10 μm.

The rough mapping for NaN99, NaN191 and NaN230 are ongoing to identify the responsible genes for each phenotype. Bd3-1 was used as the second ecotype to cross with NaN lines from the Bd21-3 background. I tested the mapping primers from each arm of the five different chromosomes. Among 7 F1 seeds from Bd3-1 X NaN99 crossing, 6 crossed seeds were confirmed real F1 except individual #5 (Fig. 4). Only rough mapping is needed to narrow down the chromosomal region due to the known candidate mutations for NaN lines being fully re-sequenced in M3/M4.

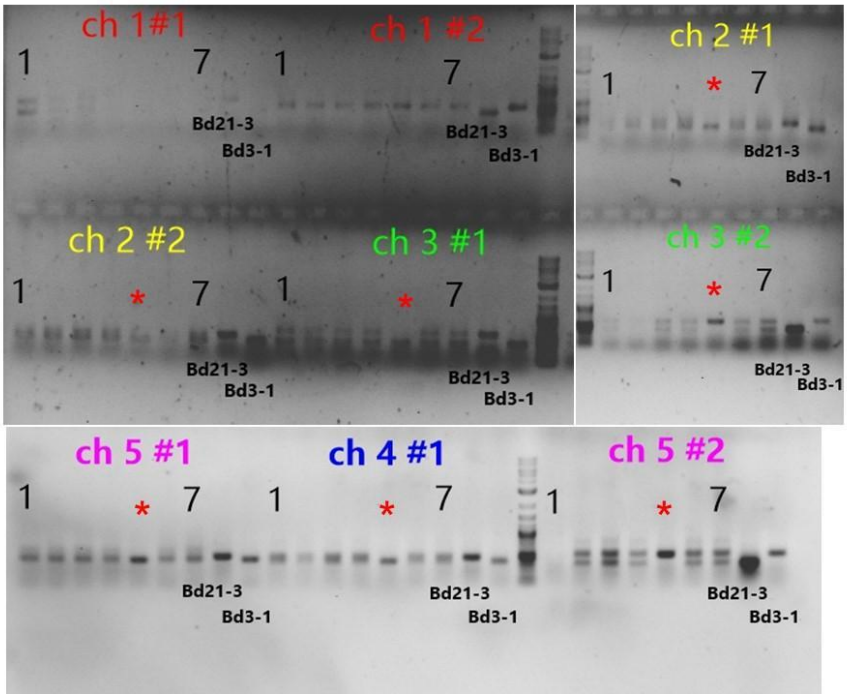

Figure 4. Test marker primers.
Primer pDZ64-pDZ80 (Table 12) were designed as markers for five different chromosomes to distinguish Bd21-3 and Bd3-1 two ecotypes in *Brachypodium.* Red asterisks indicate the individual #5 F1 plant which is not a real crossing offspring.

2. Opposite Polarity Programs Regulate Asymmetric Subsidiary Cell Divisions in Grasses

2.1 Comparative transcriptomics identify a role for BdPOLAR in SC development

To identify novel factors that participate in SC development among the grass stomatal lineage, Michael T Raissig comparatively assessed the transcriptome of the developing *Brachypodium* leaf zone from wild-type (with SCs) and *bdmute/sid* (without SCs) (Fig. 5A). In the RAN-seq results, among the 35 downregulated genes in *bdmute* (Table 1), the fourth most downregulated gene, *BdPOLAR* (Bradi3g54060) (Fig. 5B), was the homolog of *Arabidopsis POLAR* (At4g3180). POLAR protein is polarly localized with unknown function and is associated with ACD in the Arabidopsis stomatal lineage (Houbaert, Zhang et al. 2018). Its transcripts level difference between two genotypes (wild-type vs. *bdmute*) is around 12 folds. To evaluate the functional relevance of *BdPOLAR*, I performed the forward genetic approach by screening available NaN lines with high impact at *BdPOLAR* mutation sites. Additionally, reverse

genetic strategy CRISPR/Cas9 was applied to characterize the function of *BdPOLAR*.

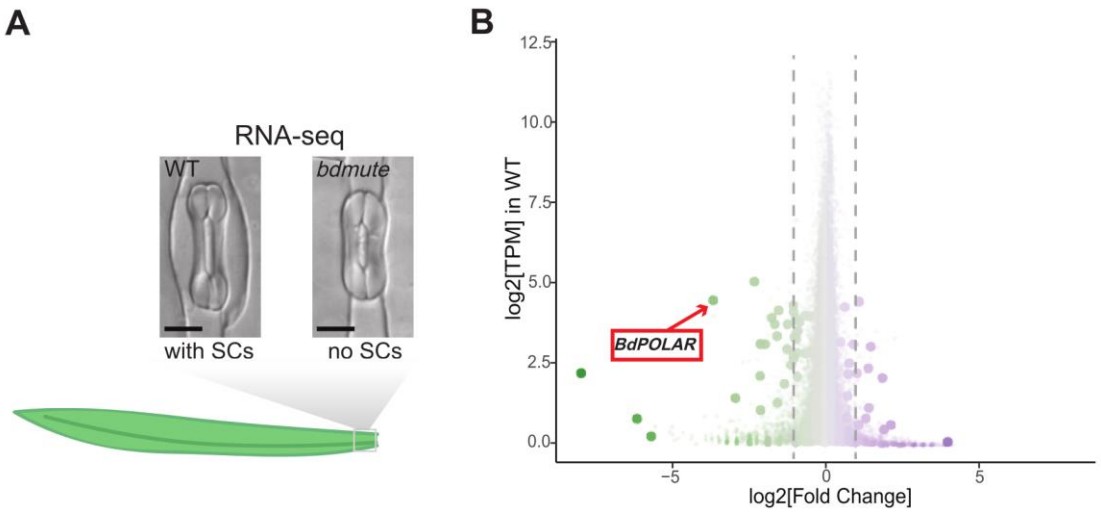

Figure 5. *BdPOLAR* is identified in comparative RNA-seq.
(A) The developmental zone of WT and *bdmute* were used for RNA-seq. (B) Volcano plot showing WT expression level (y-axis) and fold change in *bdmute* compared to WT (x-axis) of all expressed genes in the developmental zone. Each dot represents one gene. Green and large dots indicate genes significantly downregulated in *bdmute*; Purple and large dots indicate genes significantly upregulated in *bdmute*. The red circle indicates *BdPOLAR* (Bradi3g54060).

Bradi	log2 Fold Change	P value	P adj	WT dev_TPM	*sid* dev_TPM
Bradi4g28540	-7.86207	2.69E-10	7.54E-07	3.976939	0
Bradi4g33000	-6.05379	2.07E-05	0.016712	0.793241	0
Bradi2g01380	-5.60354	0.000188	0.09957	0.210068	0
Bradi3g54060	-3.60385	7.18E-63	2.01E-58	24.42838	1.969339
Bradi5g10357	-2.87745	4.12E-09	8.88E-06	1.855288	0.246654
Bradi1g45600	-2.26431	7.70E-24	7.19E-20	37.62869	7.649014
Bradi3g56507	-2.0842	6.67E-07	0.000886	3.660758	0.841113
Bradi2g54300	-2.07695	3.93E-25	5.51E-21	8.585959	1.988542
Bradi1g04970	-2.0714	1.74E-05	0.014816	1.176278	0.27623
Bradi3g13630	-1.93337	1.12E-22	7.85E-19	8.547857	2.179889
Bradi2g17530	-1.70856	1.41E-07	0.000198	16.21315	4.859469
Bradi1g69220	-1.62126	2.50E-11	7.78E-08	13.9417	4.409421
Bradi5g10027	-1.53964	8.09E-08	0.000119	10.42138	3.487401
Bradi1g73690	-1.52702	1.05E-05	0.009837	1.558272	0.526946
Bradi1g65780	-1.4824	1.98E-06	0.002225	19.26951	6.739868
Bradi3g46760	-1.30515	6.96E-07	0.000886	2.90358	1.148354

Bradi4g31740	-1.21075	1.30E-08	2.27E-05	7.536751	3.187225
Bradi5g26150	-1.19532	2.10E-09	4.90E-06	13.93905	5.934374
Bradi1g34930	-1.08792	1.69E-05	0.014816	4.940304	2.275017
Bradi2g57297	-1.02064	8.07E-10	2.06E-06	21.734	10.44486
Bradi3g10270	-1.01861	7.37E-06	0.007123	6.298562	3.03087
Bradi4g39520	-1.01057	7.48E-05	0.049931	18.7353	9.0556
Bradi2g08310	-1.00487	6.45E-05	0.04521	5.854955	2.8468
Bradi5g21140	-0.98263	3.97E-06	0.003973	10.12447	5.00305
Bradi1g13680	-0.9339	2.63E-12	1.05E-08	15.83766	8.090502
Bradi1g72960	-0.91424	1.47E-11	5.15E-08	11.18943	5.793711
Bradi1g72990	-0.91286	0.000123	0.076182	9.618805	4.978593
Bradi1g21762	-0.88685	1.62E-08	2.67E-05	6.869811	3.624976
Bradi3g02257	-0.88281	0.000128	0.076182	3.608889	1.91761
Bradi2g22810	-0.86388	4.66E-09	9.33E-06	11.87532	6.374563
Bradi2g03160	-0.80649	6.32E-09	1.18E-05	14.57846	8.141791
Bradi3g20106	-0.63392	0.000183	0.098586	17.00746	10.69328
Bradi1g74640	-0.62488	8.16E-05	0.053188	6.762258	4.284517
Bradi5g06120	-0.49836	0.000178	0.097957	7.09731	4.907766
Bradi3g57320	-0.48906	1.50E-05	0.01359	16.91029	11.76264

Table 1. 35 downregulated genes in *bdmutelsid.*
dev: developmental zone. TPM: Transcripts Per Kilobase Million.

2.2 *BdPOLAR* candidate NaN lines

To confirm the function of *BdPOLAR* is involved in SCs formation, I also identified some potentially related mutagenesis NaN lines in *BdPOLAR* gene region. The information about each NaN line was obtained from the Phytozome database. NaN2063 and NaN2140 are reported in the mutation sites track of *BdPOLAR*, containing one heterozygous R341C and A183V missense mutation present at the third and second exon separately. NaN2063 homozygotes, heterozygous and wild-type were characterized by derived cleaved amplified polymorphic sequences (dCAPS) (Fig. 6A) and sequencing analysis. Using a microscopy-based screen and examining the epidermis of the third leaf at 11 geminated days, I identified all three categories of plants with obvious phenotypes affecting SCs formation (Fig. 6B). This suggests *BdPOLAR* is not or not only the causative genes for NaN2063. I was planting 12 seeds

from NaN2140 for phenotyping, while none of the leaves from the segregation group displayed abnormal SC formation. Thus, NaN2063 and NaN2140 are not available to be used as the functional characterization for *BdPOLAR*.

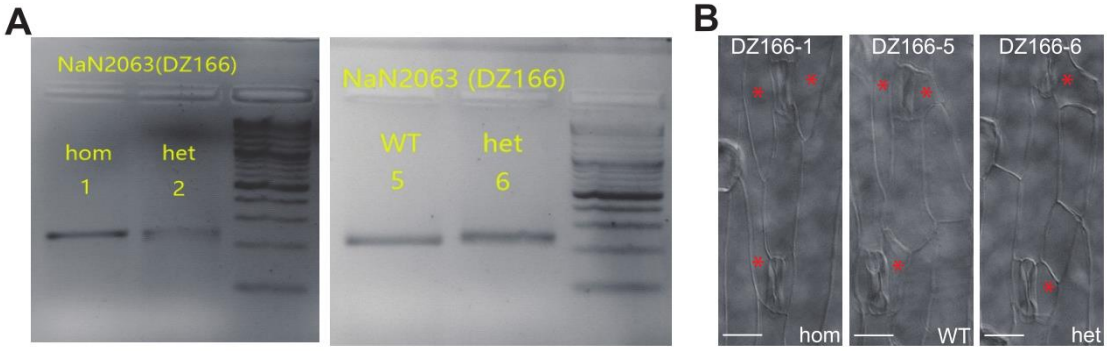

Figure 6. *BdPOLAR* is not or not only the causative genes for NaN2063.
(A) Agarose gel electrophoresis for dCAPS results of NaN2063 offspring by BglI. Homozygous lines will produce a 240bp band; Heterozygous lines will produce three bands, 27bp (invisible), 240bp and 213bp, separately; WT lines will produce two bands, 213bp and 27bp (invisible), separately. (B) Homozygous, heterozygous, and WT lines all display aberrant SCs formation. Red asterisks indicate the defective SCs. Scale bars, 15 μm.

2.3 *BdPOLAR* CRISPR/Cas9 lines display abnormal SCs formation

Available and causative NaN lines in the *BdPOLAR* gene region were not discovered, thus, I applied the reverse genetic approach, CRISPR/Cas9-mediated system, to create targeted mutations at different positions in the coding sequence of *BdPOLAR*. During the postdoc phase of Michael T Raissig at Bergmann lab, he already built one *BdPOLAR* CRISPR-editing construct, pOsUbi_Cas9_with_sgRNA-3 (pMTR57.2) against *BdPOLAR* first exon. Luckily, the first *BdPOLAR* CRISPR/Cas9 transgenic line *bdpolar-1* was generated through transformation. *bdpolar-1* contains two different mutation types in the same gene location, one T insertion and two CC deletion (Fig.10C), and there was no significant phenotypic difference between them. I utilized the individual line with one T insertion for continuing studies. The T insertion at the *BdPOLAR* gene coding region (127bp) causes the reading frameshift, and missense codons start with the 43rd amino acid Proline (P) is translated as Serine (S) (Fig.10E). Eventually, the truncated BdPOLAR is formed due to an early stop codon (Fig.11). This type of mutation results in phenotypic change along with aberrant SCs formation. Instead of bending around to form lens shape SC, the SC division cell plane expanded randomly to the distal site of GMC in *bdpolar-1*. Compared to wild-type, *bdpolar-1* showed significantly

higher (~26.3%) SC defects. This suggestively revealed *BdPOLAR* is associated with SC development (Fig.10A). To achieve fast and cost-effective phenotyping, I established the CAPS method to detect the T insertion mutation site of *bdpolar-1* (Fig.10D). In order to further prove the function of *BdPOLAR*, I was striving to generate additional *BdPOLAR* CRISPR lines with targeted mutations at different positions.

My first attempt for CRISPR design was using the Csy4-type system that followed the design protocol (Čermák, Curtin et al. 2017). This platform utilizes Csy-type (CRISPR system yersinia) ribonuclease 4 (Csy4) to create multiple guide RNAs simultaneously. Cas9 is expressed from maize (*Zea mays*) *ubiquitin* (*ZmUbi*) promoter in vector pMOD_A1510. pMOD_B2103 contains the *Cestrum Yellow Leaf Curling Virus* promoter (CmYLCV) for 2 gRNAs expressions. pMOD_C000 is an empty doner applied for Golden Gate assembly in this study. Its sibling pMOD_C3103 owns the switchgrass (*Panicum virgatum*) *ubiquitin 2* (*PvUbi2*) promoters to drive GFP expression, which provides a good way to quantify transformation efficiency. The above three modules were generated into the pTRANS_250D backbone by the Golden Gate cycle. Fig.7 presents the plasmid map of pTRAN250D-BdPOLAR guide2/4. However, I did not generate pTRAN250D-BdPOLAR guide2/4 transgenic lines successfully.

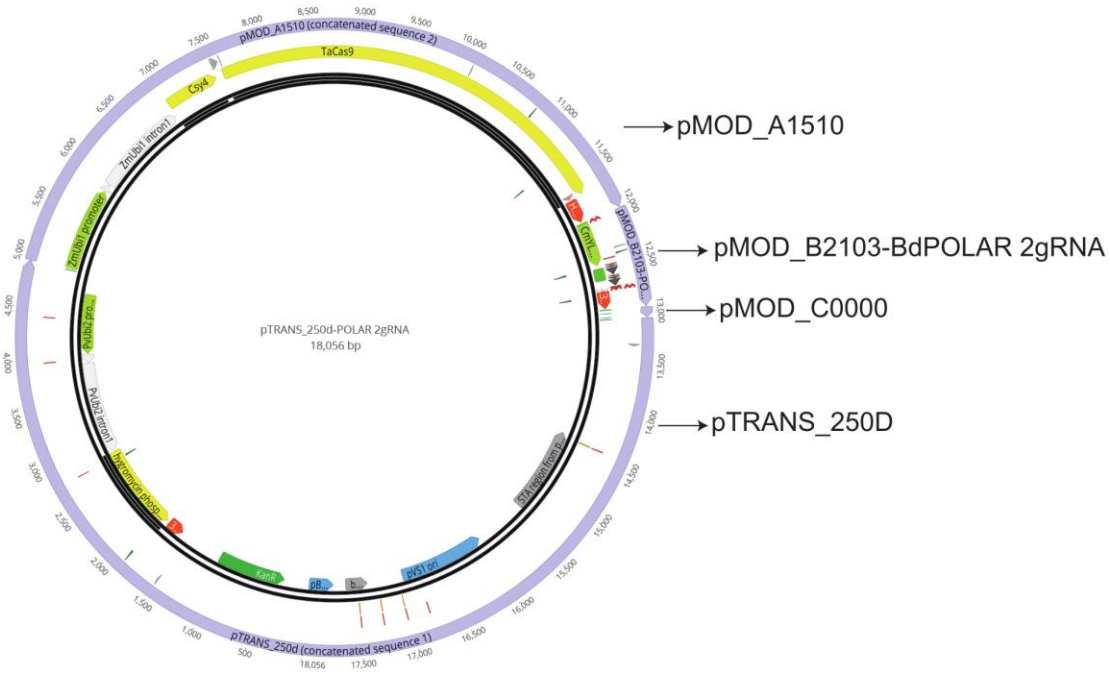

Figure 7. The plasmid map of pTRAN250D-BdPOLAR guide2/4.
Produced from Geneious. pMOD_A1510. pMOD_B2103-BdPOLAR-guide2/4 and pMOD_C000 are three entry modules, and pTRANS_250D is the destination vector.

After the Csy4-type system, I carried out CRISPR cloning by utilizing the streamlined assembly protocol (Cong, Ran et al. 2013). The first step is cloning two individual gRNA into two compatible vectors, pYPQ131C and pYPQ132C, separately. This entry vector contains the rice (Oryza sativa) U6 (OsU6) promoter for gRNA expression. The following step is integrating two gRNA expression cassettes into intermediate vector pYPQ142. At last, assembly Cas9 entry clone pYPQ167, gRNA cassettes pYPQ142, and a 35S promoter for Cas9 expression pMDC32 through Gateway recombination by LR Clonase II. Figure 8 presents the plasmid map of pMDC32-BdPOLAR-guide2/4. Unluckily, I did not generate pMDC32-BdPOLAR-guide2/4 transgenic lines.

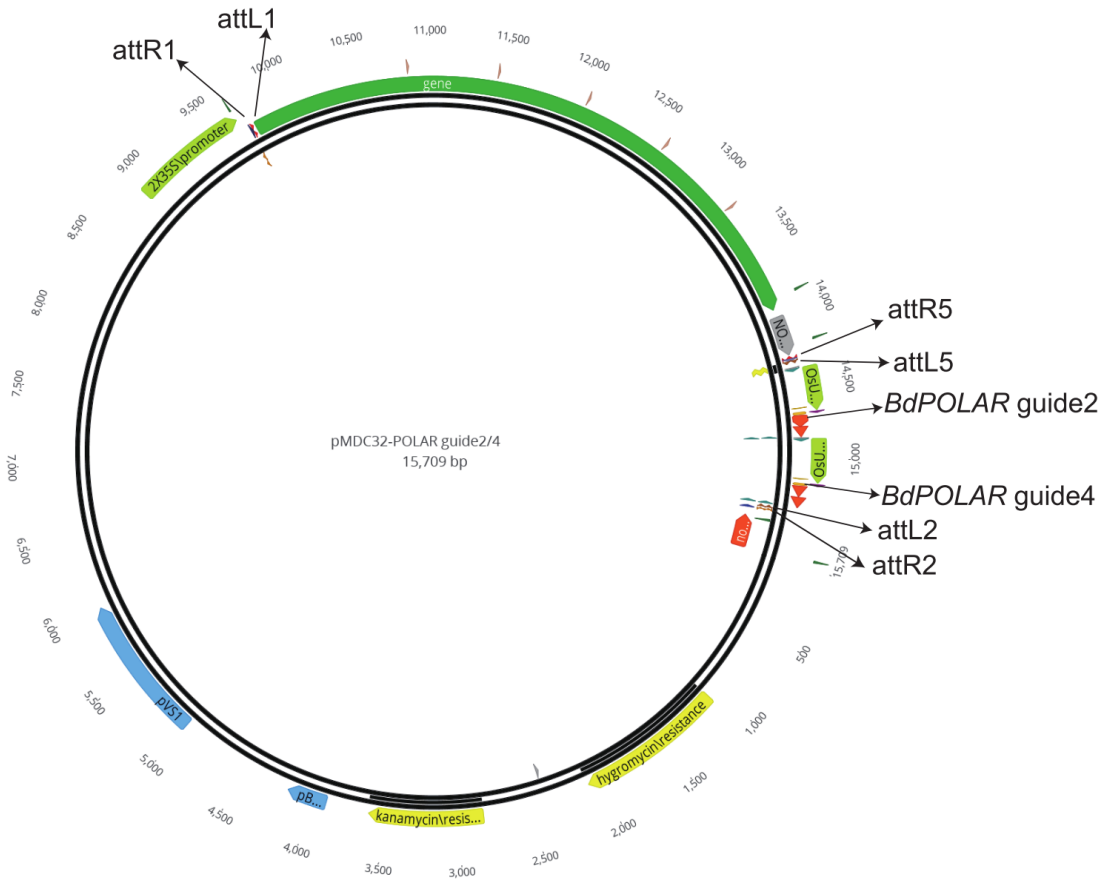

Figure 8. The plasmid map of pMDC32-BdPOLAR-guide2/4.
Produced from Geneious. pYPQ167 (Cas9) and pYPQ142-BdPOLAR-guide2/4 are integrated into pMDC32 (35S promoter) through Gateway recombination.

CRISPR-mediated targeted mutagenesis failed in the preceding two systems, GRF–GIF system was my last try. JD633_CRISPRhigheff possesses *ZmUbi* promoter drives ubiquitous expression of Cas9 and a chimeric protein GRF–GIF1. GRF–GIF is a fusion protein integrating wheat GROWTH-REGULATING FACTOR 4 (GRF4) and its cofactor GRF-INTERACTING FACTOR 1 (GIF1). GRF–GIF chimera expression significantly increases the regeneration efficiency in wheat, triticale, and rice (Debernardi, Tricoli et al. 2020). I built JD633-BdPOLAR-guide2 (Fig.9) and JD633-BdPOLAR-guide4 by following the cloning protocol attached in the appendix. Two independent CRISPR alleles, *bdpolar-2* and *bdpolar-3*, were generated by tissue culture, verified that CRISPR/Cas9 genome editing combined with GRF–GIF improves regeneration efficiency in *Brachypodium* and produces fertile and without obvious developmental defects in transgenic plants.

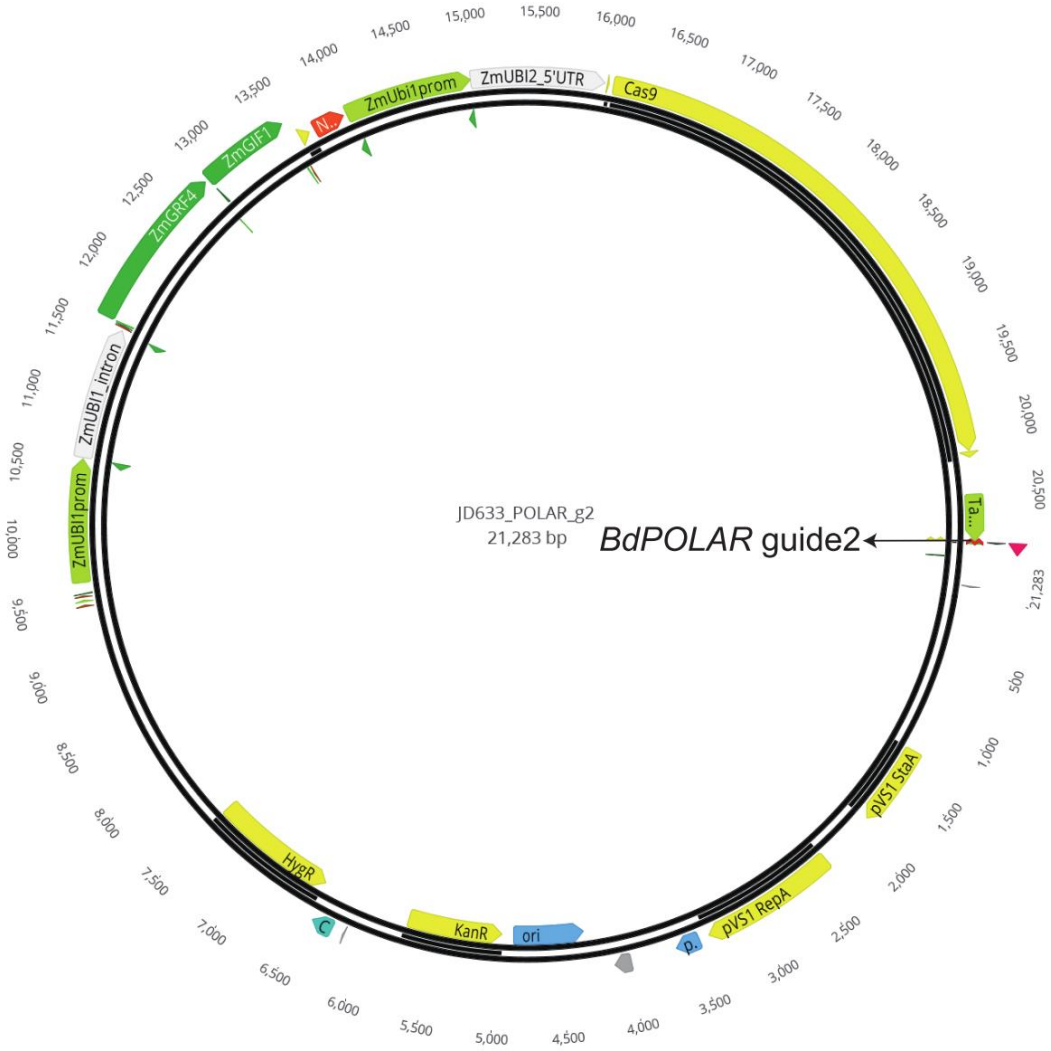

Figure 9. The plasmid map of JD633-BdPOLAR-guide2.
Produced from Geneious.

bdpolar-2 and *bdpolar-3* showed identical phenotypes as *bdpolar-1,* failing to correctly divide SCs (Fig.10A). *bdpolar-2* has uncovered a T insertion (200bp) at the first exon of *BdPOLAR* (Fig.10, C and E), creating the frameshift mutation. The consequential missense codons start with the 67th amino acid Tyrosine (Y) is translated as Lysine (L), leading to the formation of an early stop codon (Fig.11). Regarding *bdpolar-3,* CRISPR/Cas9 editing results in three different mutageneses at the same *BdPOLAR* gene location of the second exon, one T insertion, one G deletion, and one G insertion (Fig.10, C and E). All above three mutations cause framing error, for example, one T insertion leads to Alanine (A) 135 Valine (V) alteration (Fig.11). *bdpolar-2* significantly acquired more defective SCs (39.2%) than *bdpolar-3* (24.3%). This strongly suggested that

BdPOLAR played a role in regulating SC formation. The reason *bdpolar-2* appears more deformed SCs than *bdpolar-1* and *bdpolar-3* is still unknown.

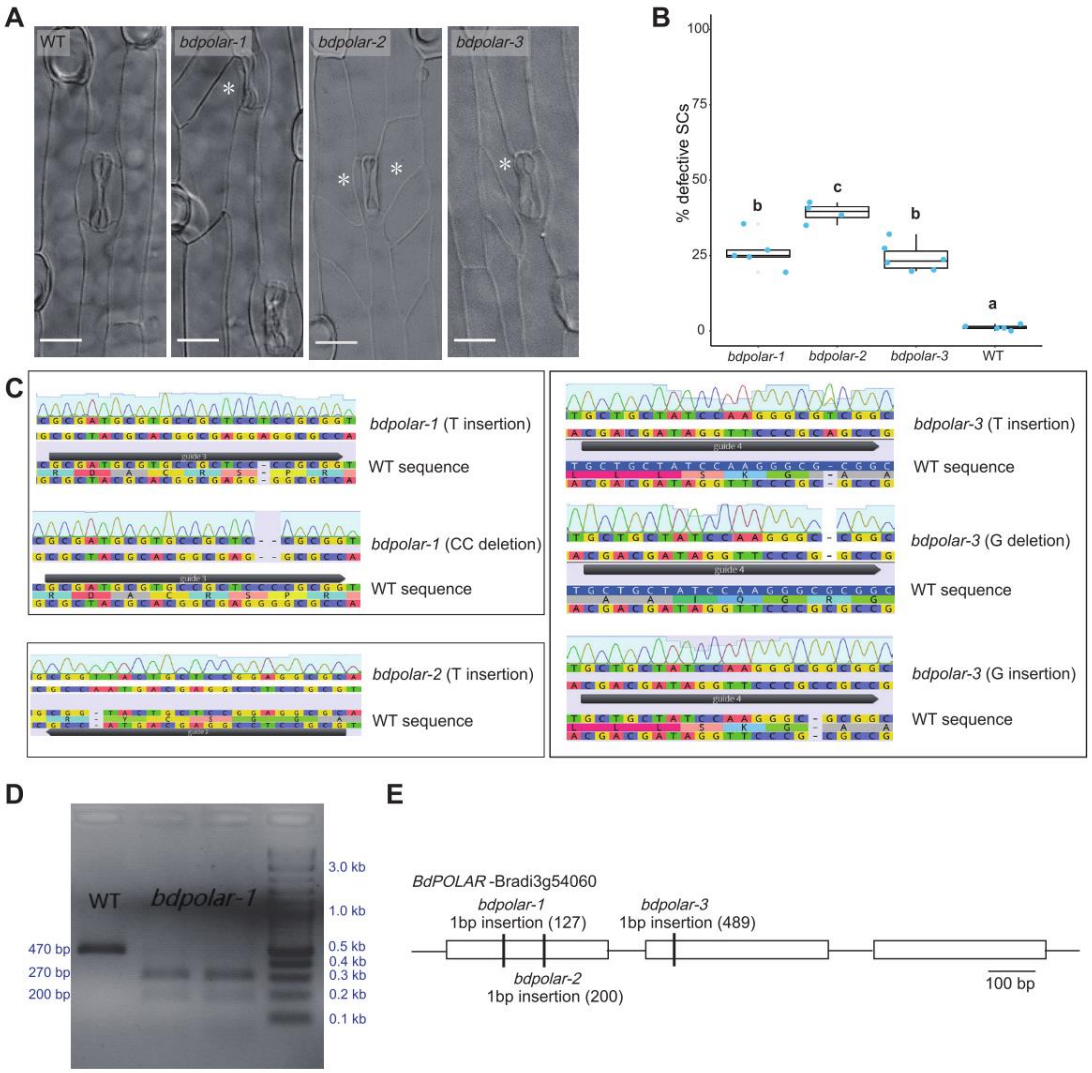

Figure 10. CRSIPR/Cas9 mutants in *BdPOLAR*.
(A) DIC images of the epidermis in WT, *bdpolar-1*, *bdpolar-2,* and *bdpolar-3* (third leaf, 19 days after germination (dag)). Abnormal SCs are indicated with white asterisks. Scale bars, 15 µm. (B) Quantifications of defective SCs in *bdpolar-1*, *bdpolar-2*, *bdpolar-3,* and WT. Samples were compared using a one-way ANOVA and post-hoc Tukey test for multiple comparisons; different letters indicate significant differences ($p<0.05$); n=4-5 individuals and 302-526 SCs. (C) Genotyping chromatogram of CRISPR induced mutations in *bdpolar-1*, *bdpolar-2,* and *bdpolar-3*. WT sequence is displayed at the bottom and mutant sequence chromatogram is displayed at the top of each panel. (D) Agarose gel electrophoresis for undigested and digested CAPS marker products. BseRI can digest PCR products from *bdpolar-1* but not from WT. DNA kilobases standard control is NEB 1kb Plus DNA Ladder. (E) Gene model of *BdPOLAR* (Bradi3g54060) with available CRISPR/Cas9-induced (*bdpolar-1*, *bdpolar-2*, *bdpolar-3*) mutations.

Figure 11. Peptide sequence alignment to compare *bdpolar-1, bdpolar-2,* and *bdpolar-3* protein with WT.
Produced from Geneious. The conserved residues are marked in green.

2.4 *BdPOLAR* and *BdPAN1* are both involved in the formative SC division

The *bdpolar* SCs abnormal formation strongly resembles classical maize SMC polarity mutants like *pangloss1* (*zmpan1*) and (*zmpan2*), which influent polarized receptor-like kinases and result in incorrect SC cell wall positioning, abnormal ACDs in SMCs (Fig.12A) (Cartwright, Humphries et al. 2009, Zhang, Facette et al. 2012). Emily Abrash identified a mutant in *BdPAN1* (Bradi3g39910) in a forward genetic screen via ethyl methanesulfonate (EMS) mutagenesis to target developmental factors related to form graminoid stomata. This mutant (*bdpan1-1*) carried a 9-base pair (bp) in-frame deletion at the 5'-end of *BdPAN1* (Fig.12C) and showed ~44% aberrant SC divisions (Fig.12B). This revealed that *bdpan1* and *bdpolar* mutants resulted in similar while differently extent phenotypes (Fig.12B).

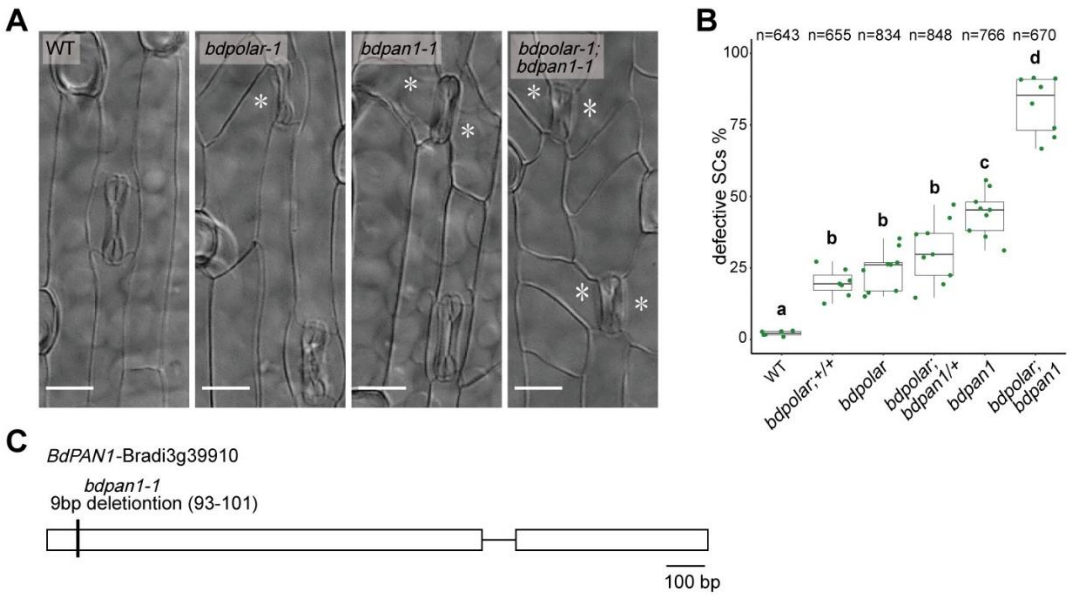

Figure 12. *BdPOLAR* and *BdPAN1* are both required to promote SMC division.
(A) DIC images of the epidermis in WT, *bdpolar-1*, *bdpan1-1,* and *bdpolar-1; bdpan1-1* (third leaf, 19 dag). Aberrant SCs are indicated with white asterisks. Scale bars, 15 µm. (B) Quantifications of defective SCs in crossing offspring lines *bdpolar-1;+/+*, *bdpolar-1;bdpan1-1/+*, and *bdpolar-1;bdpan1-1,* parental lines *bdpolar-1* and *bdpan1-1*, and WT control. n=SMC numbers were analyzed per genotype. Samples were compared using a one-way ANOVA and post-hoc Tukey test for multiple comparisons; different letters indicate significant differences ($p<0.05$); n=6-9 individuals and 643-848 SCs. (C) Gene model of *BdPAN1* (Bradi3g39910) with EMS-mutagenized *bdpan1-1* mutation.

Inspection of the developmental origins of aberrant SCs suggested that early transverse divisions producing GMCs were correct in both *bdpolar-1* and *bdpan1-1*. While, the longitudinal ACDs in SMCs showed misoriented cell division planes in mutants, where SC cell division planes integrate with distal rather than proximal cell walls (Fig.13, Fig.S1, Fig.S2, and Fig.S3). This finding indicated that misoriented ACDs caused mis-specified SC formation in mutants during SC recruitment.

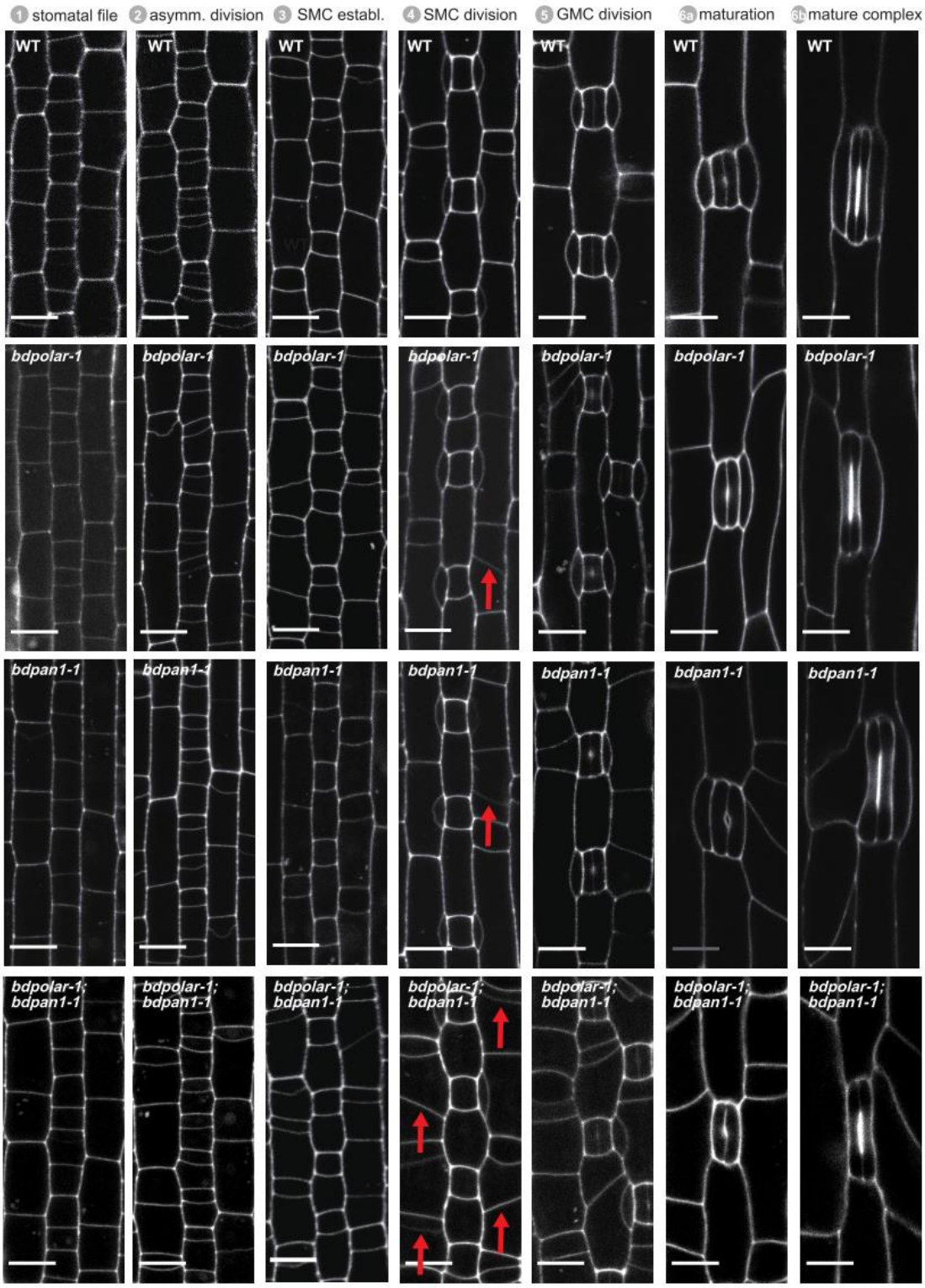

Figure 13. Misoriented SMC division planes likely caused abnormal SCs in mature leaf zones.

Single confocal plane images of the PI-stained developing epidermis showing stage 1 to stage 6 SMCs in WT, *bdpolar-1*, *bdpan1-1*, and *bdpolar-1;bdpan1-1*. Red arrows indicate misoriented division planes in SMCs. Scale bar, 10 µm.

In order to investigate the functional relationship between *BdPOLAR* and *BdPAN1*, their single mutants were crossed to yield *bdpolar-1; bdpan1-1* double mutants, which showed a strong phenotype with ~82% of aberrantly divided SCs (Fig.12, A and B). Accordingly, this misoriented division planes in SMCs phenotype were excessive in *bdpolar-1; bdpan1-1* double mutant (Fig.13 and Fig.S4). This indicated that *BdPOLAR* and *BdPAN1* act together to direct SMC divisions correctly. However, neither single nor double mutants did not display any growth or fertility phenotypes.

2.5 The polarity domains of BdPOLAR and BdPAN1 are mutually exclusive

To explore if BdPOLAR and BdPAN1 have polarized localization in *B. distachyon* SMCs, their translational reporter lines were generated. In *BdPAN1p:BdPAN1-YFP*, the signal was investigated at the periphery of all protodermal cells, inclusive of the stomatal cell lineages before SMCs are specified. Afterward, when GMCs first formed and elongated, BdPAN1 protein enriched at the GMC/SMC interface (Fig.14A, and Fig.S6). 3D imaging suggested that BdPAN1-YFP formed a ring-like structure at the GMC/SMC interface (Fig.14B). BdPAN1's expression pattern and localization are identical to the localization of ZmPAN1 as inspected via immunolocalization or translational reporter lines in *maize* (Cartwright, Humphries et al. 2009, Sutimantanapi, Pater et al. 2014). When *BdPAN1p:BdPAN1-YFP* was introduced into *bdpan1-1*, the SCs division defects in mutant were rescued, indicating that the *BdPAN1* translational construct is functional (Fig. 15).

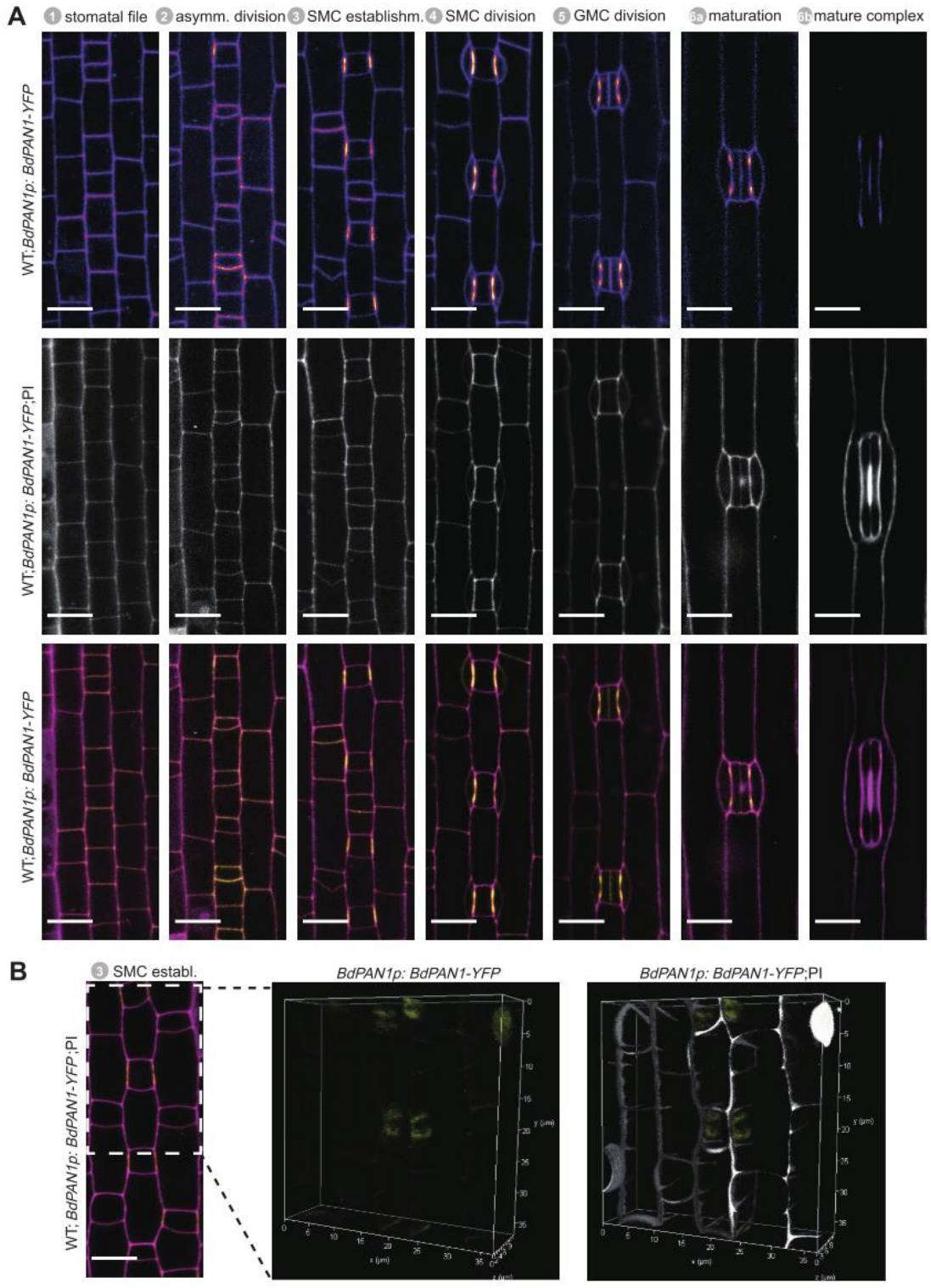

Figure 14. *BdPAN1p:BdPAN1-YFP* expression throughout stomatal development in *B. distachyon*.
(A) Fluorescence intensity images of YFP channel only (upper), images of PI-stained cell outlines only (middle), and composite images (bottom) with BdPAN1-YFP signal (yellow) and PI-stained cell outlines (magenta). (B) 3D image of stage 3 field of view as indicated in white dotted box; YFP channel only (left) and with cell outlines in grey (right). All images from the second leaf, 5 to 6 dag, T1 generation. Scale bars, 10 µm.

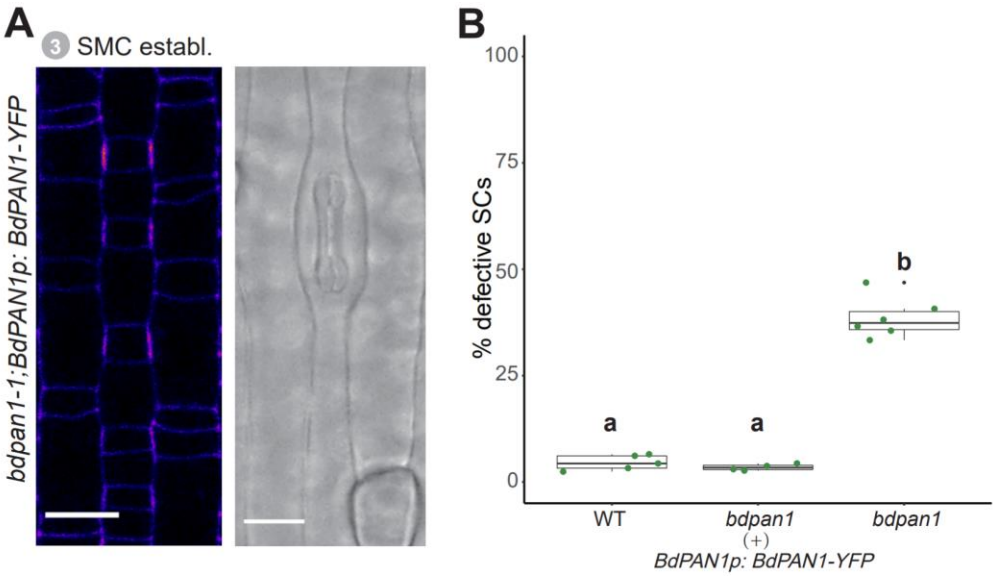

Figure 15. *BdPAN1* translational construct *BdPAN1p:BdPAN1-YFP* is functional. (A) Fluorescence intensity image of *BdPAN1p:BdPAN1-YFP* in *bdpan1-1* (left), and DIC images (right) of the epidermis in *bdpan1-1* with *BdPAN1p:BdPAN1-YFP*. (B) Quantifications of defective SCs of WT, *bdpan1-1* complemented with *BdPAN1p:BdPAN1-YFP*, and *bdpan1-1* control. n=4-6 individuals and 432-520 SCs. Samples were compared using a one-way ANOVA and post-hoc Tukey test for multiple comparisons; different letters indicate significant differences ($p<0.05$). Scale bar in DIC image, 15 µm; Scale bar in confocal image, 10 µm.

All other regulators associated with regulating SMC polarity and formative SC divisions in the *maize* SC lineage (e.g. *ZmPAN2*, *ZmROP2*, and *ZmBRK1*) polarized towards the GMC/SMC interface (Cartwright, Humphries et al. 2009, Humphries, Vejlupkova et al. 2011, Zhang, Facette et al. 2012). Therefore, this localization was considered a general hallmark for all polarity genes in developing SMCs. Thus, I expected *BdPOLAR* would have the same localization. However, in *BdPOLARp:BdPOLAR-mVenus* lines, the signal was observed at the periphery of SMCs but was precluded from the classical and prospective polarity domain at the GMC/SMC interface. Moreover, different from BdPAN1-YFP, which was expressed in all places of grass leaf epidermis and initiated polarization upon GMC elongation, *BdPOLAR-mVenus* accumulated uniquely in the stomatal lineage. Before SMCs were specified (stage 1), BdPOLAR-mVenus appeared specially in stomatal lineage cells with a bias toward the basal side of the stomatal precursor cells (Fig.16, and Fig.S5). During SMC establishment (stage 3), a very robust and specific signal was detected in SMCs (Fig.16, and Fig.S5). BdPOLAR-mVenus signal emerged in the apical and basal plasma membrane (PM) of SMCs, and basal site to GMCs

(Fig.16, and Fig.S5). Just after SMC division (stage 4), BdPOLAR fusion protein quickly dissociated from the distal PMs of SMCs. The signal got faint then preserved in the GMCs, young GCs, and young SCs until the stomatal complex matured (Fig.16, and Fig.S5). In *BdPOLAR* transcriptional reporter (*BdPOLARp:3XNLS-eGFP*) line, *BdPOLAR* promoter activity was first observed in SMCs, and only later in GMCs (Fig.17, and Fig.S7). Its absent expression in early stomatal cell files (stage 1) suggested that the BdPOLAR-mVenus signal during stage 1 was driven by intronic or exonic elements not present in the transcriptional reporter. Thus, BdPOLAR translational reporter showed a novel polarity domain in SMCs, and the first identified one with localization distal to future division plane in grasses. The polarity domains from BdPOLAR and BdPAN1 fabricate a reciprocal opposite domain at the GMC/SMC interface.

To quantify the degree of polarization of BdPOLAR-mVenus and BdPAN1-YFP in SMCs, Inés Hidalgo Prados performed the Polarity Measurement (POME) to quantify the fraction of the plasma membrane occupied by the protein of interest and to obtain the polarity index (PI) (Gong, Varnau et al. 2020, Gong, Alassimone et al. 2021). As expected, the more wide-spread BdPOLAR-mVenus showed a much higher average PI (less polarized) than BdPAN1-YFP (Fig.19B, D). In summary, the opposite polarity domains of BdPOLAR and BdPAN1 were almost mutually exclusive, with a highly polarized BdPAN1 domain at the GMC/SMC interface and a broader, distal BdPOLAR polarization domain.

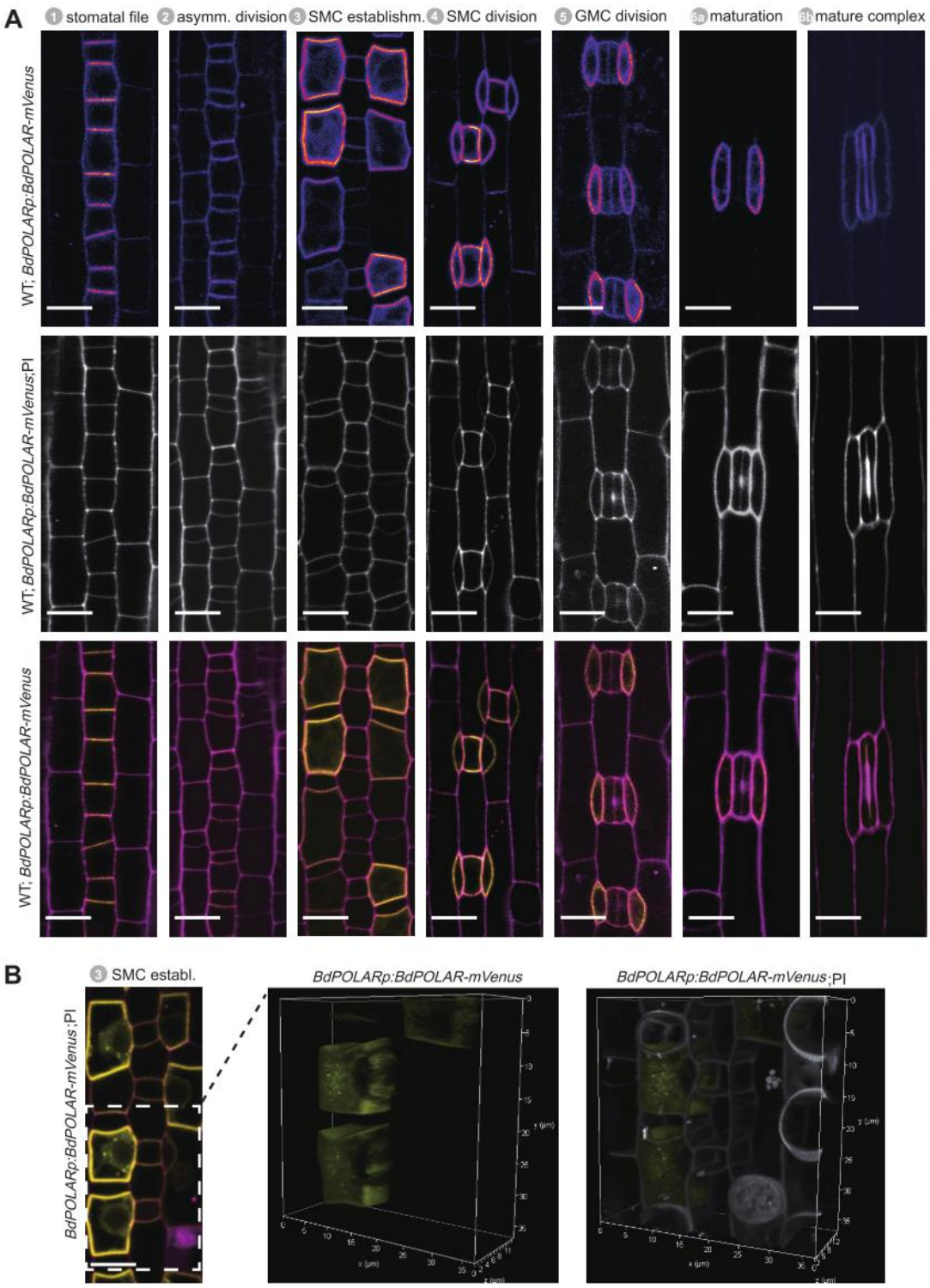

Figure 16. *BdPOLARp:BdPOLAR-mVenus* expression throughout stomatal development in *B. distachyon*.
(A) Fluorescence intensity images of mVenus channel only (upper), images of PI-stained cell outlines only (middle), and composite images (bottom) with BdPOLAR- mVenus signal (yellow) and PI-stained cell outlines (magenta). (B) 3D image of stage 3 field of view as indicated in white dotted box; mVenus channel only (left) and with cell outlines in grey (right). All images from the second leaf, 5 to 6 dag, T1 generation. Scale bars, 10 µm.

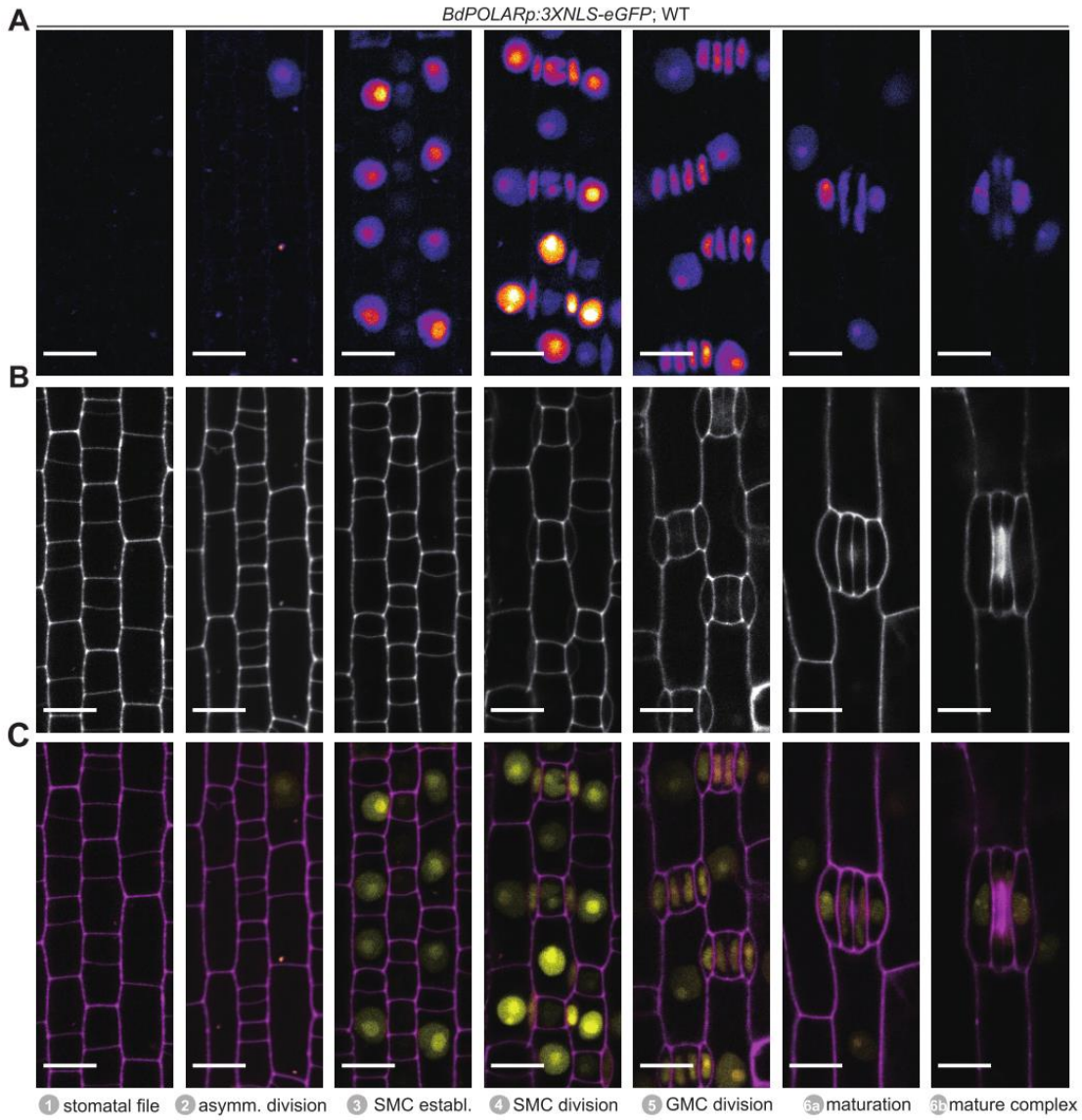

Figure 17. *BdPOLARp:3XNLS-eGFP* expression throughout stomatal development in *B. distachyon*.
(A) Fluorescence intensity images of GFP channel only. (B) Images of PI-stained cell outlines only. (C) Composite images with BdPOLAR-eGFP signal (yellow) and PI-stained cell outlines (magenta). All images from the second leaf, 5 to 6 dag, T1 generation. Scale bars, 10 µm.

2.6 *BdMUTE* is required for *BdPOLAR* expression

Since *BdPOLAR* was 12-fold downregulated in *bdmute* compared to wild-type (Table 1), if *BdPOLAR* expression indeed relies on *BdMUTE* is unknown. *BdPOLARp:BdPOLAR-mVenus* was transformed into *bdmute* through tissue culture to get more insights concerning this. Because different transgenic lines were used for comparison, I set up laser intensities to acquire the similar expression pattern in the stage 1 GC lineage files between *bdmute* and wild-type. Twice as much laser was required to excite BdPOLAR-mVenus signal at

stage 3 compared to stage 1 in the case of *bdmute* (20% vs. 38%). However, very little laser is adequate for a robust signal in wild-type (Fig.18; stage1: 2% vs. stage3: 8%). Combined with the comparative RNA-seq data, this finding supported that *BdMUTE* was required for *BdPOLAR* expression.

On the contrary, *BdPAN1p:BdPAN1-YFP* expression was not determined by *BdMUTE*. In addition, also BdPAN1-YFP polarization at the GMC/SMC interface persisted in *bdmute* (Fig.18). This observation indicated that BdPAN1 polarization did not seem dependent on SC lineage establishment in GMC neighboring cell files. Therefore, biochemical or mechanical polarization cues releasing from the elongating GMC were sufficient to build the BdPAN1 polarity domain.

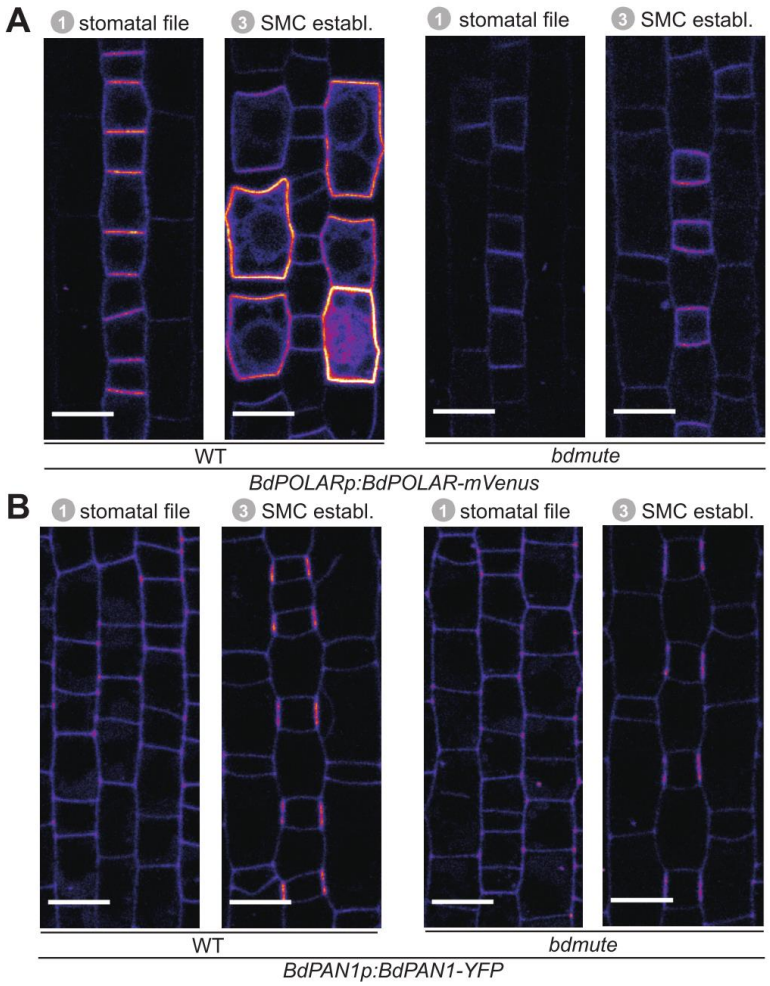

Figure 18. *BdMUTE* is required for *BdPOLAR* expression.
(A) Fluorescence intensity of *BdPOLARp:BdPOLAR-mVenus* in WT (left panels) and in

bdmute (right panels) at stage 1 and stage 3. (B) Fluorescence intensity of *BdPAN1p:BdPAN1-YFP* in WT (left panels) and in *bdmute* (right panels) at stage 1 and stage 3. All images from the second leaf, 5 to 6 dag, T1 generation. Scale bars, 10 µm.

2.7 *BdPAN1* is required for *BdPOLAR* polarization but not vice versa

Opposing polarity domains mediated with mutually inhibitory were described in animal systems (Nance and Zallen 2011, Muroyama and Bergmann 2019). However, this type of inhibitory relationship was not discovered in plants. To explore if the opposing BdPAN1 and BdPOLAR polarity domains possess an inhibitory relationship. I crossed the BdPOLAR-mVenus and BdPAN1-YFP reporter lines to *bdpan1-1* and *bdpolar-1*, respectively. In *bdpan1-1,* I observed an even distribution of the BdPOLAR-mVenus signal at the complete periphery of SMC, where BdPOLAR-mVenus also occupied the BdPAN1 domain at the GMC/SMC interface (Fig.19A). Indeed, the polarity index (PI) of BdPOLAR-mVenus in *bdpan1-1* displayed a significantly increased (less polarization) compared with the PI of BdPOLAR-mVenus in wild-type (Fig. 19B). In contrast, BdPAN1-YFP maintained its polarization at the GMC/SMC interface in the *bdpolar1-1* mutant background (Fig.19C, D). Thus, polarized localization of BdPOLAR is dependent on functional BdPAN1, but BdPAN1 localization was independent of the presence or absence of functional BdPOLAR. This indicated that a one-way rather than a mutual inhibition relationship belongs to BdPAN1 and BdPOLAR opposing polarization patterns. This might be because BdPAN1 was expressed and accumulated at the GMC/SMC interface earlier than BdPOLAR was expressed.

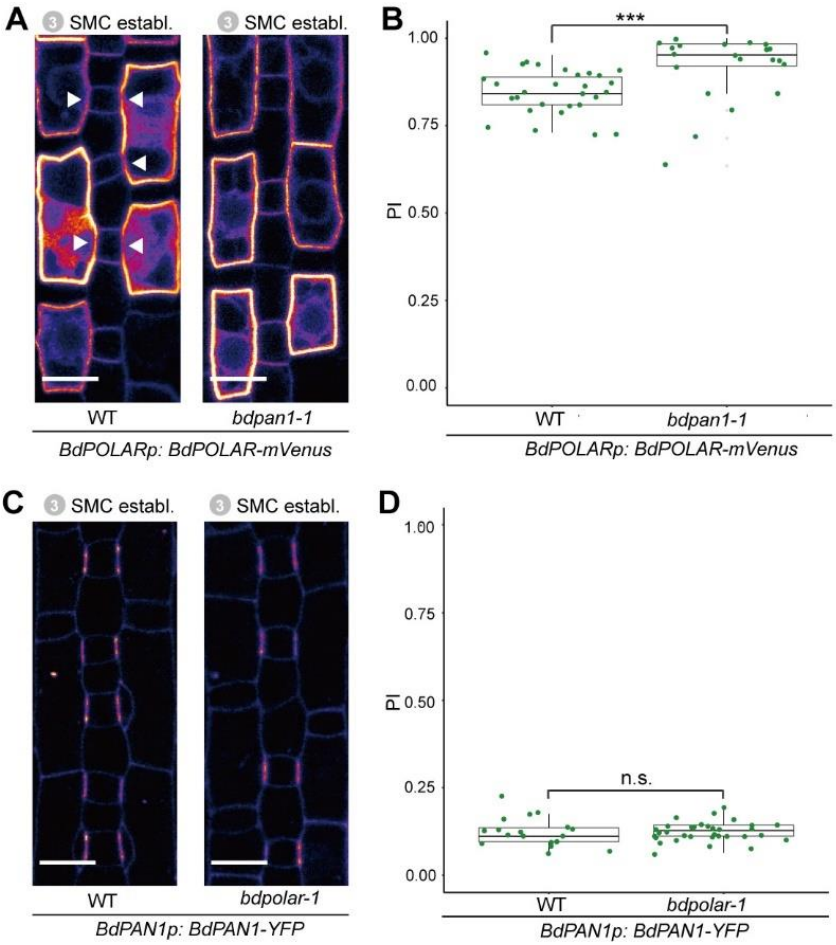

Figure 19. *BdPAN1* is required for BdPOLAR polarization.
(A) Fluorescence intensity of *BdPOLARp:BdPOLAR-mVenus* in WT (left) and *bdpan1-1* (right) at stage 3. The absence of *BdPOLAR* at GMC/SMC interfaces in WT are indicated with white arrowheads. (B) Quantification of the polarity index (PI) of *BdPOLAR-mVenus* in WT (n=29 SMCs) and *bdpan1-1* (n=22 SMCs). (C) Fluorescence intensity of *BdPAN1p:BdPAN1-YFP* in WT (left) and *bdpolar-1* (right) at stage 3. (D) Quantification of the PI of *BdPAN1-YFP* in WT (n=19 SMCs) and *bdpolar-1* (n=33 SMCs). Statistical difference was test with an unpaired Mann-Whitney U-test; *** = p-value < 0.001; n.s. = non-significant. Scale bar, 10 µm.

2.8 Accurate dosage and stability of BdPOLAR is necessary for its function

Besides the unpolarized localization of BdPOLAR-mVenus in *bdpan1-1*, BdPOLAR-mVenus expression in *bdpan1-1* extremely affect the SC division (Fig. 20A). 86% of SMCs showed aberrant formation in *bdpan1-1* plants with BdPOLAR-mVenus signal compared to only 30% in *bdpan1-1* plants without BdPOLAR-mVenus signal (Fig. 20B). In addition, strong *BdPOLARp:BdPOLAR-mVenus* and ubiquitously BdPOLAR-mVenus expression caused (19% and 10%, respectively) SC defects in wild-type (Fig.

20B and Fig. 21C, D). This suggested that BdPOLAR-mVenus fusion protein potentially influent SC divisions, and the dosage and/or stability of BdPOLAR were crucial for its function. Moreover, weak BdPOLAR-mVenus expression in *bdpolar-1* was capable of partially rescuing SC defects, while strong BdPOLAR-mVenus completely failed to complement *bdpolar-1* (Fig. 21A, B).

On the contrary, the SC phenotypes in wild-type or *bdpolar-1* retained the same with or without BdPAN1-YFP expression. This result indicated that BdPAN1-YFP did not display a dosage or stability effect (Fig. 20C, D).

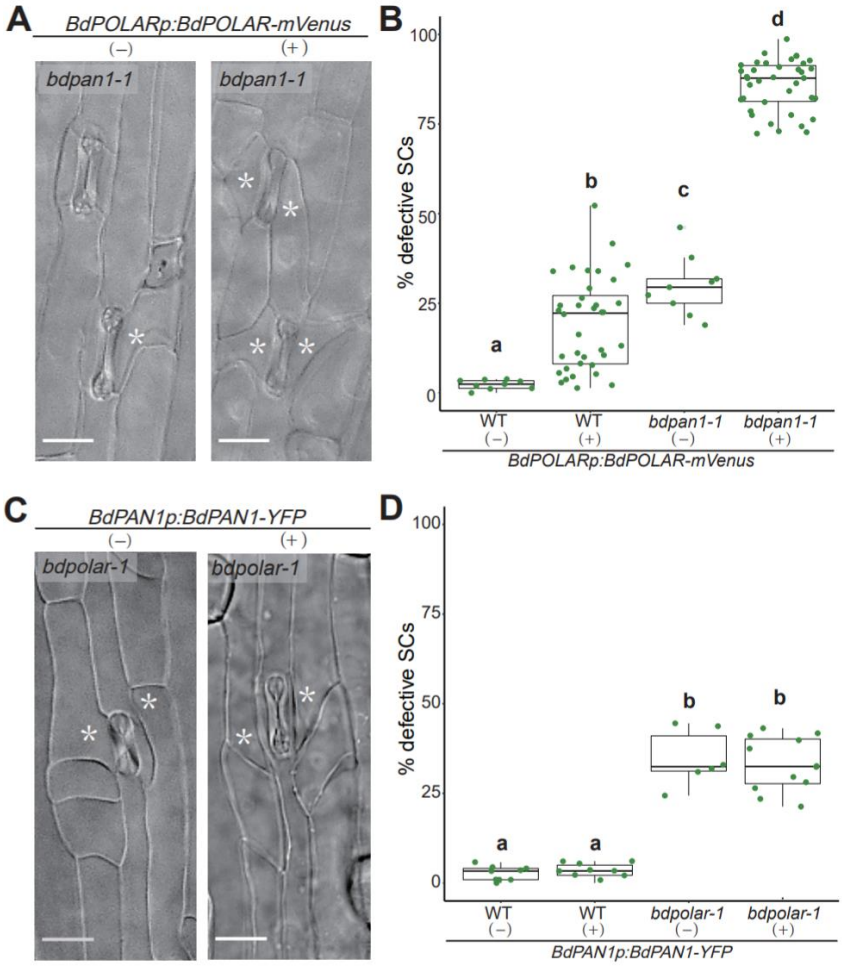

Figure 20. *bdpan1-1* is sensitized to BdPOLAR-mVenus expression.
(A) DIC images of the epidermis in *bdpan1-1* with (+) or without (-) *BdPOLARp:BdPOLAR-mVenus* expression. (B) Quantifications of defective SCs in WT and *bdpan1-1* with (+) or without (-) *BdPOLARp:BdPOLAR-mVenus* expression; n=762-3018 SMCs. (C) DIC images of the epidermis in *bdpolar-1* with (+) or without (-) *BdPAN1p:BdPAN1-YFP* expression. (D) Quantifications of defective SCs in WT and *bdpolar-1* with (+) or without (-) *BdPAN1p:BdPAN1-YFP* expression. n=560-1271 SMCs. Abnormal SCs are indicated with white asterisks. Samples were compared using a one-way ANOVA and post-hoc Tukey test for multiple comparisons; different letters indicate significant differences ($p<0.05$). All images from the third leaf, 16 to 19 dag. Scale bars, 15 µm.

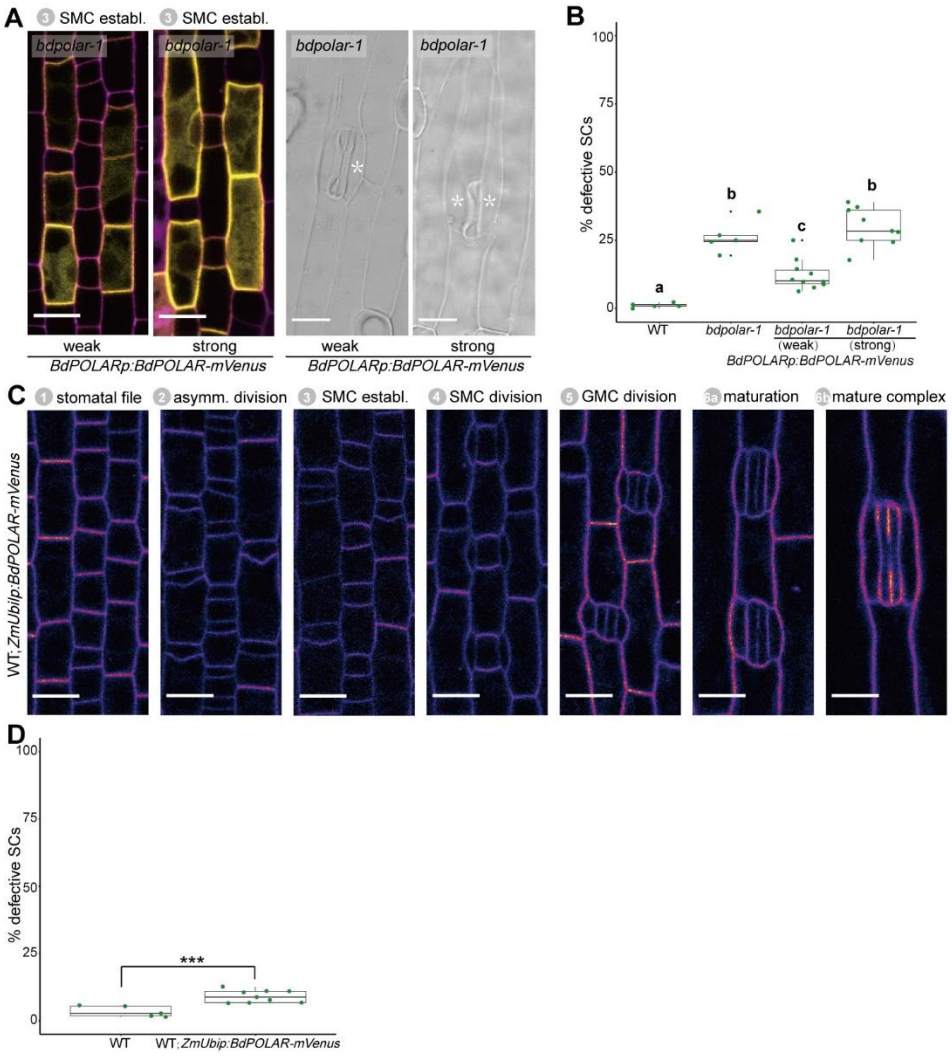

Figure 21. The dosage and/or stability of BdPOLAR are crucial for its function.
(A) Composite images (left) with strong and weak BdPOLAR-mVenus signal (yellow) and PI-stained cell outlines (magenta) in *bdpolar-1*, and DIC images (right) of the epidermis in *bdpolar-1* with strong and weak *BdPOLARp:BdPOLAR-mVenus* expression. Aberrant SCs are indicated with white asterisks. n=428-744 SMCs. (B) Quantifications of defective SCs in *bdpolar-1* with weak and strong *BdPOLARp:BdPOLAR-mVenus* signal, and WT, *bdpolar-1* control. Samples were compared using a one-way ANOVA and post-hoc Tukey test for multiple comparisons; different letters indicate significant differences ($p<0.05$). (C) Fluorescence intensity of *ZmUbip:BdPOLAR-mVenus* in WT. (D) Quantifications of defective SCs in WT with and without *ZmUbip:BdPOLAR-mVenus* expression. For comparisons between two groups, a Welch t-test was used; *** = p-value < 0.001. Scale bar in DIC image, 15 µm; Scale bar in confocal image, 10 µm.

2.9 BdPAN1 dominates the nuclear polarization to orientate SMC divisions

BdPOLAR and BdPAN1 protein established the oppositely polarized domains, and they acted together to promote SMC polarization and SC division, suggesting that *BdPOLAR* and *BdPAN1* played roles in parallel pathways and

potentially obtained different functions. To confirm this possibility, I carefully inspected and quantified the different defects in mutants.

It was previously reported that the ZmPAN1 polarity domain is involved in guiding nuclear migration during SMC pre-mitotic division (Cartwright, Humphries et al. 2009, Zhang, Facette et al. 2012). In order to test if BdPAN1 is also required for this process in *Brachypodium* and if BdPOLAR also contributes, I developed an assay to track pre-mitotic SMC polarization and nuclear migration. The distance of the SMC nucleus to the GMC/SMC interface was measured to as a proxy (Fig. 22A). When imaging developing wild-type leaf zones with stained nuclei and cell outlines, I observed that most SMCs had polarized nuclei (Fig. 22B, and Fig. S8). In *bdpolar-1,* only few SMCs had defects in nuclear polarization (Fig. 22B, and Fig. S9), whereas many unpolarized nuclei were detected in *bdpan1-1* and *bdpolar-1;bdpan1-1* SMCs (Fig. 22B, Fig. S10, and Fig. S11).

To precisely quantify nuclear position to represent distinct SMCs developmental stages, I not only measured the (d) distance, which is the distance from the SMC nuclear center to the middle of the GMC/SMC interface, but also the length and width of the neighboring GMC (Fig. 22A). The length-to-width ratio (LWR) is increasing along with GMC longitudinal growth. As a proof of concept, in wild-type, SMC nuclei were located more proximal to the GMC/SMC interface when GMCs become more mature (higher LWR of GMCs) (Fig. 23A). This correlation tendency was reduced slightly in *bdpolar-1* and *bdpan1-1*(Fig. 23, B and C), whereas it was absent in *bdpolar-1;bdpan1-1* due to the chaotic SMC divisions (Fig. 23D). To avoid deviations of d distance measurement due to imaging at different Z-axis positions, I also measured the nuclear diameters per genotype, and they did not show a significant difference (Fig. 23E). Based on d distance distribution during GMC growth of wild-type, I chose a GMC LWR of 0.9 as the cut-off since >93% of the SMC nuclei, in this case, appeared below 4 μm toward to GMC/SMC domain, and were considered as polarized nuclei (Fig. 23F). When GMC LWR >1.2, the numbers of available pre-mitotic SMC strikingly decreased in all genotypes because most SMC have divided (Fig. 23F). When GMC LWR >0.9, in wild-type, the average distance of

SMC nuclei to the GMC was (3.19 µm)—lower than the distance values of other genotypes (Fig. 23F). Despite being significantly different from the wild-type, distance d in *bdpolar-1* was only marginally increased (3.48 µm), and near 80% of the nuclei were positioned within 4µm away from the GMC/SMC interface (Fig. 23F). In *bdpan1-1*, however, the distance (3.78 µm) was highly increased, and almost 35% of nuclei located further 4µm cut-off implying that *BdPAN1* influenced nuclear polarization more than *BdPOLAR* did (Fig. 23F). Finally, the *bdpolar-1;bdpan1-1* showed similar d distance values and unpolarized nuclei distribution (3.89 µm, and >37% unpolarized nuclei (Fig. 23F) as *bdpan1-1* single albeit the SC defects were close to double (Fig. 12B). This indicated that nuclear polarization defects in the double mutant were mostly due to the loss-of-function of *BdPAN1,* and suggested that nuclear migration is more governed by *BdPAN1* than *BdPOLAR.* In addition, the intense SC defects in *bdpolar-1;bdpan1-1* might be caused by nuclear migration defects from *bdpan1-1* and another unknown obstruction caused by the loss-of-function of *BdPOLAR*, suggesting an additional yet novel function of *BdPOLAR*.

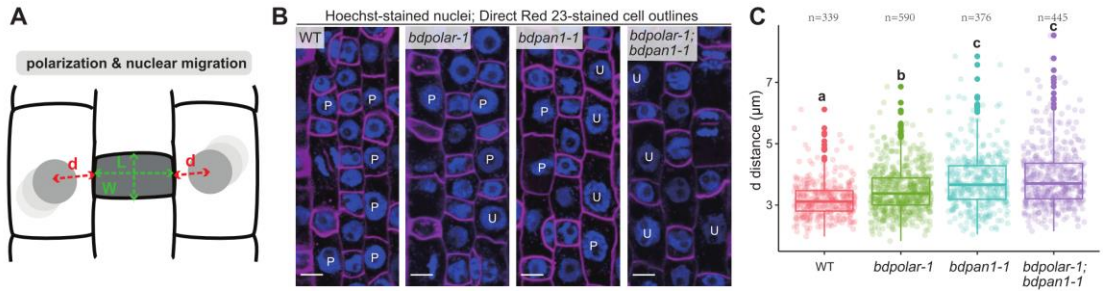

Figure 22. *BdPAN1* dominates the nuclear polarization to orientate SMC divisions.
(A) Schematic of the quantification of nuclear migration. L (green): GMC length; W (green): GMC width; d (red): the distance between nuclear center to middle of GMC/SMC interface. (B) Single confocal plane images Hoechst-stained nuclei (blue) and Direct Red 23-stained cell outlines (magenta) of stage 3 to stage 4 SMCs in WT, *bdpolar-1*, *bdpan1-1*, and *bdpolar-1;bdpan1-1*; P, polarized nucleus; U, unpolarized nucleus. Scale bar, 10 µm. (C) Quantification of d distance in SMCs of WT, *bdpolar-1*, *bdpan1-1*, and *bdpolar-1;bdpan1-1*; only SMCs flanking GMCs with a LWR>0.9 are shown. Number of SMCs measured are indicated. Samples were compared using a one-way ANOVA and post-hoc Tukey test for multiple comparisons; different letters indicate significant differences ($p<0.05$). Scale bars, 10 µm.

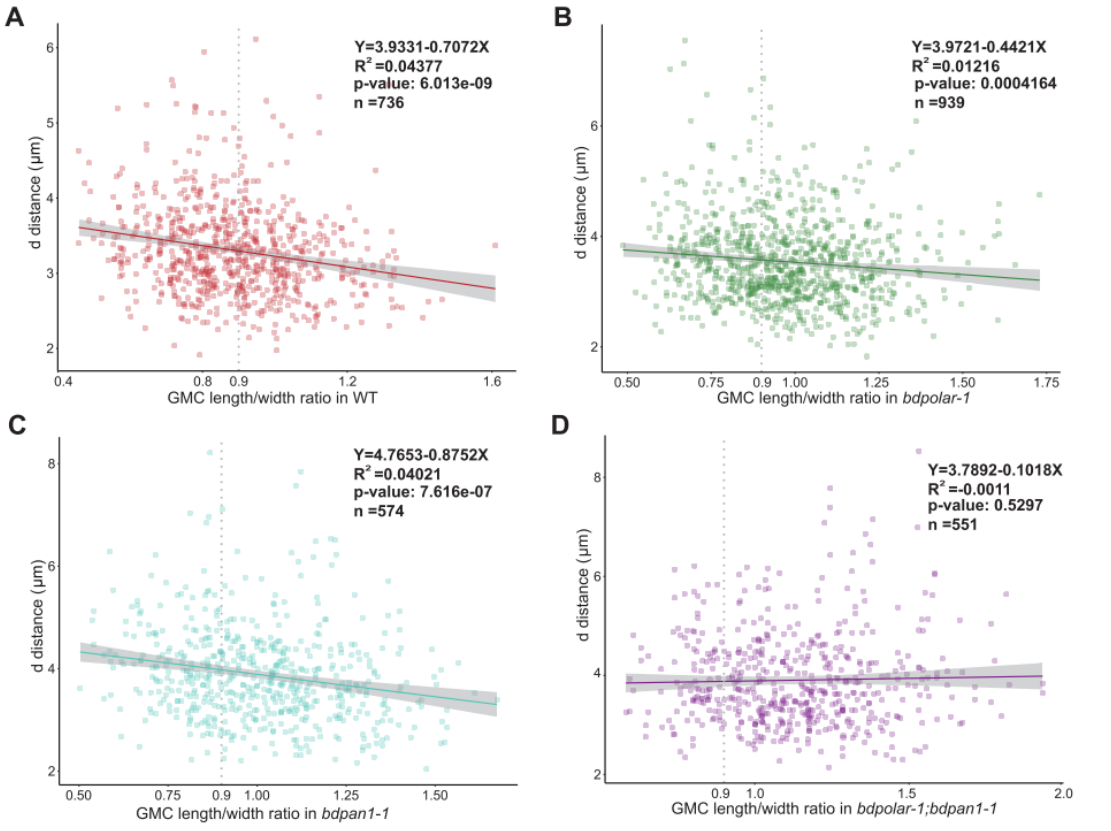

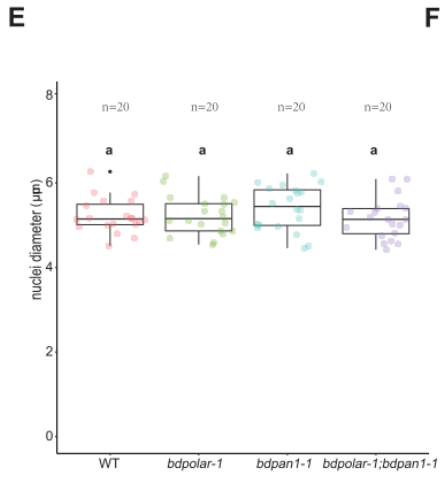

F

GMC LWR > 0.9

Genotypes	Total nuclei (n)	d distance (µm)	Polarized nuclei (n)	Nuclei polarization %
WT	339	3.189794	316	93.22%
bdpolar-1	590	3.476963	469	79.49%
bdpan1-1	376	3.775290	243	64.63%
bdpolar-1; bdpan1-1	445	3.888517	279	62.70%

GMC LWR > 1.2

Genotypes	Total nuclei (n)	d distance (µm)	Polarized nuclei (n)	Nuclei polarization %
WT	44	3.047114	42	95.45%
bdpolar-1	123	3.47613	93	75.61%
bdpan1-1	117	3.606658	84	71.79%
bdpolar-1; bdpan1-1	207	4.006087	125	60.39%

Figure 23. Nuclear migration correlated with GMC length to width ratio.
(A to D) Scatter plot displaying a distance (µm; y-axis) as a function of GMC length/width ratio (LWR; x-axis) in SMCs of WT (n=736 SMCs), *bdpolar-1* (n=939 SMCs), *bdpan1-1* (n=574 SMCs), and *bdpolar-1;bdpan1-1* (n=551 SMCs). Gray dashed line indicates GMC LWR=0.9. The linear regression is indicated and the regression equation, R^2 value, and p-value are indicated at the top right. (E) Quantification of the SMC nuclei diameter in WT, *bdpolar-1*, *bdpan1-1* and *bdpolar-1*;*bdpan1-1* (n=20 SMCs). Samples were compared using a one-way ANOVA and post-hoc Tukey test for multiple comparisons; different letters indicate significant differences ($p<0.05$). (F) Summary table of total number of quantified nuclei, average d distance (µm) when GMC LWR>0.9 and >1.2, and number and percentage of polarized nuclei within 4µm range when GMC LWR>0.9 and >1.2 in WT, *bdpolar-1*, *bdpan1-1* and *bdpolar-1*;*bdpan1-1.*

2.10 *BdPOLAR* regulates cortical division site orientation

Because BdPOLAR's role did not seem to lie mainly in nuclear migration, I thought about its potential functions in the light of BdPOLAR subcellular localization and *bdpolar-1* phenotypes. According to *BdPOLAR* translational signal, apart from the apparent absence of BdPOLAR-mVenus signal at the GMC/SMC interface, I also found it locates lacking at the cortical division sites just above and below the GMC/SMC interface. This was visible in 2D and 3D images of BdPOLAR-mVenus localization in SMCs (Fig. 16B). Thus, I supposed that BdPOLAR probably was associated with cortical division sites specification and cell division orientation. To investigate this presumption, I cloned the cortical division sites marker *BdPOLARp:BdTANGLED1(BdTAN1)-mCitrine* reporter lines that were able to be expressed explicitly in pre-mitotic SMCs and young GMCs. Through confocal imaging, I observed that BdTAN1 could be detected stably at cortical division sites during SMC, and GMC divisions resemble its homolog in maize (Martinez, Luo et al. 2017). Furthermore, it is also expressed at the SMCs nuclei (Fig. 24, 25, and 26). In wild-type 33 individual SMCs, BdTAN1 faithfully and correctly localized above and below the GMC/SMC interface to predict future SC division plane (Fig. 24, 27, Fig. S12, and Fig. S13). In *bdpan1-1* 40 individual SMCs, BdTAN1 displayed mostly proper localization (92.5%, Fig. 26, 27, Fig. S16, and Fig. S17). In *bdpolar-1* 32 individual SMCs, BdTAN1 is mis-placed to the proximal and distal PM forming a transverse rather than longitudinal curved division plane in 28.1% SMCs (Fig. 25, 27, Fig. S14, and Fig. S15). In addition, in 12.5% of cases, BdTAN1 located three cortical sites in SMCs (Fig. 27B, C). This indicated a role for *BdPOLAR* in orienting cell division planes in SMCs.

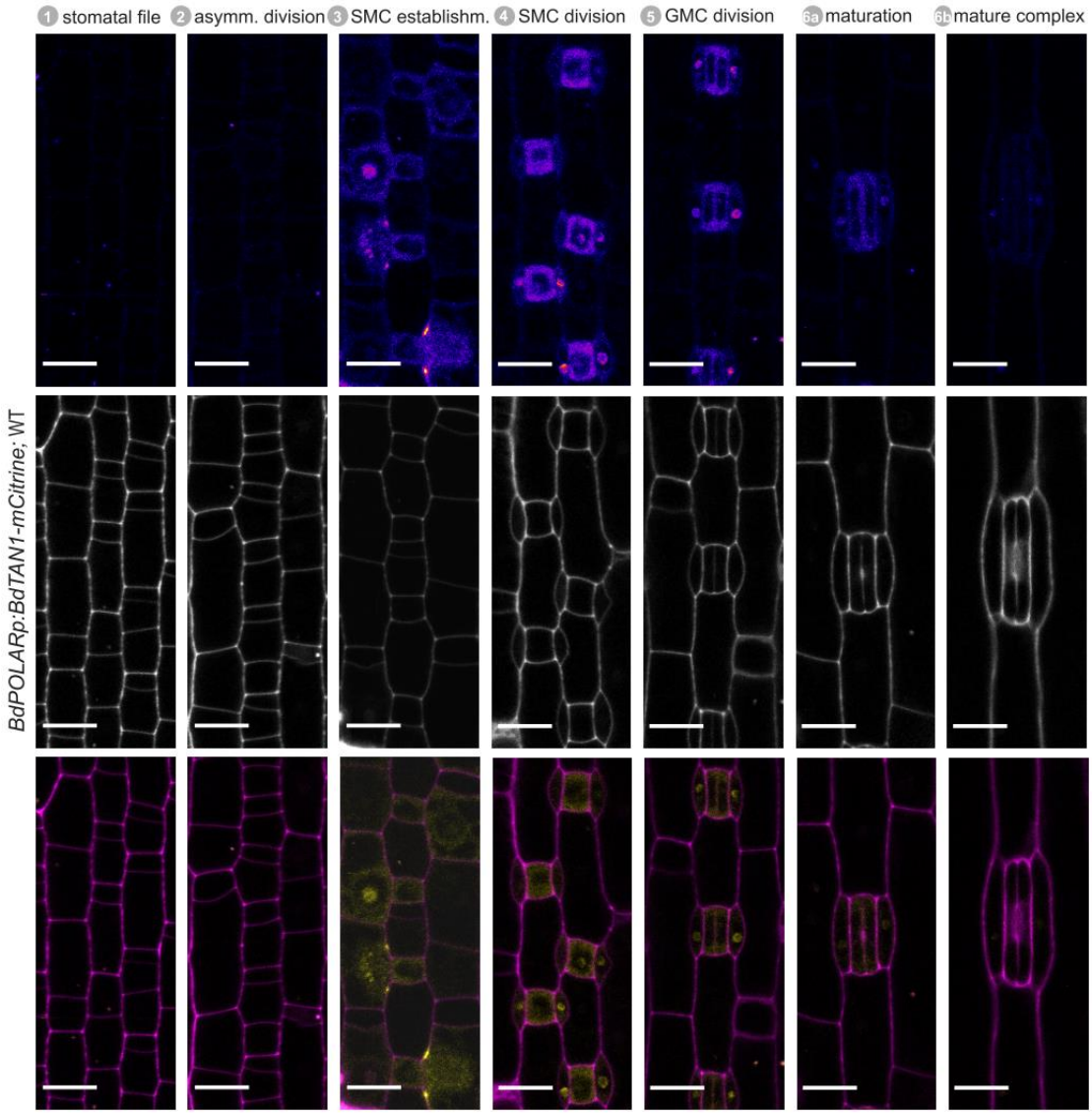

Figure 24. *BdPOLARp:BdTANGLED1(BdTAN1)-mCitrine* expression throughout stomatal development in WT.
Fluorescence intensity images of mCitrine channel only (upper), images of PI-stained cell outlines only (middle), and composite images (bottom) with BdTAN1-mCitrine signal (yellow) and PI-stained cell outlines (magenta). All images from the second leaf, 5 to 6 dag. Scale bars, 10 µm.

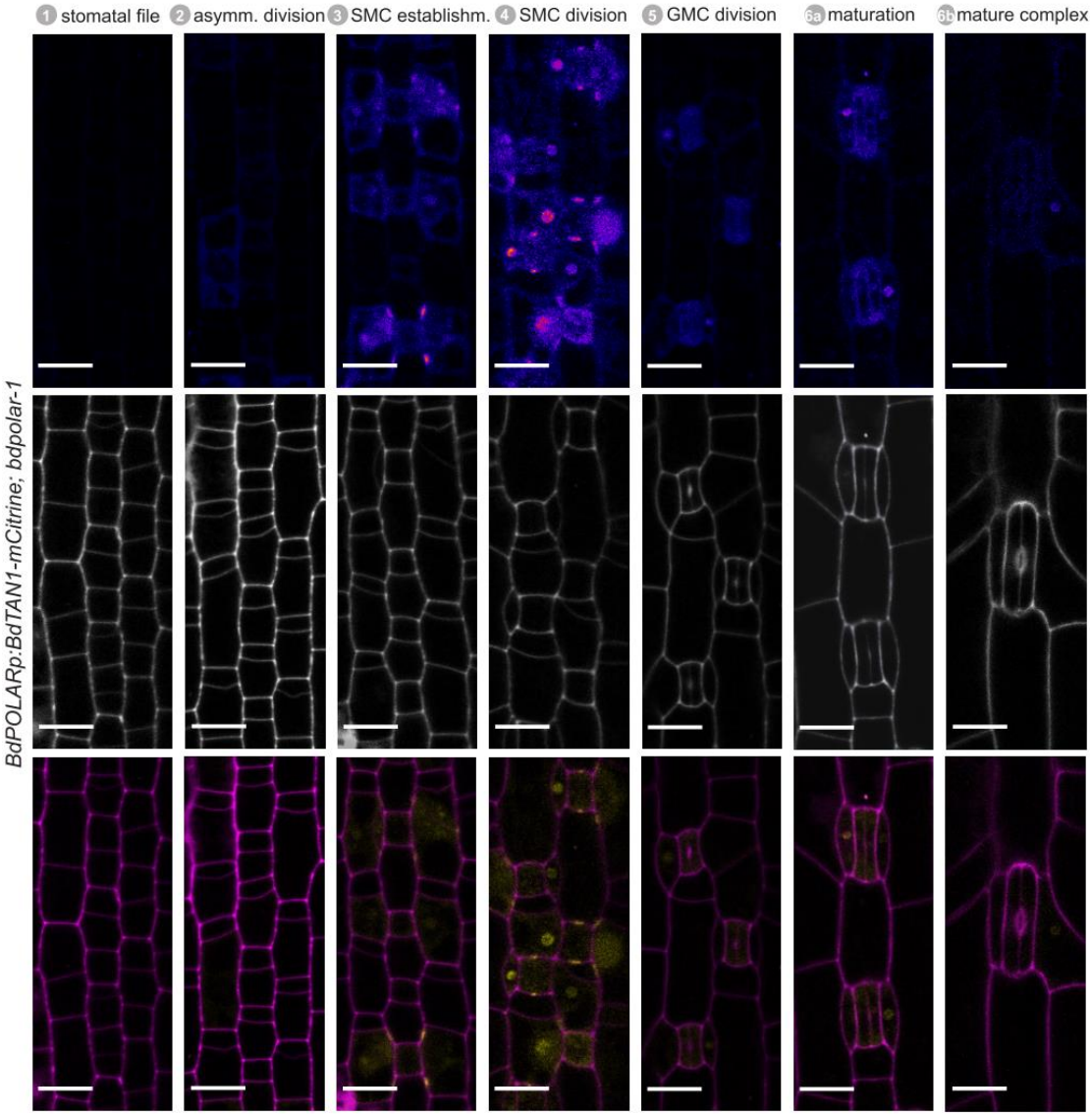

Figure 25. *BdPOLARp:BdTAN1-mCitrine* expression throughout stomatal development in *bdpolar-1*.
Fluorescence intensity images of mCitrine channel only (upper), images of PI-stained cell outlines only (middle), and composite images (bottom) with BdTAN1-mCitrine signal (yellow) and PI-stained cell outlines (magenta). All images from the second leaf, 5 to 6 dag. Scale bars, 10 µm.

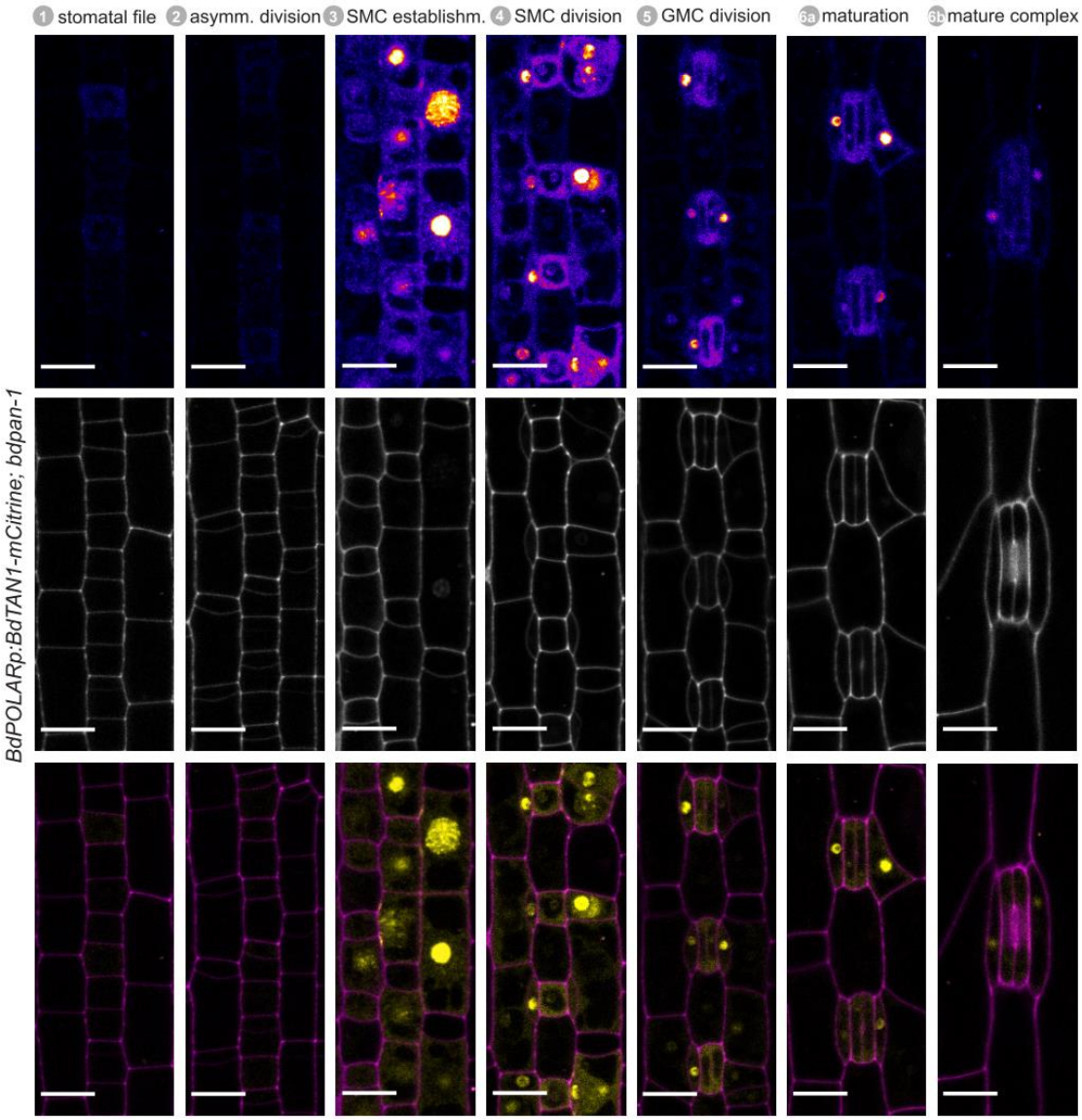

Figure 26. *BdPOLARp:BdTAN1-mCitrine* expression throughout stomatal development in *bdpan1-1*.
Fluorescence intensity images of mCitrine channel only (upper), images of PI-stained cell outlines only (middle), and composite images (bottom) with BdTAN1-mCitrine signal (yellow) and PI-stained cell outlines (magenta). All images from the second leaf, 5 to 6 dag. Scale bars, 10 µm.

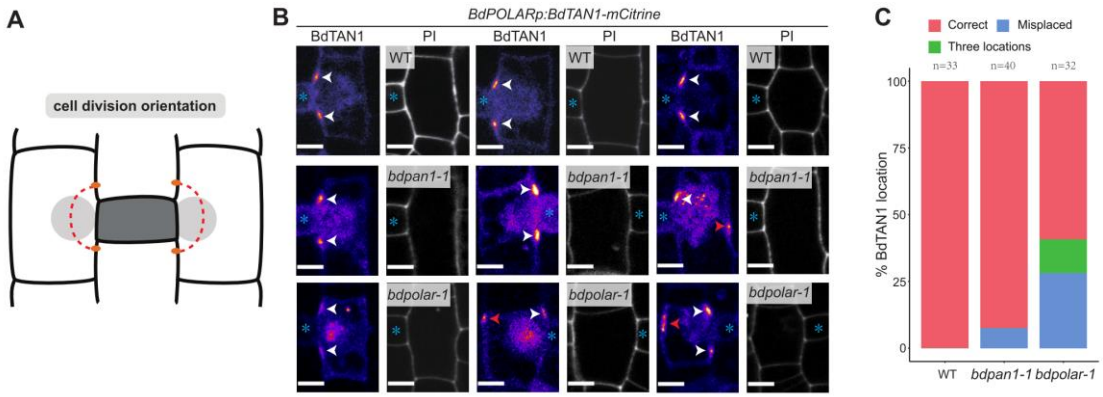

Figure 27. *BdPOLAR* regulates cortical division site orientation in SMC.
(A) Schematic showing future division plane and expected BdTAN1 localization (orange) at the cortical division site in WT. (B) *BdPOLARp:BdTAN1-mCitrine* expressed in WT, *bdpan1-1,* and *bdpolar-1*. Correct cortical division sites indicated by BdTAN1-mCitrine signal are indicated with white arrowheads; misplaced cortical division sites are indicated with red arrowheads. GMCs are indicated with blue asterisks. Scale bar, 5 µm. (C) Percentages of correct, misplaced, and three cortical division sites in WT, *bdpolar-1* and *bdpan1-1*; number of SMCs analyzed are indicated.

2.11 *BdPOLAR* controls cell division potential

In addition, I hypothesize that *BdPOLAR* yields the ability to regulate cell division potential (Fig. 28A). Two detections supported this presumption. Firstly, I examined the number of different types of aberrant ACDs in individual SMC; some SMCs failed to divide completely (reminiscent of the *bdmute* phenotype) belonging to the “No division” category (Fig. 28B; Purple). However, most SMCs in *bdpolar-1*, *bdpan1-1*, and the double mutant *bdpolar-1;bdpan1-1* divided 1 to 4 times with misoriented division planes (Fig. 28B; Blue, green, olive, red in order). In *bdpolar-1,* less section of SMCs showed one time abnormal division (25.7%) compared to *bdpan1-1* (44.6%) (Fig. 28C). In contrast, the populations of two (58.4%) and three times (13.9%) aberrant divisions in *bdpolar-1* were larger than in *bdpan1-1* (50.4% and 5%, respectively; Fig. 28C). Moreover, only SMCs in *bdpolar-1* showed even four rounds of aberrant cell divisions (1.5%; Fig. 28C). Generally, SMCs in *bdpolar-1* divided 1.9 times and only 1.6 times in SMCs of *bdpan1-1* in average.

Secondly, I quantified the LWR of the GMCs flanking by one and two SCs in wild-type and mutants. In both cases, *bdpolar-1* and *bdpolar-1;bdpan1-1* showed significantly higher LWR than wild-type and *bdpan1-1* (Fig. 29). When GMCs accompanied with two divided SCs, *bdpolar-1;bdpan1-1* double and *bdpolar-1* single mutants contained the identical and higher GMC LWR compared to wild-type and *bdpan1-1* single mutant, which also had the same ratio (Fig. 29, C and D). This indicated that GMCs neighboring with divided SCs were developmentally more mature in *bdpolar-1* than *bdpan1-1* and wild-type. This is possible caused by a potential growth delay in *bdpolar-1*, or more probable because the SMCs in *bdpolar-1* acquired higher division potential (Fig.

28A), inducing more times of division occurred until eventually accomplished a correct division.

In conclusion, these studies suggested that *BdPOLAR* not just serves as a cell division orientation regulator in SMCs, and also controls their cell division capacity.

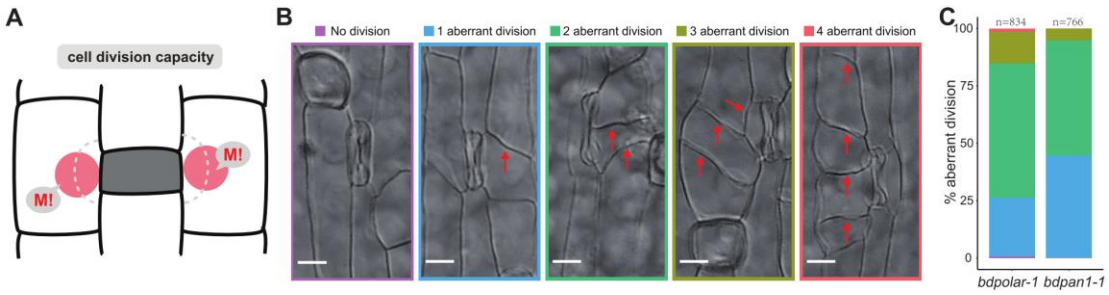

Figure 28. *BdPOLAR* controls division capacity in grass SMC.
(A) Diagram indicating polarized nuclei and SMC division potential (M!). (B) DIC images of different SMC division frequencies observed in the mature leaf epidermis of *bdpolar-1* and *bdpan1-1*; No division (purple), 1 aberrant division (blue), 2 aberrant divisions (green), 3 aberrant divisions (olive); 4 aberrant division (red). The division planes are indicated with red arrows. Scale bar, 10 µm. (C) Percentages of different SMC division types in *bdpolar-1* and *bdpan1-1*; numbers of SMCs analyzed are indicated.

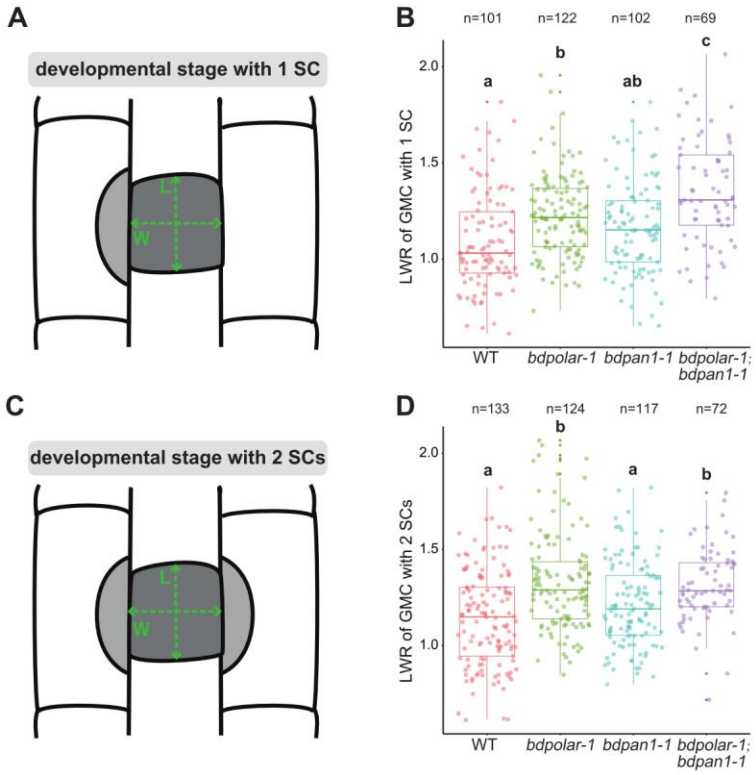

Figure 29. GMCs that successfully recruited SCs displayed a higher GMC LWR in *bdpolar-1* compared to *bdpan1-1.*
(A, C) Diagrams showing GMCs that recruited one (A) or two SCs (C). L (green): GMC length; W (green): GMC width. (B, D) Quantifications of GMC LWR in WT, *bdpolar-1*, *bdpan1-1* and *bdpolar-1*;*bdpan1-1* when GMCs recruited one (B) and two SCs (D); Samples were compared using a one-way ANOVA and post-hoc Tukey test for multiple comparisons; different letters indicate significant differences ($p<0.05$). Numbers of GMCs analyzed per genotype are indicated.

2.12 Correctly divided SCs improve stomatal gas exchange

Previous work identified that stomatal complexes lacked the ability to recruit SCs in *bdmute*, leading to seriously decreased gas exchange dynamics and capacity (Raissig, Matos et al. 2017). In my study, *bdpolar-1;bdpan1-1* double mutant displayed almost 82% of SCs failed to form normally. In this circumstance, the GMCs neighboring cells still yielded SC lineage identity specified by *BdMUTE;* however, behaving SC divisions abortion phenotypes. To test if SMC polarity mutants show defects in stomatal opening and closing, Tiago DG Nunes performed LI-6800 measurements in a changing light system to quantify gas exchange efficiency and water vapor exiting speed through the stomata.

bdpolar-1, bdpan1-1 single mutants, and *bdpolar-1;bdpan1-1* all displayed lower absolute stomatal conductance (g_{sw}) that seemed proportional to the their numbers of defective SCs, but their stomatal densities were not significantly altered (Fig. 30, A, C, and E, and Fig. 31A). These decreased g_{sw} in mutants could be due to their aberrantly divided SCs. The relative g_{sw} (normalized to maximum stomatal conductance) is representative of stomatal opening and closing speed. *bdpolar-1;bdpan1-1* clearly displayed slower stomatal movements (Fig. 30F) but not *bdpolar-1* and *bdpan1-1* (Fig. 30, B and D), and the difference in stomatal opening and closing kinetics was only observed in *bdpolar-1;bdpan1-1* (Fig. 30F, and Fig. 31, C, D and E). This indicated that a large number of SCs must be defective to influent stomatal speed. *bdpolar-1* and *bdpan1-1* single mutants did not display severe defects concerning relative g_{sw} but exhibited lower absolute g_{sw} (Fig. 30, A, B, C and D). Paired with the fact that stomatal densities were not different in the single mutants (Fig. 31A), this indicates that the lower extent of SC defects in single mutants affected gas

exchange efficiency but not stomatal movement. In addition, GC length was dramatically significantly shorter in *bdpolar-1;bdpan1-1* double mutant than wild-type and *bdpolar-1,* and *bdpan1-1* single mutant also displayed significantly decreased GC length (Fig. 31B), suggesting that abnormally SCs formation would affect GCs morphogenesis. Thereby, the graminoid stomatal function performs fully demands the correct SCs formation and morphology. In addition, *bdpolar-1;bdpan1-1* displayed less severe on stomatal speediness compared to *bdmute* (Raissig, Matos et al. 2017) suggesting that the aberrant cells flanking the GCs in *bdpolar-1;bdpan1-1* might maintain residual SC identity.

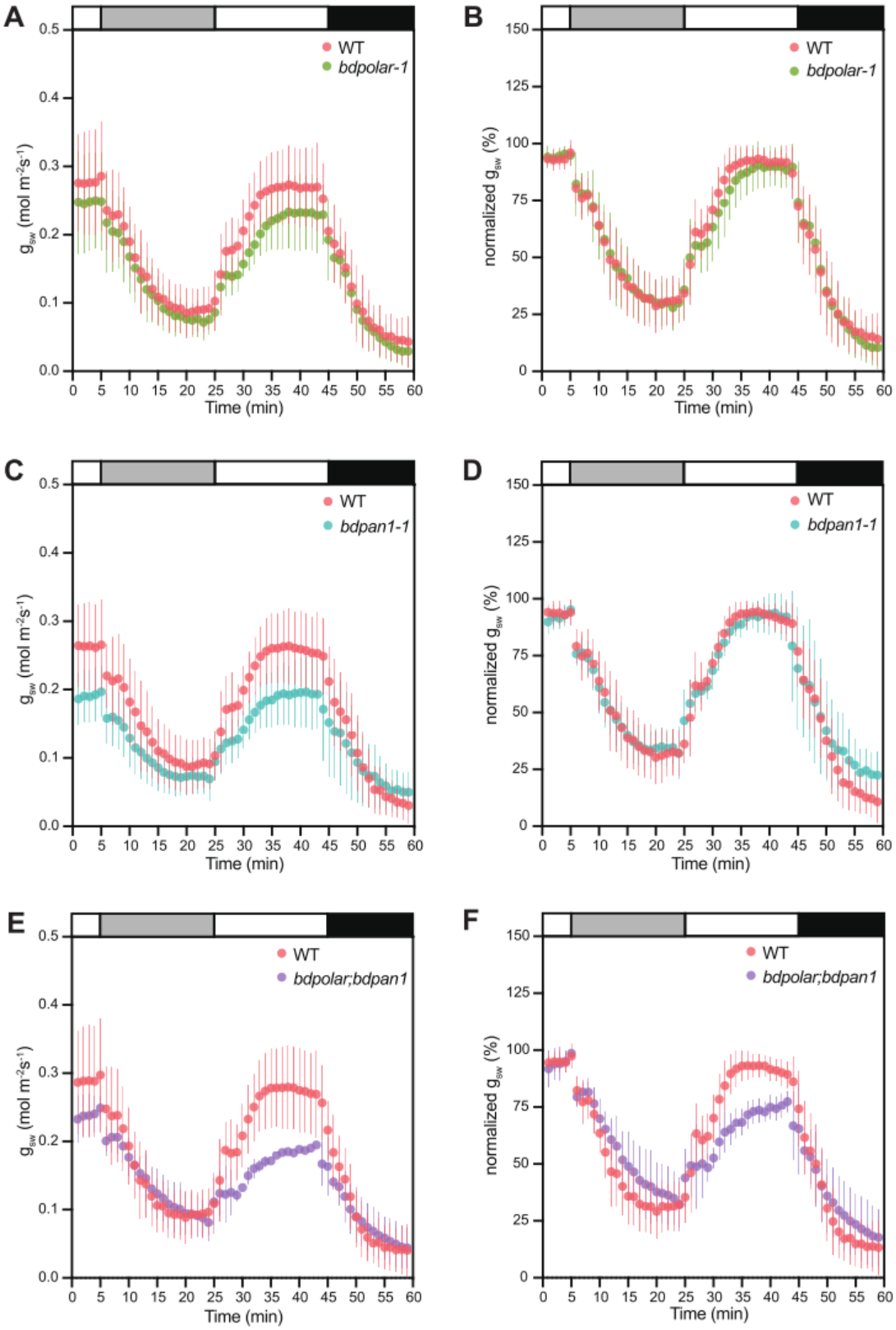

Figure 30. Wrongly divided SCs affect stomatal gas exchange levels and stomatal movement.
(A, C, and E) Absolute stomatal conductance (g_{sw}) in response to light transitions (1000 PAR - 100 PAR - 1000 PAR - 0 PAR) in *bdpolar-1* (A), *bdpan1-1* (C), and *bdpolar-1; bdpan1-1* (E) compared to paired WT measurements. (B, D, and F) Relative stomatal

conductance (g_{sw} normalized to highest g_{sw} observed) in response to light transitions (1000 PAR - 100 PAR - 1000 PAR - 0 PAR) in *bdpolar-1* (B), *bdpan1-1* (D), and *bdpolar-1; bdpan1-1* (F) compared to paired WT measurements. n=5 individuals per mutant genotype and 7 WT individuals.

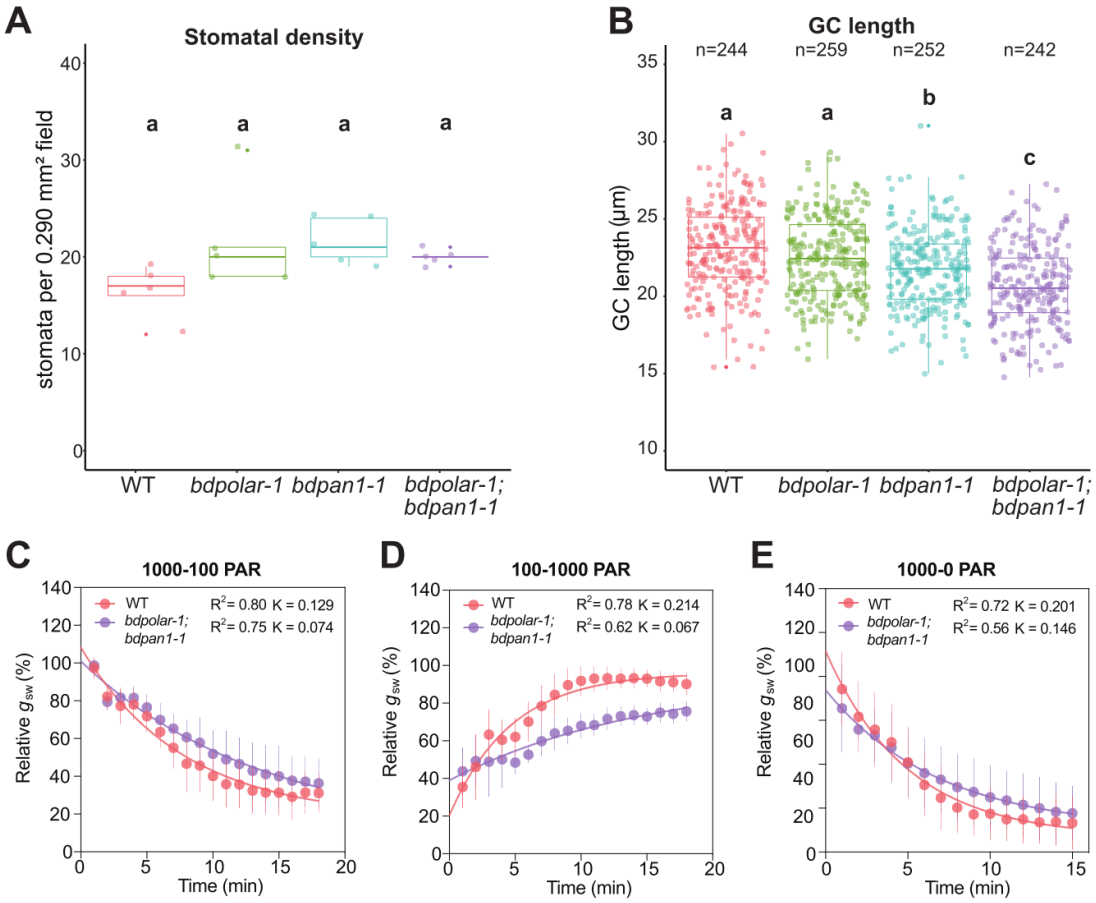

Figure 31. The stomatal opening and closing kinetics was affected in *bdpolar-1;bdpan1-1.*
(A) Stomatal density was quantified using the leaf areas that were used for stomatal conductance measurements in Fig. 30. n=5 individuals and 364-418 stomatal complexes. (B) GC length was quantified using the leaf areas that were used for stomatal conductance measurements in Fig. 30. Numbers of GCs analyzed per genotype are indicated. (C) One-phase decay exponential regression for the transition 1000 to 100 PAR. (D) One-phase association exponential regression for the transition 100 to 1000 PAR. (E) One-phase decay exponential regression for the transition 1000 to 0 PAR. R^2 value and constant rate (K) are indicated. Samples were compared using a one-way ANOVA and post-hoc Tukey test for multiple comparisons; different letters indicate significant differences ($p<0.05$).

2.13 The localization of BdPOLAR is important for its function

To explore if the polarized localization of BdPOLAR and BdPAN1 are required for their functions, Lea Berg created BdPOLAR and BdPAN1 myristoylated constructs. Myristoylation is one way to implement the protein-lipid modification. I expected the BdPOLAR and BdPAN1 would change localization

patterns on the SMC plasma membrane after myristoylated modification. *BdPOLARp: myristoylation (MYR)-BdPOLAR-mCitrine* and *BdPAN1p: MYR-BdPAN1-mCitrine* were transformed into *bdpolar-1* and *bdpan1-1* separately. BdPOLAR myristoylation version T0 lines displayed "patchy" pattern localization, uneven BdPOLAR intensity observed on SMC membrane (Fig. 33). In addition, BdPOLAR partially dissociated from the plasma membrane to the intracellular and localized to the cytoplasm (Fig. 33). In individuals from one T1 myristoylation version, BdPOLAR lost "patchy" pattern localization; however, it retained the cytoplasmic localization (Fig. 32, Fig. S18, Fig. S19, and Fig. S20). More independent T1 lines will be inspected to confirm whether this "patchy" pattern is truthful. When I quantified the defective SCs from T1 individuals shown in Fig. 32, they displayed different defects percentages, some partially rescued production of SCs in the *bdpolar-1* epidermal cells. In contrast, some even showed more severe SC defects than *bdpolar-1* (Fig. 34). Even though these scattered defective SCs percentages seem not associated with the MYR-BdPOLAR signal intensity, it might suggest that polarized localization of BdPOLAR is important for its function.

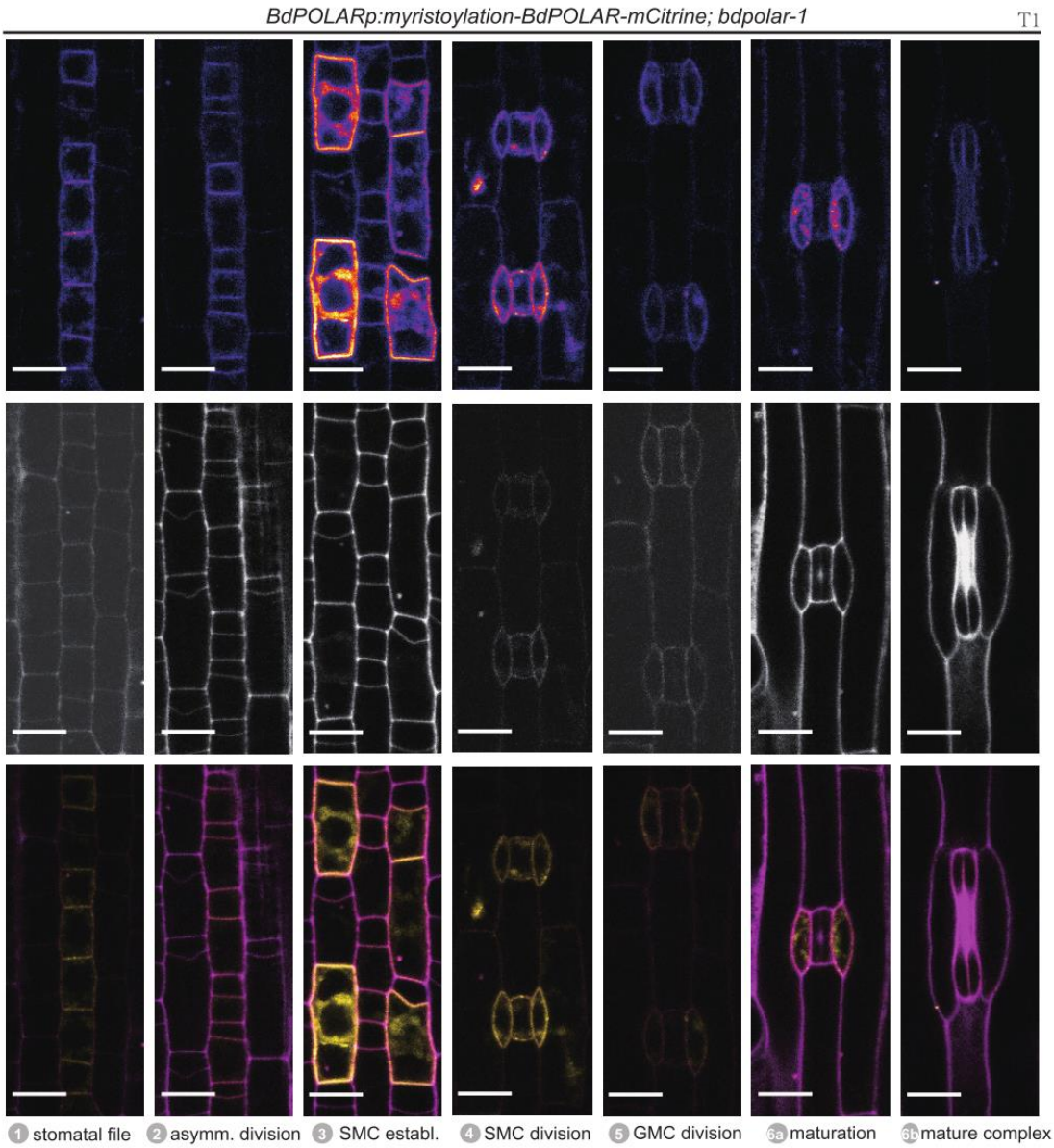

Figure 32. *BdPOLARp:myristoylation (MYR)-BdPOLAR-mCitrine* expression throughout stomatal development in *bdpolar-1*.
Fluorescence intensity images of mCitrine channel only (upper), images of PI-stained cell outlines only (middle), and composite images (bottom) with MYR-BdPOLAR-mCitrine signal (yellow) and PI-stained cell outlines (magenta). All images from the second leaf, 5 to 6 dag, T1 generation. Scale bars, 10 µm.

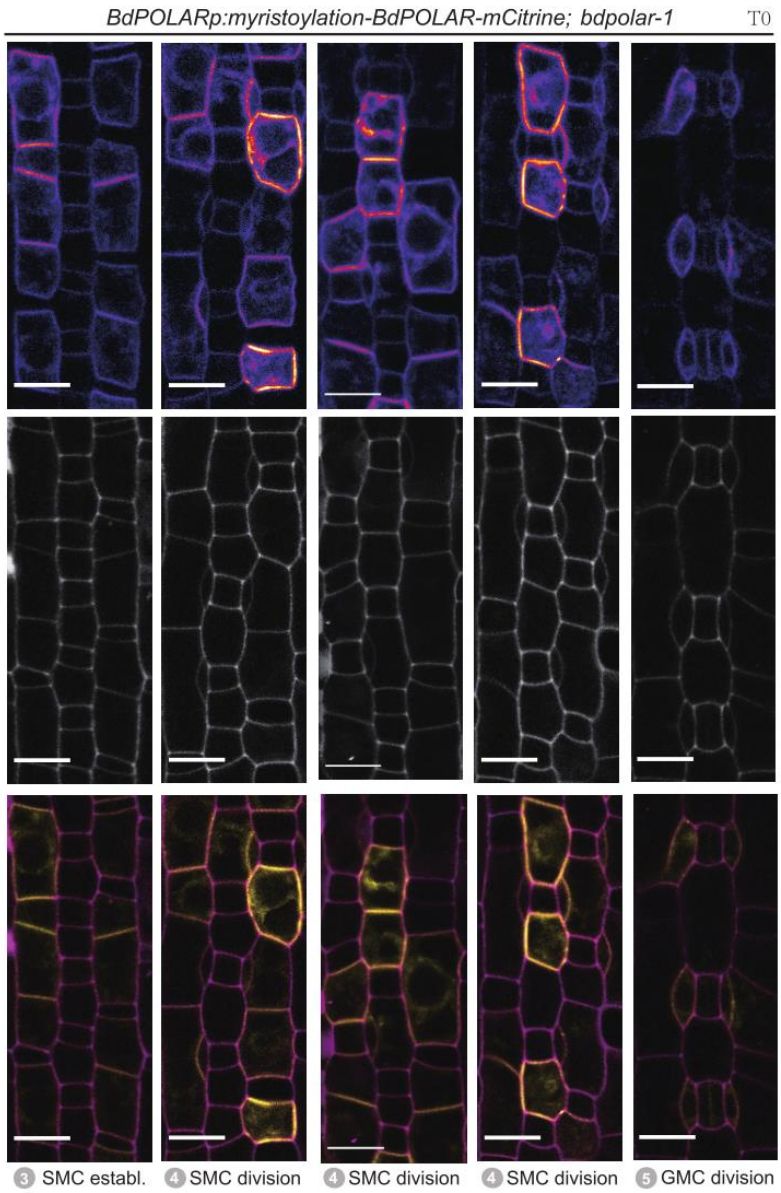

Figure 33. *BdPOLARp:MYR-BdPOLAR-mCitrine* expression at stage 3, 4 and 5 in *bdpolar-1*.
Fluorescence intensity images of mCitrine channel only (upper), images of PI-stained cell outlines only (middle), and composite images (bottom) with MYR-BdPOLAR-mCitrine signal (yellow) and PI-stained cell outlines (magenta). T0 generation. Scale bars, 10 µm.

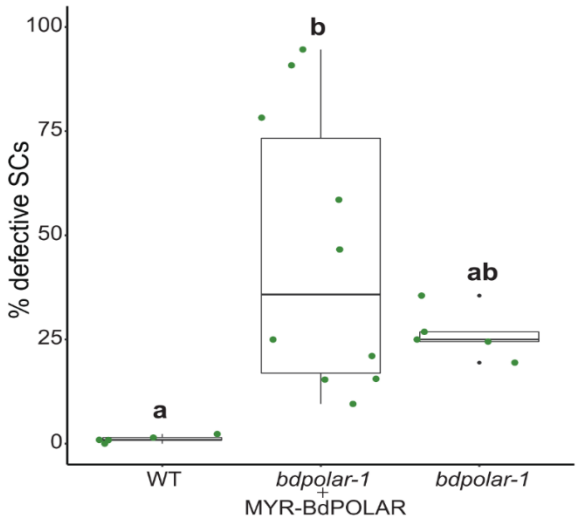

Figure 34. The localization of BdPOLAR affects SCs division.
Quantifications of defective SCs of WT, *bdpolar-1* expressed with *BdPOLARp:MYR-BdPOLAR-mCitrine*, and *bdpolar-1* control. Samples were compared using a one-way ANOVA and post-hoc Tukey test for multiple comparisons; different letters indicate significant differences ($p<0.05$). n=428-852 SMCs.

Since BdPAN1 integrates with the cell membrane through its transmembrane domain, it tightly spans the entire membrane. The myristoylated modification cannot detach BdPAN1 protein from the cell membrane. Thus, MYR-BdPAN1-mCitrine maintained the intimate attachment at the GMC/SMC interface as previous localization was found from BdPAN1-YFP (Fig. 35). To get insight into the relationship between the polarization and function of BdPAN1, a *BdPAN1* reporter line with a truncated BdPAN1 transmembrane domain will be generated.

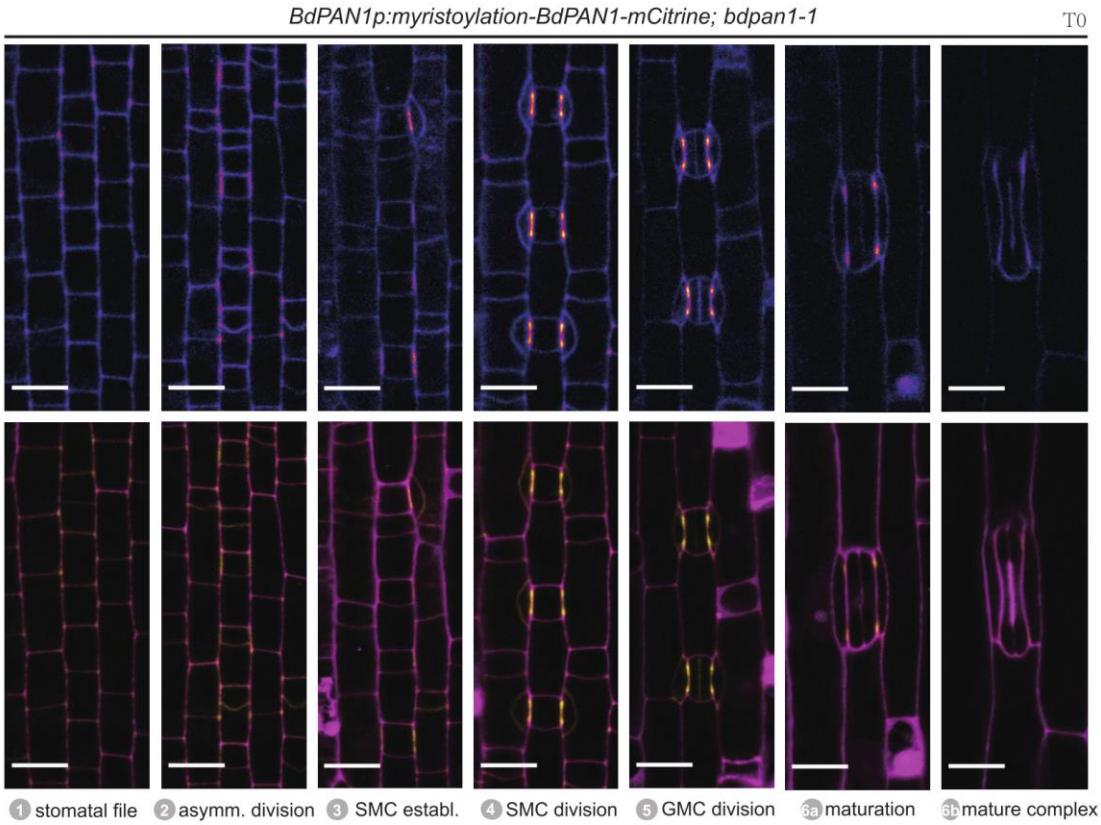

Figure 35. *BdPAN1p:MYR-BdPAN1-mCitrine* expression throughout stomatal development in *bdpan1-1*.
Fluorescence intensity images of mCitrine channel only (upper), and composite images (bottom) with MYR-BdPAN1-mCitrine signal (yellow) and PI-stained cell outlines (magenta). T0 generation. Scale bars, 10 µm.

2.14 The opposite tagged *BdPOLAR* overexpression affects SC division differently

Since the dosage and/or stability of BdPOLAR is crucial for its function, I hypothesize that overexpression of *BdPOLAR* will result in defective SCs or other phenotypes. To verify this conjecture, constructs with *ZmUbi* promoter drives ubiquitous expression of *BdPOLAR* tagged N-terminal and C-terminal mVenus were produced and transformed. The BdPOLAR signal was observable everywhere of leaf epidermal in both overexpression transgenic lines (Fig. 36, Fig. 37 and Fig. S21), proving that both constructs were functional. Unexpectedly, I did not observe aberrant SCs formation from the N-terminal overexpression line, probably due to the influence of the N-terminal mVenus tag. In contrast, ubiquitously BdPOLAR-mVenus expressing caused 10% SC defects in wild-type (Fig. 21, C and D, Fig. 37, and Fig. S21),

suggesting the statement about dosage and/or stability of BdPOLAR is verified successfully only with C-terminal tagged fusion protein.

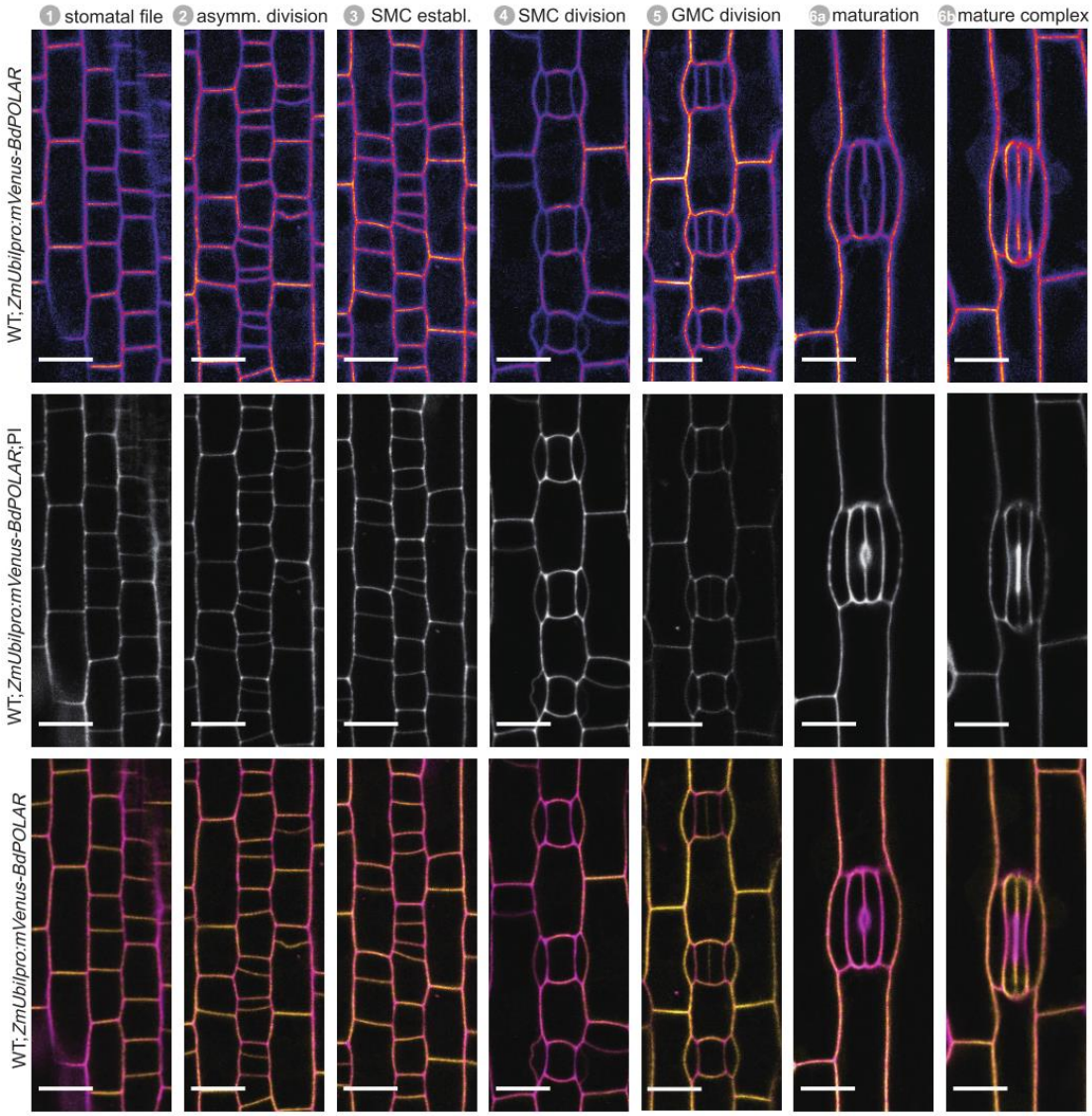

Figure 36. *ZmUbip:mVenus-BdPOLAR* expression throughout stomatal development in *B. distachyon*.
Fluorescence intensity images of mVenus channel only (upper), images of PI-stained cell outlines only (middle), and composite images (bottom) with mVenus-BdPOLAR overexpression signal (yellow) and PI-stained cell outlines (magenta). All images from the second leaf, 5 to 6 dag, T1 generation. Scale bars, 10 µm.

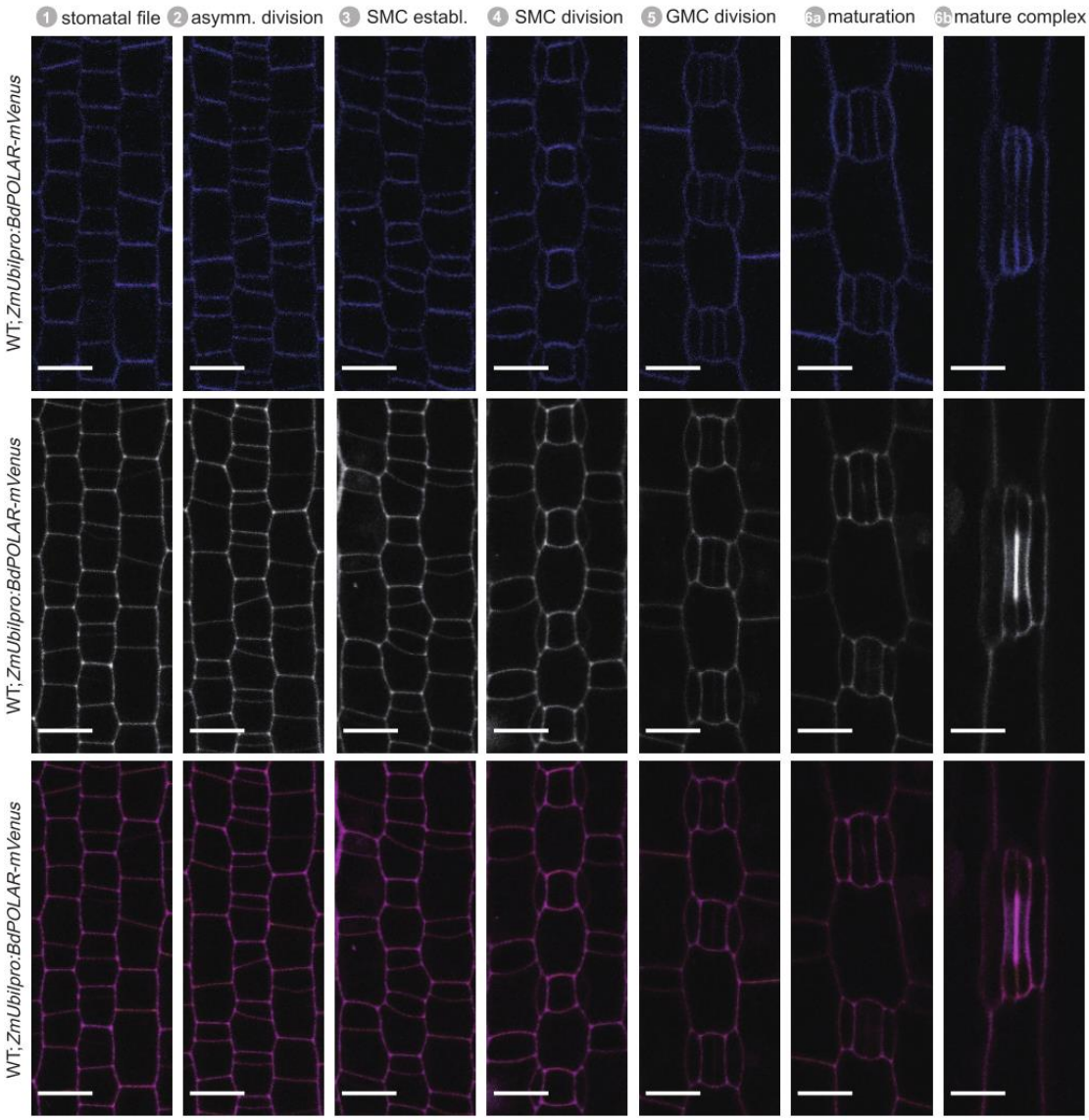

Figure 37. *ZmUbip:BdPOLAR-mVenus* expression throughout stomatal development in *B. distachyon*.
Fluorescence intensity images of mVenus channel only (upper), images of PI-stained cell outlines only (middle), and composite images (bottom) with BdPOLAR-mVenus overexpression signal (yellow) and PI-stained cell outlines (magenta). T0 generation. Scale bars, 10 µm.

2.15 The visualization of actin reporter line in SC polarity mutants

It was reported that actin displayed dis-localization in *pan1* mutant in maize (Cartwright, Humphries et al. 2009). To investigate further if actin-patch formation is affected in *Brachypodium* SMC polarity mutants, *bdpolar-1*, and *bdpan1-1*, and to create actin marker lines in epidermal and SC-specific lineage of *Brachypodium* leaf, ABD2 gene in *Arabidopsis* was adopted to build

constructs *pGGZ004_ZmUbipro-PmTurquoise-ABD2* and *pGGZ004_BdPOLARpro-PmTurquoise-ABD2*. Unfortunately, I encountered some cloning issues and failed with the final cloning step (see Materials and Methods). Later, Inés Hidalgo Prados cloned pGGC-LifeAct and *pGGZ004_BdPOLARpro-LifeAct-mcherry*, which can be applied to visualize actin localization and organization. *BdPOLARp:LifeAct-mcherry* were transformed into wild-type, *bdpolar-1* and *bdpan1-1.* In wild-type, actin-patch was properly formed at GMC/SMC interface (Fig. 39). Unexpectedly, compared to wild-type, *bdpolar-1* and *bdpan1-1* did not show an obvious difference in length and intensity of actin-patch (Fig. 39, and Fig. 40). However, not every SMC possesses a clear actin-patch in mutants and WT. Careful quantification is required to figure out if *BdPOLAR* and *BdPAN1* affect actin formation. The actin filaments were detectable via the LifeAct signal in GCs from some mature stomatal complexes. Thus, this reporter line provides the possibility to track the actin reorganization during GCs morphogenesis.

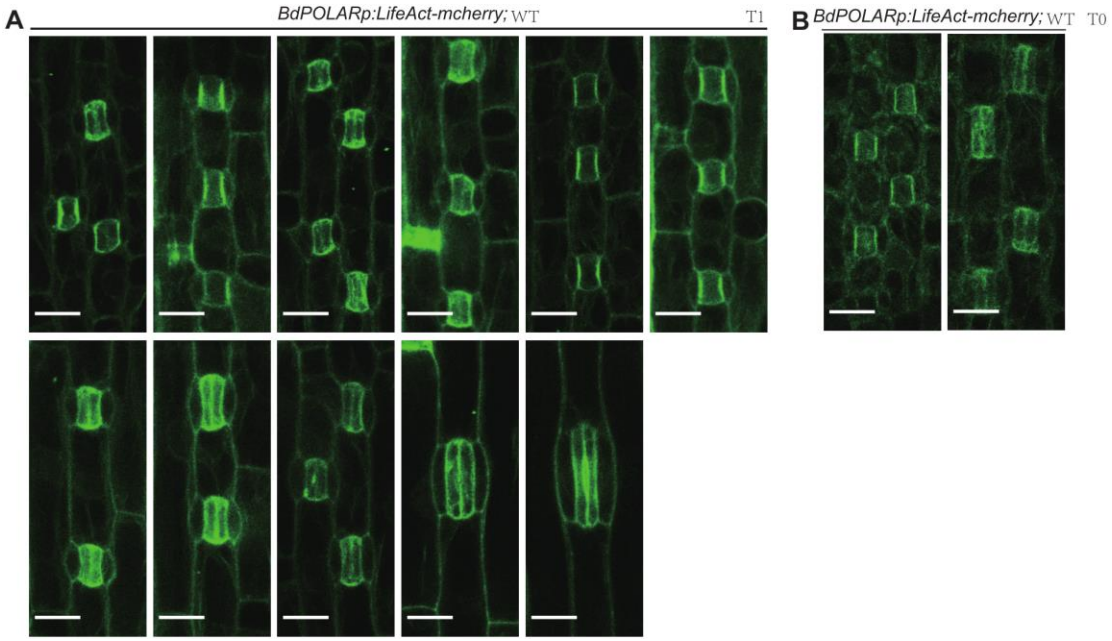

Figure 38. *BdPOLARp:LifeAct-mcherry* expression during stomatal development in WT.
confocal images of LifeAct-mcherry signal (green) in T1 generation (A) and T0 generation (B). Scale bars, 10 µm.

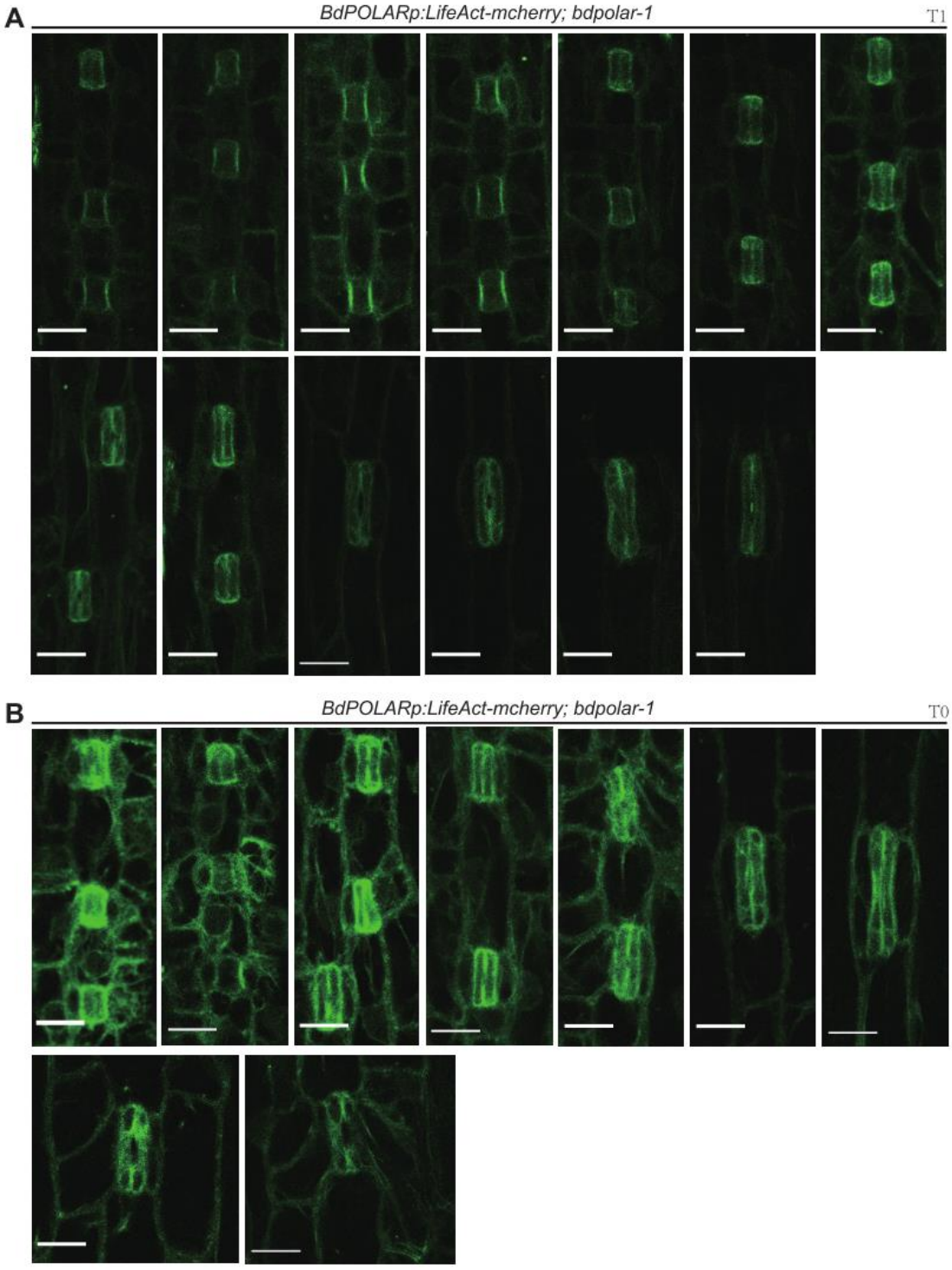

Figure 39. *BdPOLARp:LifeAct-mcherry* expression during stomatal development in *bdpolar-1*.
confocal images of LifeAct-mcherry signal (green) in T1 generation (A) and T0 generation (B). Scale bars, 10 µm.

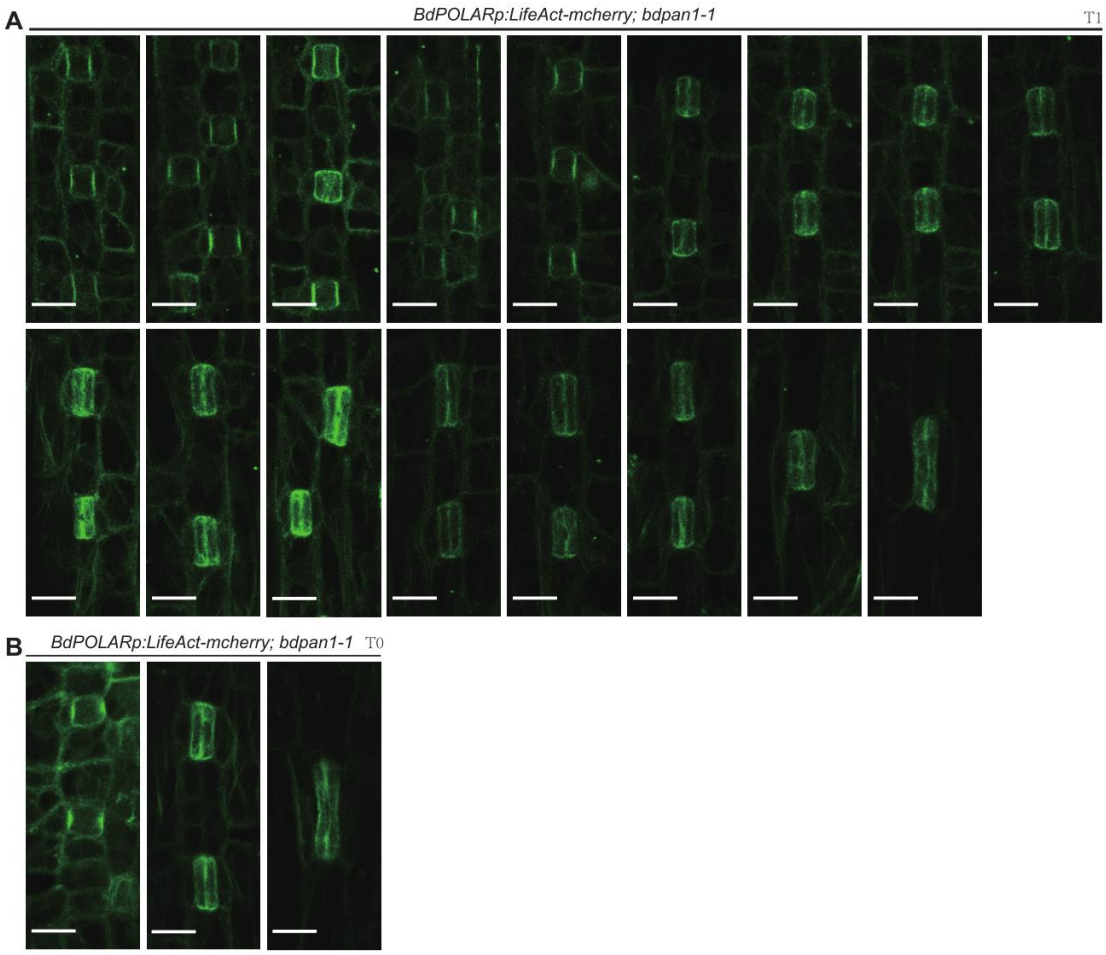

Figure 40. *BdPOLARp:LifeAct-mcherry* expression during stomatal development in *bdpan1-1*.
confocal images of LifeAct-mcherry signal (green) in T1 generation (A) and T0 generation (B). Scale bars, 10 µm.

To generate the MTs marker lines in epidermal and SC-specific, I created an MTs marker version employing the chimeric protein in which Turquoise was fused to the N-terminus of BdTUB6 (Bradi2g21340). Separately, *pGGZ004_ZmUbipro-PmTurquoise-BdTUB6* and *pGGZ004_BdPOLARpro-PmTurquoise-BdTUB6* were constructed. However, based on the initial examination of translational reporter T0 plants, both constructs do not seem to produce proper MTs signals. Signal was observed to accumulate densely at the bottom area but not evenly distributed in the whole stomata complex. This indicates *BdTUB6* is not an appropriate marker for MTs visualization in *Brachypodium*.

2.16 The fluorescent staining of actin in SC polarity mutants

To study the cytoskeleton organization during SMC divisions, I tried to establish the double labeling by using immunofluorescent staining for microtubules and fluorescent phalloidin staining for actin filaments, which has been applied to visualize actin filaments and microtubules in fixed maize leaf tissues (Nan, Mendoza et al. 2019). I followed the whole-mount procedure described in the above protocol and optimized some steps, such as trying different leaf areas, cutting leaf division zone, and adjusting enzyme digestion time and staining time. However, I did not achieve the dual-labeling in *Brachypodium* leaf tissues. Afterward, I attempted to stain microtubules and actin filaments separately. The bright Alexa Fluor 488 signal was detected in the epidermal cells from wild-type, *bdpolar-1*, *bdpan1-1,* and *bdpolar-1;bapan1-1.* In stomatal cell lineages, precise and robust actin patches were observed at GMC contact sites during SCs recruitment (Fig. 41). Again, the issue still exists that distinguishes the actin difference in mutants compared with wild-type. Therefore, the delocalized actin patches reported in maize *zmpan1* still need to be quantified in *Brachypodium* SMC polarity mutants. The immunofluorescent staining for microtubules alone did not generate a signal over the whole epidermal cells but only the edges of leaf tissues. Thus, it still needs to be optimized.

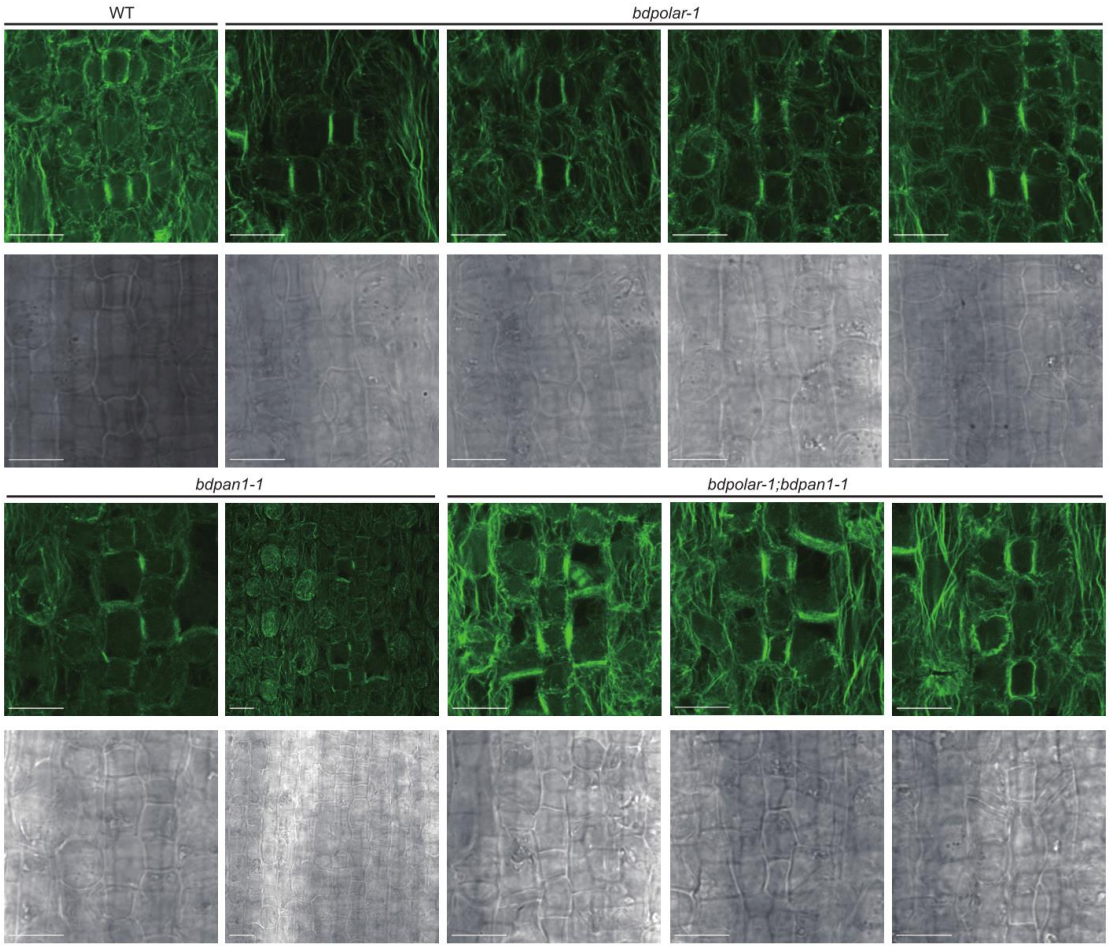

Figure 41. The actin cytoskeleton of epidermal cells is visualized using the green-fluorescent Alexa Fluor 488 Phalloidin.
Confocal images of actin filaments (upper) and images of bright field (bottom). Scale bars, 10 µm.

2.17 The proximity labeling of BdPOLAR and BdPAN1

To identify potential partners of SMC polarity regulators *BdPOLAR* and *BdPAN1* and to obtain protein complexes and proteomes in SMC-specific cell types, I applied the proximity labeling (PL) approach in this study. The biotin ligase constructs *BdPOLARp:BdPOLAR-mCitrine-TurboID* and *BdPOLARp:BdPAN-mCitrine-TurboID* were cloned, and transformed into *bdpolar-1* and *bdpan1-1*, separately. Biotinylated BdPOLAR proteins still preserve the same polarization pattern as BdPOLAR-mVenus, showing an absent signal at the GMC/SMC interface and cortical division sites (Fig. 42). Biotinylated BdPAN1 proteins were successfully expressed and still enriched at GMC/SMC interface. However, its subcellular localization showed more on

the SMC membrane than BdPAN1's original translational line (Fig. 43). Afterward, biotinylation activity, labeling time, temperature, biotin concentration, and biotin application will be tested in the workflow of the experimental procedure.

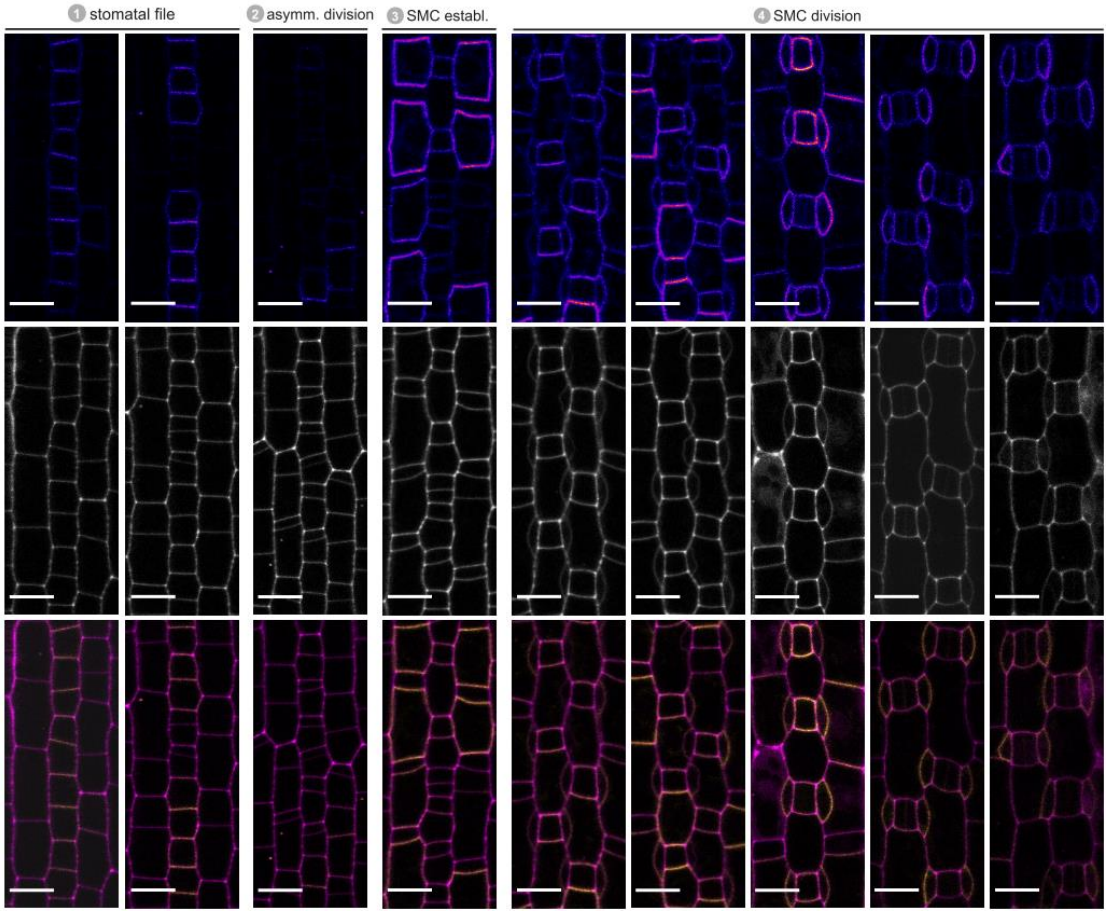

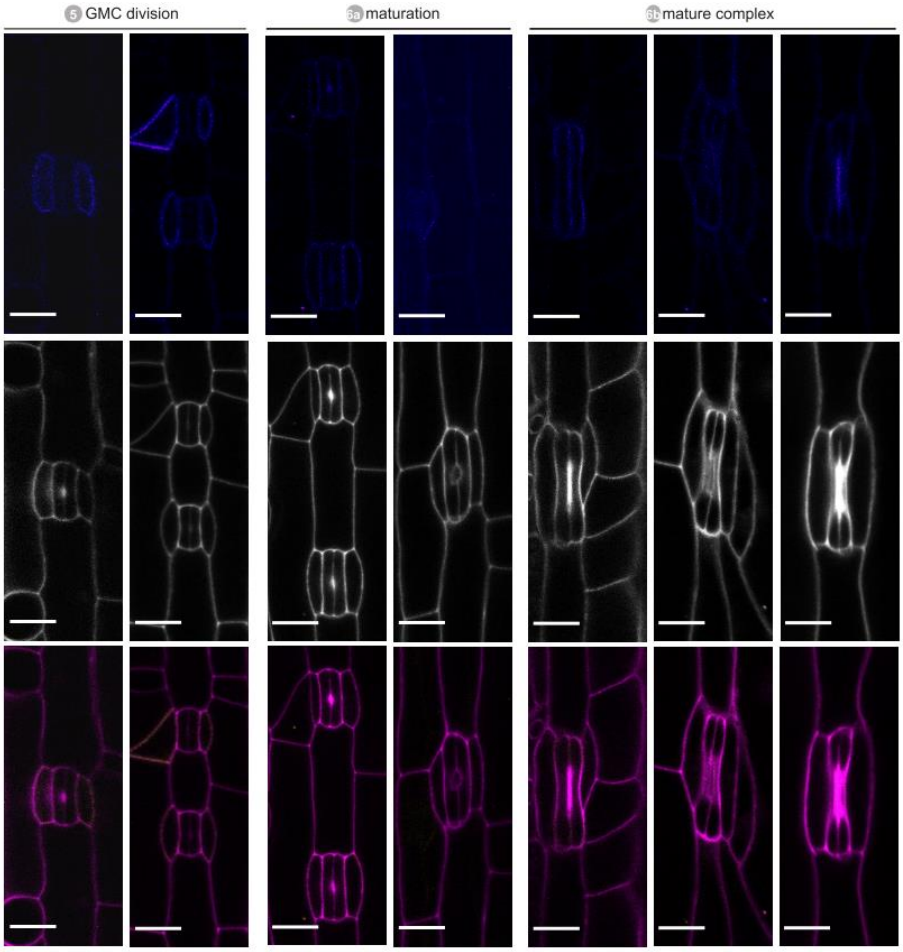

Figure 42. *BdPOLARp:BdPOLAR-mCitrine-TurboID* expression throughout stomatal development in *bdpolar-1*.
Fluorescence intensity images of mCitrine channel only (upper), images of PI-stained cell outlines only (middle), and composite images (bottom) with BdPOLAR-mCitrine-TurboID signal (yellow) and PI-stained cell outlines (magenta). T0 generation. Scale bars, 10 µm.

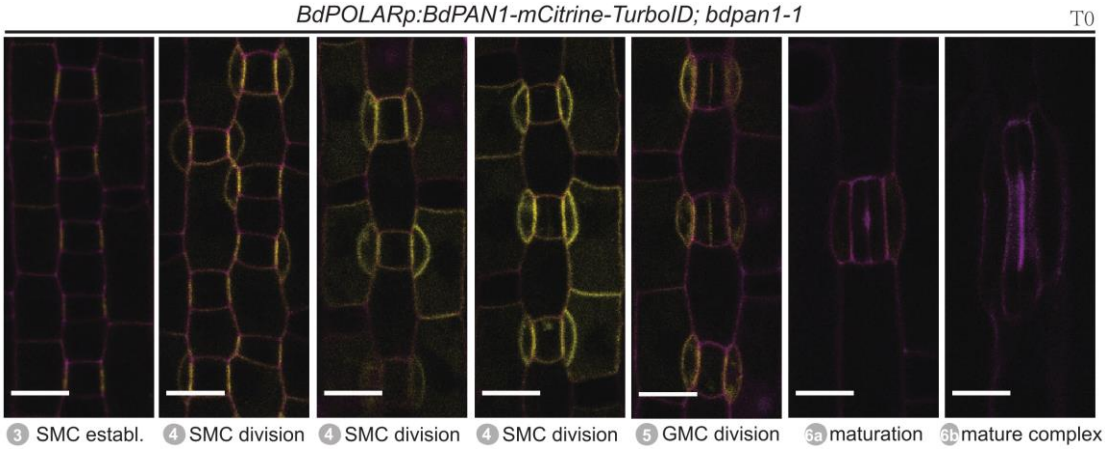

Figure 43. *BdPOLARp:BdPAN-mCitrine-TurboID* expression during stomatal development in *bdpan1-1*.
Composite images with BdPAN1-mCitrine-TurboID signal (yellow) and PI-stained cell outlines (magenta). T0 generation. Scale bars, 10 µm.

3. Decipher the Polarity Role of BdPOLAR-LIKE

Due to the weak SC defects that occur in *bdpolar* single mutants, there might be genes that play redundant roles with *BdPOLAR*. *BdPOLAR-LIKE* (Bd1g47330) is a mostly close homolog of *BdPOLAR.* In the mutation track of *BdPOLAR-LIKE*, several impactful NaN lines are described and distributed in the different gene regions. In the late third exon exists a high impactful nonsense mutation (E401*) induced protein termination from NaN1927 heterozygous. From the segregation group, plants bearing this partially unfunctional BdPOLAR- LIKE were observed with misoriented and additional SCs division in the lateral or vertical sides of GCs, and stomata cluster occasionally appeared (Fig. 44B). These defects are present frequently in homozygotes ; however, they do not appear in the heterozygous and wild-type after genotypes examined through dCAPS (Fig. 44A), indicating that the SC formation defects in NaN1927 are caused by the partly loss-of-function of *BdPOLAR-LIKE*.

Once again, in the third exon, NaN2048 and NaN2069 harbor one moderate impact resulting from A393V and L413F altered amino acid, respectively, and both are homozygotes mutation. The weakly affected SCs were noticed among some next offspring of NaN2048 (Fig. 44C) and NaN2069 (Fig. 44D). However, I faced some issues with genotyping these two lines using dCAPS. NaN633, NaN1587, NaN1824, and NaN1886 were also examined; however, their SCs seem to form normally. Effect impact, functional class, codon change, amino acid change, and exon tank about each line are accessible in Table 2. Overall, *BdPOLAR-LIKE* possibly plays a role in SCs formation based on NaN1927 characterization.

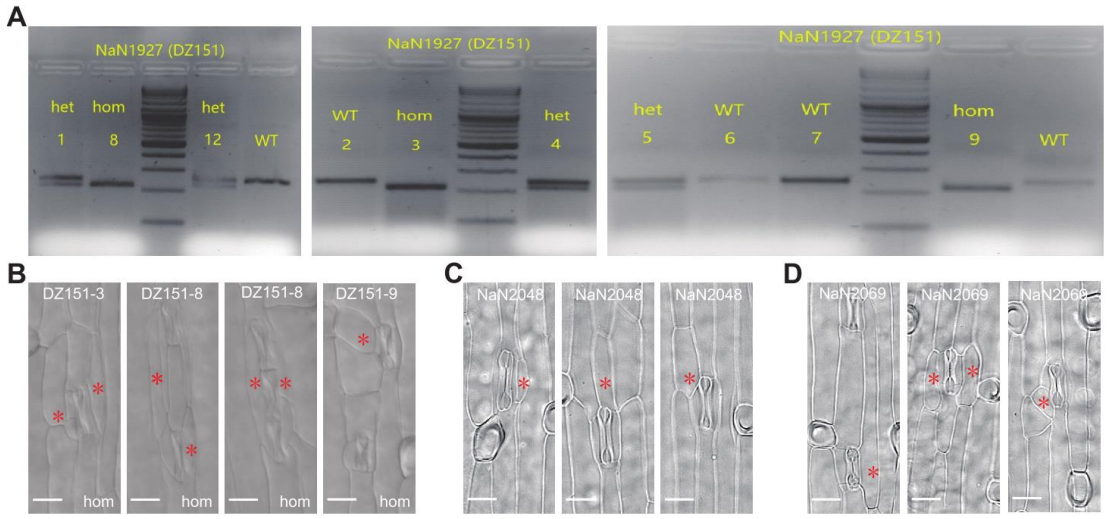

Figure 44. SC formation defects in NaN1927 are caused by the partly loss-of-function of BdPOLAR-like.
(A) Agarose gel electrophoresis for undigested and digested dCAPS marker products to genotype NaN1927 offspring. KpnI can digest PCR products from homozygous lines (209bp, and 32bp); heterozygous lines (32bp, 241bp, and 209bp); WT lines (241bp). (B) DIC images of the epidermis in NaN1927 (DZ151) homozygous lines. (C-D) DIC images of the epidermis in NaN2048 (C) and NaN2069 (D) homozygous lines. Aberrant SCs are indicated with red asterisks. Scale bars, 15 mm.

NaN	Effect	Effect Impact	Functional Class	Amino Acid change	Exon Rank	SCs defects	dCAPS
1927	Stop_gained	High	Nonsense	E401*	3	Yes	Yes
2048	Non_synonymous	Moderate	Missense	A393V	3	Yes	No
2069	Non_synonymous	Moderate	Missense	L413F	3	Yes	No
633	Non_synonymous	Moderate	Missense	A156T	2	No	No
1587	Non_synonymous	Moderate	Missense	A192V	2	No	No
1824	Non_synonymous	Moderate	Missense	R97W	1	No	No
1886	Non_synonymous	Moderate	Missense	A191T	2	No	No

Table 2. Variant annotations, SCs genotyping and phenotyping (dCAPS) results about BdPOLAR-like candidate NaN lines.

Apart from discovering causative NaN lines for *BdPOLAR-LIKE*, the reverse genetic approach, CRISPR/Cas9 gene-editing, was performed. Irem Polat cloned the CRISPR/Cas9 construct JD633-BdPOLAR-LIKE-g1 targeting the second exon of the *BdPOLAR-LIKE* gene region. Surprisingly, the transgenic T1 lines displayed not only abnormal SCs formation but also irregular hair cells formation and patterning and occasionally unusual pavement cell divisions (Fig. 45). To generate double mutant *bdpolar;bdpolar-like*, I built one pMOD_B2103 harbor one gRNA from *BdPOLAR* and *BdPOLAR-LIKE* separately. The transgenic lines pMDC32-BdPOLAR-LIKE-guide1/BdPOLAR-guide4 were produced through tissue culture. The CRISPR double mutant *bdpolar; bdpolar-like* displayed more severe SCs defects than *bdpolar* and *bdpolar-like* single

mutants, excessive hair cell clusters and aberrant pavement cell divisions (Fig. 46). This suggested *BdPOLAR-LIKE* played a role not only in stomatal cell lineage but also during hair cell development.

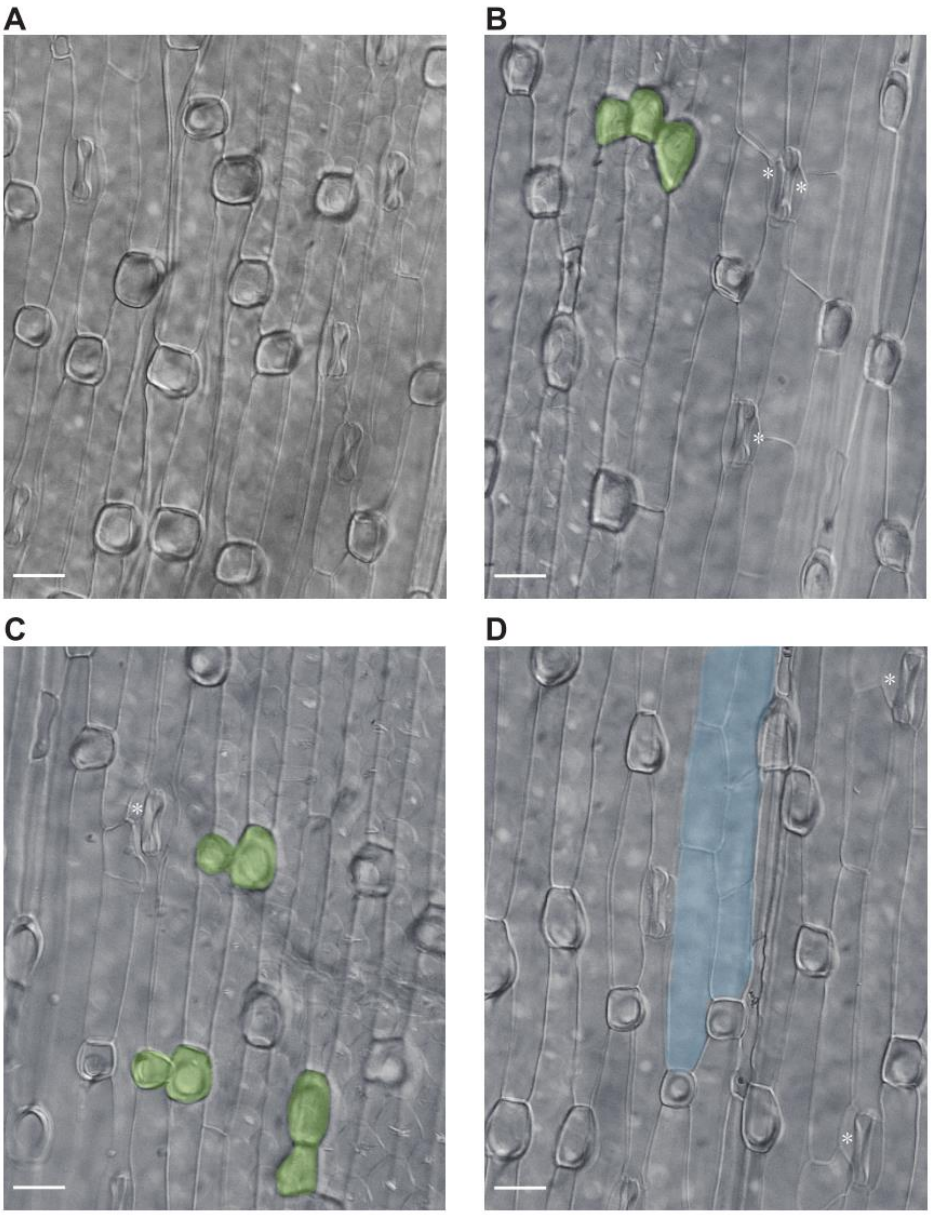

Figure 45. *BdPOLAR-LIKE* is required for hair cells and SCs formation.
(A-D) DIC images of the epidermis in *BdPOLAR-LIKE* CRISPR (JD633-BdPOLAR-LIKE-g1) T1 lines. Aberrant SCs are indicated with red asterisks. Hair cell clusters are indicated with green. Abnormal pavement cells are indicated with blue (third leaf, 16-19 dag). Scale bars, 20 µm.

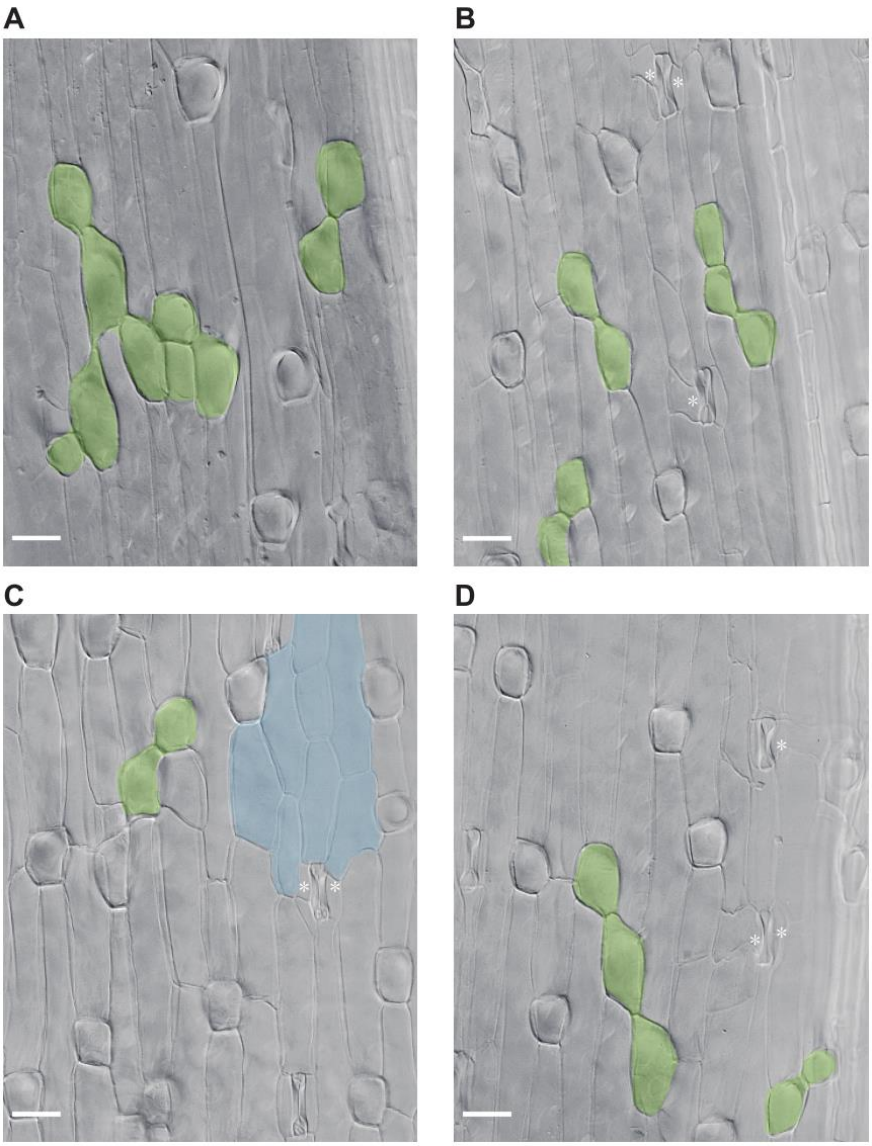

Figure 46. Loss of function of *BdPOLAR-LIKE* exaggerates SC defects in *BdPOLAR* mutant.
(A-D) DIC images of the epidermis in *BdPOLAR* and *BdPOLAR-LIKE* CRISPR (pMDC32-BdPOLAR-LIKE-guide1/BdPOLAR-guide4) T0 lines. Aberrant SCs are indicated with white asterisks. Hair cell clusters are indicated with green. Abnormal pavement cells are indicated with blue. Scale bars, 20 μm.

To decipher the cellular localization of *BdPOLAR-LIKE*, Irem Polat generated the *BdPOLAR-LIKE* translational reporter construct. Excitingly, distinct from the polarization of BdPOLAR in the SMC membrane, BdPOLAR-LIKE showed the basal localization at the stomatal precursor cells before the first ACD generating GMC. Interestingly, I also observed BdPOLAR-LIKE polarized at the basal site of hair cell precursors, which may hint at the hair cells defects in *bdpolar-like*. After the first ACD in stomatal precursor cells, the BdPOLAR-LIKE signal vanished quickly in the epidermis (Fig. 47, and Fig. 48). In particular, a faint

signal was noticed at the basal site of GMC during SMC division (Fig. 48. stage4). The localization pattern of BdPOLAR-LIKE suggested that *BdPOLAR-LIKE* worked as a polarity regulator during stomata initiation and hair cell formation. In addition, the stomata cluster occasionally appeared in *BdPOLAR-LIKE* translational lines (Fig. 48. stage6). Whether it resembles *BdPOLAR*, the dosage and/or stability of BdPOLAR-LIKE is also crucial for its function is questioned. The phenotyping of *BdPOLAR-LIKE* translational lines and *BdPOLAR-LIKE* complemented experiments will be scheduled to test this possibility.

BdPOLAR-LIKE is the most closely related homolog of *BdPOLAR* and is also expressed in the developing leaf, but earlier and not restricted to stomatal cell files. Mutation on *BdPOLAR-LIKE* results in defects in hair cell formation and SC division. Nika Gorsek generated promoter-swap constructs where the *BdPOLAR* promoter drives *BdPOLAR-LIKE-mVenus* (pGGZ004-BdPOLARpro:BdPOLAR-LIKE-mVenus), and the *BdPOLAR-LIKE* promoter drives *BdPOLAR-mVenus* (pGGZ004-BdPOLAR-LIKEpro:BdPOLAR-mVenus). This will allow us to test if the sister genes can complement each other and if these proteins simply read out a cell-intrinsic polarity map (i.e., to the basal domain in protodermal cells and the distal domain in SMCs) or if they define cell polarity by going to their respective domains irrespective of the context.

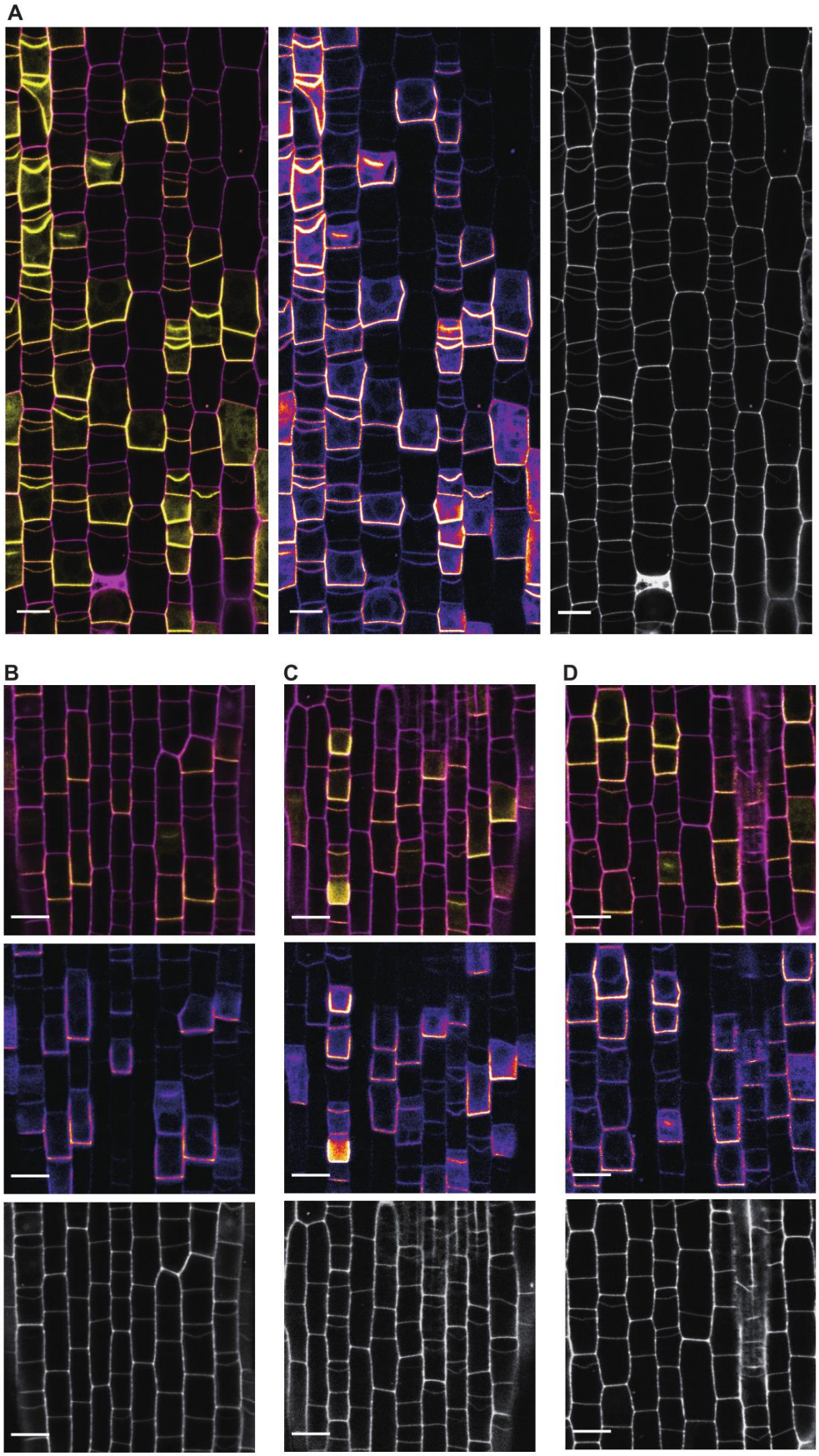

Figure 47. *BdPOLAR-LIKEp:BdPOLAR-LIKE-mVenus* expression at epidermal cells

of leaf developmental zone in *B. distachyon*.
(A-D) Composite images (left in A, upper in B-D) with BdPOLAR-LIKE-mVenus signal (yellow) and PI-stained cell outlines (magenta), fluorescence intensity images (middle) of mVenus channel only, and images of PI-stained cell outlines only (right in A, bottom in B-D). T1 generation. All images from the second leaf, 5 to 6 dag. Scale bars, 10 µm.

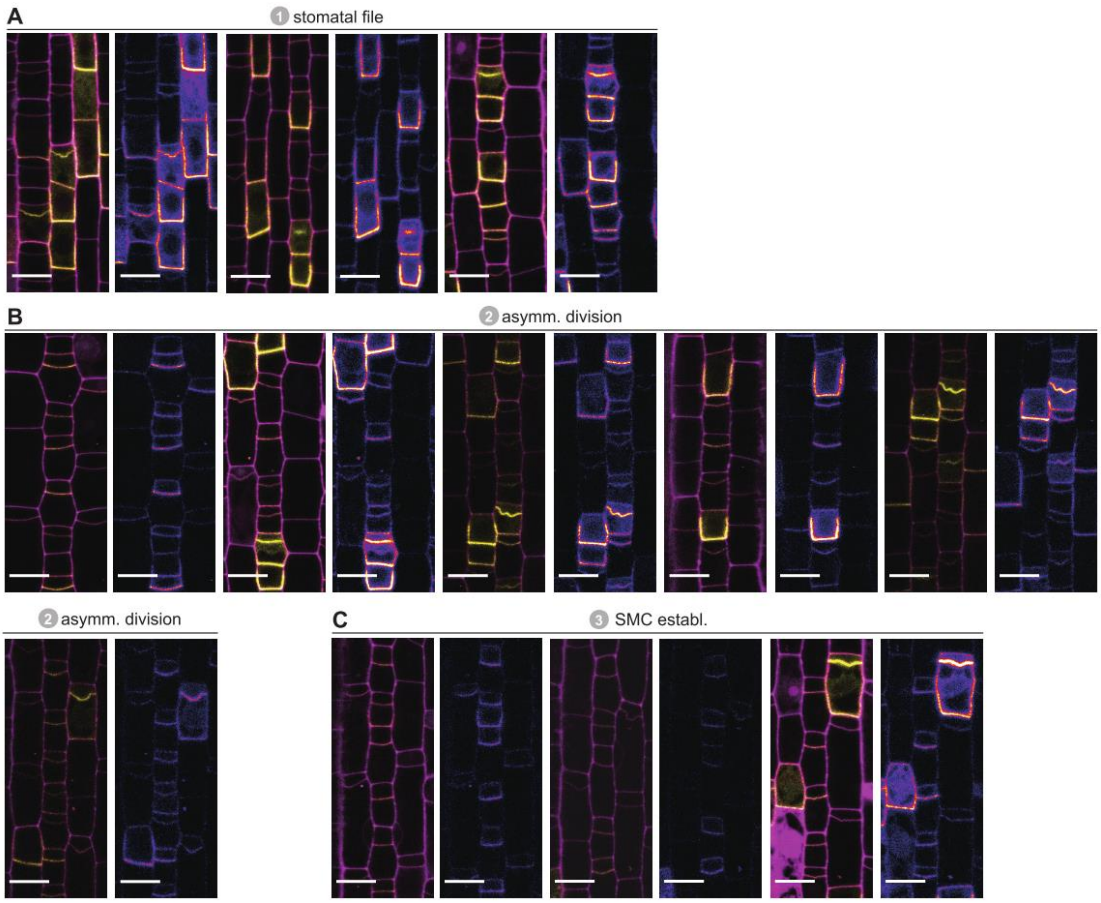

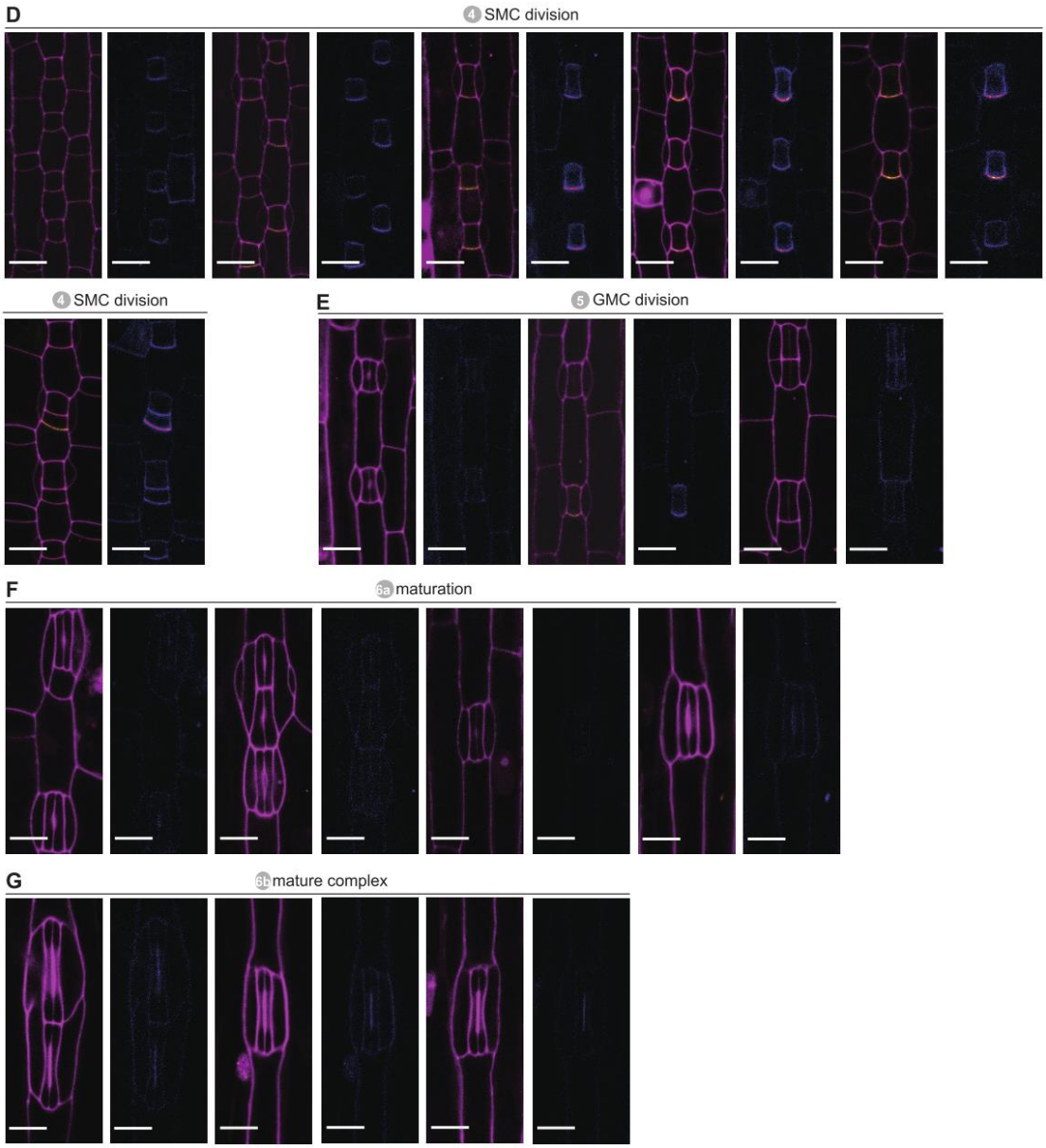

Figure 48. *BdPOLAR-LIKEp:BdPOLAR-LIKE-mVenus* expression throughout stomatal development in *B. distachyon*.
(A-G) Composite images (left) with BdPOLAR-LIKE-mVenus signal (yellow) and PI-stained cell outlines (magenta), and fluorescence intensity images (right) of mVenus channel only. T1 generation. All images from the second leaf, 5 to 6 dag. Scale bars, 10 µm.

4. The Link between *BdPOLAR* and BR Signaling/Biosynthesis in *Brachypodium*

It was reported that AtPOLAR is a scaffold for a subset of BIN2, together with BASL, to regulate ACDs during stomatal development in *Arabidopsis* (Houbaert, Zhang et al. 2018). I suspect if there is a crosstalk between BR signaling and SCs formation, and possibly via the interaction between BdPOLAR and BdBIN2. To study the effect of BRs on SCs formation and

determine if it is through the regulation of BR signaling or biosynthesis, I initially treated SMC polarity mutants with BR-related inhibitors and activators. Propiconazole (Ppz) is a specific and accessible BR biosynthetic inhibitor, and 24epi-brassinolide (BL) is a bioactive epimer of brassinolide. In addition, NaN lines associated with critical genes involved in BR signaling and biosynthesis were investigated.

Firstly, I performed the BR treatment test using wild-type (Bd21-3) before formal experiments. 2, 5, 10, and 20 µM Ppz and 5, 50, 100, and 1000 nM BL gradient concentrations were applied to establish phenotypic analysis in wild-type. Wild-type seeds were planted and germinated on the normal 1/2 MS medium for 3 days in the growth chamber. Then the equal amount of seedlings were moved to BR treated plates and grown for another 7 days. The developmental zone of the third leaf was carefully pulled out of the leaf sheath to inspect the stomatal cell lineage. BL treated leaves did not display obvious SCs phenotypes. Along with the Ppz concentration increasing, SCs and stomatal complex exhibited diverse phenotypes, such as SCs extra longitudinal and vertical divisions and stomatal clusters formation. Aberrant pavement cell patterns were noticeable under the highest Ppz treatment (20 µM) (Fig. 49). Bd21-3 seedlings grown in the medium for 7 d in the presence of 2 to 20 µM Ppz showed decreased root elongation.

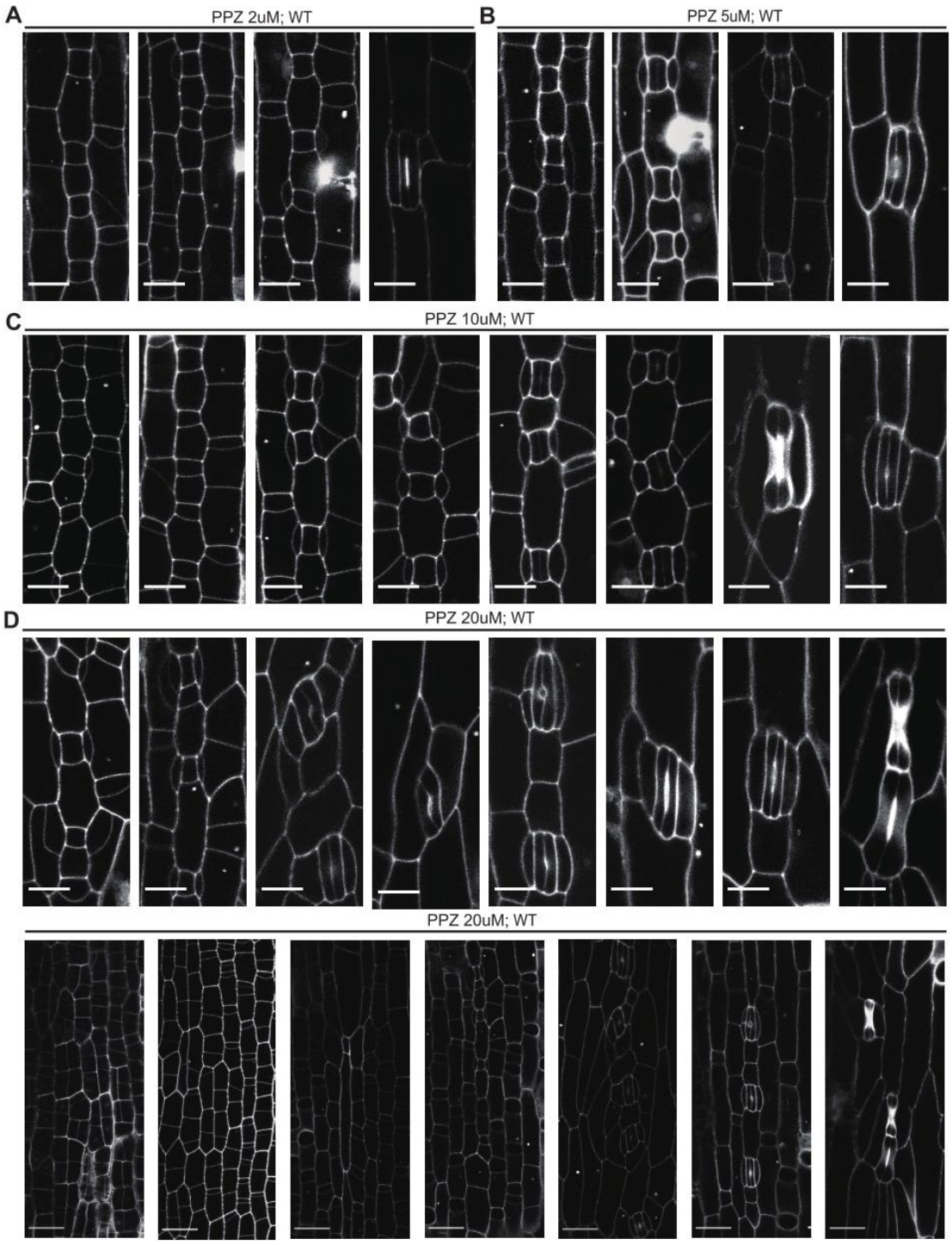

Figure 49. Ppz treatment induced SC defects in WT.
(A-D) Single confocal plane images of the PI-stained developing epidermis in WT. 3-day old WT were transferred to 1/2 MS media containing either 2, 5, 10, and 20 µM Ppz, and grown for 7 more days. All images from the third leaf. Scale bars, 10 µm.

Afterward, to investigate if treatment with BR biosynthesis inhibitor/agonist impacts SC development, Kim Janssen carried out new round BR treated experiments including *bdpolar-1*, *bdpan1-1*, *bdpolar-1;bdpan1,* and wild-type. The time-course root growth and SCs division were tracked with 10 and 20 µM Ppz, 0.1 and 1 µM BL treatments. Seeds were planted and geminated on a normal 1/2 MS medium for 2 days in the growth chamber, then roughly equal amounts of seedlings were moved to BR treated plates and grown another 2, 4, and 7 days. Subsequently, Kim evaluated the effect of Ppz and BL on primary root length. In wild-type, the results showed a dose-dependent reduction of primary root growth, where 20 µM Ppz decreased the elongation by 58% and 10 µM Ppz by 48% compared to mock conditions (Fig. 50A). Root length of wild-type plants treated with BL also displayed a lowering trend with higher concentration. These results suggest that exterior and excessive BL would inhibit the root growth in *Brachypodium*. Thus, co-application with Ppz plus BL is more sensible to inquire into BL complementation. The Ppz-induced root length inhibition was also observed in *bdpan1-1*(Fig. 50A).

Interestingly, compared to wild-type plants, *bdpolar-1* was less sensitive toward lower 10 µM Ppz, and *bdpolar-1;bdpan1-1* was insensitive to Ppz (10 and 20 µM) and lowered 0.1 µM BL. Together these findings suggest that Ppz specifically influences *BdPOLAR* associated pathway.

Ppz treatment also affects SCs polarity and division in third leaves of wild-type (Bd21-3) seedlings during the first try. However, apart from the weak defects noticed from *bdpan1-1,* Kim did not observe the same inhibitory effect from second leaves (induced 1 week) this time; accordingly, she harvested third leaves (induced 3 weeks) to inspect SCs phenotypes. After 3 weeks of Ppz induction, seedlings developed with shorter and thicker leaves than in mock conditions. Induced epidermal tissues displayed not only SC flaws but also pavement cells defects. Instead of being framed rigidly and squarely, pavement cell walls formed obliquely in Ppz-treated third leaves (Fig. 50C, D). Wild-type plants treated with 20 µM Ppz showed ~8% SCs abnormal formation, whereas *bdpan1-1* mutants were more resistant to Ppz applications and showed no difference compared to mock. *bdpolar-1;bdpan1-1* applied with 20 µM Ppz

showed slightly increased SC defects (Fig. 50B, orange). On the other hand, 1 µM BL-induction alleviated SC faults in *bdpan1-1* and *bdpolar-1;bdpan1-1* (Fig. 50B, green, and E). This reveals that BL can promote SCs division properly. Significantly, *bdpolar-1* did not respond to Ppz treatment (Fig. 50B, purple and orange). This result is consistent with our previous findings in root growth for *bdpolar-1* to Ppz sensitivity. It supports my hypothesis that there is a link between *BdPOLAR* and BR signaling or biosynthesis pathway.

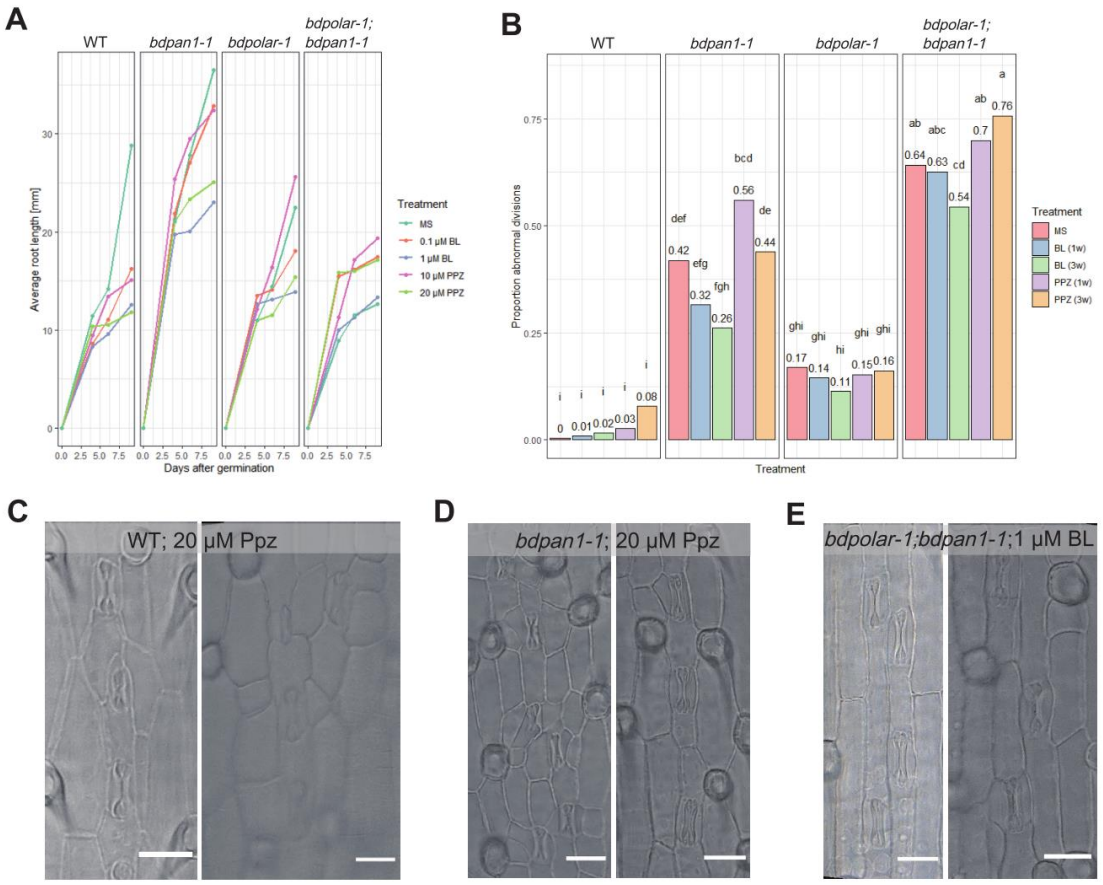

Figure 50. Ppz and BL treatment in WT and SC polarity mutants.
(A) Average root lengths of WT, *bdpan1-1*, *bdpolar-1,* and *bdpolar-1;bdpan1-1* growing on media containing 10 and 20 µM Ppz or 0.1 and 1 µM BL for 2, 4 and 7 days. (B) Quantitative analysis of defective SCs in WT, *bdpan1-1*, *bdpolar-1,* and *bdpolar-1;bdpan1-1* after treatments with 20 µM Ppz and 1 µM BL for 1 and 3 weeks. (C-D) DIC images of the epidermis in WT and *bdpan1-1* applied with 20 µM Ppz for 3 weeks. (E) DIC image of the epidermis in *bdpolar-1;bdpan1-1* applied with 1 µM BL for 3 weeks. Scale bars, 10 µm. Data and figures are produced by Kim Janssen.

To further investigate the roles of BRs play during SC formation, Kim genotyped and phenotyped some BR biosynthesis and signaling mutants. NaN1917 is a candidate mutant of DWF4 in *Brachypodium*, which acts as the rate-limiting enzyme in *Arabidopsis* BR biosynthesis. NaN1917 heterozygous and

homozygous lines did not show typical dwarf stature as described in *Arabidopsis* mutants, suggesting that DWF4 possibly divergent its role in *Brachypodium.* BdDWF4 seems to regulate SC formation since the weak SC defects were detected in *bddwf4* mutant. The transcription factor BZR1 controls thousands of BR-regulated gene expression and regulate growth and development events in *Arabidopsis* (Wang, Nakano et al. 2002). The homozygous mutants of BdBZR1 displayed dwarf phenotypes. This indicates that BZR1 is conserved mainly among *Arabidopsis* and *Brachypodium*. *bdbzr1* did not show SCs phenotypes, indicating that BdBZR1 does not affect SC formation. Kim also built *BdBZR1* and *BdDET2* (Bradi2g55110) CRISPR/Cas9 constructs to search for more clues about the crosstalk between SC formation and BR biosynthesis/signaling pathways.

5. Time-Lapse Imaging

To describe SC formation in space and time, I want to perform high-resolution time-lapse imaging of early epidermal development in *Brachypodium* to understand the dynamics of SC recruitment and general rules and patterns of early grass epidermal development, such as where and how cells divide, elongate and differentiate. In addition, time-lapse imaging can determine when and where exactly *BdPOLARp:BdPOLAR-mVenus* is polarized and how this affects the SMC division.

The time-lapse imaging is being established using our plasma membrane (PM) marker line (*ZmUbip:mCherry-AtRCI2a*). The leaf often grew out of the scanning area, and thus, I fixed the two sides of the leaf with double-sided tape and restricted movement in z with a coverslip and MS medium (Fig. 51A). Then identify the right sample with a strong signal suitable scanning position, and set the appropriate parameters to avoid signal bleaching. I observed the simple processes for SC recruitment and GC formation via the captured video after time-lapse data had been processed (Fig. 51, B and C). However, the system still requires lots of optimization to gain a better resolution in time and adapt it to weaker signals like the one of the *BdPOLAR* reporter line. Later, I was using

the double sides tape forming a channel topped with a coverslip to fix and flatten the leaf sample, which is helpful to solve the problem of leaf moving out from the confocal scanning field. The next step is to optimize scanning parameters for high-resolution imaging quality with suitable time intervals. The 3D printing of a channel is also being considered to achieve an easier setup. Initially, I will try to set up with stable PM marker until the time-lapse imaging system is feasible and reproducible, then *BdPOLARp:BdPOLAR-mVenus* will be performed using shorter time intervals.

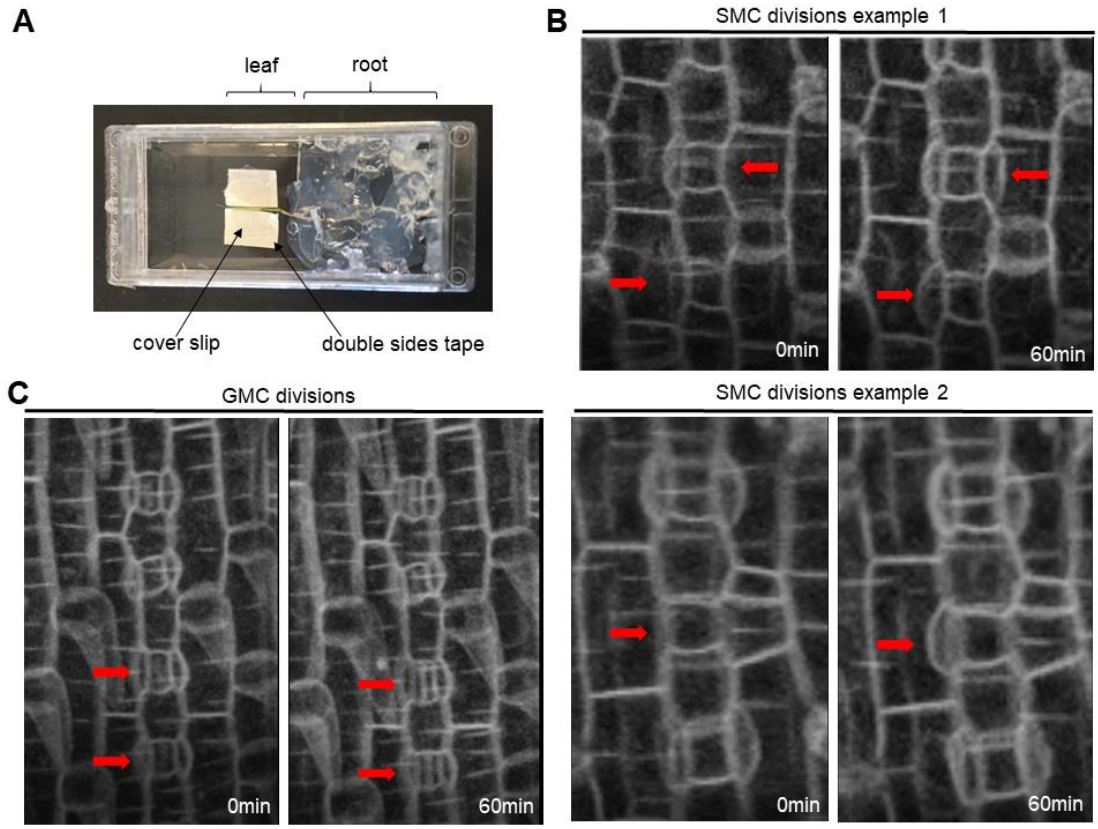

Figure 51. The preliminary results of time-lapse imaging.
(A)The setup of the time-lapse imaging device. (B) SMC divisions. Red arrows indicate SMCs, which go through asymmetric cell division. (C) GMC divisions. Red arrows indicate GMC, which goes through symmetric cell division.

Discussion and Outlook

1. NaN lines Screening and Potential Candidates in Comparative Transcriptomics

In my PhD study, I focused on discovering novel players involved in SCs formation in the model grass *Brachypodium distachyon*. In the forward genetic screening of NaN lines, I discovered NaN99 and NaN191 both showed SC defective phenotypes, and NaN230 displayed GC morphogenesis defects. The rough mapping for NaN99, NaN191 and NaN230 would be designed to identify the responsible genes for each phenotype.

I also tried to identify new players who participate in SC development among the grass stomatal lineage from comparative transcriptomics (WT vs. *bdmute*). Based on differential gene expression analysis (Table 1), *BdTPX6-like* (Bradi4g28540) significantly showed the highest log2 Fold Change (-7.86207). It belongs to the T-box transcription factor family and is required to determine the fate of axial stem cells (Takemoto, Uchikawa et al. 2011). *BdTPX6-like* CRISPR lines were generated, whereas unfortunately, I did not observe SCs phenotype. Bradi4g33000 displayed the second-highest log2 Fold Change (-6.05379), homolog gene of *ADOF1* from *Arabidopsis* and rice. DOF proteins family is plant-specific transcription factors with unique zinc-finger DNA-binding domains group. Their family members have been identified to perform different functions in gene regulation of distinct plant development and growth processes (Lijavetzky, Carbonero et al. 2003). However, I did not obtain any *BdDOF1-like* CRISPR seeds. For other candidates, *BdEXL2* (Bradi1g45600) is close to *EXL2* in *Arabidopsis*, which may assist plants to adapt carbon-deficiency and energy-limited environment (Schroder, Lisso et al. 2012); Bradi2g54300 shows high residues conserved similarity to *ABCG16*, which performs ABC-type transporter activity (Liu, Zhao et al. 2020); *BdNAC-like* (Bradi3g13630) is the homolog of *Arabidopsis* NAC domain-containing protein 35 that acts as a floral repressor (Yoo, Kim et al. 2007); Bradi1g69220 displays sequence significant similarity with *ATPSK2*, which is able to code phytosulfokines precursor (Yang, Matsubayashi et al. 2001). CRISPR lines will be generated and examined for the above candidates.

2. Further Decipher of some Transgenic Lines

In addition, here are some transgenic lines produced in this study that possibly provide broader and distinct directions to comprehend SMC polarization and division. Except for possible “patchy” pattern localization in *BdPOLARp: MYR-BdPOLAR-mCitrine* expressing in *bdpolar-1* lines, myristoylated BdPOLAR also showed strong accumulated around nuclear as soon as SMC established before pre-mitotic, and few aggregates accumulate at the plasma membrane and cytoplasm of SMC (Fig. 32, and Fig. 33), this was also observed in BdPOLAR translational reporter lines (Fig. 16B). Whether BdPOLAR indeed localizes to some organelles in the cytosol, such as the Endoplasmic reticulum (ER) and Golgi apparatus. Examining of colocalization between BdPOLAR and organelles markers would get more insights into this puzzle. Subsequently, if the above suppose is confirmed, it might explain the transient expression and rapid dissociation of BdPOLAR from the SMC plasma membrane once ACD ends.

In SMC of *maize*, double fluorescence labeling revealed that the nucleus surrounded by a monopolar prophase microtubule ‘‘half-spindle’’ structure distal to neighboring GMC, enabling the anchoring nucleus to migrate to its polar position GMC (Panteris, Apostolakos et al. 2006). On the other hand, the F-actin caps formed proximal to the GMCs are composed of the cortical F-actin patches and endoplasmic actin filaments, stabilizing polarized nucleus and metaphase spindle; If they are destroyed, division planes during ACDs of SMCs are misaligned. According to this concept, the unpolarized nucleus observed in *bdpan1-1* is probably due to a damaged ‘‘half-spindle’’ structure. Furthermore, whether the F-actin patches localize correctly in *bdpan1-1* should be explored since most SMCs in *ZmPAN1/2* mutations lacked F-actin patches or had delocalized patches (Cartwright, Humphries et al. 2009, Zhang, Facette et al. 2012). On the other hand, if *BdPOLAR* plays a role in determining division planes as proposed, misaligned actin filaments and metaphase spindle are expected in *bdpolar-1*.

Imaging of *BdPOLARp:LifeAct-mcherry* (in wild-type, *bdpolar-1* and *bdpan1-1*)

reporter lines help us to visualize actin organization and pattern during stomatal development, especially SC recruitment and GC differentiation and morphogenesis. Fluorescent phalloidin staining for actin also can achieve the same goal. From the confocal imaging pictures, the latter seems to be able to carry out actin filaments better. In contrast, it took a long time to follow the protocol, and staining did not show infiltration evenly in the epidermis sometimes. Meanwhile, an appropriate marker for MTs visualization has not been found in *Brachypodium*. Thus, after I preclude *BdTUB6* (Bradi2g21340), cloning of other α- and β-tubulins should be planned. Double labeling of microtubules and actin filaments also deserves to be further explored to establish the protocol in *Brachypodium.*

The stable expression lines *BdPOLARp:BdPOLAR-mCitrine-TurboID* in *bdpolar-1* and *BdPOLARp:BdPAN-mCitrine-TurboID* in *bdpan1-1* will be used to identify potential interactors of *BdPOLAR* and *BdPAN1*, and to identify protein complexes and proteomes in SMC lineage. Collect young seedlings, submerge and incubate them in biotin solution, then perform the immunoblotting to test biotinylation activity, labeling time, temperature, and biotin concentration. Once these experimental parameters are optimized, affinity purification–mass spectrometry (AP-MS) of biotinylated proteins will be carried out sequentially. The proteomes dataset will be filtered and analyzed through some known marker genes during SMCs and SCs development, such as *BdPOLAR*, *BdPAN1*, and *BdMUTE*.

3. STRING: Protein-Protein Interaction Networks of BdPOLAR and BdPAN1

To predict the protein-protein interaction network focus on BdPOLAR and BdPAN1, I used the search tool STRING, which bases on different and abundant sources, such as experimental data, various computational prediction methods and public text collections. STRING can give us a fast overview of our interested proteins and interactors and calculate different protein interactions with a confidence score. These predicted interaction networks can provide new

directions for future experimental research and help us better understand cellular processes at the system level. I input single BdPOLAR and BdPAN1 amino acids and searched their protein association networks. First, among the protein-protein interaction network of BdPOLAR, interactions between BdPOLAR with BdSPCH1/2, BdMUTE, and BdFAMA are consistent with *BdPOLAR* expressing at stomata precursor cells, SCs, and young GMCs (Fig. 16 and Fig. 52). In addition, interactions between BdPOLAR with BdEPF1-like, BdTMM, and BdSTOMAGEN might suggest that BdPOLAR plays a role during intracellular signaling in stomatal development (Fig. 52). However, most of the interactions were predicted by text mining and co-expression. They still require experimental determination.

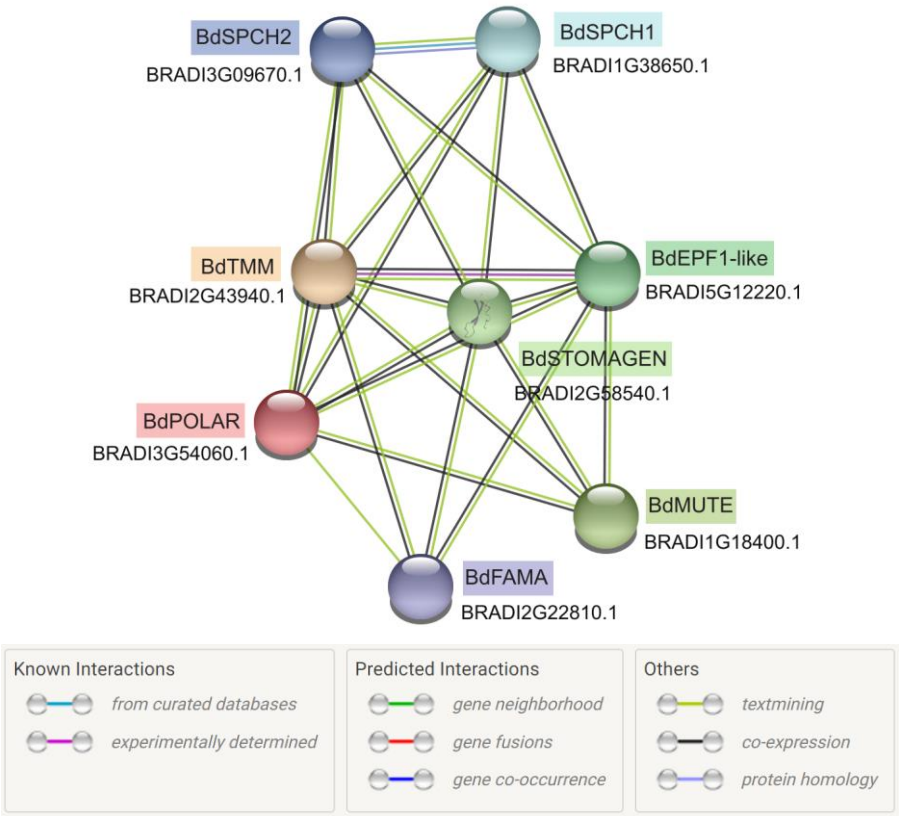

Figure 52. Protein–protein interaction network of BdPOLAR visualized by STRING.

Different color lines represent interactions verified and predicated by different sources.

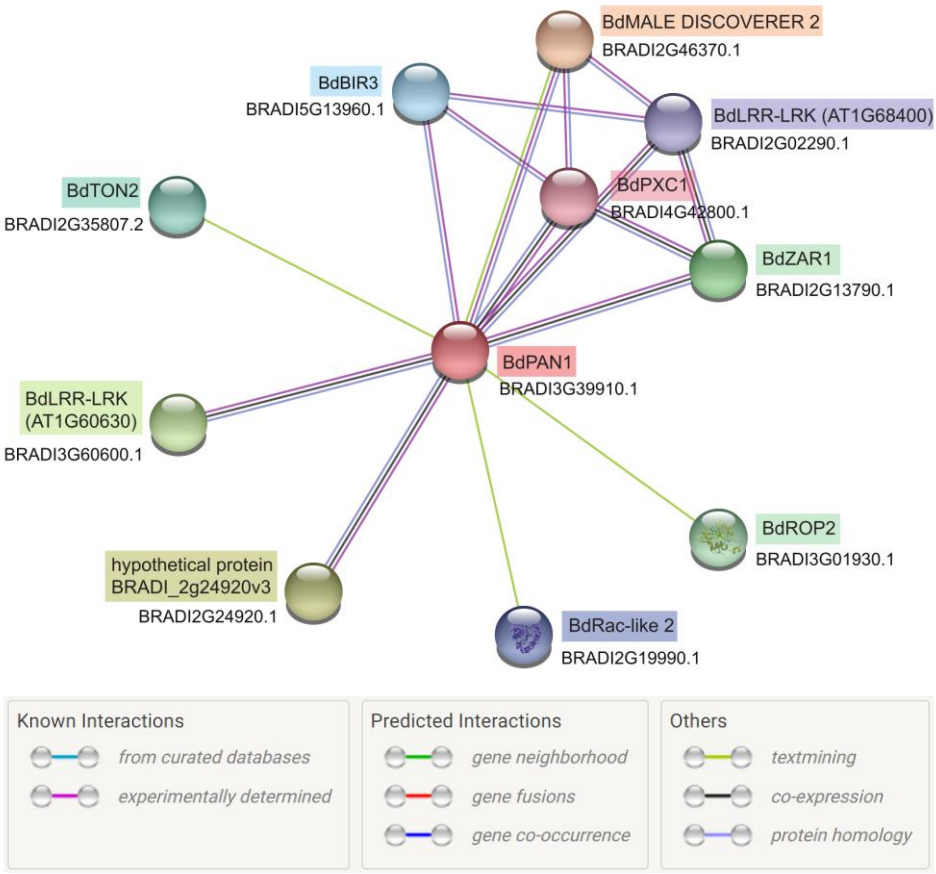

Figure 53. Protein–protein interaction network of BdPAN1 visualized by STRING. Different color lines represent interactions verified and predicated by different sources.

On the other hand, BdPAN1 showed possible interactions with proteins containing various functions and was mainly predicted by experimental determined, protein homolog, and co-expression (Fig. 53). Some potential polarity regulators were dug out, including *BdROP2* and *BdRac-like2* (Fig. 53). In *Arabidopsis*, ROP2 is a member of the Rho GTPase family. It controlled the organization of the microtubular cytoskeleton and was reported that affect pavement cell morphogenesis (Lauster, Stockle et al. 2022) and root hair development and growth (Jones, Shen et al. 2002). In maize, *ZmROP2/9* has been identified to promote the polarization of SMC divisions with *ZmPAN1* together (Humphries, Vejlupkova et al. 2011). *Rac-like2* belongs to the ROP GTPase gene family, which serves as a common switch in cell polarity development in plants (Fu and Yang 2001). It is possible that *BdPAN1* function with *BdROP2* and *BdRac-like2* together to promote SMC polarization. *TON2* encodes subunits of type 2A protein phosphatases

(PP2As) and participates in the organization of the cortical microtubule cytoskeleton, particularly the geometry of microtubule nucleation (Camilleri, Azimzadeh et al. 2002, Kirik, Ehrhardt et al. 2012). Whether BdTON2 interacts with BdPAN1 to affect the organization of microtubules during SMC pre-mitotic is deserved to explore.

In addition, BdPAN1 potentially interacts with some regulators involved in plant immunity, such as BdBIR3 and BdZAR1(Fig. 53). In *Arabidopsis*, BIR3 interacts with BAK1 and negatively impacts BR signaling, sequentially affecting the BAK1-related pathways, including innate immunity and cell death control (Imkampe, Halter et al. 2017). ZAR1 plays as an immune receptor to form a cation-specific channel, inducing an immune response and cell death in plants (Bi, Su et al. 2021). This suggests that *BdPAN1* may associate with plant immunity.

Apart from these interactions, BdPAN1 also might interact with BdPXC1, BdMALE DISCOVERER 2, and two BdLRR-RLKs (Fig. 53). In *Arabidopsis*, *PXC1* was identified to be associated with secondary cell wall formation in xylem fibers (Wang, Kucukoglu et al. 2013). *MALE DISCOVERER 2* can facilitate pollen tube to perceive female attractant (Wang, Liang et al. 2016), and also possibly plays a role in root hairs development (Jones, Raymond et al. 2006). BdLRR-RLK (At1G68400) and BdLRR-RLK (At1G60630) are both leucine-rich repeat protein kinases with unknown functions.

4. Timely and Spatially Assemble of Polarity Components during SMC ACD

The “graminoid” morphology in grasses, two dumbbell-shaped GCs accompanied by a pair of SCs, is required for faster stomatal movements and facilitates gas exchange coincides with environmental adaptation (Nunes, Zhang et al. 2020). Polarization of SMC is one critical step for SC recruitment. I identified a polarity regulator, *BdPOLAR*, which localized in the SMCs periphery while being mostly absent at the sites of GMCs, building up an opposing, almost reciprocal polarity pattern with BdPAN1. *BdPAN1* behaves

like its *maize* homolog *ZmPAN1*, which displayed polarization at GMC/SMC interface to promote nuclear polarization and SMC division (Cartwright, Humphries et al. 2009). However, the mechanisms that how newly formed division plane is maintained and ACD potential is controlled remain unclear. Here, in grass model plant *Brachypodium distachyon*, I identified *BdPOLAR* and *BdPAN1* are both required to regulate the formative SC division. In terms of dependencies among known players for SMC formation, I demonstrated that the expression and polarization of *BdPOLAR* depend on the SCs determiner *BdMUTE* and *BdPAN1,* respectively. In addition, BdTAN1 reporter imaging in different mutants suggests that *BdPOLAR* is required for cortical division site orientation. Careful quantification regarding various division categories indicating *BdPOLAR* controls the division capacity in SMCs (Fig. 54B). Finally, leaf-level gas exchange measurement discovered that correct SC formation is required for sufficient graminoid stomatal functionality.

In *Arabidopsis*, the BASL-BRX and POLAR polarity domains are distal to the future division planes in meristemoids. *BASL* is required for POLAR polarization and *BASL* overexpression extremely polarized POLAR (Houbaert, Zhang et al. 2018). POLAR serves as a scaffold protein that attracts BIN2 to the cell cortex to repress MAPK signaling from the crescent and lower its nuclear localization, thus preventing SPCH downregulation from assuring sufficient cell division potential in MMCs (Houbaert, Zhang et al. 2018, Guo, Park et al. 2021). A recent study reported that BSL family phosphatase is recruited to the polarity domain during PPB formation once mitosis is initiated (Guo, Park et al. 2021). As BSL1 enters the polarity crescent, it liberates BIN2 from the crescent and dephosphorylates YDA, thus, promoting MAPK signaling activity. Therefore, SPCH in SLGC is downregulated and degraded, suppressing both stomatal identity and ACD potential (Guo, Park et al. 2021). The co-participation of BIN2 and YDA-MAPK governs the cell fate specification in *Arabidopsis* stomatal patterning (Fig. 54A).

In *Brachypodium*, unlike BdPAN1 and other known polarity proteins accumulate at GMC/SMC interface, approaching to hereafter formed division planes,

BdPOLAR is the first regulator showing polarity domain being away from the future division planes in SMCs (meristemoids) of grasses. However, BASL orthologues have not been identified in grasses. The mechanism of how *BdPOLAR* is triggered and polarized on the SMC plasm membrane is unknown. In contrast to *AtPOLAR*, *BdPOLAR* seems predominantly expressed in the SC rather than the GC lineage but still preserved the function to regulate cell division potential. In *Arabidopsis*, BRs are required for cell division (Gonzalez-Garcia, Vilarrasa-Blasi et al. 2011) and cell elongation (Kang, Breda et al. 2017) during root growth. With limited mobility, its biosynthesis is predominantly restricted to the root elongation zone but less active in the root meristem (Vukasinovic, Wang et al. 2021). The model of AtPOLAR-BIN2 and YDA-MAPK parallelly tune the expression level of SPCH discussed above. This hint from dicot proposes the possibility that BR signaling plays a role in SCs divisions through POLAR in monocot.

Here is my hypothesis: Firstly, the GMC elongation is indispensable for GC morphogenesis and stomatal complex mature. BRs biosynthesis most likely increases in GMC during its elongation and accumulates less in SMC via short-distance transport. Thus, before ACD, the less abundant of BRs in SMCs allowed the pile-up of BdBIN2, subsequently recruited and polarized to the BdPOLAR domain. A high level of BdMUTE might sustains a high level of cell division potential in the SMCs. *BdPAN1* is responsible for attracting nuclear migration, then promoting SMC ACD. During the ACD, PPB forms upon MMC entering mitosis. BdPAN1 actively hinders BdPOLAR from entering its domain, either biochemically or by space barrier. Distal BdPOLAR inhibits cortical division site factors BdTAN1 from ectopically binding and forces it to accumulate specifically where BdPOLAR protein level is low. At the SMC PM, BdBIN2 might promote the turnover of BdPOLAR via phosphorylation that lowers the PM-association of BdBIN2. When BdBIN2 is enriched in the nucleus, it might promote BdMUTE degradation through phosphorylation. After ACD, since *BdMUTE* only expresses at newly formed SC and *BdPOLAR* expression requires *BdMUTE*, BdPOLAR quickly dissociates from SMC PM and relocates to the PM of newly formed SC, which probably also drives the spatial swift of

BdBIN2. BdBIN2 might relocate to the nucleus of pavement cell (PC) to achieve strong suppression on *BdMUTE* and lowered cell-division potential, enabling the transition from SMC to SC and the precisely one ACD (Fig. 54B). In addition, previous work investigated that BRs can induce the transcription of cyclin-dependent kinase and are required for cell cycle progression during leaf growth (Hu, Bao et al. 2000, Zhiponova, Vanhoutte et al. 2013). I suspect BRs play a regulatory role in the control of SMC division and differentiation. Whether BdPOLAR and BdMUTE are conserved phosphorylated by BdBIN2 in *Brachypodium*, if so, where *BdBIN2* will be polarized need to be chewed over.

Even though some polarity players during SMC (meristemoid) pre-mitotic were identified and characterized in maize, molecular mechanisms that contribute to meristemoid divisions in grasses are largely unknown compared to those discovered in dicot *Arabidospsis*. The comparisons between *POLAR* and *BdPOLAR* regarding their genetic dependency, expression pattern and localization, homologs, interactors, and biological function, prospectively provide us more clues to understand the conserved and divergent roles of *POLAR* gene in dicot and monocot, also get bigger pictures about SMC polarization and pre-mitotic in grasses.

5. *BdPOLAR* Acquires a Novel Function that Controls Cortical Division Orientations

BdTAN1 reporter lines at mutants imaging and quantifications suggest that *BdPOLAR* has gained a novel role in orienting the cortical division sites. Whether this function is accomplished through direct positioning of the PPB or through interaction with factors associated with the cortical division site, such as the phosphatases DCD1 (Wright, Gallagher et al. 2009) and POKs (Müller, Han et al. 2006, Lipka, Gadeyne et al. 2014, Herrmann, Livanos et al. 2018) are mysterious. At least, *BdPOLAR* seems to perform a function before cell plate formation and phragmoplast expansion and guidance, which is determined by OPAQUE1/DISCORDIA2 in SMCs (Nan, Liang et al. 2021). The time-lapse imaging of *bdpolar-1* with BdTAN1 and PPB marker in dividing SMCs would bring more lights in terms of this through the comparison of PPB

localization, phragmoplast and newly formed cell wall. The localizations of DCD1, POKs and OPAQUE1 is also worthwhile to dig out in *bdpolar-1* mutant.

6. POLAR Maintain the Ability to Regulate Cell Division Potential Cross-Species

Meristemoid harbors stem cell–like ability to keep several rounds ACDs in *Arabidopsis*. Meanwhile, BASL, POLAR, BRX these cortical proteins accumulate at one narrow corner of the meristemoid, which is away from future division planes and assemble a scaffold platform for signalling cascades. Since only the loss of physical and fate asymmetry lead to *basl* phenotypes, BASL serves as an intrinsic component to determine cell fates (Dong, MacAlister et al. 2009).

SMC possesses the limited self-renew capability to generate one SC per GMC (Stebbins and Shah 1960), only producing more than one SC when it surrounds more GMCs, suggesting that the unknown signals secreted from GMCs act as extrinsic elements to produce SMC polarization. SCAR/WAVE, PAN1/2, ROP2/9 were reported as polarity proteins to polarize sequentially at the SMC adjacent to GMC in *maize* (Cartwright, Humphries et al. 2009, Humphries, Vejlupkova et al. 2011, Facette, Park et al. 2015). *BASL* is absent in monocots, thus, *POLAR* and *BRX* possibly are conserved members of a core plant polarity toolkit. However, a role of BRX during SMC division capacity is difficult to assess because many replications of BRX in *Brachypodium*.

In *Arabidopsis*, the *polar-2 pl1-1 pl2-1* triple mutant showed a reduction in the number of small stomatal lineage cells, pavement cells and stomatal densities (Houbaert, Zhang et al. 2018). The phenotype in Brachy *polar-1* displayed an increase in SCs number. Thus, POLAR maintains the ability to regulate cell division capacity but seems reversely perform in meristemoids of dicots and SMCs of monocots. This divergent function is possibly associated with the magnitude of their polarized distribution. BdPOLAR occupies a broad polarity domain, while AtPOLAR possesses a narrow crescent. Furthermore, the difference in their intercourse routes with BRs signaling probably interprets this.

In addition, the interactions between POLAR/BdPOLAR with cell cycle components are worthwhile to be determined. Also, if high SMC division frequency in *bdpolar-1* is caused by misoriented division planes remains elusive. There is also possible functional redundancy in the *BdPOLAR* family due to the identification of the other two *BdPOLAR* homologs, *BdPOLAR-LIKE1* and *BdPOLAR-LIKE2*. *BdPOLAR-LIKE1* was also expressed in the leaf developmental zone (Fig. 47), and double *bdpolar;bdpolar-like1* displayed stronger SC defects than single mutant *bdpolar-1* (Fig. 46). The expression pattern and localization of *BdPOLAR-LIKE2*, and also SC divisions phenotypes of *bdpolar-like2* mutant remain to be determined. Whether *BdPOLAR-LIKE1* and *BdPOLAR-LIKE2* perform similar ability for division potential regulation is unknown.

7. Dosage of BdPOLAR Protein and Formation of BdPAN1 Domain

BdPOLAR is particularly expressed at stomatal lineage and strikingly increases expression level just before SMC division and quickly dissociated from the SMC membrane after completion of the ACD. In *Arabidopsis*, POLAR expression quickly diminished when the meristemoid differentiates into a GMC, indicating that POLAR emerges as a hallmark for ACDs and maintains this trait cross-species. The transient location rearrangement of BdPOLAR might relate to its sensitivity to dosage and/or stability of BdPOLAR protein. Moreover, this could be a potential interpretation for the partial rescue of the *bdpolar*-1 phenotype by transforming the translational construct. Previous work from Laurie G. Smith's group described wild-type background YFP-ROP2 transgenic plants also showed SCs defects due to overexpression of wild-type ROP2 leading to its delocalization in SMCs from maize. They also identified a correlation between YFP-ROP2 expressing levels, the polarization of YFP-ROP2 in SMCs, and subsidiary division defects (Humphries, Vejlupkova et al. 2011). *BdPOLAR* high-expressing lines and overexpression *BdPOLAR* in wild-type both cause SC defects, probably because of the same reason. To examine if this correlation also exists in BdPOLAR-mVenus transgenic plants, the percentages of aberrant SCs formation in independent transgenic lines with various

expressing levels need to be quantified to determine if high-expressing *BdPOLAR* induces its depolarization in SMCs. In addition, to exclude the potential impact from tagged fluorescence protein, I also cloned the *BdPOLAR* genomic expression construct, pGGZ004_BdPOLARgenomic and pIPKb_BdPOLARgenomic by GreenGate and Gibson, respectively. The previous one contains two dummy sequences from pGGB003 and pGGD002, but the latter one has a complete and uninterrupted *BdPOLAR* genomic region. The transformation is ongoing to generate these two transgenic lines.

Interestingly, BdPOLAR polarized at the apical, basal and distal sites of SMC membranes is BdPAN1-dependent, representing BdPOLAR would occupy the GMC/SMC interface when BdPAN1 is disrupted. This might be due to the spatial barrier built from BdPAN1 or the especially localized degradation of BdPOLAR through protein modification. In the late stages, resembling the PAN1 homologs in grasses, BdPOLAR remains signals in young GCs and SCs. Different from *ZmPAN2* obtained a function to assist SC morphogenesis (Sutimantanapi, Pater et al. 2014), grass *PAN1* homologs and *BdPOLAR* seem to have no roles in the GC lineage and in the mature SC lineage.

By contrast to the BASL-BRX and POLAR polarity domains in *Arabidopsis* and BdPOLAR domain in *Brachypodium*, the grass PAN1 polarity domain, already known ZmPAN1 and BdPAN1, localized at GMC/SMC interface is near to the division plane. In addition, PAN1 domain is essential for attracting nuclear migration to GMC sites in pre-mitotic SMCs. In my study, polarized localization of BdPAN1 appeared independently of SMC identity, therefore, most likely by receiving mechanical or biochemical cues from quicky and longitudinally elongating GMCs (Livanos, Giannoutsou et al. 2015, Giannoutsou, Apostolakos et al. 2016, Livanos, Galatis et al. 2016, Nunes, Zhang et al. 2020). Moreover, in terms of time, BdPAN1 accumulated in GMC/SMC interface earlier before SMC division than BdPOLAR, and holds its polarization faithfully until late GC mature stages, suggesting during SC development, compared to BdPOLAR domain, the BdPAN1 domain is a former attender and do not require polarity signals.

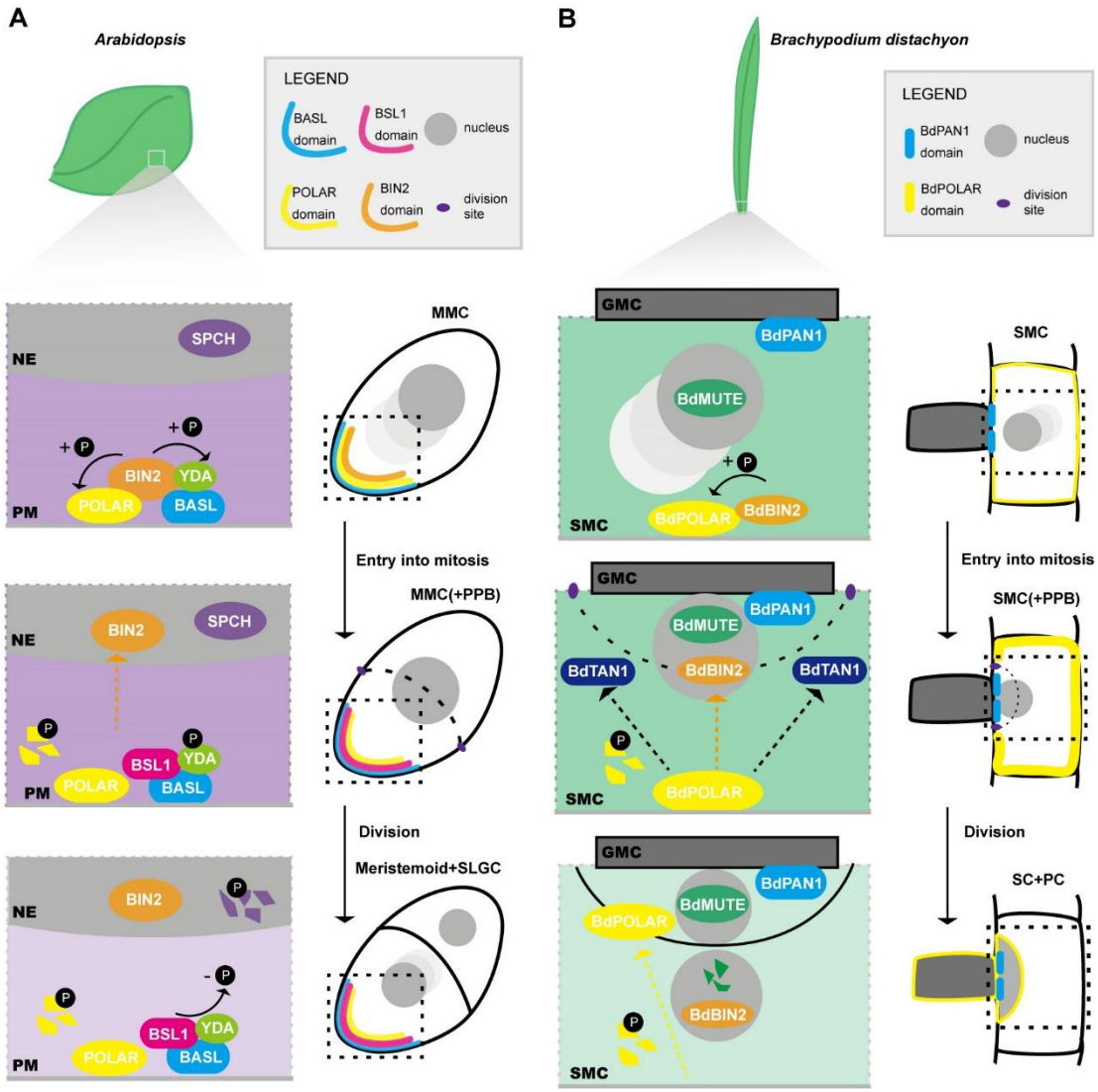

Figure 54. Timely and spatially assemble of polarity components during stomatal ACD in dicots and monocots.

(A, B) Schematic on right show subsequent events during a stomatal ACD in *Arabidopsis* and *Brachypodium*. The formation of the preprophase band (PPB, curved black dash line) indicates the cell entering mitosis. In *Arabidopsis*, the direction of nuclear migration (progressive grey) was found against and towards the polarity site, before and after the division, respectively. In *Brachypodium*, the direction of nuclear migration (progressive grey) was found towards the BdPAN1 polarity site, before division. Schematic left detail the specific changes in the components of the polarity complex inducing differential division potential of the cell at different stages. (A) In *Arabidopsis*, before an ACD in MMC, BASL (blue) and POLAR (yellow) are polarized at the cell cortex. Polarized POLAR attracts the BIN2 (orange) to suppress the kinase activity of YDA (green), causing alleviated MAPK-mediated inhibition on *SPCH* (purple). A high level of *SPCH* (dense purple background) remains a high level of cell division capacity in the MMCs. PM, plasma membrane. NE, nuclear envelope. During an ACD and when MMC enters mitosis, BSL1 (pink) interacts with BASL, and the polarization of BSL1 occurs simultaneously with the formation of the PPB. Polarized BSL1 inhibits BIN2's function at the PM via its phosphatase activity to promote the dissociation of BIN2 from the PM. As a consequence, the BIN2 repression on YDA is released, leading to rising SPCH degradation. At the PM, BIN2 may induce the turnover of POLAR through phosphorylation (broken yellow box) that alleviates the PM association of BIN2. After an ACD, once BIN2 is enriched in the nucleus, it triggers SPCH degradation (broken purple box) through phosphorylation. The BSL1-BASL-YDA multiple polarity components are inherited by SLGC. BSL1 directly activates YDA via

dephosphorylation. Thus, elevated MAPK signaling results in strong inhibition of *SPCH* and lowered cell-division potential (weak purple background). (B) In *Brachypodium*, before an ACD in SMC, BdPAN1 (blue) and BdPOLAR (yellow) are polarized at the proximal site (GMC/SMC interface) and distal site, respectively. Polarized BdPAN1 induces nuclear migration to interface and promote ACD. Polarized BdPOLAR might recruit the BdBIN2 (orange) to the distal polarized domain. A high level of *BdMUTE* (dense green background) sustains a high level of cell division potential in the SMCs. During an ACD, the PPB forms upon SMC entering mitosis. BdPAN1 actively inhibits BdPOLAR from entering its domain. Distal BdPOLAR prevents cortical division site factors BdTAN1 from ectopically binding and forces it to form specifically where BdPOLAR protein level is low. At the PM, BdBIN2 may induce the turnover of BdPOLAR through phosphorylation (broken yellow box) that alleviates the PM association of BIN2. After an ACD, BdPOLAR quickly dissociates from the distal PM and relocalizes to the newly formed SCs. Once BIN2 is enriched in the nucleus of a larger daughter cell (PC), it triggers BdMUTE degradation (broken green box) through phosphorylation, leading to a low level of *BdMUTE* expression and lowered cell-division potential (weak green background).

8. SC Identity and Cell Wall Matrix in "Graminoid" Stomata

The "graminoid" morphology performed faster stomatal movement, which benefits from the functional contribution of SCs. SCs not only act as water and ions reservoirs but also provide a mechanical advantage to support GCs (Nunes, Zhang et al. 2020). The number, morphology and arrangement of SCs are remarkably diverse. Thus, a unique molecular signature can be used to define the distinct identities between GCs and SCs, and further develop our understanding of SC's function. In my study, *bdpolar-1*;*bdpan1-1* displayed stomatal movement defects compared to WT (Fig. 30F, and Fig. 31, C, D and E). However, *bdpolar-1*;*bdpan1-1* still retain some SC-like identity in the cells flanking GCs because it maintains certain stomatal opening and closing kinetics compared to *bdmute* (Raissig, Matos et al. 2017). To interpret this phenomenon in molecular level, molecular markers are demanded to identify subsidiary cells. In *Arabidopsis*, GCs flanking cells are variable in shape, and negligible morphologically different from other epidermal cells, leading to whether *Arabidopsis* has SCs is argumentative. Previous work reported that the activation of H^+-ATPase at GCs plasma membrane is required for stomatal opening, and its translocation is controlled by PATROL1 protein (Hashimoto-Sugimoto, Higaki et al. 2013). PATROL1 is co-localized with H^+-ATPase in both GCs and neighboring pavement of GCs (Higaki, Hashimoto-Sugimoto et al. 2014). On the other hand, in grasses, the SCs are morphologically distinct from GCs. Some molecular markers have been identified from maize. As a functional glucose transporter, CST1, a SWEET-family protein was expressed in SCs

(Wang, Yan et al. 2019). A Shaker family member, ZMK1, was also specifically expressed in maize SCs and very likely involved in the inward-rectifying K+ channel (Buchsenschutz, Marten et al. 2005). If the above molecular markers are conserved across species to represent SCs identity, examination of their expression level in our mutants will gain more insight into the association intensity between SCs function and SCs identity. In addition, examination of the expression level of *BdMUTE* reporter in *bdpolar-1*;*bdpan1-1* would be helpful to determine the residual SCs identity in SC extreme defects mutant.

In terms of g_{sw} defects from *bdpolar-1;bdpan1-1*, this is possibly not only due to the partial loss of SCs identity but also the shorter GC length and continuous influence on GCs morphology and lead to shorter stomatal pore. GMCs release the morphogenetic stimulus to trigger polarization and asymmetrical division in SMCs, along with the cell wall matrix reconstitution of GMC and SMC, especially at their interface (Giannoutsou, Apostolakos et al. 2016). The modified cell wall compositions include homogalacturonans (HGAs), arabinogalactan proteins (AGPs), rhamnogalacturonans (RGAs), and other cell wall materials. Their integrated work promotes a particular chemical differentiation, then control the cell wall expansion and behavior, and also influent the division plates in GMCs and SMCs (Giannoutsou, Apostolakos et al. 2016). Examination of the distributions of the above cell wall components in *bdpolar-1;bdpan1-1* would uncover the structural sign and mechanical stresses during the establishment of polarity in SMCs, and the local differentiation of cell wall matrix during GMCs morphogenesis.

9. Elucidate the mechanisms of BdPOLAR-LIKE in place to control hair cell pattern

Strikingly, unlike BdPOLAR-mVenus, BdPOLAR-LIKE-mVenus displayed a different localization, polarizing basally not only at the stomatal precursor cells generating GMC but also at the hair cell precursors. Consistent with its expression patterns, NaN1927, BdPOLAR-LIKE causative line, showed abnormal SC formations (Fig. 44), and *bdpolar-like* CRISPR mutant displayed both SC and hair cell defects (Fig. 45). To further dissect the defects during hair

cell specification observed in *bdpolar-like,* examining the expression and behavior of hair cell lineage markers need to be determined. In addition, these patterning and proliferation defects of hair cells are very similar to in *bdyda1-1* (Abrash, Anleu Gil et al. 2018). BdYDA1-YFP displayed a broad expression pattern, not only expressed in the stomatal lineage but also presented in leaf epidermal cell types, including hair cell lineage (Abrash, Anleu Gil et al. 2018). It is likely that *BdYDA1* is a general regulator of cell fate possible targets that could enforce specific fate asymmetry in the hair cell lineage. BdPOLAR-LIKE might be downstream targets of a BdYDA1-mediated MAPK cascade.

10. Time-lapse imaging technique

The grass leaf grows from base to tip showing a streamlined and stiff developmental trajectory, showing young, epidermal initiator cells originate from the bottom and mature, differentiated cells extent to the top of the leaf. Benefiting from this advantage, we could perform high-resolution time-course imaging using a single *Brachypodium* leaf to visualize the stomatal complex progressing at different ontological stages. Particularly in my study, time-lapse imaging would be a powerful tool to capture the real-time movement of BdPOLAR and BdPAN1 simultaneously related to asymmetric divisions in SCs. To test this, *BdPOLAR* and *BdPAN1* double marker lines need to be generated. Time-lapse imaging of *BdPOLAR* reporter line will achieve spatial visualization of BdPOLAR-mVenus quickly association from SMC PM after division. Using this technology, the inspection in *polar-1* with *BdPOLARpro:BdTAN1-mCitrine* expressing will further uncover the dynamic regulation of *BdPOLAR* for cortical division site orientation and detect those three cortical division sites are specified simultaneously or by turns during SMC polarization. In addition, combined with cell cycle regulators and cytoskeleton markers will help to resolve more cellular dynamics about SMC polarizations

Materials and Methods

1. Plant Material and Growth Conditions

Peel the husk off the seeds, then put seeds into 1.5ml Eppendorf tubes with 1ml water. Vernalize seeds at 4ºC for 3 days, then plant seeds into the soil directly. Seed sterilization is required for plating seeds on 1/2 MS plate (Murashige and Skoog, Duchefa Biochemie,#M0221). De-husk seeds are incubated in sterilization solution for 15min on a rocker. Table 6 represents the preparation prescription of sterilization solution. Then rinse sterilized seeds four times with 1 mL of sterile double-distilled water on a sterile bench. Seeds are planted with the embryo side of the seed facing up and the embryo pole of the long axis of the seed pointing downward. Seal plates are at 4°C in the dark for 3-5 days, then place plates upright into light in the growth chamber for germination.

2. GreenGate cloning

Most of the expression constructs in this study were produced based on the GreenGate system, a rapid, efficient, and cheap cloning approach (Lampropoulos, Sutikovic et al. 2013).

2.1 Entry module cloning

The genomic regions of interesting targets were amplified using the Q5 High-Fidelity DNA Polymerase (NEB #M0491L). Table 4 represents the Q5 PCR reaction setup and thermocycling conditions. PCR products were verified and separated by running 1% agarose gel. Then the purifications were performed using kit NucleoSpin® Gel and PCR Clean-up (Macherey-Nagel). Nanodrop quantified PCR products. The purified PCR products and empty entry vectors were digested respectively via FastDigest Eco31I (Thermo Fisher Scientific #FD0294) at 37ºC between 1h and overnight; afterward, Eco31I would be heat-inactivated at 65ºC for 20min. To prevent self-ligation, 2µl Antarctic Phosphatase buffer (NEB #M0289S) and 1µl Antarctic Phosphatase (NEB #M0289S) were added to digested vectors, then incubated at 37ºC for 30min.

Digested PCR products were ligated to digested and dephosphorylated entry vectors using T4 ligase (Thermo Fisher Scientific #EL0013) at 16ºC overnight. The ligation reactions were set up according to the 3:1 molar ratio of inserts vs. digested vectors, calculated depending on their lengths and weights. Ligation products were transformed into chemically competent Escherichia coli (E. coli) cells.

Firstly, bacteria with positive constructs were selected by colony PCR. Colony PCR was carried out using the Taq DNA Polymerase (NEB #M0273X), which could amplify the region using forward primers (pGGA/C000-FP in Table 12) from pGGA000 or pGGC000 and reverse primers from the interested gene sequences. On the contrary, it could also be performed utilizing the reverse primers (pGGA/C000-RP in Table 12) from pGGA000 or pGGC000 and forward primers from the interested gene sequences. Table 3 represents the Taq PCR reaction set up and thermocycling conditions. The right candidates were picked by running 1% agarose gel to identify expected bands. The positive colonies were incubated overnight in a 4 ml LB liquid medium with Ampicillin resistance in a 37ºC shaker, and the next day plasmids were isolated using Mini-prep Kit NucleoSpin® Plasmid (Macherey-Nagel).

Secondly, a double-check for positive constructs was performed by test-digestion. The suitable enzyme was selected based on whether it could cut at least two to three-time on entry constructs, and those will cut on the insert genes would certainly be the best option. Then digested products were segregated in 1% agarose gel to select the correct one showing several proper fragments.

Finally, entry constructs were confirmed again through sequencing using pGGA/C000-FP and pGGA/C000-RP to verify the ligations sites. It is necessary to apply the sequence utilizing sequencing primers from the interested gene to get full sequencing results.

2.2 Intermediate module cloning

The double marker construct pGGZ004_BdPAN1-mTurquoise/BdPOLAR-

mCitrine was created via two empty intermediate modules, pGGM000 and pGGN000. The pGGG001-FH adaptor was added at the end of the first construct pGGM_BdPAN1-mTurquoise, and the pGGG002-HA adaptor was added at the beginning of the second construct pGGN_BdPOLAR-mCitrine. pGGG001-FH and pGGG002-HA serve as connections between two constructs. Only the N carries pGGN_BdPOLAR-mCitrine has the resistance cassette.

2.3 Destination module cloning

The final GreenGate reaction is based on the assembly among six entry modules (pGGA000 to pGGF000), and the pGGZ004 was used as the empty destination vector for this final reconstitution. The high concentrated plasmids are required for entry modules, which could be achieved using a homemade mini buffer. The test-digestion was essential to prove the accuracy of each plasmid. Then the pipetting volume for plasmids, 10XFD buffer, ATP, T4 DNA ligase, Eco31I, and H_2O was according to Table 5, and Table 5 represents the GreenGate cycle (GG cycle) procedure for the PCR thermocycler in GreenGate. Additionally, only the double marker construct pGGZ004_BdPAN1-mTurquoise/BdPOLAR-mCitrine final cloning, pGGM_BdPAN1-mTurquoise, and pGGN_BdPOLAR-mCitrine two intermediate modules were used instead of six entry modules. To increase efficiency, 1µl T4 Ligase and 1.5µl ATP were added to the GreenGate reaction after an overnight GG cycle and incubated for around 1h at room temperature. Transform 10µl into DH5α chemical competent cells and plate bacteria on spectinomycin plates. Bacteria with positive constructs were selected through colony PCR firstly, then double-checked by test-digestion, and every ligation site was confirmed by sequencing in the end.

3. Generation of Constructs

Cloning of *BdPOLAR* translational and transcriptional constructs was being performed by Michael Raissig. For pGGA_BdPOLARpro (pMTR73) construction, an 1137-bp region upstream of *BdPOLAR* was amplified with priDZ30 and priDZ2, sequentially ligated into empty pGGA000. For pGGC_BdPOLAR-NS (pMTR74) cloning, to remove one BsaI site located in

the first intron of the *BdPOLAR* locus, priDZ31 and priDZ35 were designed to mutate BsaI recognize site. Then two fragments of the *BdPOLAR* gene were amplified by priDZ3 and priDZ35, priDZ31 and priDZ5 separately. Finally, ligation was carried out with digested two inserts and digested pGGC000. To generate pGGZ004_BdPOLARpro:BdPOLAR-mVenus reporter, pGGA_BdPOLARpro, pGGB003, pGGC_BdPOLAR-NS, pGGD_linker-mVenus, pGGE001 and pGGF_PvUBI2pro:HyRcassete were introduced into pGGZ004 by GreenGate reaction. To construct pGGZ004_BdPOLARpro:3xNLS-eGFP, pGGA_BdPOLARpro, pGGB_3xNLS, pGGC_eGFP (pGGC014), pGGD002, pGGE001 and pGGF_PvUbi2pro:HygRcassete (pTN5) were introduced into pGGZ004 by GreenGate reaction.

As for *BdPOLAR* overexpression, I cloned *BdPOLAR* fused with N-terminal, separately with maize (*Zea mays*) *ubiquitin* (*ZmUbi*) promoter and switchgrass (*Panicum virgatum*) *ubiquitin 2* (*PvUbi2*) promoter drive expression. For the former one, pGGA_ZmUbipro (pTN2), pGGB_mVenus, pGGC_BdPOLAR-S (with stop codon) (pDZ9), pGGD002, pGGE001 and pGGF_PvUbi2pro: HyRcassete (pTN5) were integrated into pGGZ004 through GreenGate reaction. For the latter one, pGGA_PvUbi2pro (pTN3) replaces the A module in reaction. I also overexpressed a C-terminal mVenus tagged version of *BdPOLAR* under the maize ubiquitin promoter control. To accomplish this, pGGA_ZmUBIpro, pGGB003, pGGC_BdPOLAR-S, pGGD_GSL-mVenus, pGGE001, and pGGF_PvUBI2pro:HyRcassete were reconstituted into pGGZ004 by GreenGate reaction.

In terms of pGGZ004_BdPOLARgenomic cloning, I carried out the GreenGate reaction by assembling pGGA_BdPOLARpro (pMTR73), pGGB003, pGGC_BdPOLAR-NS (pMTR74), pGGD002, pGGE000_ BdPOLARterminator and pGGF_PvUBI2pro:HyRcassete into pGGZ004.

BdPAN1 translational reporter construct *BdPAN1pro:BdPAN1-YFP* were generated by Akhila Bettadapur, and transgenic lines were characterized by

Emily Abrash in Dominique's lab. In GreenGate system, for the *BdPAN1* translational reporter, fragments of the *BdPAN1* locus were amplified from Bd21-3 genomic DNA. First, to build pGGA_BdPAN1pro, a *BdPAN1* promoter fragment was generated by amplifying a 2327-bp region upstream of *BdPAN1* using priDZ100 and priDZ101. Next, Rashmi Tandon cloned pGGC_BdPAN1 with priRT01 and priRT02. Finally, pGGZ004_BdPAN1pro:BdPAN1-mCitrine was built by the GreenGate reaction. To construct the *BdPAN1* transcriptional reporter pGGZ004_BdPAN1pro:3XNLS-eGFP, separately, pGGB_3xNLS and pGGC_eGFP (pGGC014) were applied to occupy B and C module place during GreenGate reaction.

Irem Polat carried out translational and overexpression constructs cloning for *BdPOLAR-LIKE* (Bd1g47330). For *BdPOLAR-LIKE* native promoter-driven constructs, I built pGGA_BdPOLAR-LIKEpro that contains a 3525-bp region upstream of *BdPOLAR-LIKE* amplified by priDZ111 and priDZ112. After digested inserts ligated with digested pGGA000, sequencing results revealed that excess 57-bp inserts appeared inside the region of priDZ111 oddly, while the remaining sequence was correctly sequenced. I still preserve this version pGGA_BdPOLAR-LIKEpro and utilize it for translational construction. Irem performed the pGGC_BdPOLAR-LIKE (without stop codon) cloning. Firstly, since *BdPOLAR-LIKE* contains one BsaI restriction site at the late of the first exon, priDZ143 and priDZ144 were designed to mutate this site. Afterward, a shorter and a longer fragment were amplified by priDZ113 and priDZ144, priDZ143 and priDZ115 separately. Then, the above two inserts were digested by BsaI and reconstituted into digested pGGC000 in a triple ligation reaction. Finally, correct pGGC_BdPOLAR-LIKE was confirmed by colony PCR, test-digestion, and sequencing analysis. To generate *BdPOLAR-LIKE* translational construct pGGZ004_BdPOLAR-LIKEpro:BdPOLAR-LIKE-mVenus, pGGA_BdPOLAR-LIKEpro, pGGB003, pGGC_BdPOLAR-LIKE, pGGD_linker-mVenus, pGGE001 and pGGF_PvUBI2pro:HyRcassete were introduced into pGGZ004 by GreenGate reaction. Next, to generate *BdPOLAR-LIKE* overexpression construct pGGZ004_ZmUBIpro:BdPOLAR-LIKE-mVenus, pGGA_ZmUBIpro was utilized for final reconstitution.

Lea Berg performed cloning of myristoylation vectors for BdPOLAR and BdPAN1. Firstly, annealing and phosphorylating priMR456 and priMR457 to synthesize a small myristoylation peptide. Then, digest pGGB000 by BsaI and followed with dephosphorylation. Finally, pGGB-myristoylation (MYR) was generated by ligating digested pGGB000 and annealing primers. Construct was confirmed through NcoI and PvuI double digestion and sequencing analysis. To generate pGGZ004_BdPOLARp:MYR-BdPOLAR-mCitrine, pGGA_BdPOLARpro, pGGB_MYR, pGGC_BdPOLAR, pGGD_GSL-mCitrine, pGGE001 and pGGF:PvUBI2pro-HyRcassete were introduced into pGGZ004 by GreenGate reaction. Similarly, pGGZ004_BdPAN1p:MYR-BdPAN1-mCitrine was built using pGGA_BdPAN1pro and pGGC_BdPAN1 instead; For pGGZ004_BdPOLARpro:MYR-BdPAN1-mCitrine cloning, A and C module were substituted with pGGA_BdPOLARpro and pGGC-BdPAN1.

For the ABD2 marker line in *Brachypodium*, pGGC_ABD2 was first constructed as an entry vector. To accomplish this, a 1087-bp ABD2 fragment was amplified from pGreen179_CASP1pro:Citrine-ABD2_OCS plasmid using priDZ54 and priDZ55. To generate pGGZ004_ZmUbipro:PmTurquoise-ABD2 and pGGZ004_BdPOLARpro:PmTurquoise-ABD2 final constructs, GreenGate reaction was carried out based on six entry modules. However, the final cloning step failed several times due to three BsaI restriction sites on the ABD2 gene. The sequencing results by utilizing pGGZ004-FP are always messy, even though those from pGGZ004-RP are right.

Inés Hidalgo Prados performed the GreenGate reaction to construct pGGZ004_BdPOLARpro:LifeAct-mcherry. pGGA_BdPOLARpro (pMTR73), pGGB003 (B-dummy), pGGC_LifeAct, pGGD_mCherry, pGGE001, pGGF_PvUBI2pro:HyRcassete were introduced into pGGZ004.

pGGC_BdTUB6 was first generated by amplifying the BdTUB6 gene into pGGC000 empty vector using priDZ48 and priDZ49, followed by GreenGate reaction assembling six entry modules to produce

pGGZ004_ZmUbipro:PmTurquoise-BdTUB6 and pGGZ004_BdPOLARpro:PmTurquoise-BdTUB6 separately.

pGGZ004_BdPOLARpro:BdPOLAR-mCit-TurboID construct was generated by integrating pGGA_BdPOLARpro (pMTR73), pGGB003 (B-dummy), pGGC_BdPOLAR-NS (pMTR74), pGGD_Cit-TurboID, pGGE001, pGGF_PvUBI2pro:HyRcassete were introduced into pGGZ004 through GreenGate reaction. In terms of pGGZ004_BdPOLARpro:BdPAN1-mCit-TurboID, pGGC:BdPAN1 was utilized to replace pGGC_BdPOLAR-NS for the GreenGate cycle.

For *BdROP2* (Bradi3g01930) reporter pGGZ004_BdROP2pro:BdROP2-mVenus construction, I built pGGA_BdROP2pro first by amplifying 2223-bp 5'UTR upstream *BdROP2* promoter region with priAH01 and priAH02. Then, due to two BsaI restriction sites on the *BdROP2* gene, the direct ligation between the original *BdROP2* gene and pGGC000 after BsaI digested failed to create pGGC_BdROP2. To solve this problem, primers were designed to mutate two BsaI restriction sites inside the gene sequence so that the *BdROP2* gene was divided into three fragments for amplification. These three fragments (1301-bp, 356-bp, 1230-bp) were cloned by using priAH03 and priAH04, priAH05 and priAH06, priAH07 and priAH08 individually. However, neither normal ligation nor GreenGate cycle with BsaI digested pGGC000 and three PCR pieces could build pGGC-BdROP2 successfully. I did not accomplish *BdROP2* reporter construction in the end.

To generate the *BdROP9* (Bradi3g60900) reporter pGGZ004_BdROP9pro: BdROP9-mVenus, pGGA_BdROP9pro was constructed by Simon using priAH09 and priAH10 to amplify 1185-bp 5'UTR upstream region. Next, I built the pGGC_BdROP9 module with priAH11 and priAH12 primers, containing the 2766-bp *BdROP9* gene. For the final GreenGate constitution, the concentration of pGGC_BdROP9 remained too low to achieve assembly requirement. Several methods have been attempted to settle this matter, such as retransforming plasmid into new *E.coli* strain, changing bacterium incubation temperature, and increasing bacterium volume for mini-prep, while none of

them worked. The cloning procedure for the *BdROP9* reporter is stuck here.

The generation of the entry modules pGGA000, pGGB003, pGGC000, pGGD002, pGGE001, and pGGF000 are described in (Lampropoulos, Sutikovic et al. 2013). The entry modules pGGD_linker-mVenus are described in (Waadt, et al. 2020), and pGGZ004 is described in (Lupanga, et al. 2020). The pGGB_3xNLS, pGGC_eGFP, and pGGB_PmTurquoise were generously provided by Karin Schumacher's group. The pGGD009 (Linker-mCitrine) was generously provided by Jan Lohmann's group. The pGGD_Cit-TurboID and pGreen179_CASP1pro:Citrine-ABD2_OCS were kindly provided by Alexis Maizel's group. The pGGC_LifeAct (pPD0035) was kindly provided by Guido Grossmann's group. The pGGA_ZmUBIpro, pGGA_PvUbi2pro, and pGGF_PvUBI2pro-HyRcassete were cloned by Tiago DG Nunes.

4. Gibson Cloning

The Gibson enzymatic assembly approach was firstly proposed in 2009 by Dr. Daniel G Gibson and his colleagues, which is a robust, isothermal, single-reaction method for assembling multiple overlapping DNA fragments (Gibson, Young et al. 2009). It allows up to six DNA molecules to assemble in the correct order. When I performed the Gibson cloning for pIPKb_BdPOLARpro: BdTAN1-mCitrine construct, initially, I did not acquire many colonies on plates. PEG purification (Appendix) was performed to purify PCR products, increasing the Gibson assembly efficiency. A total of 0.3 pMol of DNA fragments from *BdPOLAR* promoter, *BdTAN1* gene, and mCitrine were assembled into backbone pIPK001t. During this cloning, some unexpected, variety mutations on inserts occurred during my several attempts, such as 6 bp deletion or 1bp insertion at *BdPOLAR* promoter, 1 bp mutation at *BdTAN1* gene (Bradi1g55317) or mCitrine sequence. Reducing incubation time enables less mutation frequency, and the complete sequencing for all inserts is necessary to ensure no mutation exists in the final construct.

To create the pIPKb_BdPOLARpro: BdTAN1-mCitrine construct, Gibson Assembly was performed based on the Gibson Assembly® Master Mix Kit

catalog. Firstly, design primers (priDZ123-priDZ128, Table 12) to amplify BdPOLAR promoter, BdTAN1 gene, and mCitrine fragments here https://nebuilder.neb.com. Then Set up a PCR reaction for each fragment using Q5 polymerase. PEG purification was required for PCR products to get more clean PCR products. Digest pIPK001t with OliI and HindIII at 37ºC O/N, then kill enzymes with 80º for 20 min the next day. About 100 ng digested pIPK001t was used for the final Gibson Assembly. Based on the formula: pmols = (weight in ng) x 1,000 / (base pairs x 650 daltons), considering each fragment's weight and length, the pipetting volume for each fragment was calculated. The final molar ratio I used for Gibson Assembly is pIPK001t: each insert=1:6. A total of 0.3pMol of DNA fragments from *BdPOLAR* promoter, *BdTAN1* gene, and mCitrine were assembled into backbone pIPK001t. Incubate Gibson reaction products at 50ºC for 2h. Following the transformation protocol, transform NEB 5-alpha Competent E. coli cells (provided with the kit) with 2 µl of the assembly reaction. Finally, colony PCR, test-digestion, and sequencing were performed to identify the proper colony on the plate.

As for pIPKb_BdPOLARgenomic cloning, I used priDZ123 and priDZ151 to amplify the 4366bp BdPOLARgenomic region. Purified BdPOLARgenomic PCR products and digested pIPK001t were incubated 2h at 50ºC with Gibson Assembly Master Mix. The final molar ratio I used for Gibson Assembly is pIPK001t: each insert=1:6. A total of 0.19 pmols of DNA fragments were assembled. After E. coli cells transformation, colony PCR, test-digestion, and sequencing were performed to identify the proper colony on the plate.

5. CRISPR Design

Csy4-type system: For pTRAN250D_BdPOLAR-guide2/guide4 construction, firstly, priDZ8 and priDZ9, priDZ10 and priDZ11, priDZ12 and priDZ13 amplify reaction 1, 2, and 3 respectively. Then these three inserts were introduced into empty pMODB2103 by the Golden Gate cycle to produce pMODB2103_BdPOLAR-guide2/guide4. Finally, pMOD_A1510, pMODB2103_BdPOLAR-guide2/guide4 and pMOD_C000 were reconstituted into empty pTRAN250D through Golden Gate reaction. Following the same

procedure, pTRAN250D_BdPOLAR-LIKE-guide1/guide2 and pTRAN250D_BdPOLAR-guide2/guide4-BdPOLAR-LIKE-guide1/guide2 were built sequentially. The three inserts for *BdPOLAR-LIKE* were amplified by priDZ8 and priDZ24, priDZ25 and priDZ26, priDZ27 and priDZ13 separately. I attach one protocol in the Appendix to simplify and generalize the cloning procedure for the Csy4-type system I learned from (Čermák, Curtin et al. 2017).

Multiplexed-type system: To generate pMDC32_BdPOLAR-guide2/4, initially, *BdPOLAR*-guide2 and guide 4 oligos were phosphorylation and annealing with priDZ86 and priDZ87 and priDZ88 and priDZ89, then ligated into linearized gRNA expression vector pYPQ131C and pYPQ132C separately. Next, pYPQ131C_BdPOLAR-guide2 and pYPQ132C_BdPOLAR-guide4, two gRNA expression cassettes, were cloned into pYPQ142 by Golden Gate reaction. At last, pYPQ167 and pYPQ142_BdPOLAR-guide2/4 were introduced into destination vector pMDC32 through Gateway Assembly. Similarly, following the approach used to pMDC32_BdPOLAR-guide2/4, pMDC32_BdPOLAR-LIKE-guide1/2, pMDC32_BdPOLAR-guide2/BdPOLAR-LIKE-guide2 and pMDC32_BdPOLAR-LIKE-guide1/BdPOLAR-guide4 were constructed. In particular, *BdPOLAR-LIKE*-guide1 and guide2 were synthesized by priDZ90 and priDZ91, priDZ92 and priDZ93 separately. More details about each step are available in the Appendix (Cong, Ran et al. 2013).

GRF–GIF system: JD633_CRISPRhigheff was digested and dephosphorylated, sequentially ligated with phosphorylation, and annealing oligos. I generated CRISPR constructs *J*D633_BdPOLAR-g2 and JD633_BdPOLAR-g4, targeting *BdPOLAR* first and second exon separately. Oligos *BdPOLAR* guide 2 and guide 4 were synthesized by priDZ87 and priDZ133, priDZ89 and priDZ134, respectively. Using the CRISPR GRF–GIF system, Irem Polat generated JD633_BdPOLAR-LIKE-g1 and JD633_BdPOLAR-LIKE-g2, targeting two distinct sites in the gene, one at the beginning of the second exon and the other in the edge between the first exon and intron. Respectively, priDZ91 and priDZ135, priDZ93 and priDZ136 were applied to synthesize guide 1 and guide 2. Kim Janssen cloned JD633_BdBZR1_g2 and JD633_BdBZR1_g5 to edit the

first and second exon of *BdBZR1*(Bradi1g23550) separately. Oligos *BdBZR1* guide 2 and guide 5 were synthesized by priKJ01 and priKJ02, priKJ03 and priKJ04, respectively. She also built JD633_BdDET2_g1 and JD633_BdDET2_g2 to target the *BdDET2* (Bradi2g55110) gene, guide 1 and guide 2 Oligos were synthesized by priKJ07 and priKJ08, priKJ05 and priKJ06, respectively. After several attempts, I noticed the ligation approach seems more efficient than the Golden Gate reaction in the original protocol. Our cloning procedure is attached in the Appendix.

6. DNA Extraction

The CTAB protocol was used for DNA extraction, which was modified from (Murray and Thompson 1980). Firstly, grind a small amount of plant tissue in a 1.5ml reaction tube, then add 300ul 2*CTAB buffer (Table 7) and incubate at 65℃ for a half-hour, and allow tubes to cool; Add 300ul chloroform and vortex thoroughly afterward, spin tubes briefly in a microfuge to separate phases, then transfer the upper aqueous phase to a fresh reaction tube; Add 300ul 2-Propanol to new tubes and mix well, then spin in a microfuge for 10 minutes to pellet the DNA; Remove supernatant and wash pellet with 500ul 70% ethanol, and spin tubes briefly in a microfuge; After centrifuge, carefully remove the ethanol and dry pellet at 65℃ chamber for 15mins; Finally, add 100ul water and allow the pellet to dissolve. Mix or vortex before use (use 1-2ul in a PCR reaction).

7. Tissue Culture

Transformation of *Brachypodium distachyon* in our lab are carried out by Heike Lindner, Barbara Jesenofsky, and former lab member Maria Luisa Möller Winheim. Calli derived from WT (Bd21-3), Cas9-negative *bdpolar-1*, *bdpan1*, and *bdmute*/*sid* were transformed using AGL1 *Agrobacterium tumefaciens* strain and regenerated according to standard protocols described in Alves et al., 2009, Bragg et al., 2012, and Bragg et al., 2015.

8. Crossing

Crossing of *Brachypodium* in my study followed the illustrated guide from John Vogel's lab (https://jgi.doe.gov/wp-content/uploads/2015/05/Vogel-lab-Crossing-Brachypodium-2-3-2010.pdf) with slight modifications. I checked the plants grown in soil between 4-5 weeks and chose those in a proper stage for crossing. Regarding female plants, search the basal floret of the spike starting from the top for the whole plant, and find the first basal floret that is not pollinated. Ideally, this floret also has a highly branched and opening stigma. For male parents, 20 or more mature anthers per line were collected on a slide and incubated at 28° C for 10-50 mins to induce dehiscence. During the incubation, I performed emasculation on proper female florets under a binocular. Afterward, I used tweezer to bring the dehisce anther and brush across the stigma. A small piece of tape was then applied at the tip of the flower to ensure that the palea and lemma are tightly closed. I also labelled the genotype and date on tape for the record. Reporter lines were always used as pollen donors so detected signals in the F1 generation revealed a successful cross. In the F2 generation, I and screened for reporter signals and genotyped the mutant alleles to identify required individuals for analysis. *BdPOLARp:BdPOLAR-mVenus* and *BdPAN1p:BdPAN1-YFP* were crossed as males with *bdpan1-1* and *bdpolar-1* to generate *bdpan1-1;BdPOLARp:BdPOLAR-mVenus* and *bdpolar-1 ;BdPAN1p:BdPAN1-YFP,* respectively. *BdPOLARp:BdPOLAR-mVenus* and *BdPAN1p:BdPAN1-YFP* were crossed as males with *bdpolar-1* and *bdpan1-1* to generate complementation lines *bdpolar-1;BdPOLARp:BdPOLAR-mVenus* and *bdpan1-1;BdPAN1p:BdPAN1-YFP,* respectively.

9. Genotyping

bdpolar-1 has a +T insertion, which creates a BseRI restriction site in the mutant allele and allowes us to design a CAPS marker where only the mutant allele is cut. Taq PCR was performed to amplify *BdPOLAR* using priDZ6 and priDZ83 (Table 12) with an annealing temperature of 57.6℃ and 35 seconds elongation

time. Then PCR products could be digested directly by BseRI (NEB #R0581) in 10XCutsmart buffer (NEB #B7204S). Run a 2% gel at 80 voltages via a big comb in a small gel tank for 30min and 40min. After digestion, WT shows a band with 470bp (WT *BdPOLAR* sequence could not be digested), *bdpolar-1* homozygous will be digested into two bands (200bp and 270bp), and *bdpolar-1* heterozygous will show three bands (470bp, 270bp, and 200bp) (Fig.10D).

bdpolar-2 and *bdpolar-3* contained mutations on *BdPOLAR* the first and second exon separately. To investigate their mutation sites, Taq PCR was performed to amplify the *BdPOLAR* gene region (665bp) using priDZ6 and priDZ7 (Table 12). After gel confirmation and PCR products purification, priDZ6 and priDZ7 were applied as sequencing primers to check if *bdpolar-2* and *bdpolar-3* T0 and T1 lines have mutation sites.

The dCAPS assay was utilized for NaN2063 genotyping. Taq PCR was performed using priDZ105 and priDZ106 (Table 12) to amplify the *BdPOLAR* gene region (240bp) and create a BgII restriction site at *BdPOLAR* WT samples. Thus, homozygous lines will not be digested and produce a 240bp band; heterozygous lines will produce three bands, 27bp (invisible on 1% gel), 240bp, and 213bp, separately; WT lines will produce two bands, 213bp and 27bp (invisible on 1% gel), separately.

bdpan1-1 contains a 9bp deletion in *BdPAN1* gene sequence. I amplified a very short PCR fragment and resolve the size difference (84bp vs. 75bp) on a 3% agarose gel. Taq PCR was performed to amplify *BdPAN1* using priDZ81 and priDZ82 (Table 12). 57.6℃ was taken as the annealing temperature, and 30 seconds as the elongation time in PCR procedure. Then run a 3% gel at 70 voltages with a small comb in a small gel tank. This high percentage gel could distinguish this 9bp difference after 30-40 mins or longer depending on the running situation. WT will show a band with 84bp, and *bdpan1-1* will show a band with 75bp. Heterozygous plants will display a smear-like band.

NaN1917 genotyping was carried out using priDZ149 and priDZ150 (Table 12) to amplify *BdDWF4* (Bradi1g69040) gene fragment (598bp), and PCR products were sent for sequencing. NaN1047 genotyping was performed using priKJ09 and priKJ10 (Table 12) to amplify *BdBZR1* (Bradi1g23550) gene fragment (603bp), and PCR products were analyzed by sequencing.

10. Phenotyping

After 17~19 days of sowing, the third leaf was collected and cleared in 7:1 Ethanol: Acetic acid solution and incubated overnight to clear away chlorophyll. Mature zone tissue was selected and washed twice, then mounted with Hoyer's solution (Liu and Meinke 1998) on the slides. Table 8 represents the ingredients to prepare Hoyer's solution. SCs with transverse or oblique divisions but not correct longitudinal divisions were defined as defective SCs. To quantify the SCs division defects, 10-11 DIC (Differential interference contrast) pictures were taken randomly from each individual under 40X objective lens using Leica DM5000B. The number of total SCs and defective SCs of abaxial side were counted and recorded simultaneously from each DIC picture on a computer. For each defective SC, the frequency of SC divided was counted to distinguish and classify SC division categories (Fig.28B). To quantify stomata density, 4 abaxial fields per leaf were captured under 20X objective using Leica DM5000B. The number of stomatal complex was counted from DIC pictures on a computer. The GC length was measured from the top middle point to the bottom middle point of the GC using the “straight” tool in Fiji. The stomata density and GC length were quantified using the leaf areas that were used for stomatal conductance measurements in Fig. 30.

11. Gene Database

The genome sequence of *Brachypodium distachyon* was released by The International Brachypodium Initiative on (International Brachypodium 2010). The reference sequence and transcript for each gene could be accessed and downloaded from The Plant Genomics Resources Phytozome (Goodstein, Shu et al. 2012) (Brachypodium distachyon Bd21-3 v1.1 DOE-JGI,

http://phytozome.jgi.doe.gov/). The effect impact, functional class, codon change, and other information about mutation sites of each NaN line are also annotated there.

12. Confocal Laser Scanning Microscopy (CLSM)

Confocal images for transgenic reporter lines are acquired under 63X glycerol immersion objective in Leica TCS SP8 Microscope. Before confocal imaging, Propidium Iodide (PI) (Thermo Fisher Scientific #P3566) staining is needed to observe cell wall structure. The 2nd (5~6 dpg) and 3rd (8-10 dpg) leaves were carefully pulled out from the division zones which were covered by the sheaths of older leaves, and stained in PI (10 μg/ml) for 5 min, then mounted on a slide with water and covered with a coverslip. The Emission wavelength and Excitation wavelength for fluorescence used in this study are described in Table 9. Image analysis and processing were carried out in Fiji.

13. Nuclear Staining and Measurement

I used the basal 0.5~1cm developmental zone from the 2nd (5~6 dpg) leaf for Nuclear staining experiments. To visualize the nuclear position, Direct red 23 (Sigma-Aldrich #3441-14-3) and Hoechst 33342 (Thermo Fisher Scientific #62249) were used to stain cell walls and nuclear separately. Firstly, 1% (w/v) Direct red 23 intermediate stock was prepared first via diluting in 1XPBS, then the working concentration for cell wall staining is 0.1% (w/v). The original concentration of Hoechst 33342 stock solution is 20mM, and then the intermediate stock of 1mg/ml was prepared by diluting in 1XPBST. 1ng/ml was used as the working concentration for nuclear staining. Then, the 2nd leaves were carefully taken out from the division zone of seedlings growing on 1/2 MS plate. Cut the base developmental zone (0.5~1cm) and use leaf strips for staining.

To combine nuclear and cell wall staining at the same time, I performed the staining experiment as described below: Firstly, I washed leaf strips for 10min with 1XPBST 3 times in vials, then I removed 1XPBST solution and added

1ng/ml Hoechst 33342 solution into vials, and applied vacuum 3 times for 10 min each. Leaf strips were stained for an additional 1h at room temperature with gentle shaking. Next, I removed 1ng/ml Hoechst 33342solution from vials and washed leaf strips for 10min with 1XPBST 3 times, then added 0.1% Direct red 23 staining into vials, and applied vacuum 3 times for 10 min each. Leaf strips were stained an additional 1h at room temperature with gentle shaking. Then, I washed leaf strips again in 1XPBST 3 times for 10min each. In the end, I dried leaf strips with paper and mounted them with 50% Glycerol on the slide.

Images were captured with the following excitation (Ex) and emission (Em) wavelengths (Ex/Em): Direct red 23 561 nm/600–650 nm and Hoechst 33342 405 nm/425–475 nm. Images were processed in Fiji. The d distance, GMC length, and width were measured in Fiji via the “straight” tool. I measured the d distance starting from the middle point of nuclei in SMC and ending at the middle point of the GMC/SMC interface. The GMC length was measured from the middle point of the apical side to the middle point of the basal side of the GMC. The GMC width was measured from the middle point of the left side to the middle point of the right side of the GMC. To avoid deviations of d distance measurement due to imaging at different Z-axis positions, I also measured the nuclear diameters per genotype, and they did not show a significant difference (Fig.23E).

14. POME and Polarity Index

Inés Hidalgo Prados performed the POME and Polarity Index assays. Regarding POME measurements (Gong, Varnau et al. 2020), the developmental zone of the 2nd (5~6 dpg) leaves from *BdPAN1* and *BdPOLAR* reporter lines in WT and mutant backgrounds were used for confocal imaging. After staining with PI for 5 minutes, leaves were mounted with water on slides and acquired with a 63x glycerol immersion objective. The scan format is expressed as 1024X1024 pixels and uses a 2X zoom factor. Individual SMCs at stomatal development stage 3 were selected for the analysis. 19 to 33 SMCs were analyzed for each condition. SMCs with clear and strong signals were selected. Additionally, recently and incorrectly divided SMCs in the mutants

background were excluded. In the case of raw fluorescence image Z-stacks, three with the better reporter signal were projected in Fiji. Fluorescence intensity at each pixel and angle was obtained in Fiji as described by (Gong, Varnau et al. 2020). Before running POME on a selected cell, each cell's input parameters were specified in the POME Fiji macro. The obtained measurements were then imported, summarized, and analyzed in RStudio (details available in (Gong, Varnau et al. 2020)). The polarity index was calculated as the fraction of fluorescence intensity values above the half maximum (Gong, Varnau et al. 2020). Briefly, the maximum fluorescence intensity of each cell was determined, and the fraction of values above half of this maximum was calculated. The polarity index of all analyzed cells of the same condition was grouped and statistically compared to the other conditions with unpaired Mann-Whitney U-tests.

15. Physiology

Tiago DG Nunes performed the leaf-level gas exchange measurements. The protocols were specified in (Nunes, Slawinska et al. 2022) and simply described here: LI-6800 Portable Photosynthesis System (Li-COR Biosciences Inc.) performed measurements using the youngest, fully expanded leaf (17-21 days after sowing). The LI-6800 provided a Multiphase Flash Fluorometer (6800-01A) chamber with conditions as follows: flow rate, 500 µmol s^{-1}; fan speed, 10000 rpm; leaf temperature, 28^{o}C; relative humidity (RH), 40 %; [CO_2], 400 µmol mol^{-1}; photosynthetic active radiation (PAR), 1000 – 100 – 1000 – 0 µmol PAR m^{-2} s^{-1} (20 min per light step). Stomatal conductance (g_{sw}) measurements were automatically logged every minute. Relative g_{sw} was computed by normalizing g_{sw} to the maximum g_{sw} value observed to assess the kinetics of stomatal response, excluding variation in absolute g_{sw}. 5 individual each genotype 5 *bdpolar-1*, 5 *bdpan1-1*, 5 *bdpolar-1;bdpan1-1* and 7 wild-types were measured between February, March, October, and December of 2021.

16. Statistical Analysis and Plotting

Statistical analysis was carried out in R and Graphpad. For multiple comparisons, firstly, One-way ANOVA was applied to determine whether the means of all groups were statistically significantly different. Then Post hoc test was applied to map out which groups were different from other groups. Different letters represent significant differences. For comparisons of two groups, I used either an unpaired Mann-Whitney U-test (Fig.19) or a Welch two sample t-test (Fig.21) as indicated in the figure legends. Asterisks indicate significant differences. All plots were done in R using ggplot2 or basic R plotting commands. Boxplots were generated using the boxplot function. Plots of stomatal conductance (g_{sw}), relative g_{sw}, and exponential regressions were done in Graphpad Prism version 9.1.0 by Tiago DG Nunes.

Table 3. Taq PCR reaction setup and thermocycling conditions.

Component	25 µl reaction	Temperature	Time	Number of cycles
10XStandard Taq reaction buffer	2.5 µl	95 ºC	30 s	
10 mM dNTPs	0.5 µl	95 ºC	30 s	
10 µM forward primer	0.5 µl	58 ºC	30 s	35
10 µM reverse primer	0.5 µl	68 ºC	1 min/kb	
Template DNA/colony	Variable	68 ºC	5 min	
Taq DNA Polymerase	0.125 µl	16 ºC		
Nuclease-free water	To 25 µl			

Table 4. Q5 PCR reaction setup and thermocycling conditions.

Component	50 µl reaction	Temperature	Time	Number of cycles
5XQ5 reaction buffer	10 µl	98 ºC	30 s	
10 mM dNTPs	1 µl	98ºC	10 s	
10 µM forward primer	2.5 µl	58 ºC	20 s	35
10 µM reverse primer	2.5 µl	72 ºC	20-30 s/kb	
Template DNA	Variable	72 ºC	2 min	
Q5 high-fidelity DNA Polymerase	0.5 µl	16 ºC		
5XQ5 high GC enhancer(optional)	(10 µl)			
Nuclease-free water	To 50 µl			

Table 5. GreenGate reaction setup and thermocycling conditions.

Component	20 µl reaction	Temperature	Time	Number of cycles
Entry clone promoter	1.5 µl	37 ºC	5 min	
Entry clone N-tag	1.5 µl	16 ºC	2 min	30
Entry clone CDS	1.5 µl	50 ºC	5 min	
Entry clone C-tag	1.5 µl	80 ºC	5 min	
Entry clone terminator	1.5 µl			
Entry clone Plant resistance	1.5 µl			
Destination vector pGGZ004	1 µl			
10XFast Digest buffer	2 µl			
ATP (10 mM)	2 µl			
T4 DNA ligase	0.5 µl			

Eco31I	0.5 µl	
Nuclease-free water	5 µl	

Table 6. Sterilization solution recipe.

Component	Stock concentration	Work concentration	50 ml
bleach	20%	5.25%	10 ml
Triton-100	100%	0.1%	50 µl
Water			40 ml

Table 7. 2XCTAB solution recipe.

Component	Stock concentration	Work concentration	100 ml
NaCl	5 M	1.4 M	28 ml
Tris-HCl (PH 8.0)	1 M	100 mM	10 ml
EDTA	0.5 M	20 mM	4 ml
CTAB			2 gram
Water			To 100 ml

Table 8. Hoyer's solution recipe.

Component	Work concentration	100 ml
glycerol	100 mM	20 ml
chloral hydrate	20 mM	200 gram
gum arabic		15 gram
Water		To 100 ml

Ingredients:

15 gram gum arabic
25 ml H_2O
200 gram chloral hydrate
20 ml glycerol

Add 15 gram gum arabic to 25 ml H_2O, heat up to 60 ℃ and stir overnight. Add 200 gram chloral hydrate and 20 ml glycerol.

Table 9. Emission wavelength and Excitation wavelength used with SP8.

Fluorescence	Excitation [nm]	Emission [nm]
mVenus	514	520-570
mCitrine	514	520-570
YFP	514	520-570
GFP	488	510-560
mTurquoise	458	460-510
PI	561	600-650
Direct red 23	561	600-650
Hoechst 33342	405	425-475

Table 10. List of antibiotics.

Antibiotic	Stock conc.	Work conc.	Solvent	Catalogue
Ampicillin	100 mg/ml	100 µg/ml	Water	Sigma-Aldrich #69-52-3
Carbenicillin	100 mg/ml	50 µg/ml	Water	ROTH Nr.6344.2
Chloramphenicol	25 mg/ml	25 µg/ml	EtOH	ROTH Nr.3886.2
Gentamicin	10 mg/ml	10 µg/ml	Water	ROTH Nr.0233.3
Hygromycin B	50 mg/ml	40 µg/ml	Water	ROTH Nr.10843555001
Kanamycin	50 mg/ml	50 µg/ml	Water	ROTH Nr.T832.4
Spectinomycin	50 mg/ml	50 µg/ml	Water	Sigma-Aldrich#22189-32-8
Tetracycline	10 mg/ml	10 µg/ml	Water	ROTH Nr.0237.1

Table 11. Plasmids created in this study.

Plasmid number	Plasmid name	Creator
pDZ1	pGGA_BdPOLAR promoter (with BsaI site)	Dan Zhang
pDZ2	pGGC_BdPOLAR gene with stop codon (with BsaI site)	Dan Zhang

pDZ3	pGGC_BdPOLAR gene without stop codon (with BsaI site)	Dan Zhang
pDZ4	pMODB2103_BdPOLAR guide2 guide4	Dan Zhang
pDZ5	pMODB2103_BdPOLAR-LIKE guide1 guide2	Dan Zhang
pDZ6	pTRAN250D_BdPOLAR guide2 guide4	Dan Zhang
pDZ7	pTRAN250D_BdPOLAR-LIKE guide1 guide2	Dan Zhang
pDZ8	pTRAN250D_BdPOLAR/BdPOLAR-LIKE	Dan Zhang
pDZ9	pGGC_BdPOLAR gene with stop codon (without BsaI site)	Dan Zhang
pDZ10	pGGZ004_BdPOLARpro:mVenus-BdPOLAR	Dan Zhang
pDZ11	pGGE000_BdPOLARterminator	Dan Zhang
pDZ12	pMODB2103_BdPOLAR guide2 guide4/BdPOLAR-LIKE guide1 guide2	Dan Zhang
pDZ13	pGZ004_PvUbi2pro:mVenus-BdPOLAR	Dan Zhang
pDZ14	pGZ004_ZmUbipro:mVenus-BdPOLAR	Dan Zhang
pDZ15	pGGA_BdROP9pro	Simon
pDZ16	pGGC_ABD2	Dan Zhang
pDZ17	pGGC_TUB6	Dan Zhang
pDZ18	pGGZ004_ZmUbipro:pmmTurquoise-TUB6	Dan Zhang
pDZ19	pGGZ004_BdPOLARpro:pmmTurquoise-TUB6	Dan Zhang
pDZ20	pGGC_BdROP9	Dan Zhang
pDZ21	pGGA_BdROP2pro	Dan Zhang
pDZ22	pGGC_BdPAN1	Rashmi Tandon
pDZ23	pGGZ004_BdPOLARpro:BdPAN1-mCit-TurboID	Rashmi Tandon
pDZ24	pGGZ004_BdPOLARpro:BdPOLAR-mCit-TurboID	Dan Zhang
pDZ25	pYPQ131C_BdPOLAR-guide2	Dan Zhang
pDZ26	pYPQ132C_BdPOLAR-guide4	Dan Zhang
pDZ27	pYPQ132C_BdPOLAR-LIKE-guide2	Dan Zhang
pDZ28	pYPQ131C_BdPOLAR-LIKE-guide1	Dan Zhang
pDZ29	pYPQ142_BdPOLAR-guide2/4	Dan Zhang
pDZ30	pYPQ142_BdPOLAR-LIKE-guide1/2	Dan Zhang
pDZ31	pMDC32_BdPOLAR-guide2/4	Dan Zhang
pDZ32	pYPQ142_BdPOLAR-guide2/BdPOLAR-LIKE-guide2	Dan Zhang
pDZ33	pYPQ142_BdPOLAR-LIKE-guide1/BdPOLAR-guide4	Dan Zhang
pDZ34	pGGA_BdPAN1pro	Dan Zhang
pDZ35	pMDC32_BdPOLAR-LIKE-guide1/2	Dan Zhang
pDZ36	pMDC32_BdPOLAR-guide2/BdPOLAR-LIKE-guide2	Dan Zhang
pDZ37	pMDC32_BdPOLAR-LIKE -guide1/BdPOLAR-guide4	Dan Zhang
pDZ38	pGGM_BdPAN1-mTurquoise	Dan Zhang

pDZ39	pGGN_BdPOLAR-mCitrine	Dan Zhang
pDZ40	pGGZ004_BdPAN1-mTurquoise/BdPOLAR-mCitrine	Dan Zhang
pDZ41	pGGZ004_BdPAN1pro:3XNLS-eGFP	Dan Zhang
pDZ42	pGGA_BdPOLAR-LIKEpro	Dan Zhang
pDZ44	JD633_BdPOLAR-g2	Dan Zhang
pDZ45	JD633_BdPOLAR-g4	Dan Zhang
pDZ46	pGGZ004 BdPAN1pro:BdPAN1-mCitrine	Dan Zhang
pDZ47	pIPKb_BdPOLARpro:TAN1-mCitrine	Dan Zhang
pDZ48	pGGZ004_BdPOLARpro:MYR-BdPAN1-mCitrine	Dan Zhang
pDZ49	pGGZ004_BdPAN1pro:MYR_BdPAN1-mCitrine	Dan Zhang
pDZ50	pGGZ004_ZmUbi1pro:BdPOLAR-NS-mVenus	Dan Zhang
pDZ51	pGGZ004-BdPOLARgenomic	Dan Zhang
pDZ52	pIPKb_BdPOLARgenomic	Dan Zhang
pMTR73	pGGA_BdPOLARprom_noBsaI	Michael Raissig
pMTR74	pGGC_BdPOLARgene_noBsaI_-20bp_firstINTRON	Michael Raissig
pMTR75	pGGZ004_BdPOLARpro:BdPOLAR-mVenus	Michael Raissig
pMTR76	pGGZ004_BdPOLARpro:3xNLS-eGFP	Michael Raissig
pMTR77	pGGZ004_BdPOLARpro:AtH2B-3xGFP	Michael Raissig
pIH1	pGGZ004_BdPOLARpro:LifeAct-mcherry	Inés Hidalgo Prados
pLB1	pGGB_MYR(myrestoylation)	Lea Berg
pLB2	pGGZ004_BdPOLARpro:MYR-BdPOLAR-mCitrine	Lea Berg
pIP1	pGGC000_BdPOLAR-LIKE	Irem Polat
pIP2	JD633_BdPOLAR-LIKE-g1	Irem Polat
pIP3	JD633_BdPOLAR-LIKE-g2	Irem Polat
pIP4	pGGZ004_ZmUbipro:BdPOLAR-LIKE-mVenus	Irem Polat
pIP5	pGGZ004_BdPOLAR-LIKEpro:BdPOLAR- LIKE -mVenus	Irem Polat
pKJ1	JD633_BdBZR1_g2	Kim Janssen
pKJ2	JD633_BdDET2_g2	Kim Janssen
pKJ3	JD633_BdDET2_g1	Kim Janssen
pKJ4	JD633_BdBZR1_g5	Kim Janssen
pNG1	pGGZ004-BdPOLARpro:BdPOLAR-LIKE-mVenus	Nika Gorsek
pNG2	pGGZ004-BdPOLAR-LIKEpro:BdPOLAR-mVenus	Nika Gorsek

Table 12. Primers used in this study.

Primer name	Sequence [5'-3']	Comments

priDZ1	AACAGGTCTCAACCTACGCCATGCCAAATAGGATC	FP: Amplify *BdPOLAR* promoter with BsaI site
priDZ2	AACAGGTCTCATGTTTTGGTGACGATGGATGATGT	RP: Amplify *BdPOLAR* promoter with BsaI site
priDZ3	AACAGGTCTCAGGCTCCATGGCGACCGAGAGCAGC	FP：Amplify *BdPOLAR* CDS (TCC makes Ser)
priDZ4	AACAGGTCTCACTGACTACCTGAGCCGGGACTC	RP：Amplify *BdPOLAR* CDS (with stop codon)
priDZ5	AACAGGTCTCACTGACCTGAGCCGGGACTCGTC	RP: Amplify *BdPOLAR* CDS (without stop codon)
priDZ6	CGACCGATCCTCCAAACATT	FP: Genotyping CRISPR *BdPOLAR* (pMTR57 pMTR58)
priDZ7	TTTCGTCTGCGTCATTGCT	RP: Genotyping CRISPR *BdPOLAR* (pMTR57 pMTR58)
priDZ8	TGCTCTTCGCGCTGGCAGACATACTGTCCCAC	FP: CmYLCV in CRISPR pMODB2103
priDZ9	TGGTCTCCCTCCGGAGGCGCCTGCCTATACGGCAGTGAAC	RP: CRISPR *BdPOLAR* guide2
priDZ10	TGGTCTCAGGAGCAGTACCGGTTTTAGAGCTAGAAATAGC	FP: CRISPR *BdPOLAR* guide2
priDZ11	TGGTCTCCTTGGATAGCAGCCTGCCTATACGGCAGTGAAC	RP: CRISPR *BdPOLAR* guide4
priDZ12	TGGTCTCACCAAGGGCGCGGGTTTTAGAGCTAGAAATAGC	FP: CRISPR *BdPOLAR* guide4
priDZ13	TGCTCTTCTGACCTGCCTATACGGCAGTGAAC	RP: CmYLCV in CRISPR pMODB2103
priDZ14	CTGGAGTCGGAGCTGGAG	Sequencing-FP: located on pGGC-BdPOLARgene-withSTOP
priDZ15	gctctaatgtgcgaagtctccagcccggc	FP: *BdPOLAR* promoter mutagenesis
priDZ16	gccgggctggagacttcgcacattagagc	RP: *BdPOLAR* promoter mutagenesis
priDZ17	cgtgcgcgtccatggacagaccagtgaa	FP: *BdPOLAR* CDS mutagenesis
priDZ18	ttcactggtctgtccatggacgcgcacg	RP: *BdPOLAR* CDS mutagenesis
priDZ19	AACACGCCCACATTTACAGT	Sequencing-RP: located on *BdPOLAR*pro
priDZ20	GTGCTCACTTTCTTAGCCGA	Sequencing-FP: located on pTN5(pGGF-PvUBI2:HygR)
priDZ21	AACAGGTCTCACGTCCATGGAGAGACGAGT	FP: mutate BsaI site in *BdPOLAR*
priDZ22	AACAGGTCTCAGACGCGCACGCACGTACC	RP: mutate BsaI site in *BdPOLAR*
priDZ23	AACAGGTCTCAACCTTAATGTGCGAAGTCTCCAGC	FP：Amplify *BdPOLAR* promoter
priDZ24	TGGTCTCCTTGGACAGCAGCCTGCCTATACGGCAGTGAAC	RP: CRISPR *BdPOLAR*-LIKE guide1
priDZ25	TGGTCTCACCAAGAGCGCCGGTTTTAGAGCTAGAAATAGC	FP: CRISPR *BdPOLAR*-LIKE guide1
priDZ26	TGGTCTCCATGCATCCATCCCTGCCTATACGGCAGTGAAC	RP: CRISPR *BdPOLAR*-LIKE guide2
priDZ27	TGGTCTCAGCATGCATACCGGTTTTAGAGCTAGAAATAGC	FP: CRISPR *BdPOLAR*-LIKE guide2
priDZ28	CTAGAAGTAGTCAAGGCGGC	Colony PCR and sequencing FP CmYLCV TC320
priDZ29	GGAACCCTAATTCCCTTATCTGG	Colony PCR and sequencing RP CmYLCV TC089R
priDZ30	AACAGGTCTCAACCTCCGGGGAGATGGACATATGT	FP：Amplify *BdPOLAR* promoter without BsaI site
priDZ31	AACAGGTCTCGAGCATGCTCTCTCCATGGAC	FP: mutate BsaI site in *BdPOLAR*
priDZ32	AACAGGTCTCACTGCTCTCTCCATGGACGCG	RP: mutate BsaI site in *BdPOLAR*
priDZ33	GTAAAACGACGGCCAGT	M13F
priDZ34	GTTGGATCTCTTCTGCAGCA	TC430-binds to HSP terminator
priDZ35	AACAGGTCTCATGCTCTCTCCATGGACGCG	RP: mutate BsaI site in *BdPOLAR*
priDZ36	AAAGTTCGACAGCGTgTCCG	Hyg-FP

priDZ37	AATACGAGGTCGCCAACATC	Hyg-RP
priDZ38	AACAGGTCTCACTGCATTATCCAACCTGCACGGAC	FP：Amplify *BdPOLAR* terminator
priDZ39	AACAGGTCTCATAGTCAGACCAAGATGCTGATCCC	RP：Amplify *BdPOLAR* terminator
priDZ40	CGATGCGTGCCGCTCT	FP (dCAPS): genotyping *polar-1* T insertion
priDZ41	AGAGCAGCGACCCCGG	FP (dCAPS): genotyping polar-1 CC deletion
priDZ42	GTCTAGCGGCAACAATGTCT	FP: genotyping CRISPR *BdPOLAR*-LIKE (guide1 and guid2)
priDZ43	GTAGTGCTAGAGCTGCCTTC	RP: genotyping CRISPR *BdPOLAR*-LIKE (guide1 and guid2)
priDZ44	GCGAGTACTTCTACACAGCC	Hyg-FP
priDZ45	GCGAAGAATCTCGTGCTTTC	Hyg-RP
priDZ46	TCGACGAACAGCTGCTTTT	Cas9-FP
priDZ47	GGACAAGGGCAGGGATTTC	Cas9-RP
priDZ48	AACAGGTCTCAGGCTCCATGAGGGAGATCCTCCAC	FP：Amplify *BdTUB6* CDS（TCC makes Ser)
priDZ49	AACAGGTCTCACTGATCACTCCTCCTCGGCCTGC	RP：Amplify *BdTUB6* CDS (with stop codon)
priDZ50	CGCTCCTAGTTTGAGAGTGG	FP: genotyping *polar* CRISPR line
priDZ51	GAAGACGGTCGGCTCTATGA	RP: genotyping *polar* CRISPR line
priDZ52	GTGCGACCTCACGTATACTC	FP: genotyping *pan1*
priDZ53	CTCGGACAGCAGGGAGAG	RP: genotyping *pan1*
priDZ54	AACAGGTCTCAGGCTCCTCTTGAAAGAGCTGAATTGGTT	FP：Amplify *ABD2* CDS
priDZ55	AACAGGTCTCACTGACTATTCGATGGATGCTTCCTCT	RP：Amplify *ABD2* CDS (with stop codon)
priDZ56	AGGCGCTGAACACGGACGGGCTGGCGCTGCC	FP (dCAPS): genotyping *pan1* 9bp deletion mutant cut wild type (HpaII: CCGG)
priDZ57	TGAGCCTTACAATGCCACTC	*BdTUB6* sequencing primer FP
priDZ58	GAGGGTGAGCTTTCCGTAAG	RP: pGGB-pmmTurquoise
priDZ59	CCTATCGGAGATGGACCTGT	FP: pGGB-pmmTurquoise
priDZ60	AGGCCACGATTTGACACATT	RP: pGGE001
priDZ61	AGTATCAGCGTTAACTTTTTCA	FP: *BdROP2* promoter
priDZ62	TTCTCAGGTGTTGGTTTCCG	RP: *BdROP2* promoter
priDZ64	GCTGATTTCTGTTAGCCTCG	Bd1_24.1mb-1R
priDZ63	ACCTTTAGGAACTGAAATAGCC	Bd1_24.1mb-1F Bd1:24,052,857 685 bp (Bd21-3), 451 bp (Bd3-1)
priDZ65	AGAAGTATCTAGCGGTTCAACC	Bd1_48.8mb-2F (BLAST to find actual position) Checked - real 445 bp (Bd21-3), 550 bp (Bd3-1)
priDZ66	ATCATGCATGTTGTCTGTTCC	Bd1_48.8mb-2R
priDZ67	TGCAAGTTCTTGGATGTCCC	Bd2_21.1mb-1F Bd2: 21,127,979..21,128,661 455 bp (Bd21-3), 356 bp (Bd3-1)
priDZ68	CCAGTTGCCTTGTAAACAGG	Bd2_21.1mb-1R
priDZ69	TATGGATGGTCACGCACG	Bd2_45.4mb-1F Bd2: 45,448,330..45,449,012 Checked – real 508 bp (Bd21-3), 395 bp (Bd3-1)
priDZ70	GAGCTATCATTGGTCAAAGCC	Bd2_45.4mb-1R
priDZ71	AACCTCTCCTTCTCTGTATTCC	Bd3_21.5mb-1F Bd3: 21,540,815..21,541,497 609 bp

		(Bd21-3), 415 bp (Bd3-1)
priDZ72	TTTCGACGGATCCCAACC	Bd3_21.5mb-1R
priDZ73	CCAAGCCTGACACATATCCG	Bd3_45.3mb-1F Bd3: 45,265,279..45,265,961 630 bp (Bd3-1), 450 bp (Bd21-3)
priDZ74	AGAAGTGCATCCTTGTCAGC	Bd3_45.3mb-1R
priDZ75	CTTGCCTTGATCAGTACTGGG	Bd4_31.3mb-1F Bd4: 31,296,605..31,297,287 475 bp (Bd21-3), 407 bp (Bd3-1)
priDZ76	GAATCTCAGAGATGGGTTTCCC	Bd4_31.3mb-1R
priDZ77	CATCCAGATGCAAACAGCC	Bd5_1.9mb-1F Bd5: 1,923,832..1,924,514 503 bp (Bd21-3), 391 bp (Bd3-1)
priDZ78	AGACACCGAGTCTTCTTTCC	Bd5_1.9mb-1R
priDZ79	GAATTGAAGCTCGAGACTTGG	Bd5_20.8mb-1F Bd5: 20,814,332.. 20,814,489 526 bp (Bd3-1), 390 bp (Bd21-3)
priDZ80	TGCTGTTCCATTACCCTCC	Bd5_20.8mb-1R
priDZ81	GTGTTGGTGGCGGCATTA	FP: genotyping *pan1*
priDZ82	GGACACCGCGAACTTGAG	RP: genotyping *pan1*
priDZ83	CCGCCATTAATCTCTCTCGG	RP: genotyping *polar-1*. BseRI cut *polar-1* reverse mutantion site.
priDZ84	gtgtGTACCGAAAGAGCTTCGCGG	BdPOLAR-gR1-OsU6-F (guide 1)
priDZ85	aaacCCGCGAAGCTCTTTCGGTAC	BdPOLAR-gR1-OsU6-R (guide 1)
priDZ86	gtgtGCGCCTCCGGAGCAGTACCG	BdPOLAR-gR2-OsU6-F (guide 2)
priDZ87	aaacCGGTACTGCTCCGGAGGCGC	BdPOLAR-gR2-OsU6-R (guide 2)
priDZ88	gtgtGCTGCTATCCAAGGGCGCGG	BdPOLAR-gR3-OsU6-F (guide 4)
priDZ89	aaacCCGCGCCCTTGGATAGCAGC	BdPOLAR-gR3-OsU6-R (guide 4)
priDZ90	gtgtGCTGCTGTCCAAGAGCGCCG	BdPOLAR-LIKE-gR1-OsU6-F (guide 1)
priDZ91	aaacCGGCGCTCTTGGACAGCAGC	BdPOLAR-LIKE-gR1-OsU6-R (guide 1)
priDZ92	gtgtGGATGGATGCATGCATACCG	BdPOLAR-LIKE-gR2-OsU6-F (guide 2)
priDZ93	aaacCGGTATGCATGCATCCATCC	BdPOLAR-LIKE-gR2-OsU6-R (guide 2)
priDZ94	ATTCCTGTCGCCGTGAGC	FP: located on BdPAN1-CDS
priDZ95	CGAGACACCCCAACGTCG	FP: located on BdPAN1-CDS
priDZ96	CAAGCCTGATTGGGAGAAAA	pTC14_F2 primer
priDZ97	ACTCGTATCGACCTTTCCCA	pMD32 equencing primer on Cas9
priDZ98	AACAGGTCTCAACCTACTAGCAGCTGCCTGTTTTT	FP：Amplify *BdPAN1* promoter
priDZ99	AACAGGTCTCATGTTTGCGAGCTACGGAGGAAG	RP：Amplify *BdPAN1* promoter
priDZ100	AACAGGTCTCAACCTGTTGGGTTACCGATGATATGC	FP：Amplify *BdPAN1* promoter (from Emily's thesis)
priDZ101	AACAGGTCTCATGTTGAGCTACGGAGGAAGCAC	RP：Amplify BdPAN1 promoter (from Emily's thesis)
priDZ102	CGCTCACTGCAGATTCTAGG	FP: located on *BdPAN1* promoter
priDZ103	AGGCATCAAACTAAGCAGAAG	87-E2 from AG Greb
priDZ104	CGTTTCCCGTTGAATATGGC	87-E3 from AG Greb
priDZ105	AGAAGGAGCGCGAGGTGCCCCGGTGG	NaN2063 dCAPs-FP（BglI）-240bp,cut wt into 27bp and 213bp
priDZ106	GTCTTCCTTTCGCGGAGATG	NaN2063 dCAPs-RP（BglI）-240bp,cut wt into 27bp and 213bp
priDZ107	CGATGAAGACGAGGATGAGG	NaN1927 dCAPs-FP(KpnI)-241bp, cut mutant into 32bp and

		209bp
priDZ108	GGCGTCGCGCCACCAGACGACCTCGCGGT	NaN1927 dCAPs-RP(KpnI)-241bp, cut mutant into 32bp and 209bp
priDZ109	AACGAAGACGACGAGGAATG	NaN2063 genotyping
priDZ110	AATTTACACACCCACACGCA	NaN1927 genotyping
priDZ111	AACAGGTCTCAACCTTCACGTACGCTTAAGAAGGC	FP: Amplify *BdPOLAR-LIKE* promoter
priDZ112	AACAGGTCTCATGTTCGATCCGATCCTTCAATTAC	RP ： Amplify *BdPOLAR-LIKE* promoter
priDZ113	AACAGGTCTCAGGCTCCATGGCGAGTAATTCTGTT	FP ： Amplify *BdPOLAR-LIKE* CDS（TCC makes Ser)
priDZ114	AACAGGTCTCACTGATTAAGCGGCGCGCGGCCG	RP ： Amplify *BdPOLAR-LIKE* CDS (with stop codon)
priDZ115	AACAGGTCTCACTGAAGCGGCGCGCGGCCGAGC	RP ： Amplify *BdPOLAR-LIKE* CDS (without stop codon)
priDZ116	TGGCACCCCTCTTTCATTTC	FP: located on *BdPOLAR-LIKE* promoter
priDZ117	CCTGAGTTTATCACGGTCCG	FP: located on *BdPOLAR-LIKE* promoter
priDZ118	CAGCTTCCCGGAAAAGACAG	RP: located on *BdPOLAR-LIKE* promoter
priDZ119	CTCTTGGCTTGGCTGTAACT	FP: located on pGGA_BdML1-like1_Bradi3g15327
priDZ120	CGCCTACAACGTCAACATCA	FP: located on pGGD-GSL-mCherry
priDZ121	AGGGCTAAACTTGTCCATGC	RP: located on *BdPOLAR-LIKE* promoter
priDZ122	CCTCTTCCTTCCCCGATCTT	FP: located on pGGA_BdML1-like3_Bradi3g14500
priDZ123	acgtctacgtaggcgcgccaACGCCATGCCAAATAGGATC	Gibson: BdPOLARprom_fwd (pIPKb_BdPOLARp_TAN1_mCitrine)
priDZ124	tcgcgaccatTTGGTGACGATGGATGATG	Gibson: BdPOLARprom_rev (pIPKb_BdPOLARp_TAN1_mCitrine)
priDZ125	tcgtcaccaaATGGTCGCGAGGAGCCCC	Gibson: BdTAN1_fwd (pIPKb_BdPOLARp_TAN1_mCitrine)
priDZ126	tgctcaccatAGATGATATTCTGCTTGAGACCGTCCG	Gibson: BdTAN1_rev
priDZ127	aatatcatctATGGTGAGCAAGGGCGAG	Gibson: mCitrine_fwd
priDZ128	gggaaattcgagctccaccgCTACTTGTACAGCTCGTCCATG	Gibson: mCitrine_rev
priDZ129	acgtctacgtaggcgcgccaGGCTCTCTCTCTCTCTCC	Gibson: BdML3pro_fwd (pIPKb_BdML3p_TAN1_mCitrine)
priDZ130	tcgcgaccatTGTATTTGGCCCGATCGATC	Gibson: BdML3pro_rev (pIPKb_BdML3p_TAN1_mCitrine)
priDZ131	gccaaatacaATGGTCGCGAGGAGCCCC	Gibson: BdTAN1_fwd (pIPKb_BdML3p_TAN1_mCitrine)
priDZ132	ACTTGGTACCGAAAGAGCTTCGCGG	BdPOLAR-gR1-OsU6-F (guide 1) used in GRF4–GIF1 system
priDZ133	ACTTGGCGCCTCCGGAGCAGTACCG	BdPOLAR-gR2-OsU6-F (guide 2) used in GRF4–GIF1 system
priDZ134	ACTTGGCTGCTATCCAAGGGCGCGG	BdPOLAR-gR3-OsU6-F (guide 4) used in GRF4–GIF1 system
priDZ135	ACTTGGCTGCTGTCCAAGAGCGCCG	BdPOLAR-LIKE-gR1-OsU6-F (guide 1) used in GRF4–GIF1 system
priDZ136	ACTTGGGATGGATGCATGCATACCG	BdPOLAR- LIKE -gR2-OsU6-F (guide 2) used in GRF4–GIF1

		system
priDZ137	CCAGGATACAGTTCAAGCCC	FP: located on BdTAN1
priDZ138	ACACACGGTTTGCTGACATA	RP: located on BdTAN1
priDZ139	TCTCTTAGGTTTACCCGCCA	FP-pIPKb001t
priDZ140	TTTATCCTAGTTTGCGCGCT	RP-pIPKb001t
priDZ141	CGAATCCCCCATCTGAACTG	FP: located on BdTAN1
priDZ142	GGAACTGTATCGGATCGAGC	RP: located on BdTAN1
priDZ143	AACAGGTCTCAGGAGCTGCCCGCCGAGTCCC	FP：Amplify BdPOLAR-LIKE mutate BsaI
priDZ144	AACAGGTCTCACTCCGGCGCGGGCCTCTCGA	RP：Amplify BdPOLAR-LIKE mutate BsaI
priDZ145	TGGAGCTGCAGGCGGCGCTGGACGGCC	NaN2048 dCAPs-FP（PstI）used with priDZ110-241bp,cut mutant into 31bp and 210bp
priDZ146	ACTCGTCGCGGCGGTGGGAGACAA	NaN2069 dCAPs-RP（HindIII）used with priDZ107-272bp,cut wt into 23bp and 249bp
priDZ147	TCACCAATGGCGACCGAGA	FP: genotyping *polar-1* (+T)
priDZ148	GCACGTACCGAAAGAGCTT	RP: genotyping *polar-1* (+T)
priDZ149	ATTTAGCCCTCCCTCTGTGT	FP: genotyping NaN1917
priDZ150	GAGGAAGTTGAGCGAGATGG	RP: genotyping NaN1917
priDZ151	gggaaattcgagctccaccgTTACACACATTGCACTTCCG	Gibson:BdPOLARter_rev (pIPKb_BdPOLARgenomic)
priDZ152	GGTCTTAATTCGGCTGTCGT	FP: located on BdPOLAR terminator
priDZ153	AGCCATGCCTTCCTTTCAAA	FP: located on BdPOLAR terminator
priDZ154	TGAAATGAAAGAGGGGTGCC	RP: located on BdPOLAR-LIKE promoter
priDZ155	CGTCCATCTCGCCATTTACA	FP: located on BdPOLAR promoter
priKJ01	ACTTGCTCAAGGAGCTCTGCCGCG	BdBZR1-gR1-OsU6-F(guide 2)
priKJ02	AAACCGCGGCAGAGCTCCTTGAGC	BdBZR1-gR1-OsU6-F(guide 2)
priKJ03	ACTTGCCCAAGATCCAGAAGCAGGG	BdBZR1-gR1-OsU6-F(guide 5)
priKJ04	AAACCCCTGCTTCTGGATCTTGGGC	BdBZR1-gR1-OsU6-F(guide 5)
priKJ05	ACTTGCTCCCGCCCGCGCTCTACG	BdDET2-gR1-OsU6-F(guide 2)
priKJ06	AAACCGTAGAGCGCGGGCGGGAGC	BdDET2-gR1-OsU6-F(guide 2)
priKJ07	ACTTGGGCGGGTACAAGATCCCCA	BdDET2-gR1-OsU6-F(guide 1)
priKJ08	AAACTGGGGATCTTGTACCCGCCC	BdDET2-gR1-OsU6-F(guide 1)
priMR343	GGCAGCGATGCGTGCCGCTCCCCG	FP: BdPOLAR-gR3-OsU6 (guide 3)
priMR344	AAACCGGGGAGCGGCACGCATCGC	FP: BdPOLAR-gR3-OsU6 (guide 3)

Appendix

1. Csy4-type System

1.1 Design primers for each gRNA:

1.1.1 Get the *Brachypodium* number of the gene you want to mutate

1.1.2 Go to http://crispr.hzau.edu.cn/cgi-bin/CRISPR2/CRISPR

1.1.3 Change target genome to "Brachypodium distachyon"

1.1.4 Enter Brachypodium gene number in locus tag

1.1.5 Hit submit, wait until it shows a list of possible guides

- take guides in exon
- take guides early in gene
- with little off-targets (high on-target score)
- Assemble type IIS sites, gRNA repeat sequences with your gRNA spacers (Please follow the design protocol in the supplemental data of (Čermák, Curtin et al. 2017).

1.2 Set up a PCR reaction for each gRNA using Q5 polymerase. Use the target cloning vector (pMOD_B2103) as template. Here is the example for *BdPOLAR* 2 gRNA spacers cloning:

Assembly of *BdPOLAR* 2 gRNA spacers:

-reaction #1: promoter specific primer (priDZ8) + CSY_ gRNA1 (priDZ9) ~500bp

-reaction #2: REP_gRNA1 (priDZ10) + CSY_ gRNA2 (priDZ11) ~136bp

-reaction #3: REP_gRNA2 (priDZ12) + CSY_ term (priDZ13) ~136bp

Q5 PCR reaction setup and thermocycling conditions

Component	50 µl reaction	Temperature	Time	Number of cycles
5XQ5 reaction buffer	10 µl	98 ºC	30 s	
10 mM dNTPs	1 µl	98ºC	10 s	
10 µM forward primer	2.5 µl	60 ºC	15 s	30
10 µM reverse primer	2.5 µl	72 ºC	15 s	
pMOD_B2103 (~10ng)	0.5 µl	72 ºC	2 min	
Q5 high-fidelity DNA Polymerase	0.5 µl	16 ºC	hold	
Nuclease-free water	33 µl			

Note: A. priDZ8 and priDZ13 are common primers for CmYLCV promoter amplification. Other primers are specific guides sequences for your gene.

B. Dilute pMOD_B2103 with water if the concentration is too high for PCR.

C. Assembly of 6 gRNA could be done by this protocol.

1.3 Run 5ul PCR products in a gel, and do PCR products purification for left 45ul if get right bands.

1.4 Nanodrop purified PCR products.

1.5 Set up a Golden Gate reaction:

Golden Gate setup and thermocycling conditions

Component	20 µl reaction	Temperature	Time	Number of cycles
POLAR reaction1(1-5ng)	a µl	37 ºC	5 min	10
POLAR reaction2 (1-5ng)	b µl	25 ºC	10 min	
POLAR reaction3 (1-5ng)	c µl	16 ºC	hold	
pMODB2103(~50ng)	1.5 µl			
SapI	0.5 µl			
BsaI(NEB)/Eco31I(Theromo)	0.5 µl			
T4 DNA ligase	1 µl			
10XT4 DNA ligase buffer	2 µl			
Nuclease-free water	To 20 µl			

Note: A. Dilute purified PCR products if necessary to make the pipette precisely.

B. SapI enzyme has to be mixed by pipetting up and down several times before adding to the reaction.

C. T4 DNA ligase buffer could be replaced by Tango buffer (for SapI) if BsaI (NEB) is used here, while the efficiency is the same after testing.

1.6 Transform 5 ul of the Golden Gate reaction into NEB DH5a and plate on LB (+ 50 mg/l Ampicillin). Grow O/N in 37 ºC chamber.

1.7 Screen 5-10 colonies with primers TC320 (priDZ28) and TC089R (priDZ29). If 2-3 gRNA spacers are cloned, screening 3-5 colonies should be sufficient to identify correct clones.

Taq PCR reaction setup and thermocycling conditions

Component	25 µl reaction	Temperature	Time	Number of cycles
10XStandard Taq reaction buffer	2.5 µl	95 ºC	5 min	
10 mM dNTPs	0.5 µl	95 ºC	30 s	
10 µM TC320	0.5 µl	52 ºC	20 s	30
10 µM TC089R	0.5 µl	68 ºC	1 min/kb	
colony	Variable	68 ºC	5 min	
Taq DNA Polymerase	0.125 µl	16 ºC	hold	
Nuclease-free water	To 25 µl			

1.8 Pick colonies and grow in liquid LB (+ 50 mg/l Ampicillin) O/N.

1.9 Mini-Prep and Digestion confirm by AarI.

AarI digestion setup

Component	20 µl reaction	Temperature	Time
AarI (Thermo Fisher Scientific #ER1581)	0.5 µl	37 ºC	1 h
10X Buffer AarI	2 µl		
Plasmids	5 µl		
50Xoligonucleotide	0.4 µl		
Nuclease-free water	12.1µl		

1.10 Send a correctly digested clone for sequencing (primer: TC320 or TC089R).

1.11 Glycerol stock for pMODB2103_your gene in *E.coli*.

1.12 Set up a Golden Gate reaction:

Golden Gate setup and thermocycling conditions

Component	20 µl reaction	Temperature	Time	Number of cycles
pMOD_A1510 (300ng)	a µl	37 ºC	5 min	50
pMOD_B2103-your gene guides (300ng)	b µl	16 ºC	5 min	
		37 ºC	15 min	
pMOD_C000 (300ng)	c µl	80 ºC	5 min	
pTRANS_250D (150ng)	d µl	16 ºC	hold	
AarI	0.5 µl			
50Xoligonucleotide	0.4 µl			
10X Buffer AarI	2 µl			
T4 DNA ligase	0.5 µl			
ATP	2 µl			
Nuclease-free water	To 20 µl			

Note: The above is the standard amount for each module, you could also calculate the more accurate amount based on your plasmids' concentrations and lengths.
pMODA insert is 7075bp - total plasmid 9000 (80% insert)
pModB insert is 947bp - total plasmid 3500 (30% insert)
pModC insert is 102bp - total plasmid 2100 (5% insert)
pTRANS250D backbone is 9900bp - total plasmid 2100 (86% insert)
If this don't work, calculate the amounts based on molar ratio (backbone vector: inserted vector=1:3) will be helpful.

1.13 Transform 10ul of the Golden Gate reaction into NEB DH5a and plate on LB (50 mg/l Kanamycin). Grow O/N in 37 ºC chamber.

1.14 Correct clones can be identified by PCR on 2-3 colonies, using primers TC320(priDZ28)/M13F(priDZ33) and TC430(priDZ34)/TC089R(priDZ29) for colony PCR separately.

1.15 Digestion confirmed by XhoI.

1.16 Isolate the plasmid DNA for one correct clone and send for sequencing (primer: M13F and TC430).

1.17 Glycerol stock for pTRANS250D_your gene in *E.coli*.

1.18 Agrobacterium transformation into *AGL1*.

1.19 Glycerol stock for pTRANS250D_your gene in *AGL1*.

2. GRF–GIF System

2.1 gRNA oligo synthesis

Follow the first step in Csy4-type system protocol

F: ACTTGXXXXXXXXXXXXXXXXXXX

R: AAACXXXXXXXXXXXXXXXXXXC

2.2 Phosphorylate the oligos

Oligo phosphorylation and annealing

Component	20 µl reaction
100µM sense gRNA	3 µl
100µM antisense gRNA	3 µl
T4 DNA ligase buffer (contains ATP)	3 µl
T4 PNK	2 µl
Nuclease-free water	19 µl

Set up PCR machine to:
Incubate 1 hour at 37°C, then 95°C for 5min, ramping down to 85°C at -2°C/second, sequentially ramping down to 25°C at 1°C/second. Hold at 16°C.

2.3 Digest and dephosphorylate JD633_CRISPRhigheff

AarI digestion setup

Component	20 µl reaction	Temperature	Time
AarI	2 µl	37 ºC	Overnight
10X Buffer AarI	2 µl		
JD633_CRISPRhigheff	3.6 µl		
50Xoligonucleotide	0.4 µl		
Nuclease-free water	12 µl		

2.3.1 Heat kills the enzyme: 65ºC for 20 min.

2.3.2 Dephosphorylate digested JD633_CRISPRhigheff:

-Add 2µl Antarctic Phosphatase buffer and 1µl Antarctic Phosphatase;

Incubate at 37 ºC for 30 min;

-Heat inactivate the Antarctic Phosphatase: 80 ºC for 2 min.

2.4 Ligate annealed oligos into digested and dephosphorylated JD633_CRISPRhigheff

Ligation setup

Component	10 µl reaction	Temperature	Time
JD633_CRISPRhigheff (150ng)	1 µl	16 ºC	Overnight
8X diluted annealed oligo	1 µl		
10XT4 DNA ligase buffer	1 µl		
T4 DNA ligase	1 µl		
Nuclease-free water	6 µl		

2.5 Transformation of ligation products into NEB DH5a and plate on LB (50 mg/l Kanamycin). Grow O/N in 37 ºC chamber.

2.6 Colony PCR using M13F and your gRNA Fowerd primer.

2.7 Isolate the plasmid DNA for one correct clone and sequence using M13F.

2.8 Glycerol stock for JD633__your gene in *E.coli*.

2.9 Agrobacterium transformation into *AGL1*.

2.10 Glycerol stock for JD633__your gene in *AGL1*.

3. PEG Purification of PCR Products

3.1 Add a 1:1 volume of PEG to the PCR product, for example into the reaction tube.

3.2 Vortex briefly.

3.3 Warm at 37 ºC for 30 mins.

3.4 Microcentrifuge for 15 mins at maximum rpm.

3.5 Pipette off supernatant.

3.6 Wash pellets with excess 150 µl 80% cold ethanol.

3.7 Spin for 10 mins at maximum rpm.

3.8 Pipette off ethanol.

3.9 Dry down at 60 ºC for 30 mins.

3.10 Microcentrifuge for 15 mins at maximum rpm.

3.11 Pipette off supernatant.

3.12 Re-suspend in 12 µl of nuclease-free water.

Ingredients for PEG solution: Add 3 gram PEG 8000 and 2.19 gram NaCl to 15 ml nuclease-free water. This solution lasts for at least 30 days at 4 ºC.

4. Supplemental Figures

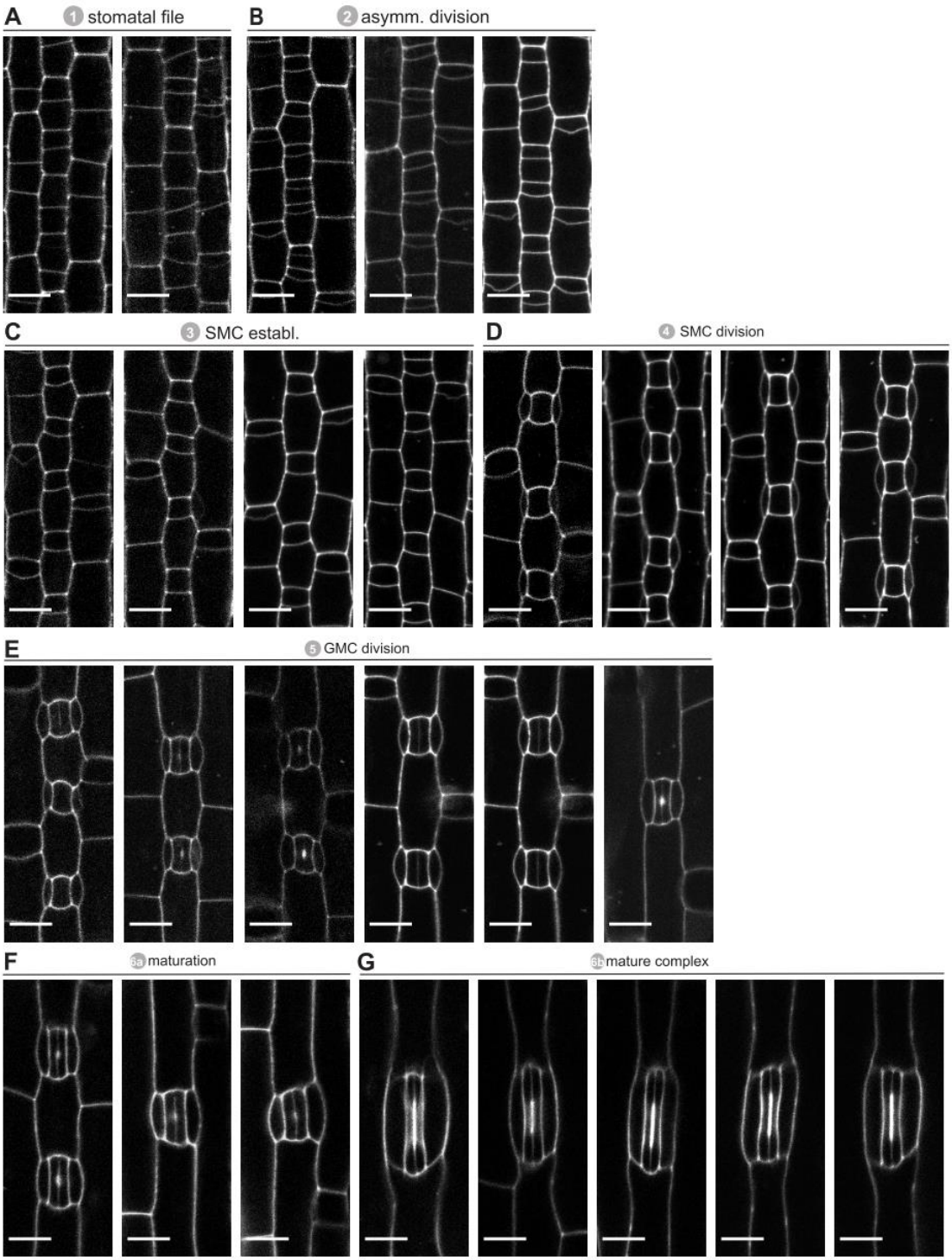

Figure S1. Single confocal plane images of the epidermis throughout stomatal development in WT.
PI-stained developing epidermis showing all stomata developmental stages in WT. Scale bars, 10 µm.

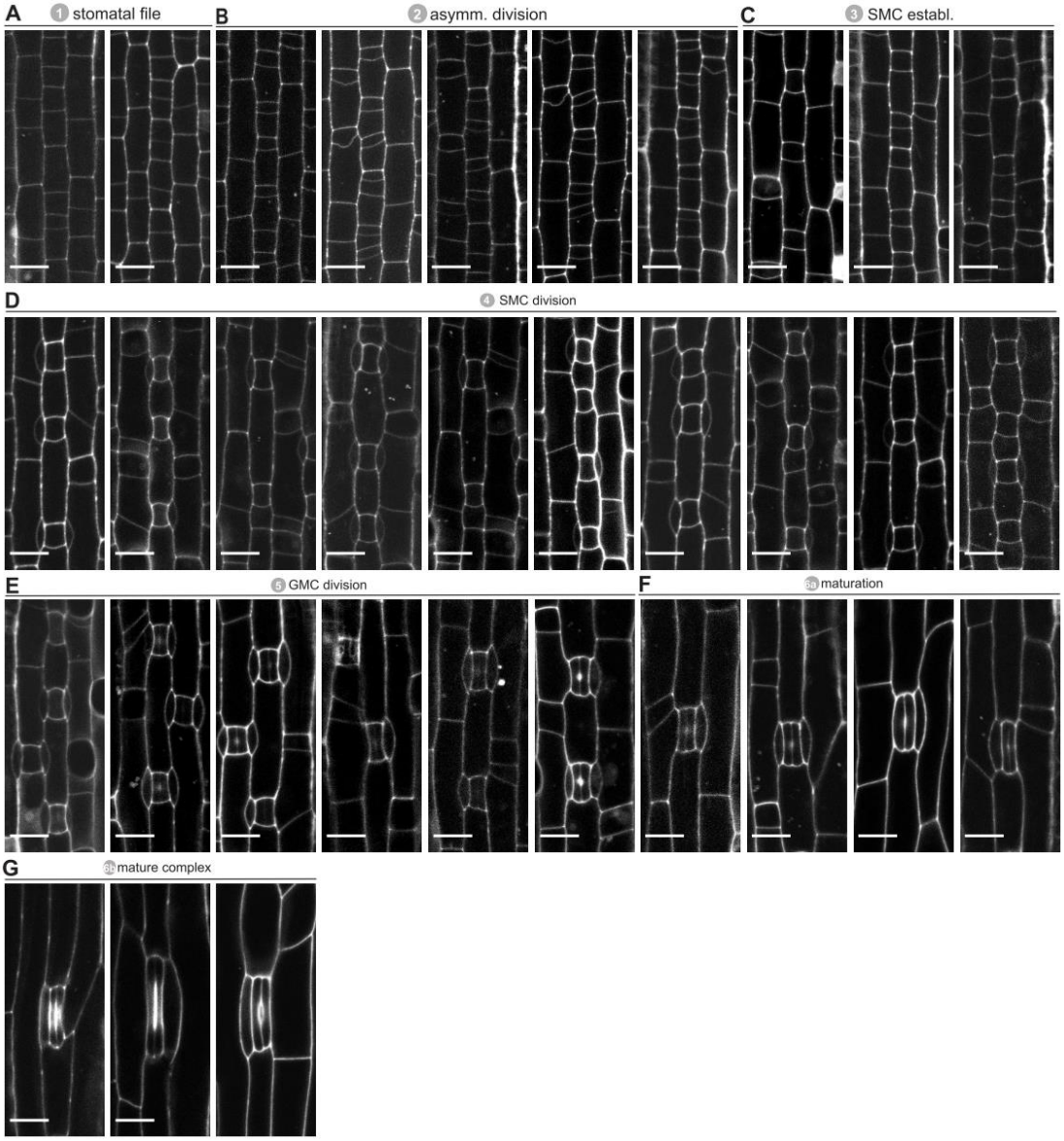

Figure S2. Single confocal plane images of the epidermis throughout stomatal development in *bdpolar-1*.

PI-stained developing epidermis showing all stomata developmental stages in *bdpolar-1*. Scale bars, 10 µm.

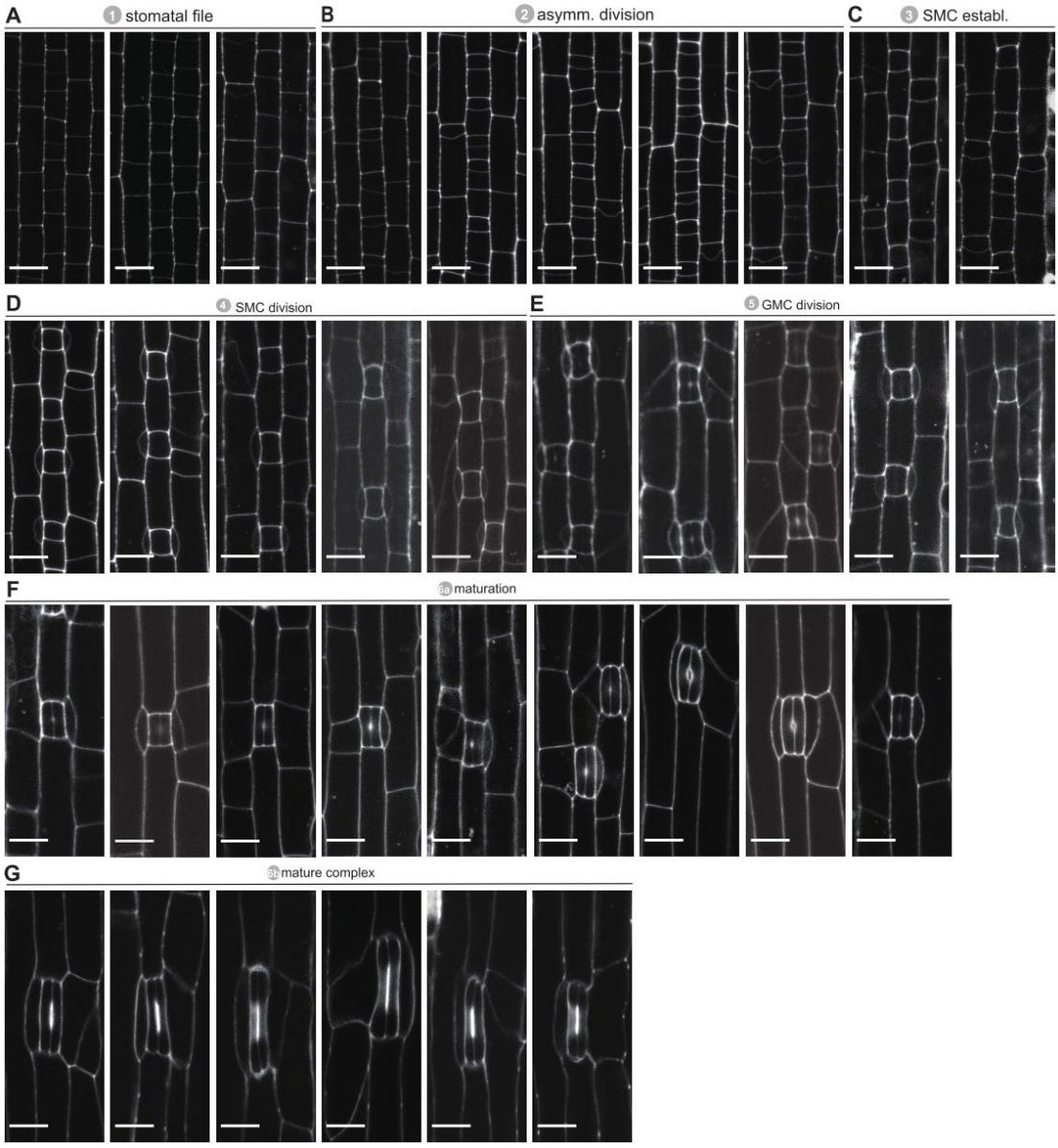

Figure S3. Single confocal plane images of the epidermis throughout stomatal development in *bdpan1-1*.

PI-stained developing epidermis showing all stomata developmental stages in *bdpan1-1*. Scale bars, 10 µm.

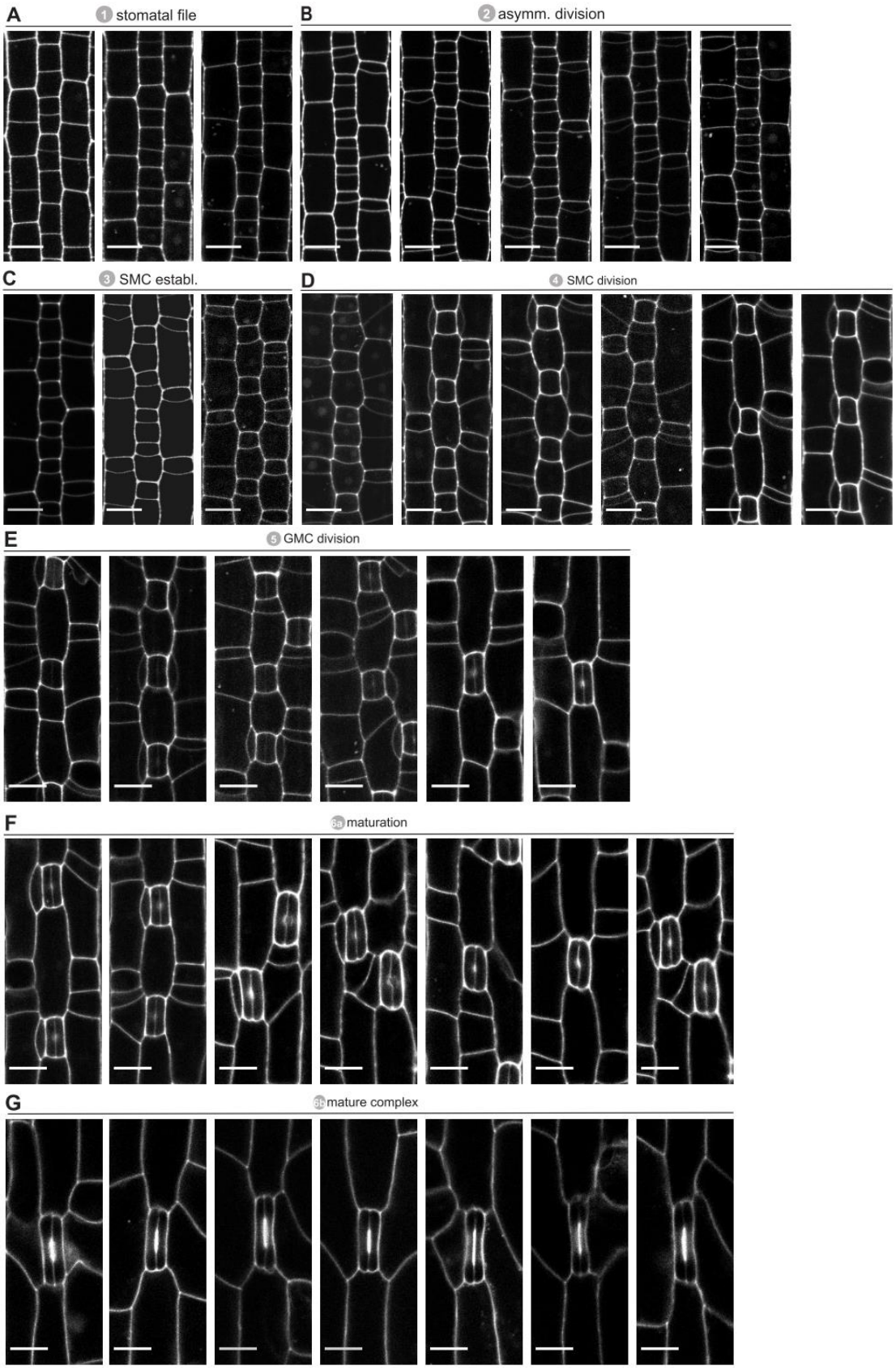

Figure S4. Single confocal plane images of the epidermis throughout stomatal development in *bdpolar-1; bdpan1-1*.

PI-stained developing epidermis showing all stomata developmental stages in *bdpolar-1; bdpan1-1*. Scale bars, 10 µm.

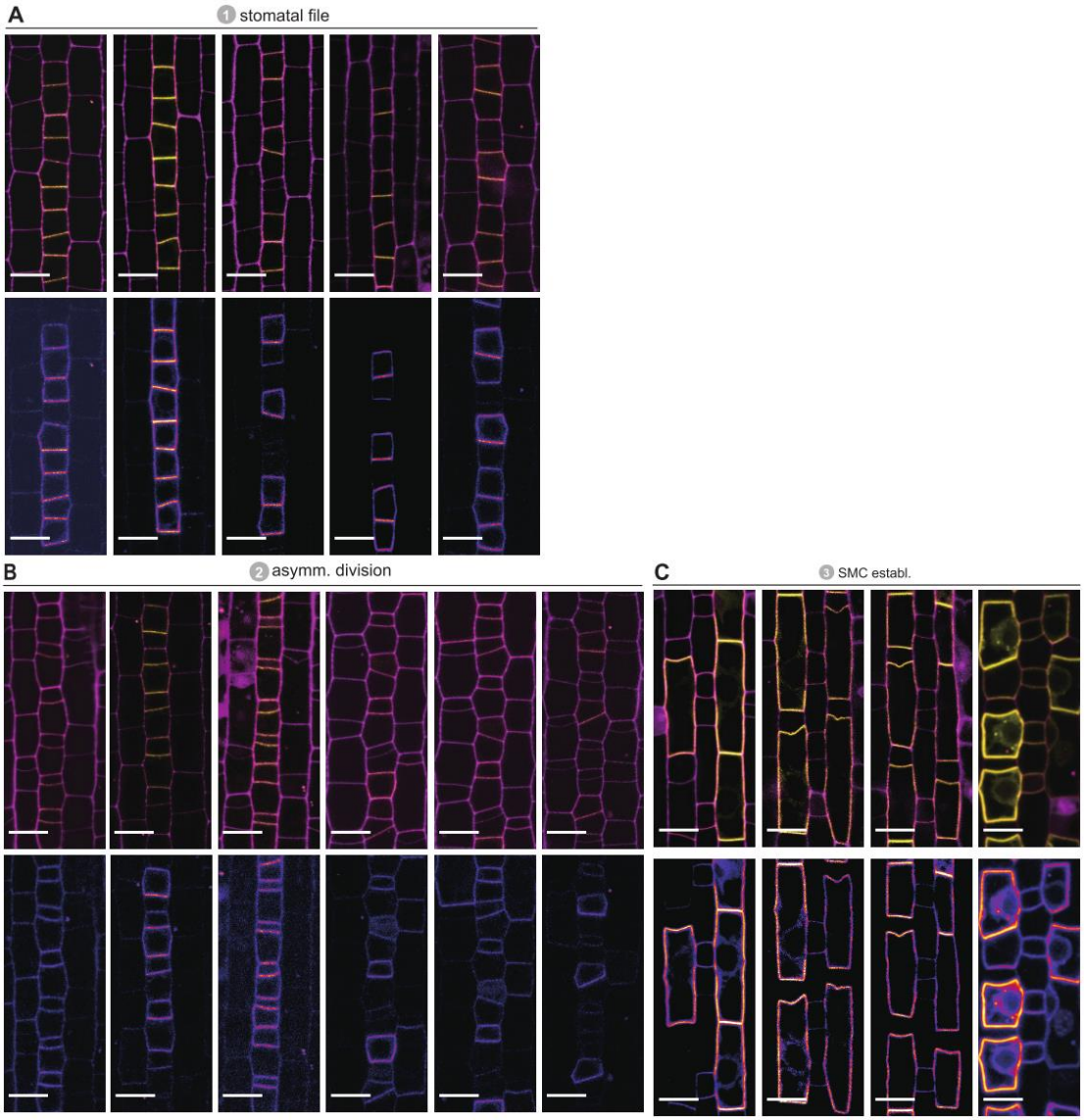
A
1 stomatal file
B
2 asymm. division
C
3 SMC establ.

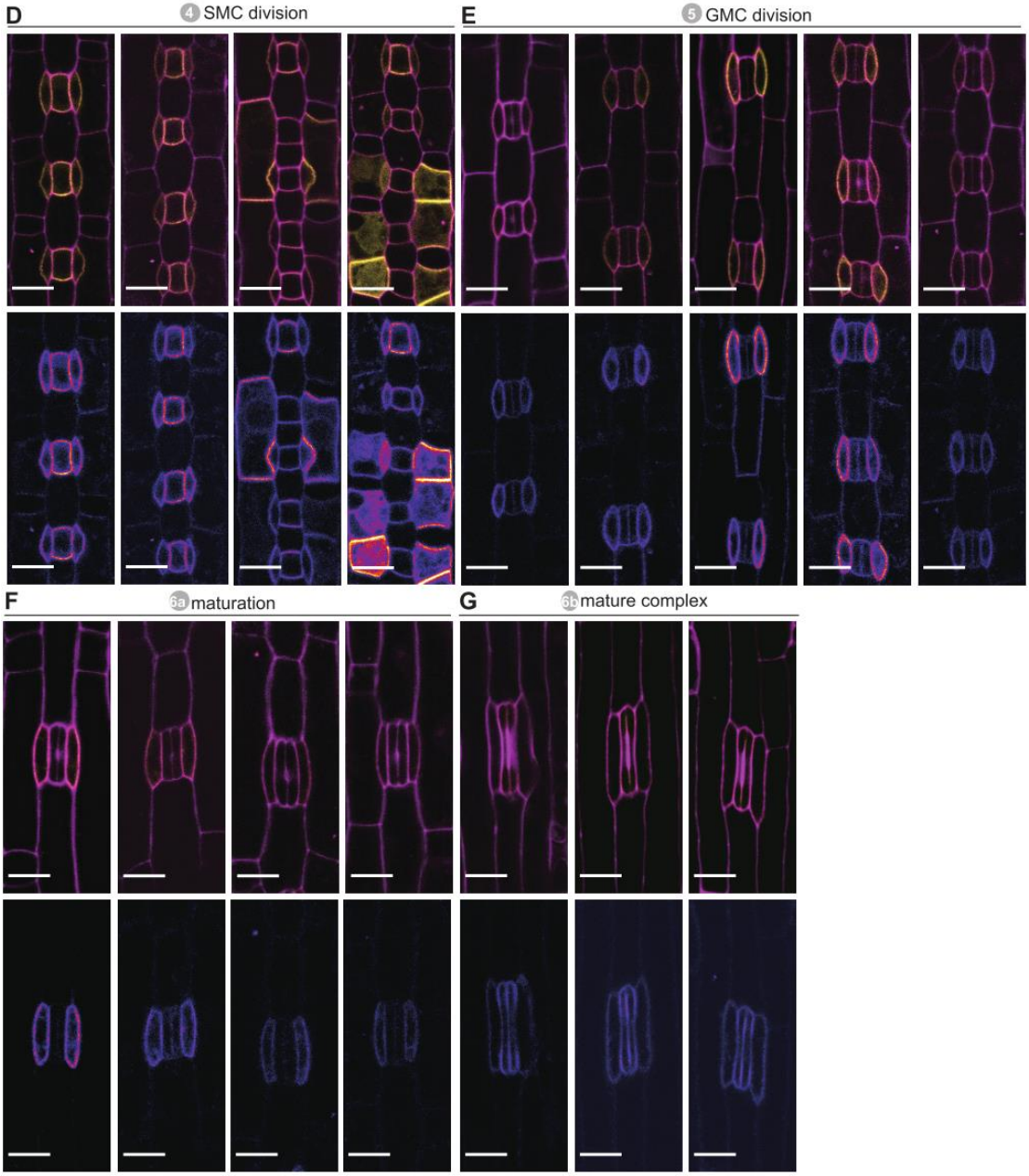

Figure S5. *BdPOLARp:BdPOLAR-mVenus* expression throughout stomatal development in *B. distachyon*.
Composite images (upper) with BdPOLAR-mVenus signal (yellow) and PI-stained cell outlines (magenta); Fluorescence intensity images of mVenus channel only (bottom). All images from the second leaf, 5 to 6 dag. Scale bars, 10 µm.

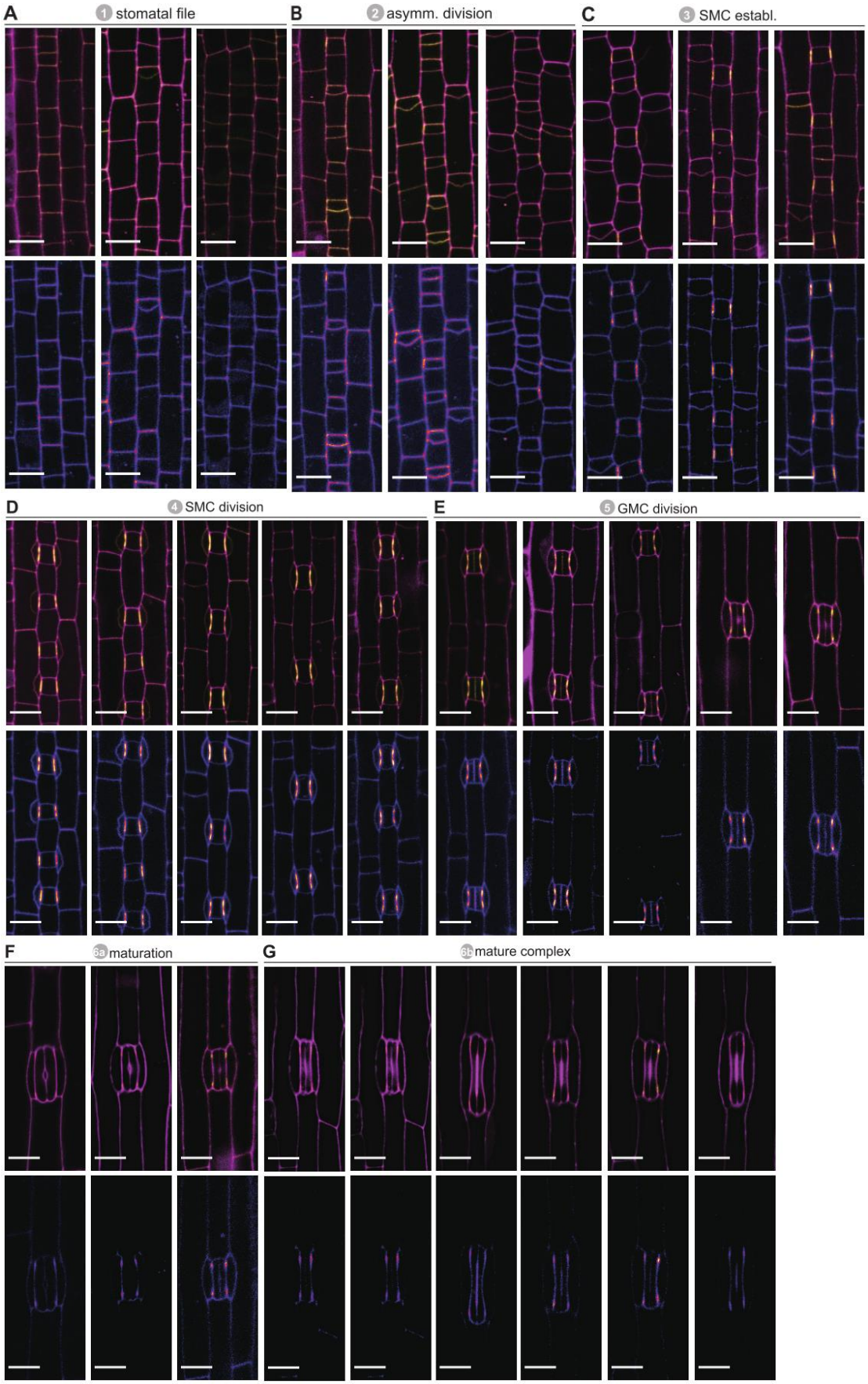

Figure S6. *BdPAN1p:BdPAN1-YFP* expression throughout stomatal development in *B. distachyon*.

Composite images (upper) with BdPAN1-YFP signal (yellow) and PI-stained cell outlines (magenta); Fluorescence intensity images of YFP channel only (bottom). All images from the second leaf, 5 to 6 dag. Scale bars, 10 µm.

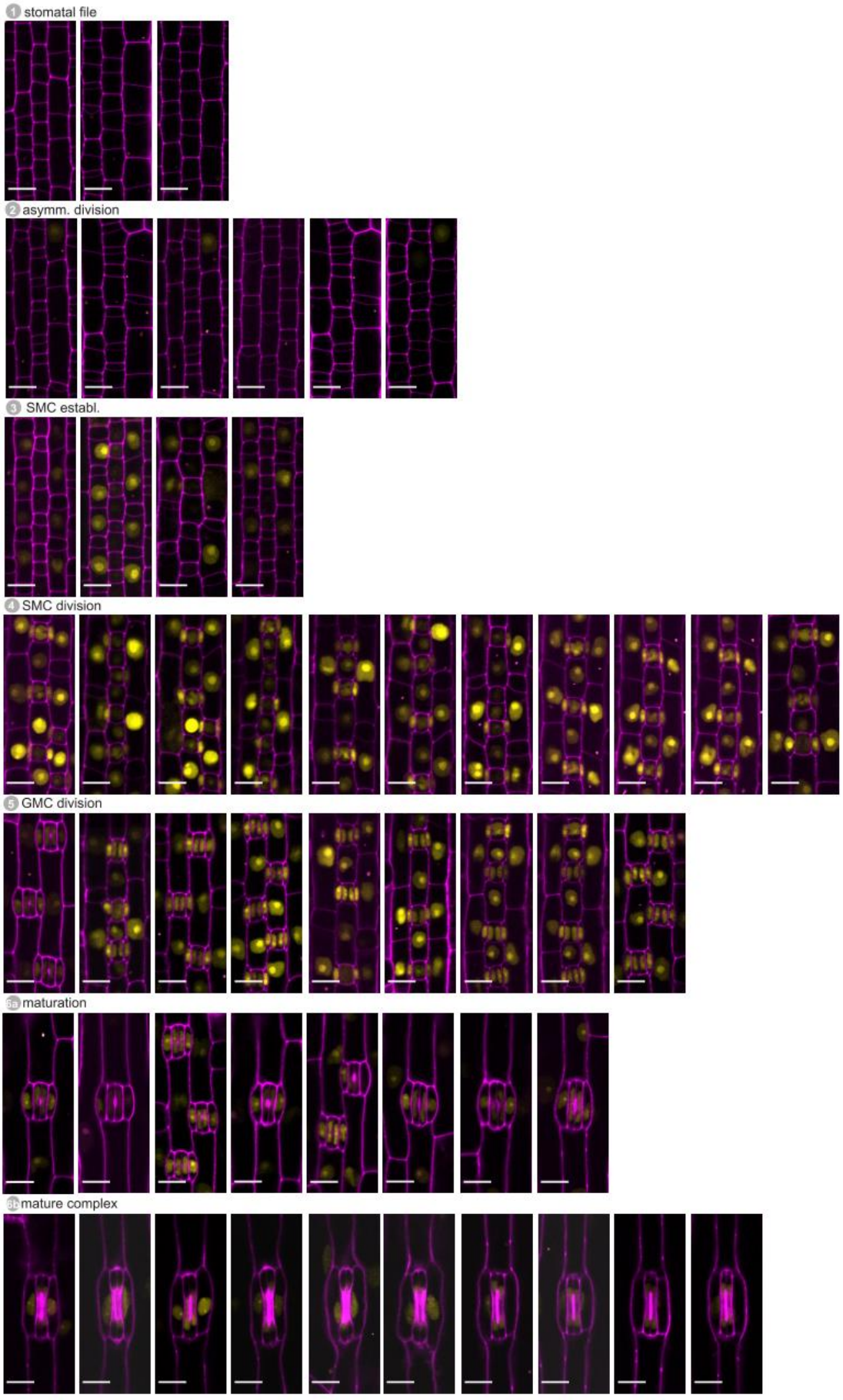
1 stomatal file
2 asymm. division
3 SMC establ.
4 SMC division
5 GMC division
5a maturation
5b mature complex

Figure S7. *BdPOLARp:3XNLS-eGFP* expression throughout stomatal development in *B. distachyon*.
Composite images with *BdPOLARp:3XNLS-eGFP* signal (yellow) and PI-stained cell outlines (magenta). All images from the second leaf, 5 to 6 dag. Scale bars, 10 µm.

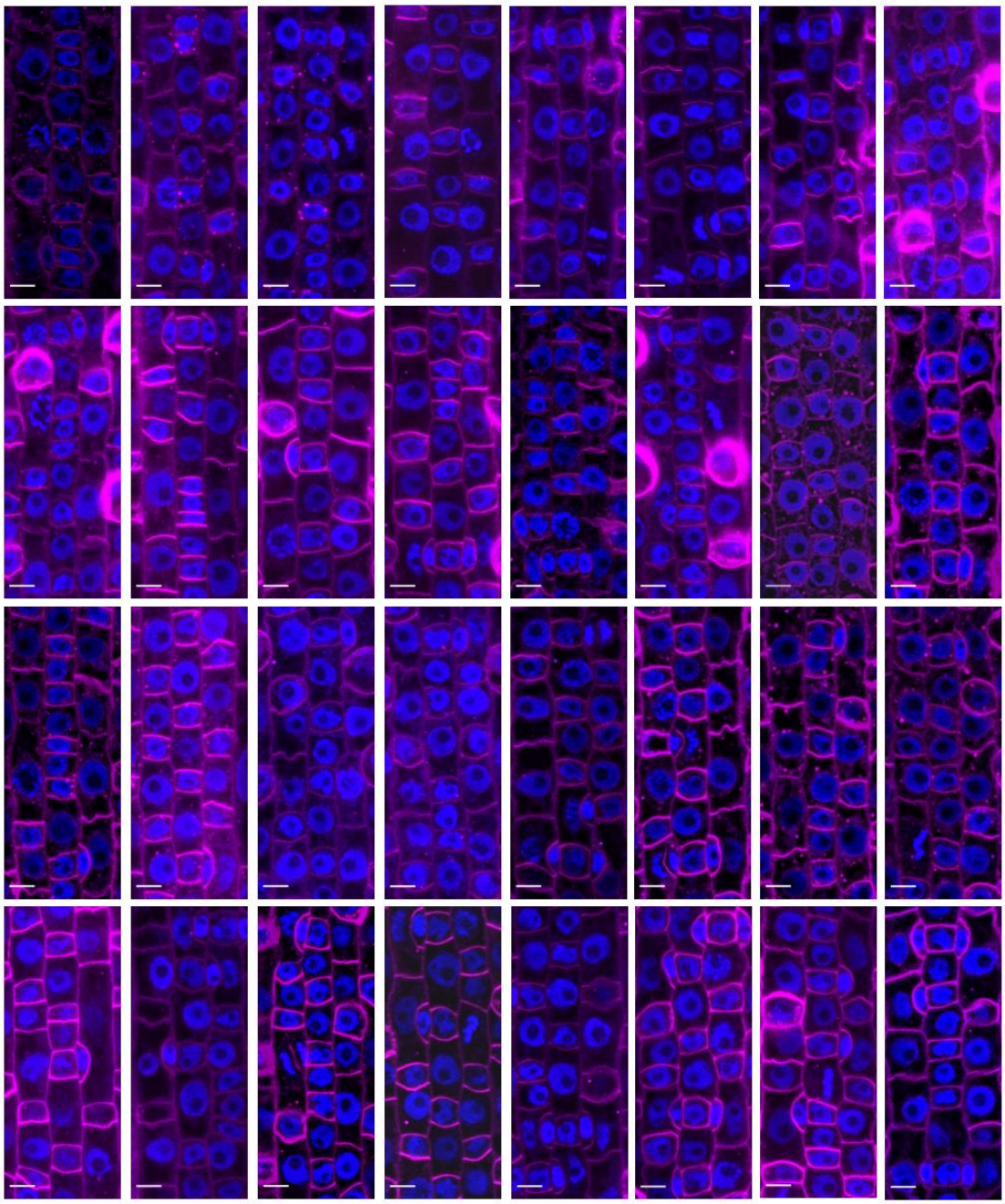

Figure S8. Premitotic nuclear migration in WT.
Single confocal plane images Hoechst-stained nuclei (blue) and Direct Red 23-stained cell outlines (magenta) of stage 3 to stage 4 SMCs in WT. Scale bar, 10 µm.

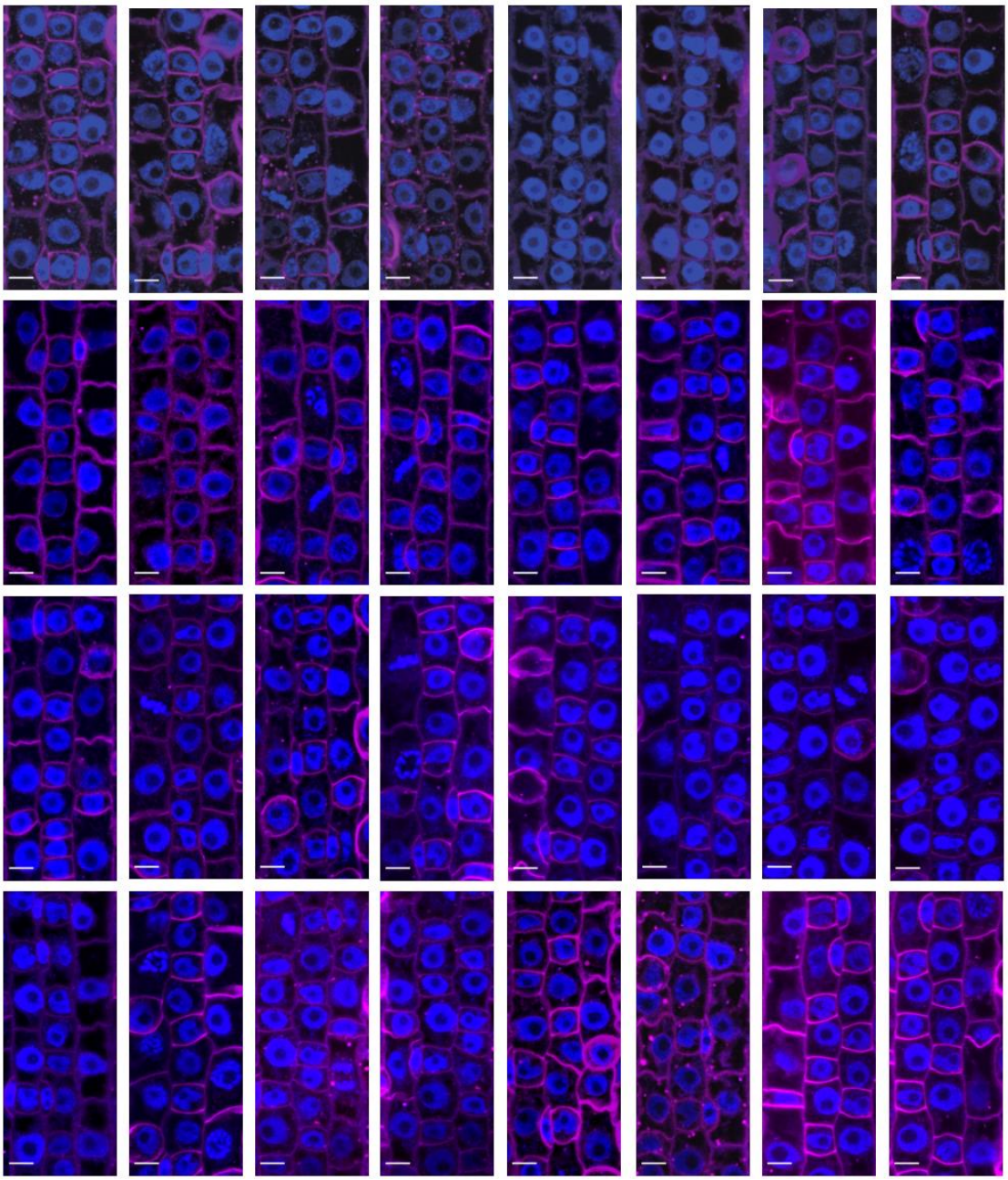

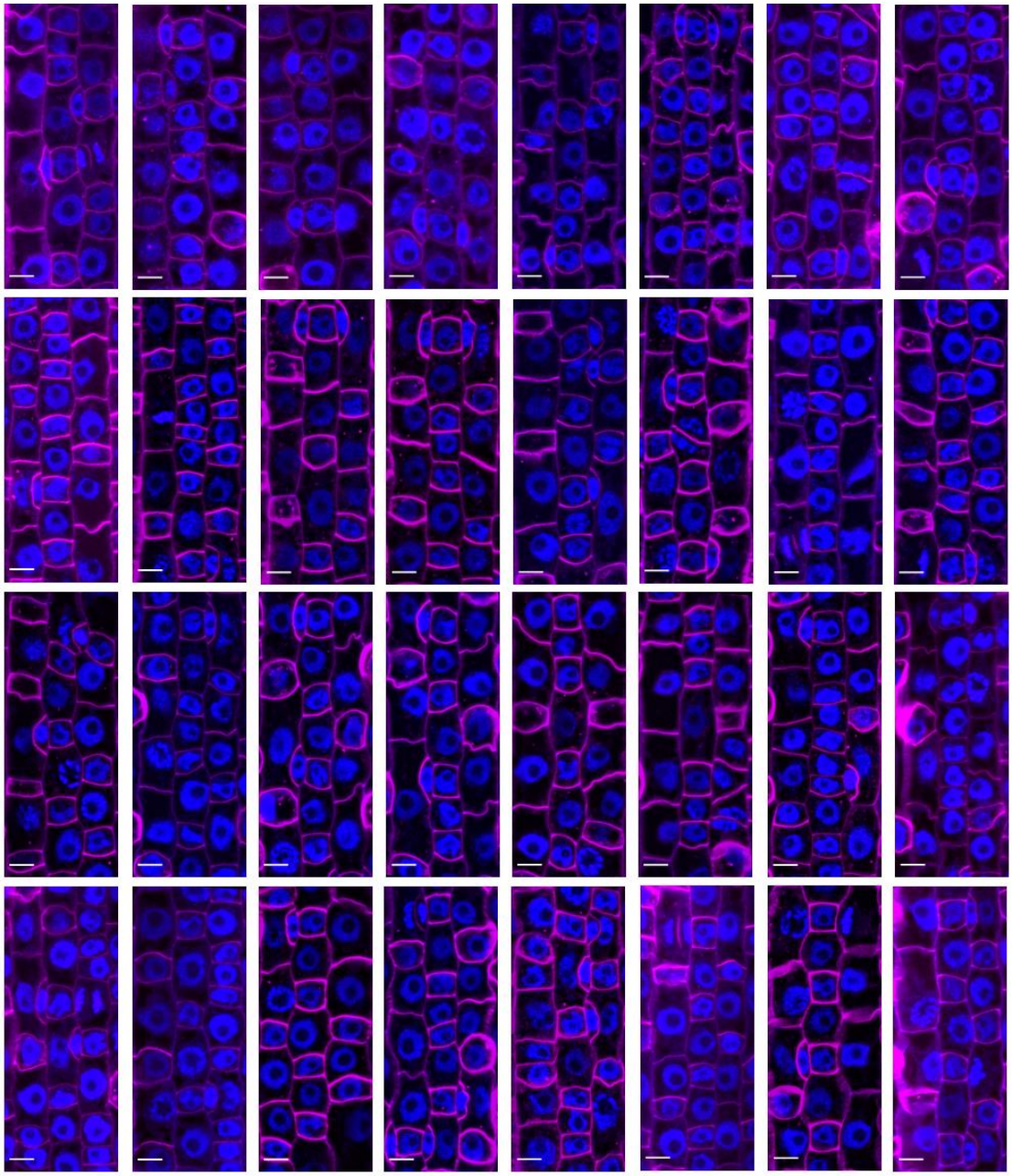

Figure S9. Premitotic nuclear migration in *bdpolar-1*.
Single confocal plane images Hoechst-stained nuclei (blue) and Direct Red 23-stained cell outlines (magenta) of stage 3 to stage 4 SMCs in *bdpolar-1*. Scale bar, 10 µm.

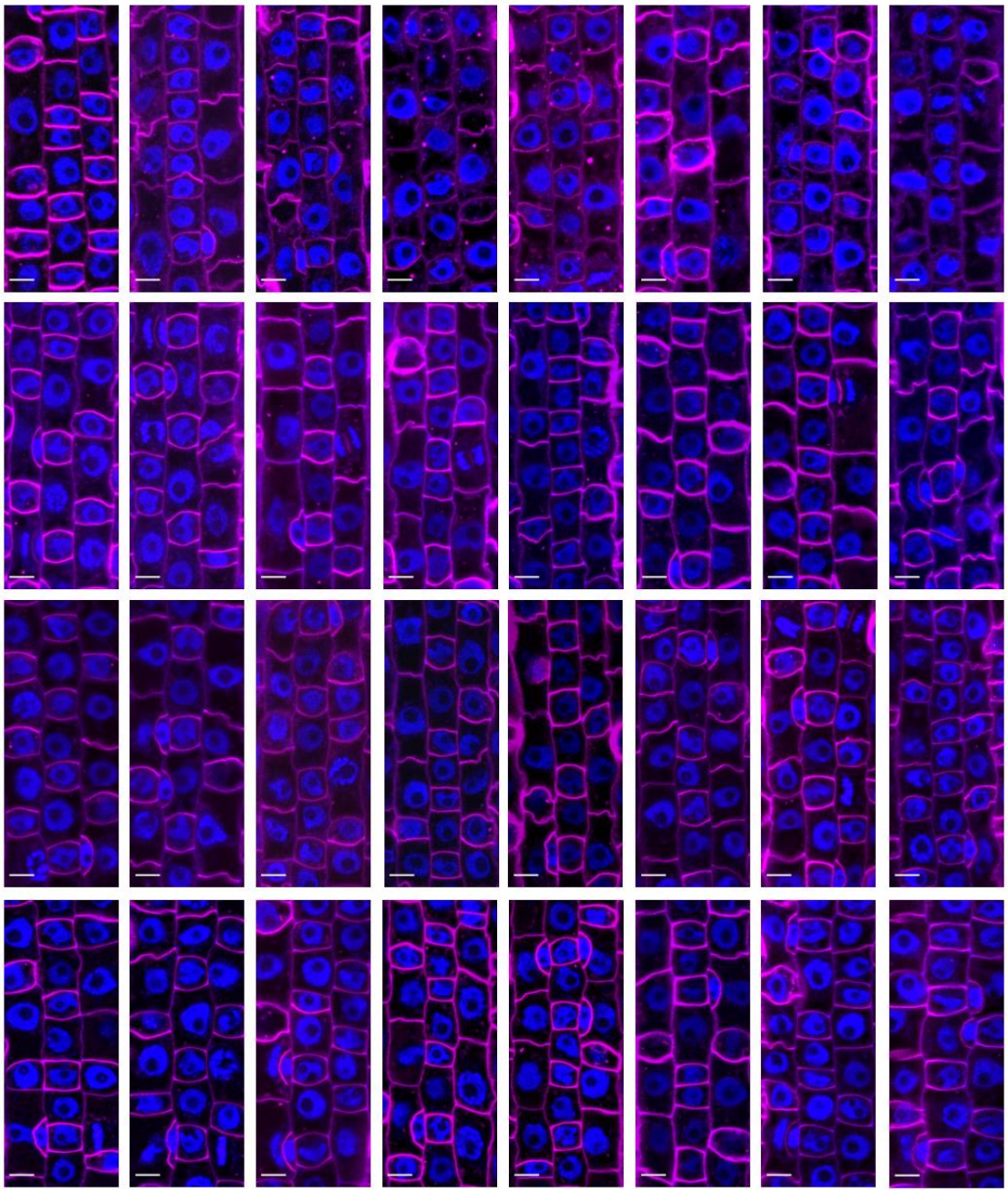

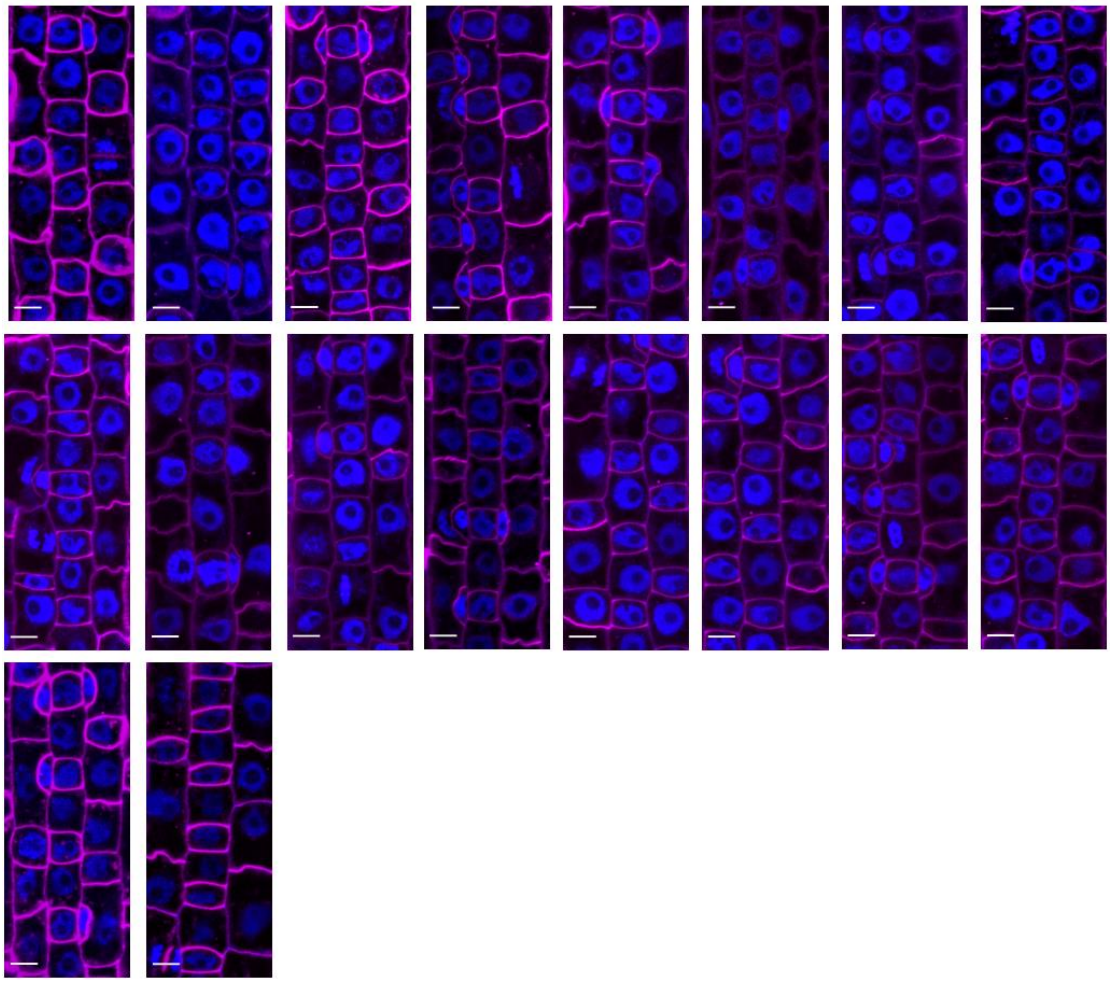

Figure S10. Premitotic nuclear migration in *bdpan1-1*.
Single confocal plane images Hoechst-stained nuclei (blue) and Direct Red 23-stained cell outlines (magenta) of stage 3 to stage 4 SMCs in *bdpan1-1*. Scale bar, 10 µm.

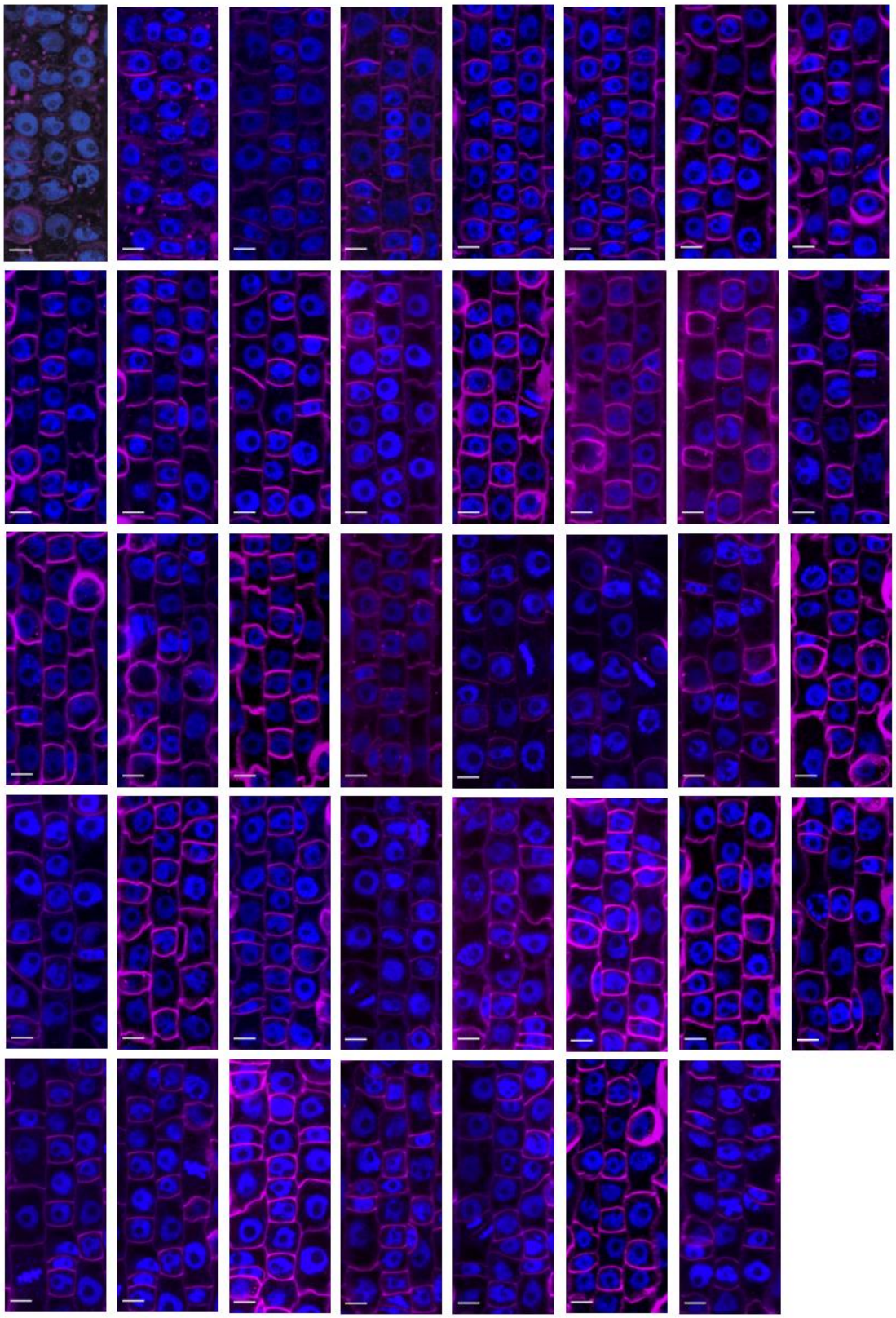

Figure S11. Premitotic nuclear migration in *bdpolar-1;bdpan1-1*.
Single confocal plane images Hoechst-stained nuclei (blue) and Direct Red 23-stained cell outlines (magenta) of stage 3 to stage 4 SMCs in *bdpolar-1;bdpan1-1*. Scale bar, 10 µm.

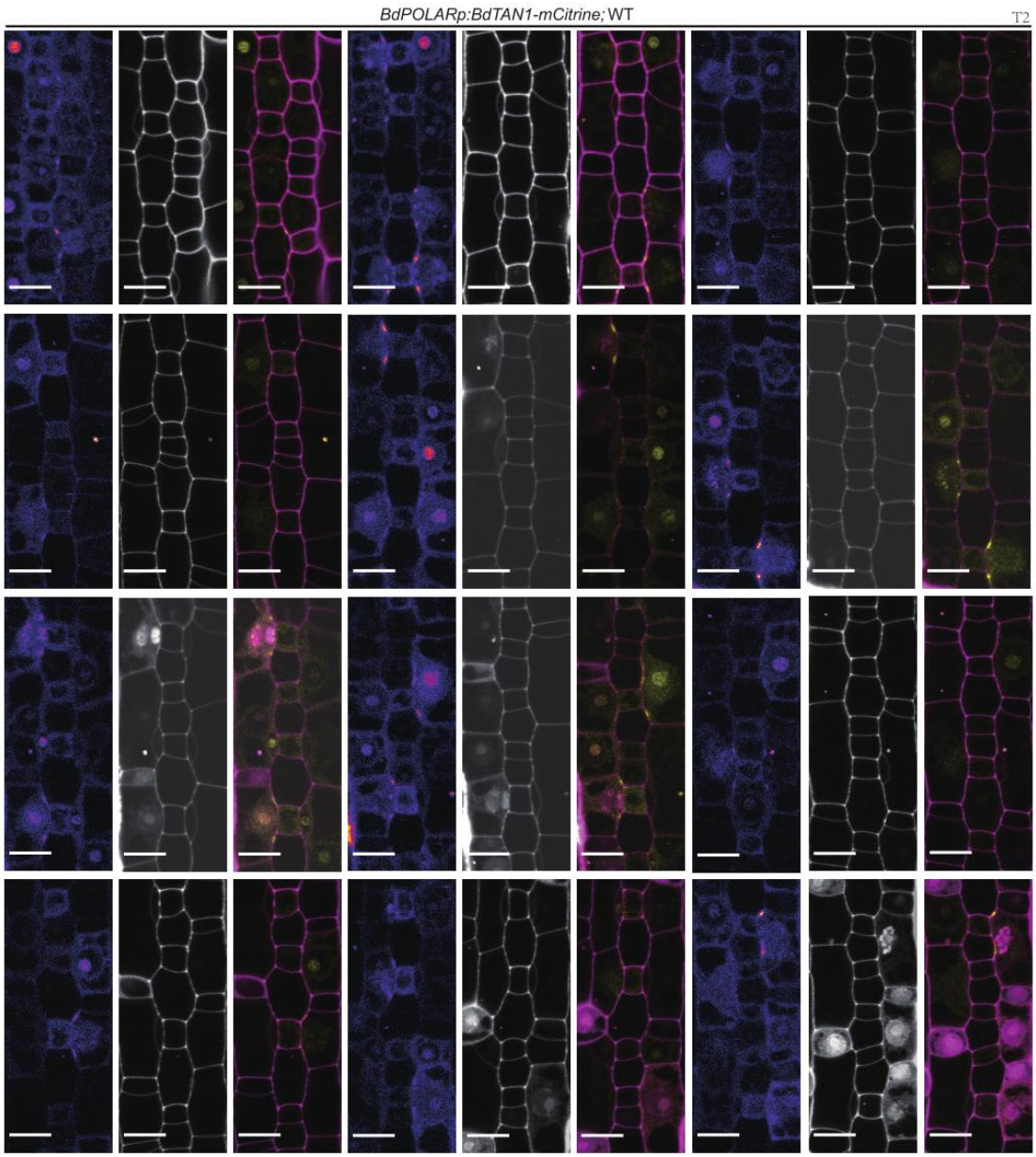
BdPOLARp:BdTAN1-mCitrine; WT
T2

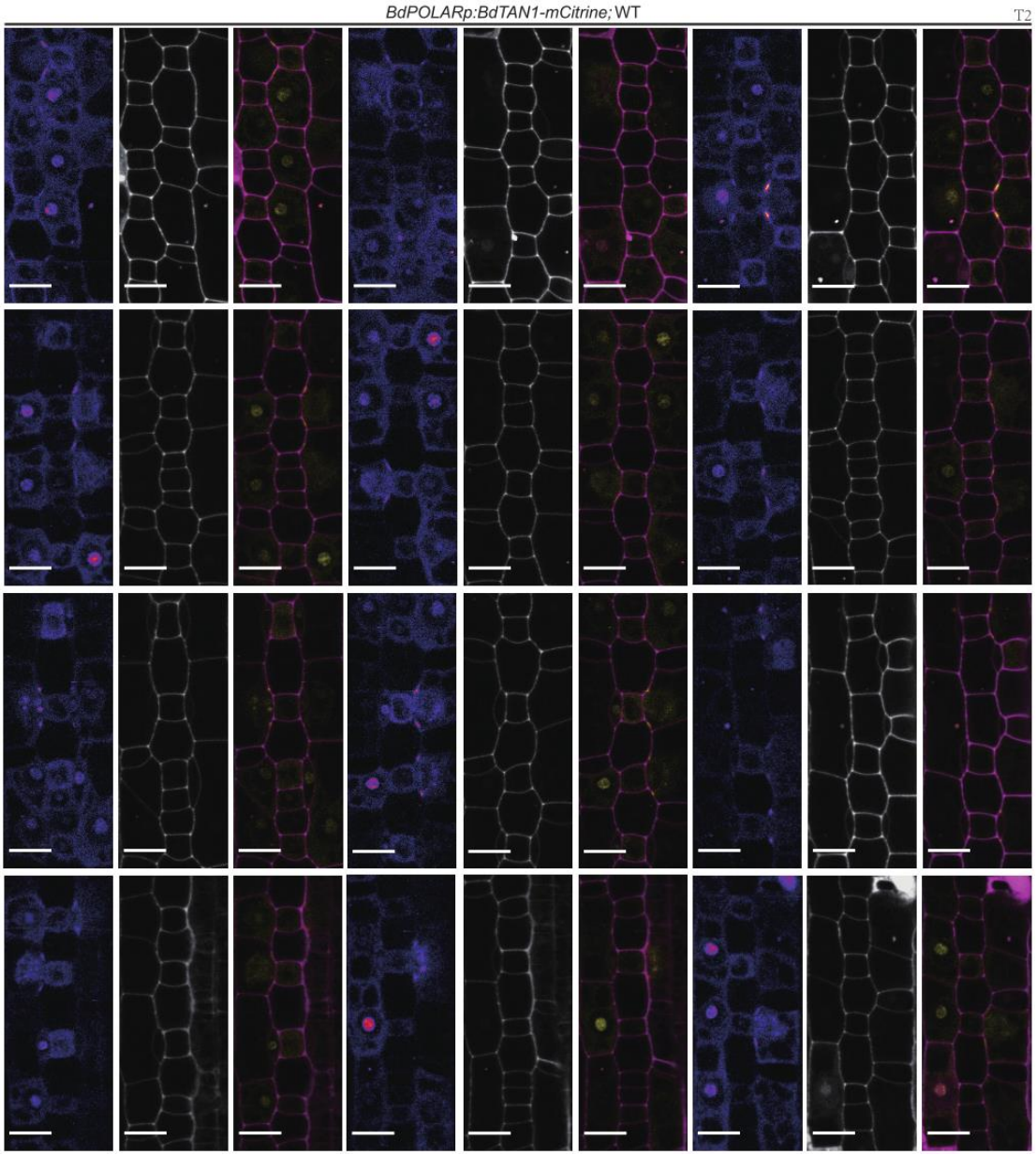

Figure S12. *BdPOLARp:BdTAN1-mCitrine* expression of stage 3 to stage 4 SMCs in WT.

Fluorescence intensity images of mCitrine channel only (left), images of PI-stained cell outlines only (middle), and composite images (right) with BdTAN1-mCitrine signal (yellow) and PI-stained cell outlines (magenta). All images from the second leaf, 5 to 6 dag. Scale bars, 10 µm.

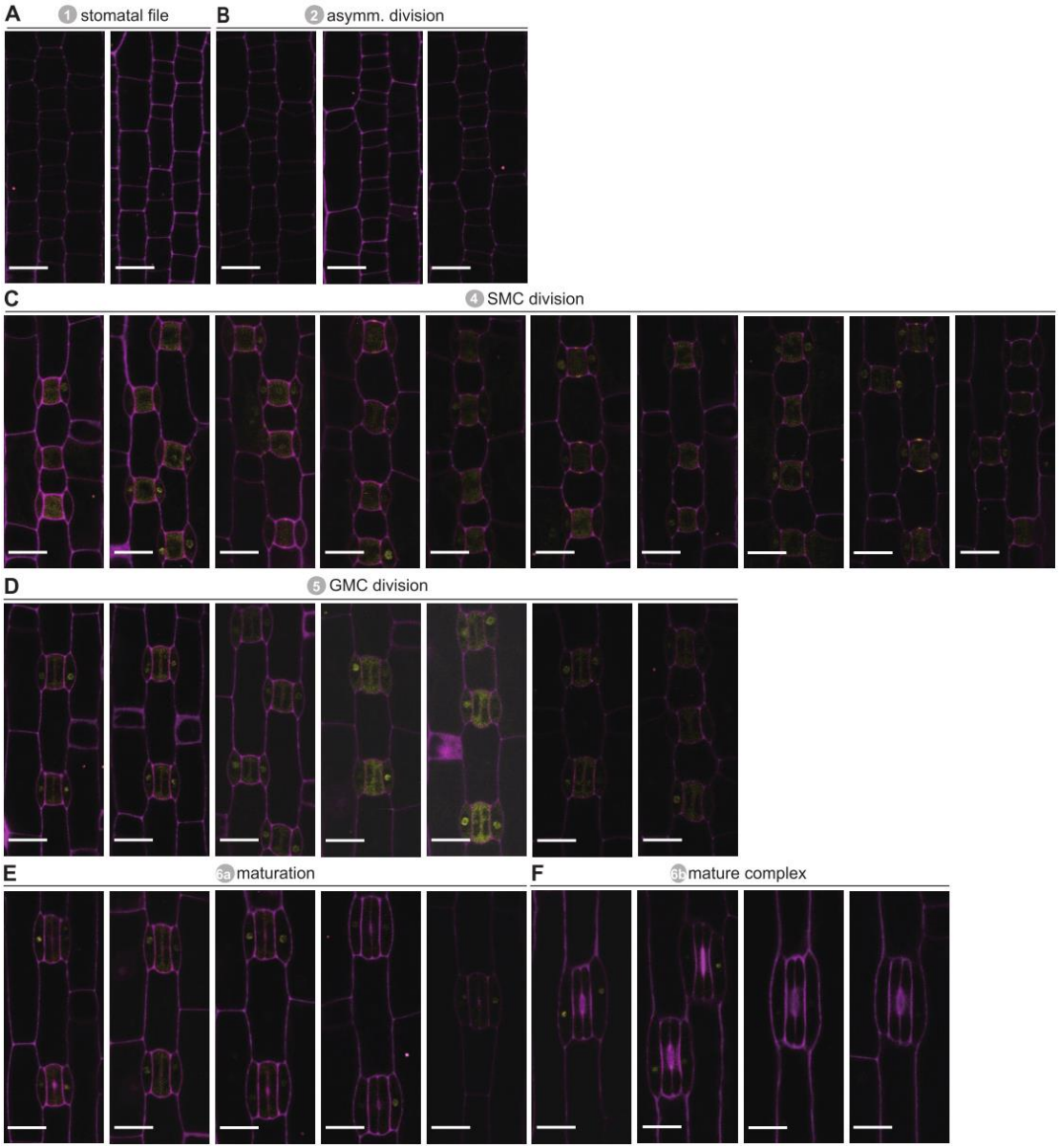

Figure S13. *BdPOLARp:BdTAN1-mCitrine* expression throughout stomatal development in WT.

Except stage3 showed at Figure S12. Composite images with BdTAN1-mCitrine signal (yellow) and PI-stained cell outlines (magenta). All images from the second leaf, 5 to 6 dag. T2 generation. Scale bars, 10 µm.

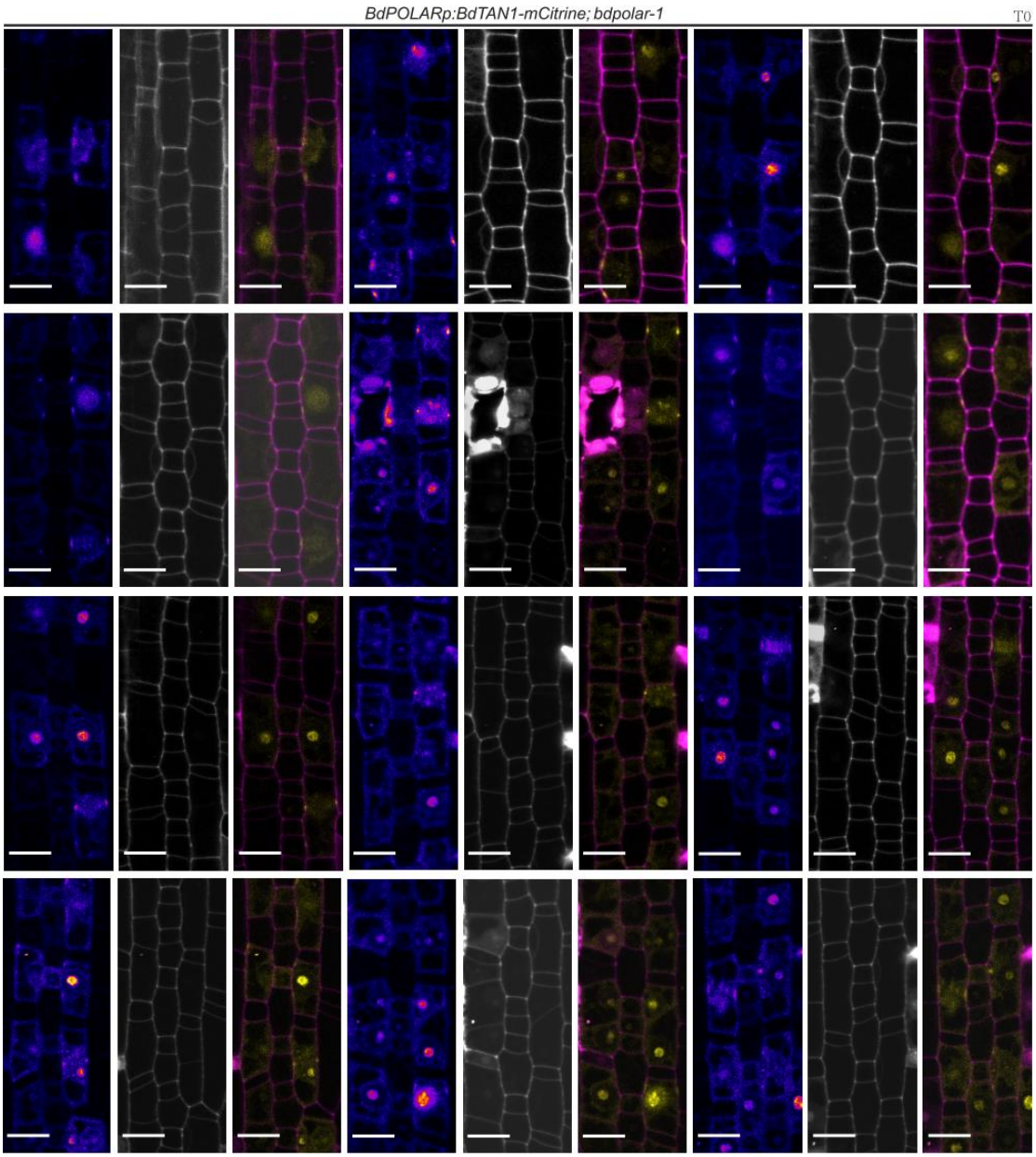
BdPOLARp:BdTAN1-mCitrine; bdpolar-1
T0

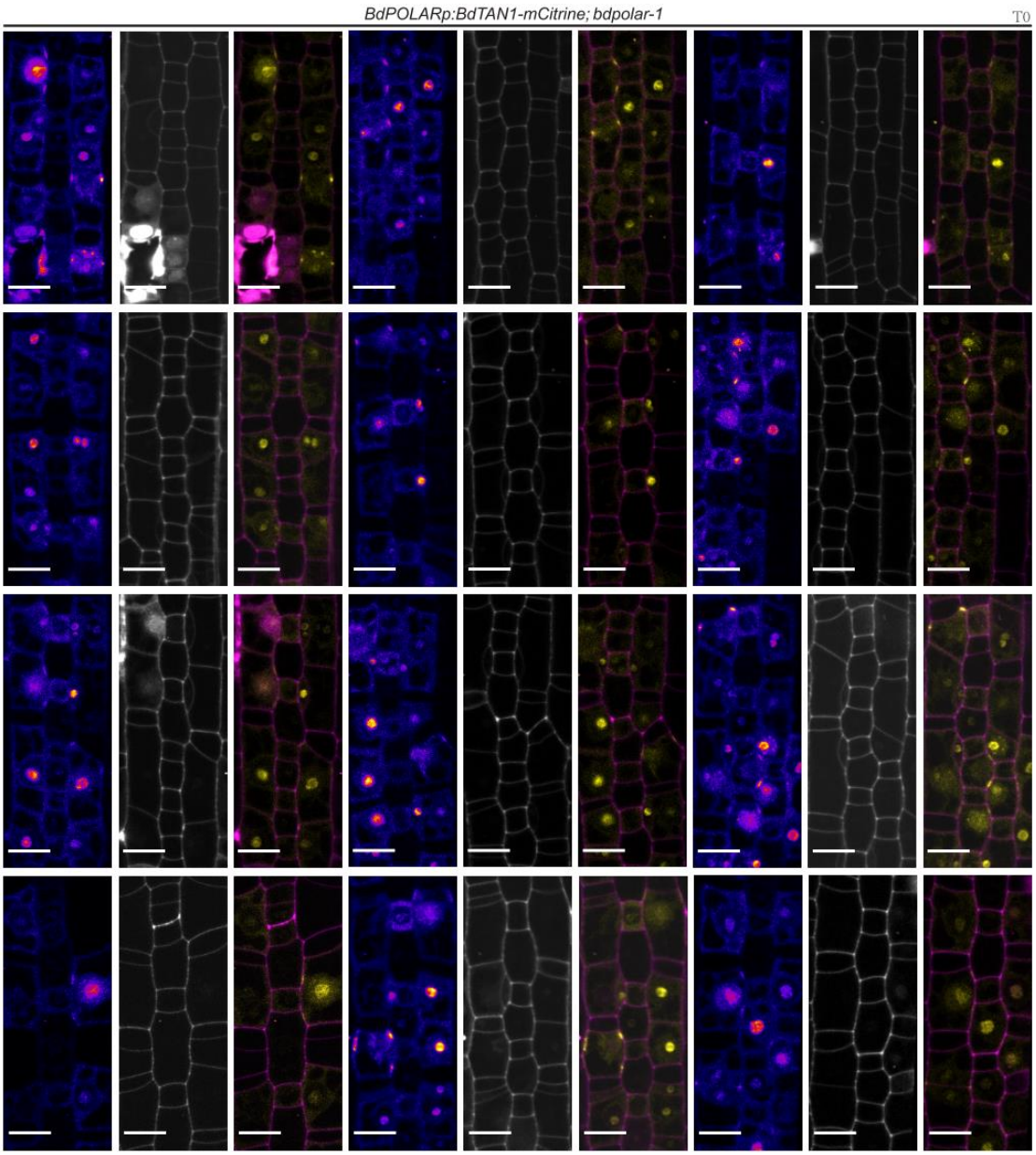
BdPOLARp:BdTAN1-mCitrine; bdpolar-1
T0

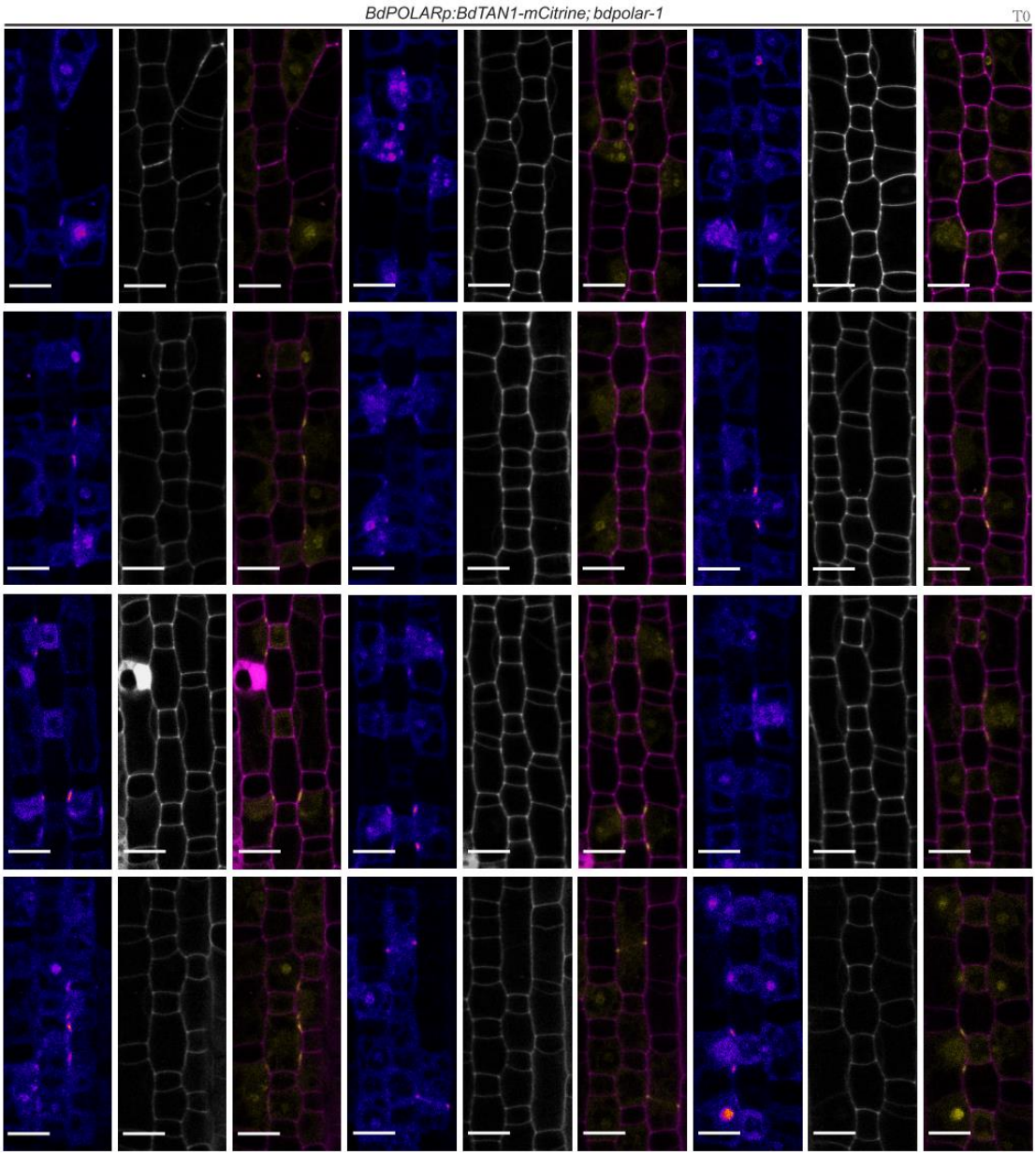
BdPOLARp:BdTAN1-mCitrine; bdpolar-1
T0

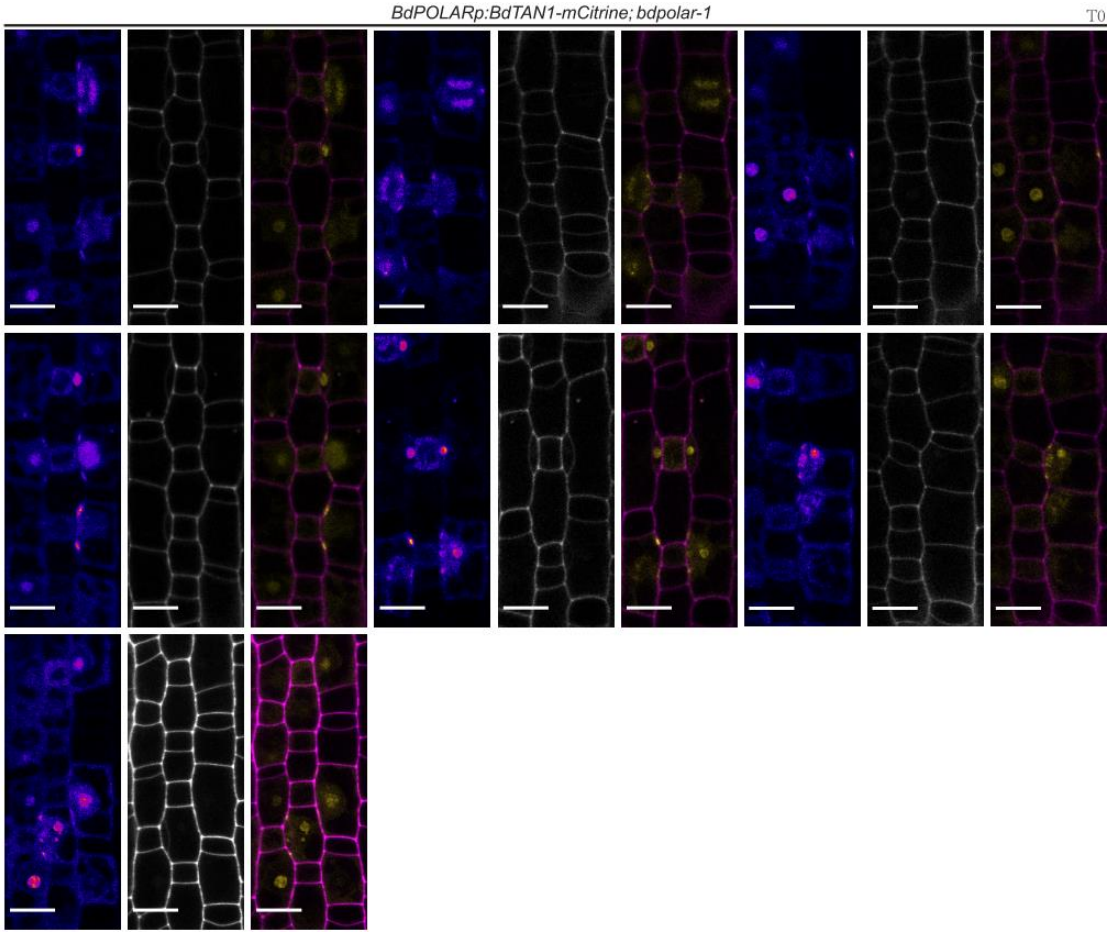
BdPOLARp:BdTAN1-mCitrine; bdpolar-1
T0

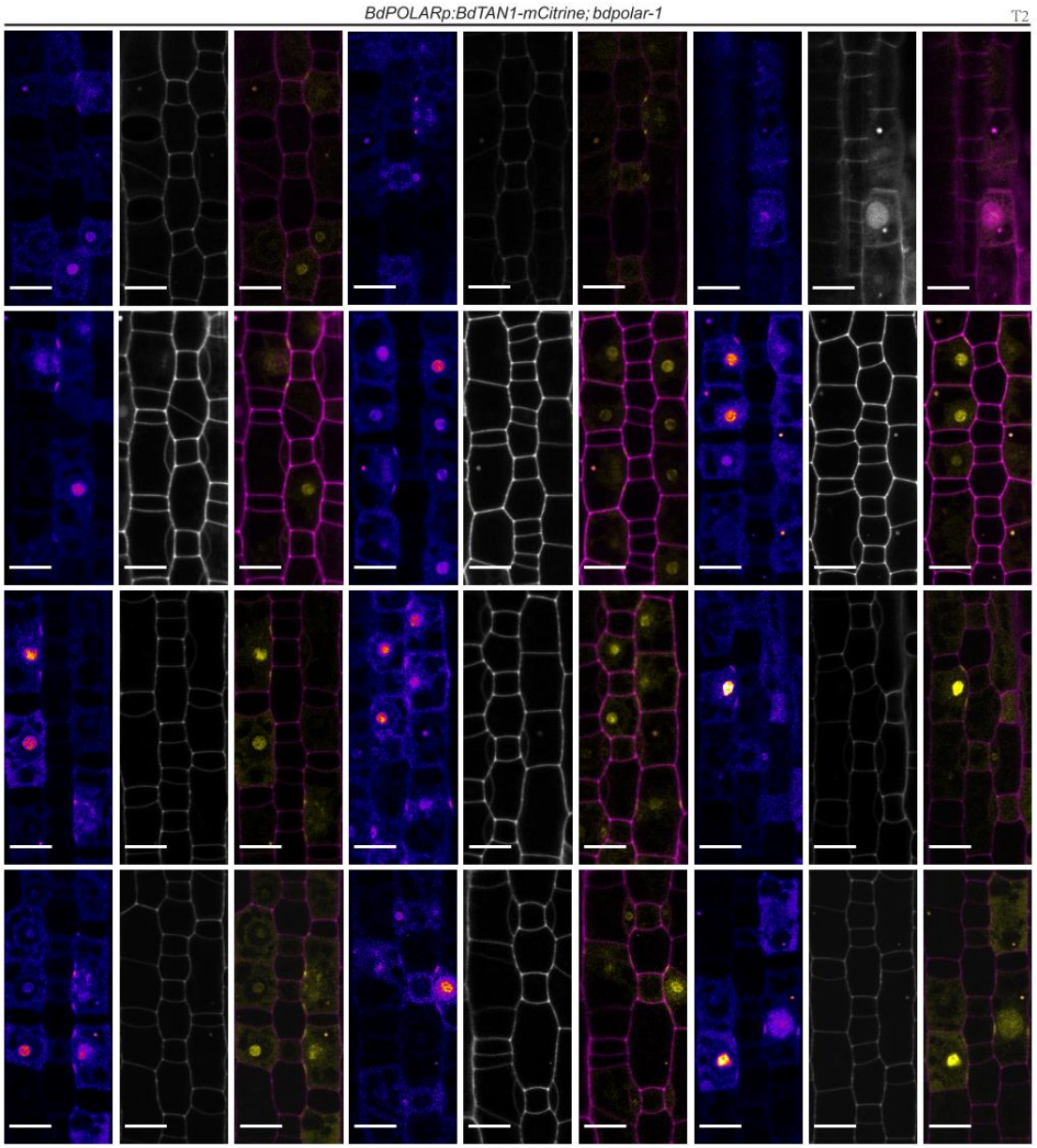
BdPOLARp:BdTAN1-mCitrine; bdpolar-1
T2

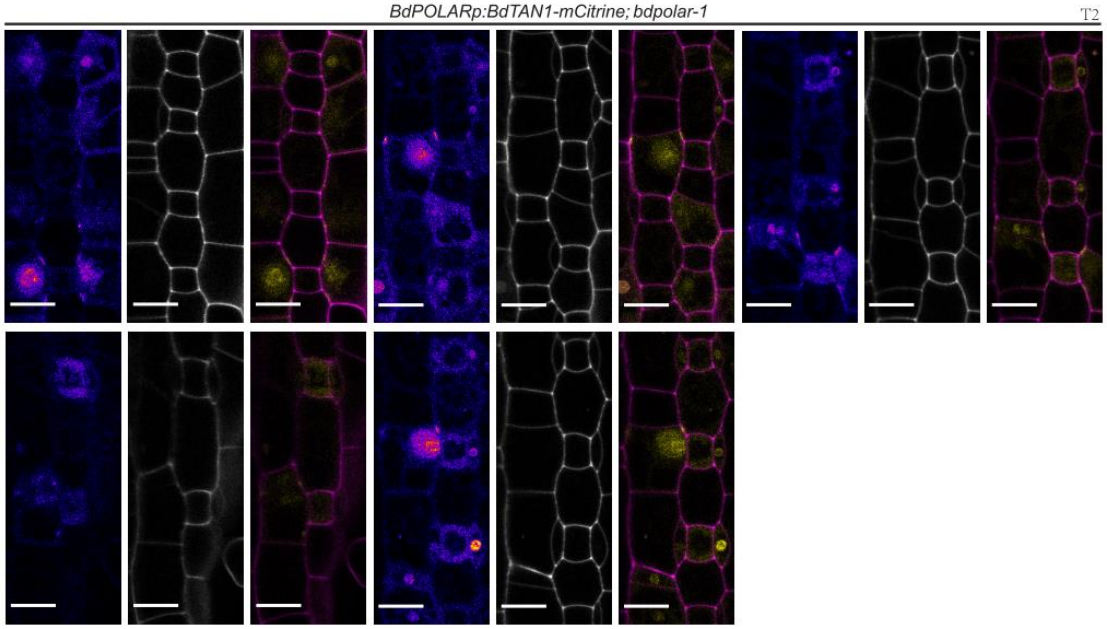
BdPOLARp:BdTAN1-mCitrine; bdpolar-1
T2

Figure S14. *BdPOLARp:BdTAN1-mCitrine* expression of stage 3 to stage 4 SMCs in *bdpolar-1*.
Fluorescence intensity images of mCitrine channel only (left), images of PI-stained cell outlines only (middle), and composite images (right) with BdTAN1-mCitrine signal (yellow) and PI-stained cell outlines (magenta). All images from the second leaf, 5 to 6 dag. T0 and T2 generations. Scale bars, 10 µm.

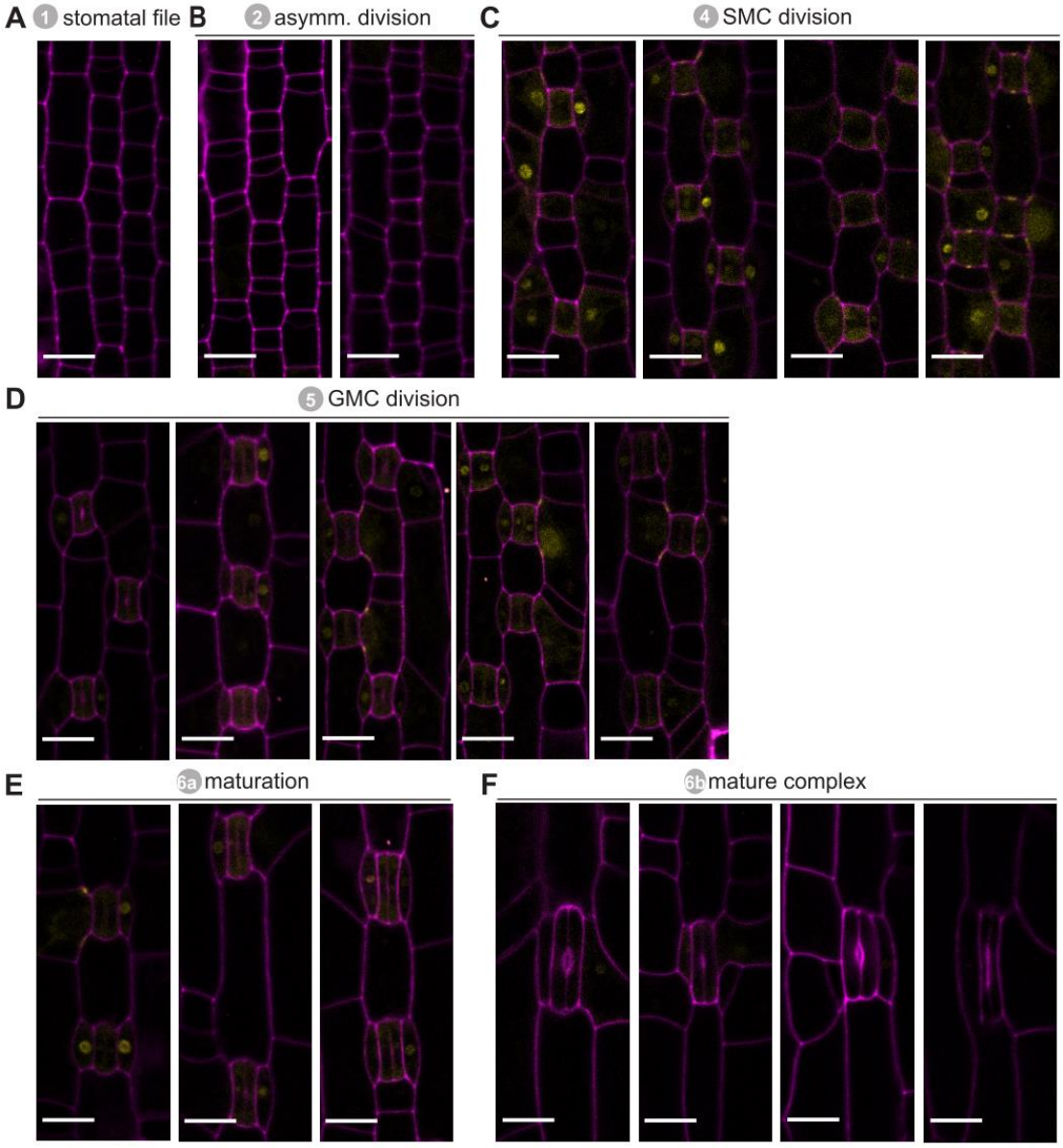

Figure S15. *BdPOLARp:BdTAN1-mCitrine* expression throughout stomatal development in *bdpolar-1*.
Except stage3 showed at Figure S14. Composite images with BdTAN1-mCitrine signal (yellow) and PI-stained cell outlines (magenta). All images from the second leaf, 5 to 6 dag. T0 and T2 generation. Scale bars, 10 µm.

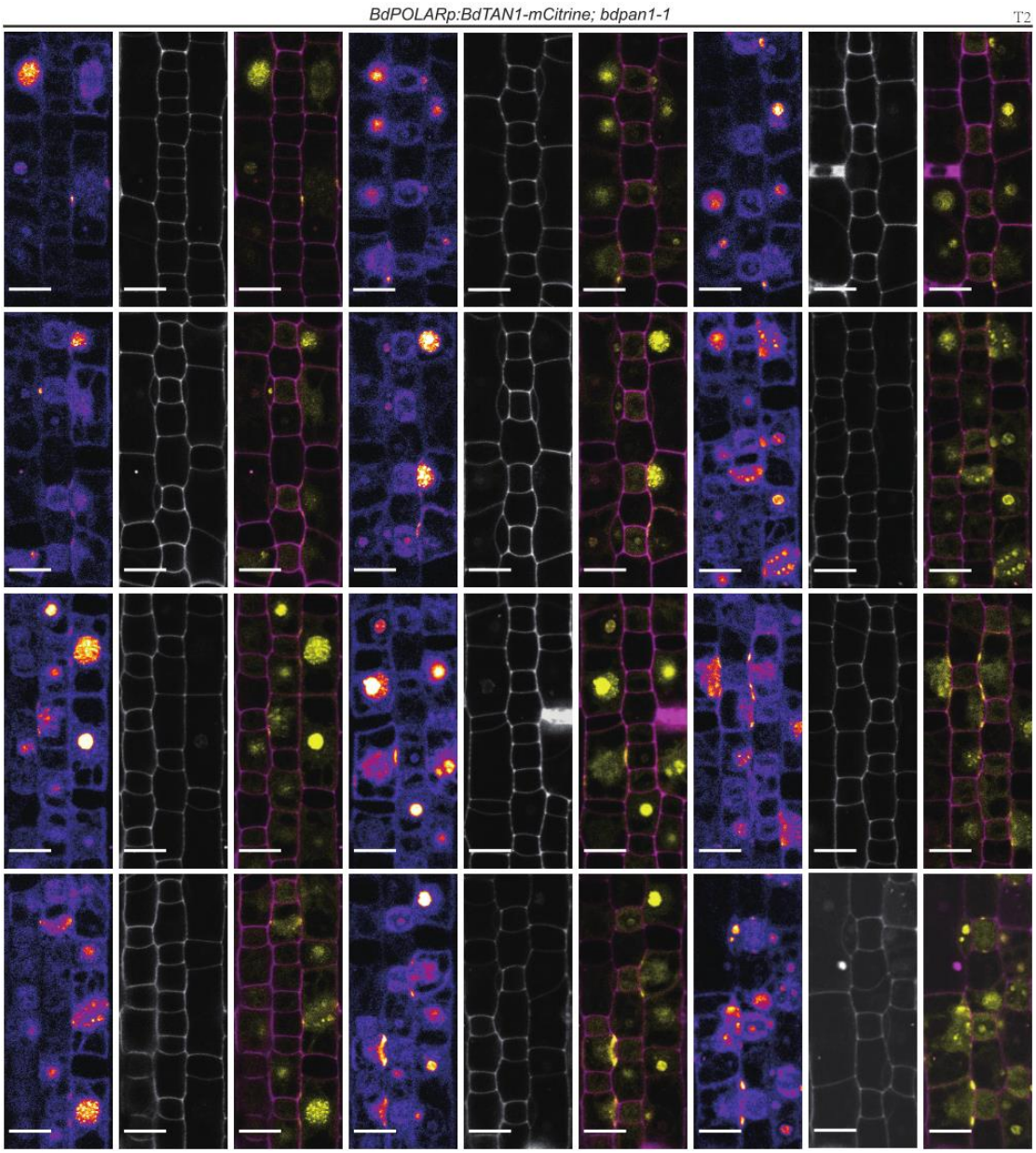
BdPOLARp:BdTAN1-mCitrine; bdpan1-1
T2

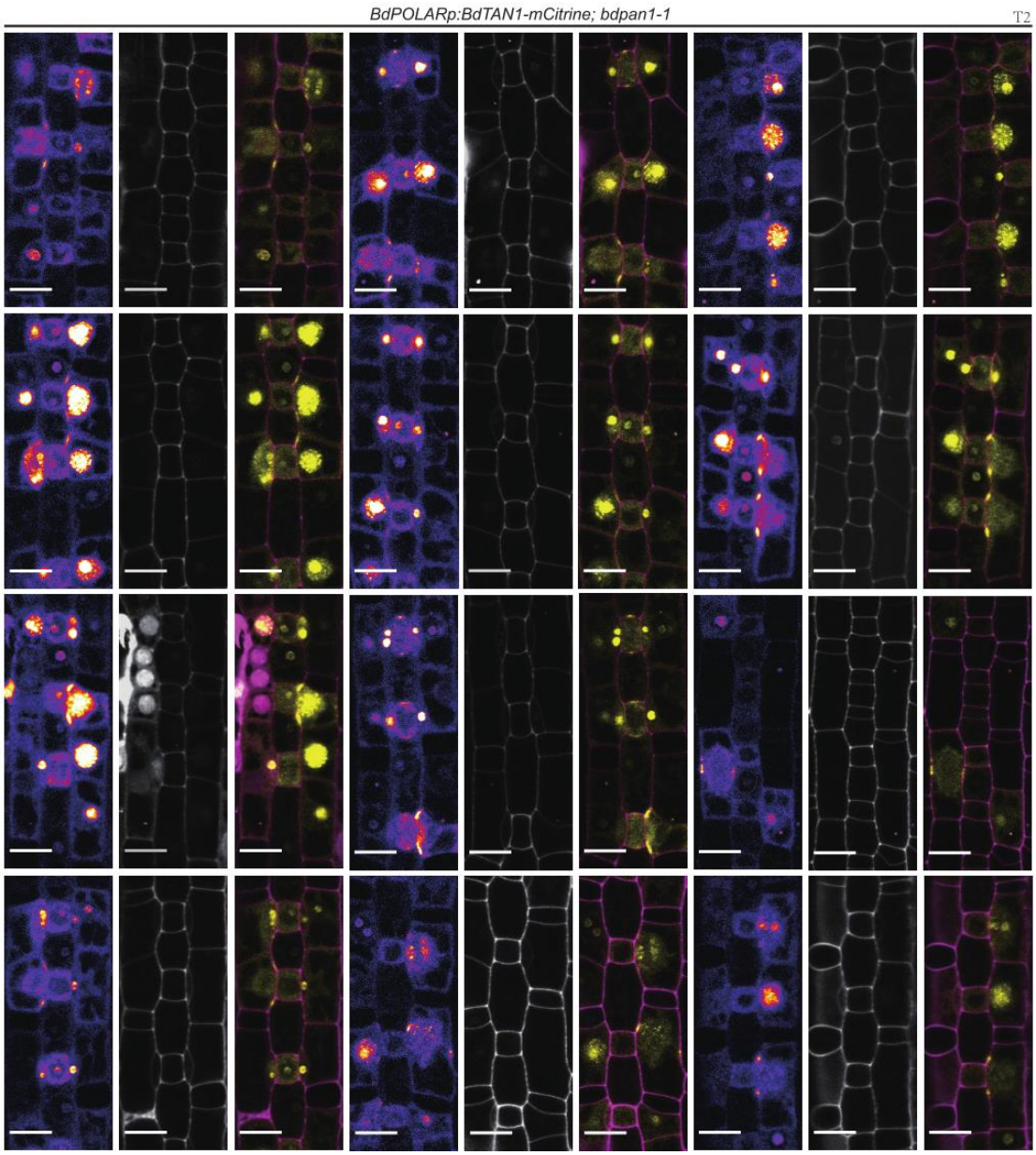
BdPOLARp:BdTAN1-mCitrine; bdpan1-1
T2

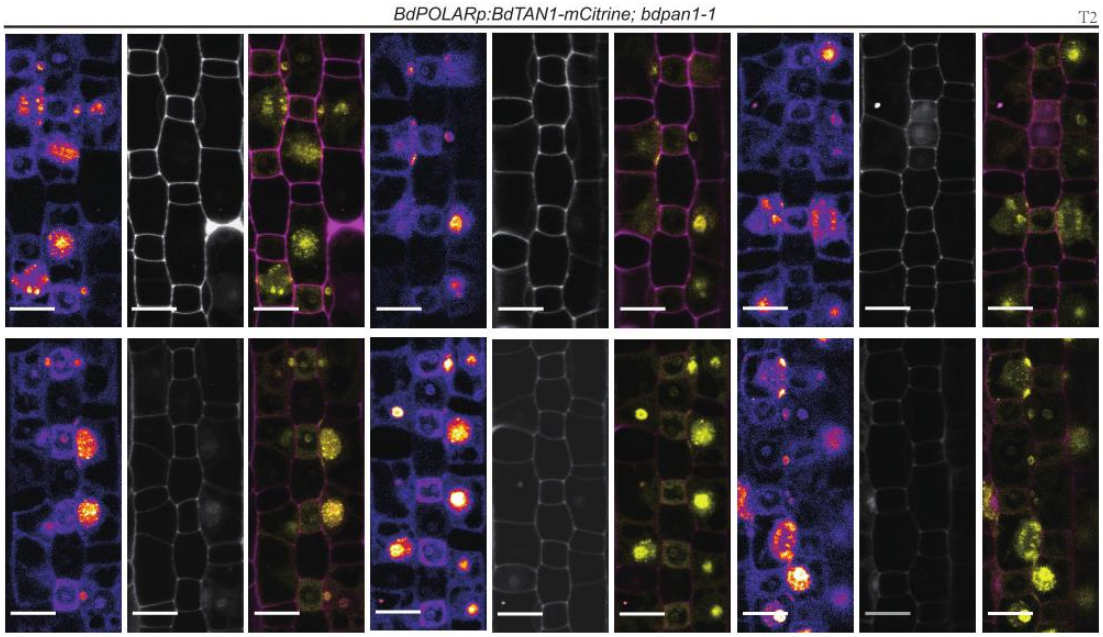

Figure S16. *BdPOLARp:BdTAN1-mCitrine* expression of stage 3 to stage 4 SMCs in *bdpan1-1*.
Fluorescence intensity images of mCitrine channel only (left), images of PI-stained cell outlines only (middle), and composite images (right) with BdTAN1-mCitrine signal (yellow) and PI-stained cell outlines (magenta). All images from the second leaf, 5 to 6 dag. T2 generation. Scale bars, 10 µm.

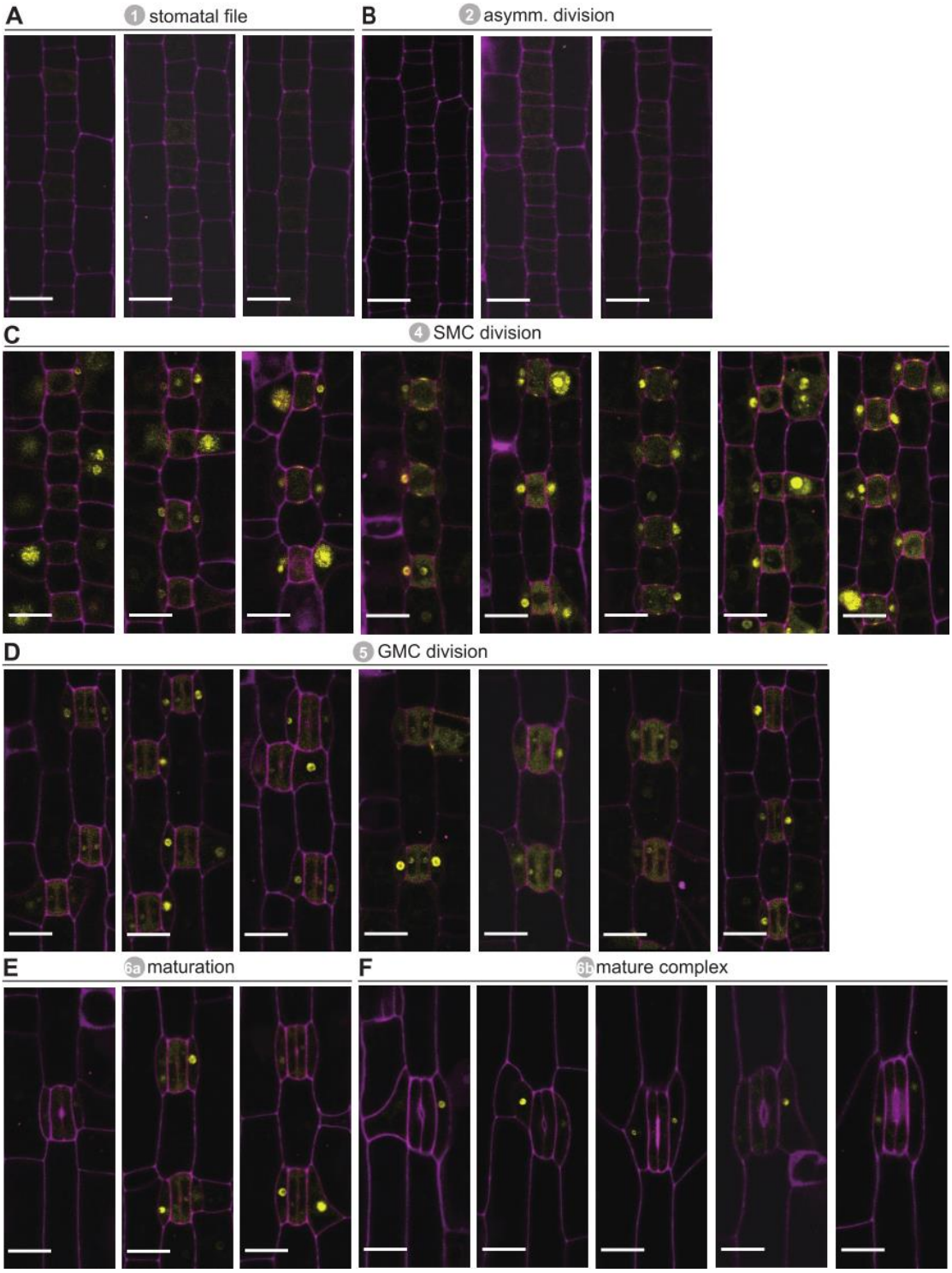

Figure S17. *BdPOLARp:BdTAN1-mCitrine* expression throughout stomatal development in *bdpan1-1*.

Except stage3 showed at Figure S16. Composite images with BdTAN1-mCitrine signal (yellow) and PI-stained cell outlines (magenta). All images from the second leaf, 5 to 6 dag. T2 generation. Scale bars, 10 µm.

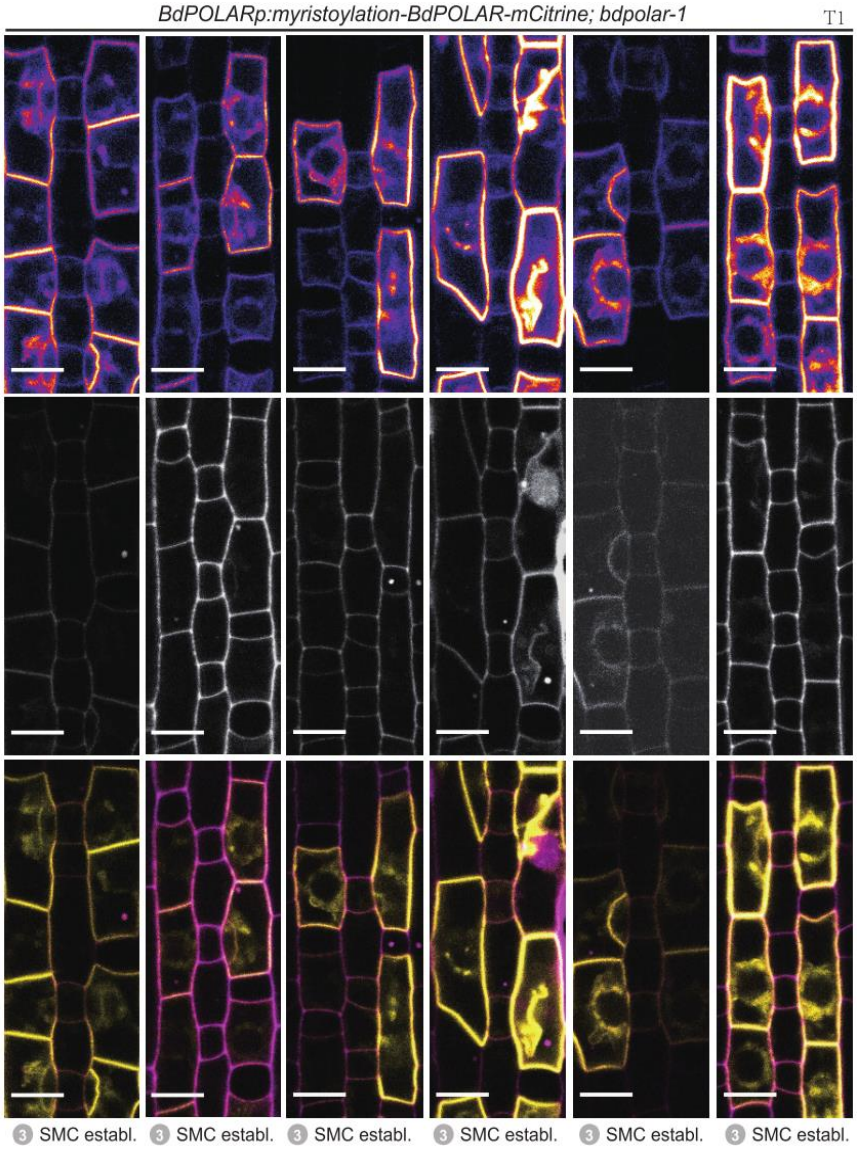

Figure S18. *BdPOLARp:MYR-BdPOLAR-mCitrine* expression at stage 3 in *bdpolar-1*.

Fluorescence intensity images of mCitrine channel only (upper), images of PI-stained cell outlines only (middle), and composite images (bottom) with MYR-BdPOLAR-mCitrine signal (yellow) and PI-stained cell outlines (magenta). All images from the second leaf, 5 to 6 dag, T1 generation. Scale bars, 10 µm.

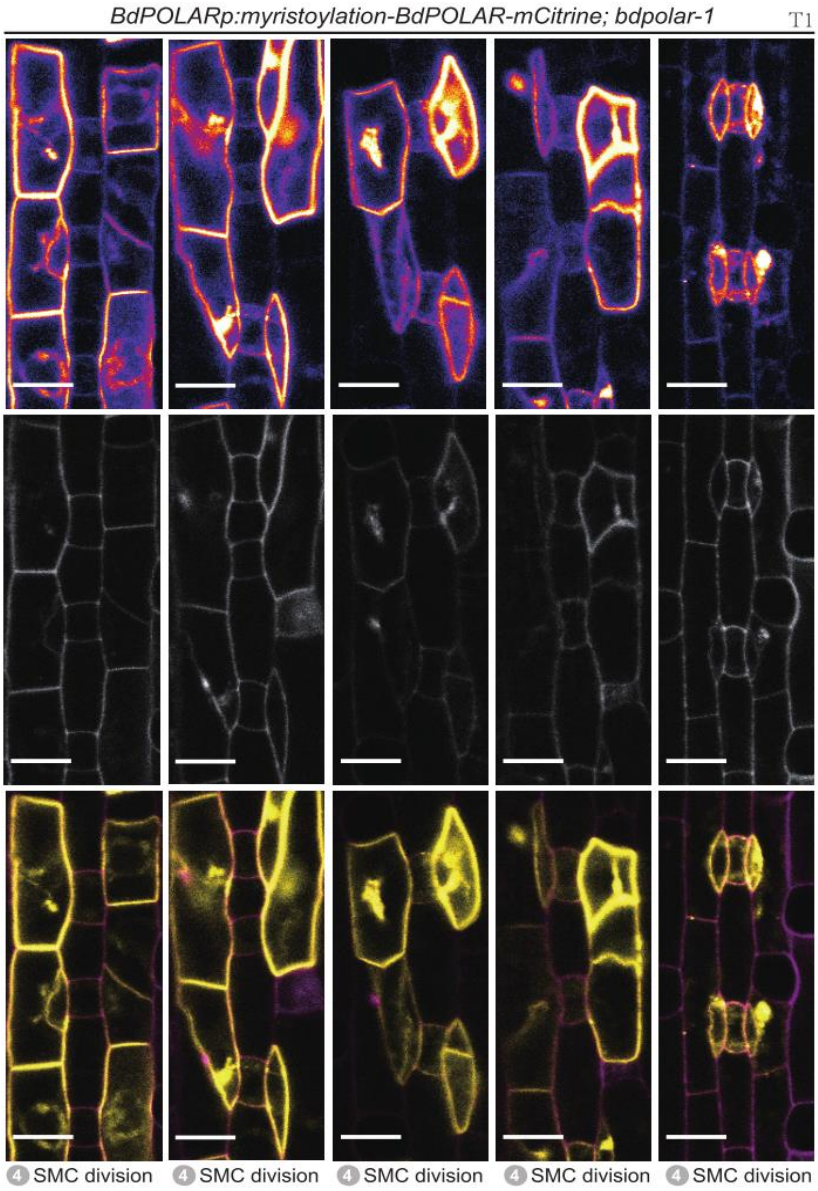

Figure S19. *BdPOLARp:MYR-BdPOLAR-mCitrine* expression at stage 4 in *bdpolar-1*.

Fluorescence intensity images of mCitrine channel only (upper), images of PI-stained cell outlines only (middle), and composite images (bottom) with MYR-BdPOLAR-mCitrine signal (yellow) and PI-stained cell outlines (magenta). All images from the second leaf, 5 to 6 dag, T1 generation. Scale bars, 10 µm.

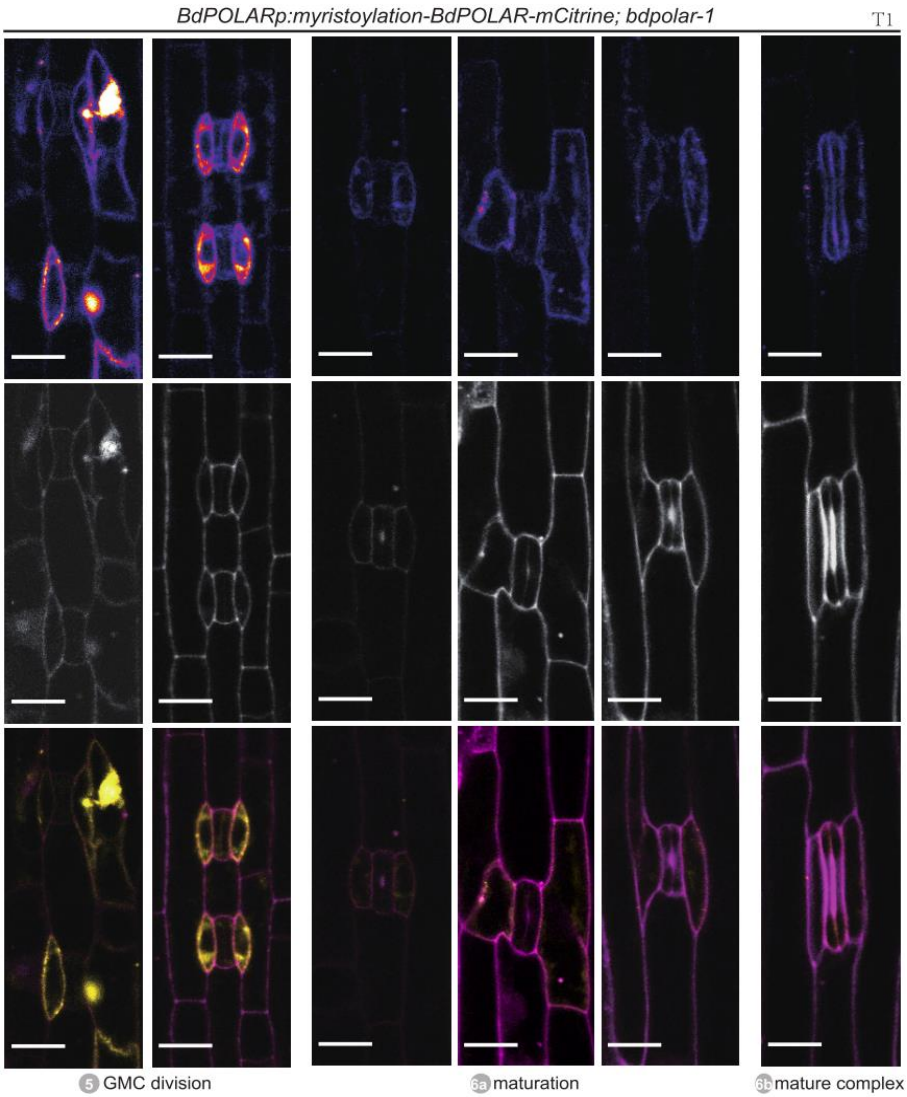

Figure S20. *BdPOLARp:MYR-BdPOLAR-mCitrine* expression at stage 5, 6a and 6b in *bdpolar-1*.

Fluorescence intensity images of mCitrine channel only (upper), images of PI-stained cell outlines only (middle), and composite images (bottom) with MYR-BdPOLAR-mCitrine signal (yellow) and PI-stained cell outlines (magenta). All images from the second leaf, 5 to 6 dag, T1 generation. Scale bars, 10 µm.

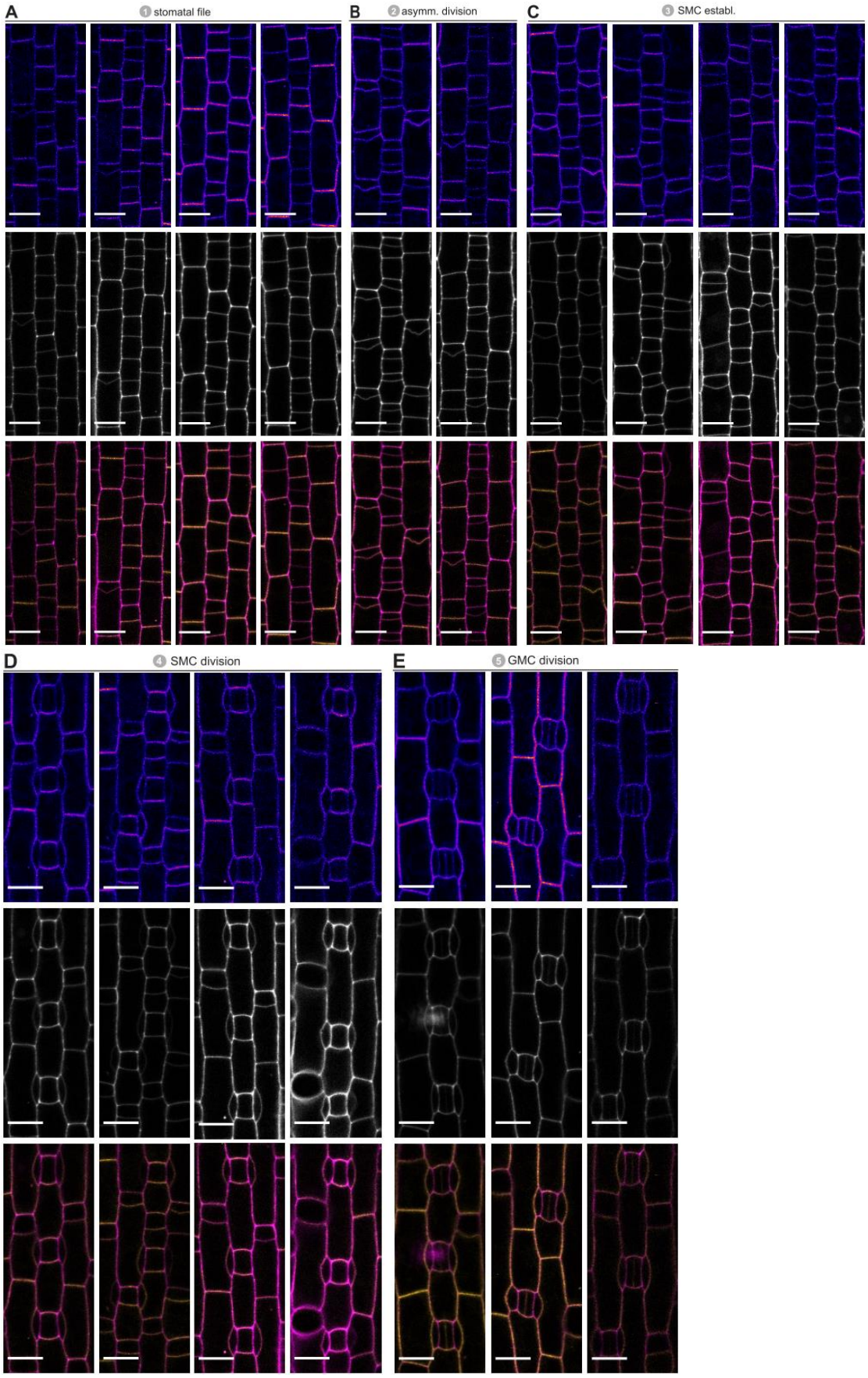
A
1 stomatal file
B
2 asymm. division
C
3 SMC establ.
D
4 SMC division
E
5 GMC division

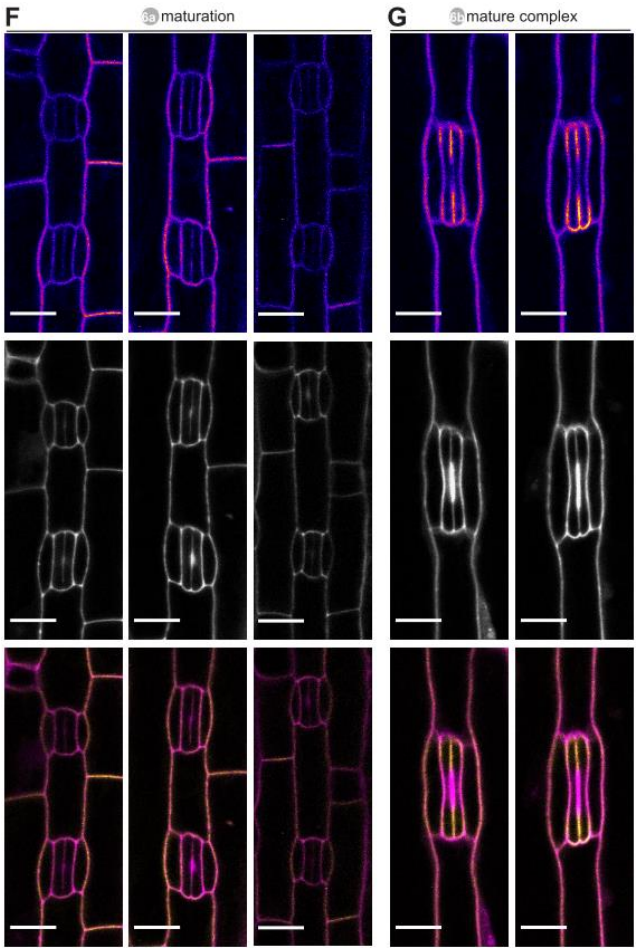

Figure S21. *ZmUbip:BdPOLAR-mVenus* expression throughout stomatal development in *B. distachyon*.
Fluorescence intensity images of mVenus channel only (upper), images of PI-stained cell outlines only (middle), and composite images (bottom) with BdPOLAR-mVenus overexpression signal (yellow) and PI-stained cell outlines (magenta). All images from the second leaf, 5 to 6 dag, T2 generation. Scale bars, 10 µm.

5. Data Track on Server

Figure 1:
PhD/processed/intro/figure 1

Figure 2:
PhD/processed/intro/figure 2

Figure 3:
PhD/NaN screen/pictures

Figure 4:
PhD/pictures/gel/2020.02

Figure 6A:
PhD/pictures/gel/2020.09

Figure 6B:
PhD/POLAR/POLAR NaN lines/20201001POLAR F2 NaN2063 DZ166

Figure 7:
Geneious/Plasmids map/pDZ6

Figure 8:
Geneious/Plasmids map/pDZ31

Figure 9:
Geneious/Plasmids map/pDZ44

Figure 10A:
WT: PhD/POLAR/Quantification/DIC pictures/R1 DZ130 20200311 pictures/WT-2/field 5;
bdpolar-1: PhD/POLAR/Quantification/DIC pictures/R1 DZ130 20200311 pictures/polar1-2/field 8-1;
bdpolar-2: PhD/POLAR/CRISPR T1/20211113 DZ220 TO73 516-1/516-1 5/image 004;
bdpolar-3: PhD/POLAR/CRISPR T1/20211008 DZ221 T071 517-5/Line 1/image 005

Figure 10B:
Input file: PhD/POLAR/CRISPR T1/all polar mutants.csv
Code file: PhD/POLAR/CRISPR T1/all polar mutants.R
Output file: PhD/POLAR/CRISPR T1/all polar mutants.pdf

Figure 10C:
bdpolar-1 (T inserition): Geneious/Sequencing/20190322_POLAR genotyping/DZ74-11;
bdpolar-1 (CC deletion): Geneious/Sequencing/20190322_POLAR genotyping/DZ75-11;
bdpolar-2 (T inserition): Geneious/Sequencing/20211111 DZ220 T073 516-1/DZ220 T073 516-1 #2;
bdpolar-3 (T inserition): Geneious/Sequencing/20211023 PAN1 in polar and CRISPR T1/DZ221 T071 517-5 #2;
bdpolar-3 (G deletion): Geneious//Sequencing20211008 CRISPR T1/DZ221 T073 517-3 line1;
bdpolar-3 (G inserition): Geneious/Sequencing/20211023 PAN1 in polar and CRISPR T1/DZ221 T071 517-5 #4

Figure 10D:
PhD/pictures/gel/2020.05 (labbook 2020.05.20)

Figure 11:
Geneious/BdPOLAR Bd3g54060/polar mutants peptides/Protein alignment

Figure 12A:
WT: PhD/POLAR/Quantification/DIC pictures/R1 DZ130 20200311 pictures/WT-2/field 5;
bdpolar-1: PhD/POLAR/Quantification/DIC pictures/R1 DZ130 20200311 pictures/polar1-2/field 8-1;
bdpan1-1: PhD/POLAR/Quantification/DIC pictures/R1 DZ130 20200311 pictures/pan1-1/field 5;
bdpolar-1;bdpan1-1: PhD/POLAR/Quantification/DIC pictures/R1 DZ130 20200311 pictures/DZ130-10/filed 9

Figure 12B:
Input file: PhD/POLAR/Quantification/new counting/DZ130 DZ142 all_new_relevel.csv
Code file: PhD/POLAR/Quantification/new counting/DZ130 DZ142 all_new_relevel.R
Output file: PhD/POLAR/Quantification/DZ130 DZ142 all_new_relevel.pdf

Figure 13:
WT:
lif file: PhD/pictures/confocal/20210114 wt 5days PI

Processed file: WT: PhD/processed/20210114 wt 5days

bdpolar-1 (stage 1, 2, 4, 5, 6a, 6b):
lif file: PhD/pictures/confocal/20201221 polar-1 5days PI
Processed file: PhD/processed/20201221 polar-1 5days

bdpolar-1 (stage 3):
lif file: PhD/pictures/confocal/20210306 polar 5days
Processed file: PhD/processed/20210306 polar 5days

*bdpan1-1 (*stage 1, 2, 3, 4, 6b):
lif file: PhD/pictures/confocal/20201221 pan1 5days PI
Processed file: PhD/processed/20201221 pan1 5days

*bdpan1-1 (*stage 5):
lif file: PhD/pictures/confocal/20200723 pan1 6days 2nd
Processed file: PhD/processed/20200723 pan1 6days 2nd

*bdpan1-1 (*stage 6a):
lif file: PhD/pictures/confocal/20200706 pan1 6 days
Processed file: PhD/processed/20200706 pan1 6days

bdpolar-1;bdpan1-1(stage 1, 2, 4, 5, 6a, 6b):
lif file: PhD/pictures/confocal/20210114 polarpan1 5days PI
Processed file: PhD/processed/20210114 polarpan1 5days

bdpolar-1;bdpan1-1(stage 3):
lif file: PhD/pictures/confocal/20200829 polarpan1
Processed file: PhD/processed/20200829 polarpan1

Figure 14A:
lif file: PhD/pictures/confocal/20201221 PAN1-YFP wt 5days
Processed file: PhD/processed/20201221 PAN1-YFP wt 5days

Figure 14B:
lif file: PhD/pictures/confocal/20211203 PAN1 3D
Processed file: PhD/processed/20211203 PAN1 3D

Figure 15A:
confocal:
lif file: PhD/pictures/confocal/20210625 pan1 complemented DZ216 DZ217
Processed file: PhD/processed/20210625 pan1 complemented DZ216 DZ217
DIC:
tif file: PhD/pictures/confocal/20210625 pan1 complemented DZ216 DZ217
Processed file: PhD/POLAR/pan1 complemented/20210727 DZ216 DZ217/DZ216-1/image002

Figure 15B:
Input file: PhD/POLAR/pan1 complemented/DZ216 DZ217.csv
Code file: PhD/POLAR/pan1 complemented/DZ216 DZ217.R
Output file: PhD/POLAR/pan1 complemented/DZ216 DZ217.pdf

Figure 16A:
stage 1, 2:
lif file: PhD/pictures/confocal/20210225 POLAR in wt vs sid 5days
Processed file: PhD/processed/20210225 POLAR in wt vs sid 5days/POLAR in wt

stage 3:
lif file: PhD/pictures/confocal/20200708 POLAR-mVenus WT third leaf T2
Processed file: PhD/processed/20200708 POLAR-mVenus WT third leaf T2

stage 4, 6b:
lif file: PhD/pictures/confocal/20201221 POLAR-mVenus wt 5days
Processed file: PhD/processed/20201221 POLAR-mVenus wt 5days

stage 5:
lif file: PhD/pictures/confocal/20210306 POLAR-mVenus wt 5days
Processed file: PhD/processed/20210306 POLAR-mVenus wt

stage 6a:
lif file: PhD/pictures/confocal/20200715 POLAR-mVenus wt 5days second leaf
Processed file: PhD/processed/20200715 POLAR-mVenus wt 5days second leaf

Figure 16B:
lif file: PhD/pictures/confocal/20211206 POLAR 3D 3rd leaf
Processed file: PhD/processed/20211206 POLAR 3D 3rd leaf

Figure 17:
lif file: PhD/pictures/confocal/20210206 DZ126-1 POLAR-NLS 5days
Processed file: PhD/processed/20210206 DZ171 from DZ126-1 POLAR-NLS 5days

Figure 18A:
lif file: PhD/pictures/confocal/20210225 POLAR in wt vs sid 5days
Processed file: PhD/processed/20210225 POLAR in wt vs sid 5days

Figure 18B:
WT:
lif file: PhD/pictures/confocal/20210430 PAN1-YFP in WT 5 days
Processed file: PhD/processed/20210430 PAN1-YFP in WT 5 days/DZ168-1

bdmute:
lif file: PhD/pictures/confocal/20210430 PAN1-YFP in sid 5days
Processed file: PhD/processed/20210430 PAN1-YFP in sid 5days/DZ173-12

Figure 19A:
BdPOLAR in WT:
lif file: PhD/pictures/confocal/20210406 pan1 wt X POLAR 5days
Processed file: PhD/processed/20210406 pan1 wt X POLAR 5days/DZ193-3 #2 pan1_wt strong crop;

BdPOLAR in *bdpan1-1*:
lif file: PhD/pictures/confocal/20210407 pan1 homXPOLAR 6days
Processed file: PhD/processed/20210407 pan1 homXPOLAR 6days/pan1 homXPOLAR strong/fire1 DZ188-3 #1.tif (green)

Figure 19B:
Input file: PhD/POLAR/POME/raw data/20210506_POLAR;PAN1(WT).csv;
PhD/POLAR/POME/raw data/20210506_POLAR;pan1.csv
Code file: PhD/POLAR/POME/raw data/POLAR in PAN1 WT and pan1.R
Output file: PhD/POLAR/POME/raw data/POLAR in PAN1 WT and pan1.pdf

Figure 19C:
lif file: PhD/pictures/confocol/20210508 DZ200-1 polarXPAN1-YFP F2 5days
Processed file:

BdPAN1 in WT: PhD/processed/20210508 DZ214 from DZ200-1 polarXPAN1-YFP F2\#8 polar_wtXPAN1;
BdPAN1 in *bdpolar-1*: PhD/processed/20210508 DZ214 from DZ200-1 polarXPAN1-YFP F2\#16 polar_homXPAN1

Figure 20A:
bdpan1-1 without BdPOLAR:
PhD/POLAR/POLAR in pan1/R1 pan1 wt homXPOLAR/DIC pictures/20210205 DZ163/DZ183/DZ183_1/183-1-4_ch00
bdpan1-1 with BdPOLAR:
PhD/POLAR/POLAR in pan1/R1 pan1 wt homXPOLAR/DIC pictures/20210205 DZ163/DZ183/DZ183_5/183-5-6_ch00

Figure 20B:
Input file: PhD/POLAR/POLAR in pan1/pan1 and PAN1 WT with and without POLAR.csv
Code file: PhD/POLAR/POLAR in pan1/pan1 and PAN1 WT with and without POLAR.R
Output file: PhD/POLAR/POLAR in pan1/pan1 and PAN1 WT with and without POLAR.pdf

Figure 20C:
bdpolar-1 without BdPAN1:
PhD/POLAR/PAN1 in polar/20210923 DZ214/DZ214-3/image 010
bdpolar-1 with BdPAN1:
PhD/POLAR/PAN1 in polar/20210603 DZ214/DZ214-16/image 004

Figure 20D:
Input file: PhD/POLAR/PAN1 in polar/DZ214 and from DZ214.csv
Code file: PhD/POLAR/PAN1 in polar/DZ214 and from DZ214.R
Output file: PhD/POLAR/PAN1 in polar/DZ214 and from DZ214.pdf

Figure 21A:
lif file: PhD/pictures/confocal/20211013 from DZ213
Processed file:
Confocal weak POLAR: PhD/POLAR/polar complemented/figures/20211013 from DZ213 R1DZ213 6-6
Confocal Strong POLAR: PhD/POLAR/polar complemented/figures/20211013 from DZ213 R2 DZ213 5-4
DIC weak POLAR: PhD/POLAR/polar complemented/20211113 R1 from DZ213-6/6-6/image007
DIC strong POLAR: PhD/POLAR/polar complemented/figures/20211115 R2 from DZ213-5/5-4/image003

Figure 21B:
Input file: PhD/POLAR/polar complemented/from R1 R2 DZ213-Lazer.csv
Code file: PhD/POLAR/polar complemented/from R1 R2 DZ213-Lazer.R
Output file: PhD/POLAR/polar complemented/from R1 R2 DZ213-Lazer.pdf

Figure 21C:
lif file:PhD/pictures/confocal/20220117 POLAR C-OE T1
Processed file: PhD/processed/20220117 POLAR C-OE T1

Figure 21D:
Input file: PhD/POLAR/ POLAR OE/ C OE quantification.csv
Code file: PhD/POLAR/ POLAR OE/ C OE quantification. R
Output file: PhD/POLAR/ POLAR OE/ C OE quantification.pdf

Figure 22B:
WT:

lif file: PhD/pictures/confocal/20201128 R5 WT nuclei 5days
Processed file: PhD/POLAR/processed/nuclei imaging/wt/20201128 R5 WT nuclei 007-1 crop

bdpolar-1:
lif file: PhD/pictures/confocal/20201128 R5 polar nuclei 5days
Processed file: PhD/POLAR/processed/nuclei imaging/polar/R5/20201128 R5 polar 020 crop

bdpan1-1:
lif file: PhD/pictures/confocal/20201128 R5 pan1 nuclei 5days
Processed file: PhD/POLAR/processed/nuclei imaging/pan1/20201128 R5 pan1 021-1 crop

bdpolar-1;bdpan1-1:
lif file: PhD/pictures/confocal/20201122 R4 polarpan1 nuclei 5days
Processed file:PhD/POLAR/processed/nuclei imaging/polarpan1/R4/20201122 R4 polarpan1 011 crop

Figure 22C:
Input file: PhD/POLAR/Nuclei data/R3R4R5R6/R3R4R5R6_wt.csv; R3R4R5R6_polar.csv; R3R4R5R6_pan1.csv; R3R4R5R6_polarpan1.csv;
Code file: PhD/POLAR/Nuclei data/R3R4R5R6/R3R4R5R6.R
Output file: PhD/POLAR/Nuclei data/R3R4R5R6/R3456_0.9_relevel.pdf

Figure 23A:
Input file: PhD/POLAR/Nuclei data/R3R4R5R6/R3R4R5R6_wt.csv
Code file: PhD/POLAR/Nuclei data/lm/WT lm.R
Output file: PhD/POLAR/Nuclei data/lm/wt lm.pdf

Figure 23B:
Input file: PhD/POLAR/Nuclei data/R3R4R5R6/R3R4R5R6_polar.csv
Code file: PhD/POLAR/Nuclei data/lm/polar lm.R
Output file: PhD/POLAR/Nuclei data/lm/polar lm.pdf

Figure 23C:
Input file: PhD/POLAR/Nuclei data/R3R4R5R6/R3R4R5R6_pan1.csv
Code file: PhD/POLAR/Nuclei data/lm/pan1 lm.R
Output file: PhD/POLAR/Nuclei data/lm/pan1 lm.pdf

Figure 23D:
Input file: PhD/POLAR/Nuclei data/R3R4R5R6/ R3R4R5R6_polarpan1.csv
Code file: PhD/POLAR/Nuclei data/lm/ polarpan1 lm.R
Output file: PhD/POLAR/Nuclei data/lm/ polarpan1 lm.pdf

Figure 23E:
Input file: PhD/POLAR/Nuclei data/nuclei size from R4.csv
Code file: PhD/POLAR/Nuclei data/nuclei size from R4.R
Output file: PhD/POLAR/Nuclei data/nuclei size from R4.pdf

Figure 23F:
PhD/POLAR/Nuclei data/summary

Figure 24:
lif file: PhD/pictures/confocal/20220119 DZ244 TAN1 in WT T2
Processed file: PhD/POLAR/processed/TAN1 in WT and pan1/figure 24 in WT

Figure 25:
lif file: PhD/pictures/confocal/20220212 535 in polar T0; 20220307 3rd 535 in polar T2
Processed file: PhD/POLAR/processed/TAN1 in polar/figure 25 in polar

Figure 26:
lif file: PhD/pictures/confocal/20220119 DZ245 TAN1 in pan1 T2
Processed file: PhD/POLAR/processed/TAN1 in WT and pan1/figure 26 in pan1

Figure 27B:
WT:
lif file: PhD/pictures/confocal/20220119 DZ244 TAN1 in WT T2
Processed file: PhD/POLAR/processed/20220119 DZ244 TAN1 in WT T2

bdpan1-1:
lif file: PhD/pictures/confocal/20220119 DZ245 TAN1 in pan1 T2
Processed file: PhD/POLAR/processed/20220119 DZ245 TAN1 in pan1 T2

bdpolar-1:
lif file: PhD/pictures/confocol/20220207 TAN1 in polar T0; 20220301 2nd leaf 535 in polar T2; 20220307 3rd 535 in polar T2
Processed file: PhD/POLAR/processed/TAN1 in polar

Figure 27C:
Input file: PhD/POLAR/TAN1/TAN1 new.csv
Code file: PhD/POLAR/TAN1/TAN1 new.R
Output file: PhD/POLAR/TAN1/TAN1 new.pdf

Figure 28B:
DIC: PhD/POLAR/Quantification/Division quantification/division type picture

Figure 28C:
Input file: PhD/POLAR/Quantification/Division quantification/only polar and pan1.csv
Code file: PhD/POLAR/Quantification/Division quantification/only polar and pan1.R
Output file: PhD/POLAR/Quantification/Division quantification/only polar and pan1.pdf

Figure 29B:
Input file: PhD/POLAR/Nuclei data/R5R6 one two SC/one cell all.csv

Code file: PhD/POLAR/Nuclei data/R5R6 one two SC/one cell all.R
Output file: PhD/POLAR/Nuclei data/R5R6 one two SC/one cell all.pdf

Figure 29D:
PhD/POLAR/Nuclei data/R5R6 one two SC/ two SCs all.csv
Code file: PhD/POLAR/Nuclei data/R5R6 one two SC/ two SCs all.R
Output file: PhD/POLAR/Nuclei data/R5R6 one two SC/ two SCs all.pdf

Figure 30:
pdf: PhD/POLAR/Li cor/202112 li cor results

Figure 31A:
Input file: PhD/POLAR/ Li cor/LEAF/ Li cor 20X.csv
Code file: PhD/POLAR/ Li cor/LEAF/ Li cor 20X.R
Output file: PhD/POLAR/ Li cor/LEAF/ stomatal density.pdf

Figure 31B:
Input file: PhD/POLAR/ Li cor/GC length/ n=5 GC length.csv
Code file: PhD/POLAR/ Li cor/GC length/ n=5 GC length.R

Output file: PhD/POLAR/ Li cor/GC length/ n=5 GC length.pdf

Figure 31C, D and E:
pdf: PhD/POLAR/Li cor/kinetic

Figure 32:
lif file: PhD/pictures/confocal/20211013 DZ231 POLAR-MYR T1
Processed file: PhD/processed/20211013 DZ231 POLAR-MYR T1

Figure 33:
lif file: PhD/pictures/confocal/20210710 T076 529 polar T0
Processed file: PhD/processed/20210710 T076 529 polar T0

Figure 34:
Input file: PhD/POLAR/polar complemented/MYR only.csv
Code file: PhD/POLAR/polar complemented/MYR only.R
Output file: PhD/POLAR/polar complemented/MYR only.pdf

Figure 35:
lif file: PhD/pictures/confocal/20210601 #534 in pan1 #1
Processed file: PhD/processed/20210601 #534 in pan1 #1

Figure 36:
lif file: PhD/pictures/confocal/20210301 POLAR OE DZ184 5days
Processed file: PhD/processed/20210301 POLAR OE DZ184 5days

Figure 37:
lif file: PhD/pictures/confocal/20211020 T090 559 in WT T0
Processed file: PhD/processed/20211020 T090 559 in WT T0

Figure 38A:
lif file: PhD/pictures/confocal/20211013 DZ230 LifAct in WT T1
Processed file: PhD/processed/20211013 DZ230 LifAct in WT T1

Figure 38B:
lif file: PhD/pictures/confocal/20210725 498 in WT T0 RT#1
Processed file: PhD/processed/20210725 498 in WT T0 RT#1

Figure 39A:
lif file: PhD/pictures/confocal/20211013 DZ223 LifeAct in polar T1
Processed file: PhD/processed/20211013 DZ223 LifeAct in polar T1

Figure 39B:
lif file: PhD/pictures/confocal/20210601 498 in polar T0 #1
Processed file: PhD/processed/20210601 498 in polar T0 #1

Figure 40A:
lif file: PhD/pictures/confocal/20211013 DZ232 LifeAct in pan1 T1
Processed file: PhD/processed/20211013 DZ232 LifeAct in pan1 T1

Figure 40B:
lif file: PhD/pictures/confocal/20210731 T077 498 in pan1
Processed file: PhD/processed/20210731 T077 498 in pan1

Figure 41:
lif file: PhD/pictures/confocal/20200909 actin (wt/polar/pan1/polarpan1)
Processed file: PhD/processed/20200909 actin all genotypes

Figure 42:
lif file: PhD/pictures/confocal/20220126 428 in polar T0
Processed file: PhD/processed/20220126 428 in polar T0

Figure 43:
lif file: PhD/pictures/confocal/20211020 T090 429 in pan1 T0
Processed file: PhD/processed/20211020 T090 429 in pan1 T0

Figure 44A:
PhD/pictures/gel/2020.08.18 and 19

Figure 44B:
DIC: PhD/POLAR-like/POLAR-like NaN lines/20200713 F1 DZ151 NaN1927

Figure 44C and D:
DIC: PhD/POLAR-like/NaN2048 and 2069

Figure 45:
DIC: PhD/POLAR-like/20220302 DZ251 polar-like/figures

Figure 46:
DIC:PhD/POLAR/POLAR and POLAR-LIKE/20220216 452/figure

Figure 47:
lif file: PhD/pictures/confocal/20220117 POLAR-LIKE T1 2nd leaf
Processed file: PhD/processed/20220117 POLAR-LIKE T1 2nd leaf

Figure 48:
lif file: PhD/pictures/confocal/20220117 POLAR-LIKE T1 2nd leaf
Processed file: PhD/processed/20220117 POLAR-LIKE T1 2nd leaf

Figure 49:
lif file: PhD/pictures/confocal/20210518 PPZ 3+7 days 3rd
Processed file: PhD/processed/20210518 PPZ 3+7 days 3rd

Figure 50:
PhD/Kim-BR/Final Report and Presentation

Figure 51:
lif file: PhD/pictures/confocal/20200121 PM+WT 5days
Processed file: PhD/time-lapse imaging/20200121 PM+WT 5days

Figure 52:
PhD/string/POLAR

Figure 53:
PhD/string/PAN1

Figure 54:
PhD/processed/thesis model

Supplemental Figure 1:
lif file: PhD/pictures/confocal/20210114 wt 5days PI
Processed file: PhD/processed/All genotypes PI develop/20210114 wt

Supplemental Figure 2:

lif file: PhD/pictures/confocal/20201221 polar-1 5days PI
Processed file: PhD/processed/All genotypes PI develop/20201221 polar-1

Supplemental Figure 3:
lif file: PhD/pictures/confocal/20201221 pan1 5days PI
Processed file: PhD/processed/All genotypes PI develop/20201221 pan1

Supplemental Figure 4:
lif file: PhD/pictures/confocal/20210114 polarpan1 5days PI
Processed file: PhD/processed/All genotypes PI develop/20210114 polarpan1

Supplemental Figure 5:
Processed file: PhD/processed/POLAR in WT

Supplemental Figure 6:
Processed file: PhD/processed/PAN1 in WT

Supplemental Figure 7:
lif file: PhD/pictures/confocal/20210206 DZ126-1 POLAR-NLS 5days
Processed file: PhD/processed/20210206 DZ171 from DZ126-1 POLAR-NLS 5days

Supplemental Figure 8:
Processed file: PhD/processed/nuclei imaging/wt

Supplemental Figure 9:
Processed file: PhD/processed/nuclei imaging/polar

Supplemental Figure 10:
Processed file: PhD/processed/nuclei imaging/pan1

Supplemental Figure 11:
Processed file: PhD/processed/nuclei imaging/polarpan1

Supplemental Figure 12:
lif file: PhD/pictures/confocal/20220119 DZ244 TAN1 in WT T2
Processed file: PhD/processed/TAN1 in WT and pan1

Supplemental Figure 13:
lif file: PhD/pictures/confocal/20220119 DZ244 TAN1 in WT T2
Processed file: PhD/processed/TAN1 in WT and pan1/TAN1 in WT stages

Supplemental Figure 14:
Processed file: PhD/processed/TAN1 in polar

Supplemental Figure 15:
Processed file: PhD/processed/TAN1 in polar/TAN1 stages T0 and T2

Supplemental Figure 16:
lif file: PhD/pictures/confocal/20220119 DZ245 TAN1 in pan1 T2
Processed file: PhD/processed/TAN1 in WT and pan1

Supplemental Figure 17:
lif file: PhD/pictures/confocal/20220119 DZ245 TAN1 in pan1 T2
Processed file: PhD/processed/TAN1 in WT and pan1/TAN1 in pan1 stages

Supplemental Figure 18:
lif file: PhD/pictures/confocal/20211013 DZ231 POLAR-MYR T1

Processed file: PhD/processed/20211013 DZ231 POLAR-MYR T1

Supplemental Figure 19:
lif file: PhD/pictures/confocal/20211013 DZ231 POLAR-MYR T1
Processed file: PhD/processed/20211013 DZ231 POLAR-MYR T1

Supplemental Figure 20:
lif file: PhD/pictures/confocal/20211013 DZ231 POLAR-MYR T1
Processed file: PhD/processed/20211013 DZ231 POLAR-MYR T1

Supplemental Figure 21:
lif file: PhD/pictures/confocal/20220117 POLAR C-OE T1
Processed file: PhD/processed/20220117 POLAR C-OE T1

References

Abrash, E., M. X. Anleu Gil, J. L. Matos and D. C. Bergmann (2018). "Conservation and divergence of YODA MAPKKK function in regulation of grass epidermal patterning." Development 145(14).

Adamowski, M. and J. Friml (2015). "PIN-dependent auxin transport: action, regulation, and evolution." Plant Cell 27(1): 20-32.

Adams, A. E., D. Botstein and D. G. Drubin (1991). "Requirement of yeast fimbrin for actin organization and morphogenesis in vivo." Nature 354(6352): 404-408.

Al-Bassam, J., R. S. Ozer, D. Safer, S. Halpain and R. A. Milligan (2002). "MAP2 and tau bind longitudinally along the outer ridges of microtubule protofilaments." J Cell Biol 157(7): 1187-1196.

Al-Bassam, J., R. S. Ozer, D. Safer, S. Halpain and R. A. Milligan (2002). "MAP2 and tau bind longitudinally along the outer ridges of microtubule protofilaments." Journal of Cell Biology 157(7): 1187-1196.

Alves, S. C., B. Worland, V. Thole, J. W. Snape, M. W. Bevan and P. Vain (2009). "A protocol for Agrobacterium-mediated transformation of Brachypodium distachyon community standard line Bd21." Nat Protoc 4(5): 638-649.

Anne, P., M. Azzopardi, L. Gissot, S. Beaubiat, K. Hematy and J. C. Palauqui (2015). "OCTOPUS Negatively Regulates BIN2 to Control Phloem Differentiation in Arabidopsis thaliana." Curr Biol 25(19): 2584-2590.

Auerbach, D. and I. Stagljar (2005). Yeast Two-Hybrid Protein-Protein Interaction Networks. Proteomics and Protein-Protein Interactions: Biology, Chemistry, Bioinformatics, and Drug Design. G. Waksman. Boston, MA, Springer US: 19-31.

Barnhart, J. H. (1895). "Family Nomenclature." Bulletin of the Torrey Botanical Club 22(1): 1-24.

Benkova, E., M. Michniewicz, M. Sauer, T. Teichmann, D. Seifertova, G. Jurgens and J. Friml (2003). "Local, efflux-dependent auxin gradients as a common module for plant organ formation." Cell 115(5): 591-602.

Berken, A., C. Thomas and A. Wittinghofer (2005). "A new family of RhoGEFs activates the Rop molecular switch in plants." Nature 436(7054): 1176-1180.

Bi, G. Z., M. Su, N. Li, Y. Liang, S. Dang, J. C. Xu, M. J. Hu, J. Z. Wang, M. X. Zou, Y. A. Deng, Q. Y. Li, S. J. Huang, J. J. Li, J. J. Chai, K. M. He, Y. H. Chen and J. M. Zhou (2021). "The ZAR1 resistosome is a calcium-permeable channel triggering plant immune signaling." Cell 184(13): 3528-+.

Bischoff, F., L. Vahlkamp, A. Molendijk and K. Palme (2000). "Localization of AtROP4 and AtROP6 and interaction with the guanine nucleotide dissociation inhibitor AtRhoGDI1 from Arabidopsis." Plant Molecular Biology 42(3): 515-530.

Blilou, I., J. Xu, M. Wildwater, V. Willemsen, I. Paponov, J. Friml, R. Heidstra, M. Aida, K. Palme and B. Scheres (2005). "The PIN auxin efflux facilitator network controls growth and patterning in Arabidopsis roots." Nature 433(7021): 39-44.

Bragg, J. N., J. Wu, S. P. Gordon, M. E. Guttman, R. Thilmony, G. R. Lazo, Y. Q. Gu and J. P. Vogel (2012). "Generation and Characterization of the Western Regional Research

Center Brachypodium T-DNA Insertional Mutant Collection." PLOS ONE 7(9): e41916.

Branon, T. C., J. A. Bosch, A. D. Sanchez, N. D. Udeshi, T. Svinkina, S. A. Carr, J. L. Feldman, N. Perrimon and A. Y. Ting (2018). "Efficient proximity labeling in living cells and organisms with TurboID." Nat Biotechnol 36(9): 880-887.

Bresnick, A. R., V. Warren and J. Condeelis (1990). "Identification of a short sequence essential for actin binding by Dictyostelium ABP-120." Journal of Biological Chemistry 265(16): 9236-9240.

Bretscher, A. and K. Weber (1980). "Fimbrin, a New Microfilament-Associated Protein Present in Microvilli and Other Cell-Surface Structures." Journal of Cell Biology 86(1): 335-340.

Bringmann, M. and D. C. Bergmann (2017). "Tissue-wide Mechanical Forces Influence the Polarity of Stomatal Stem Cells in Arabidopsis." Curr Biol 27(6): 877-883.

Brkljacic, J., E. Grotewold, R. Scholl, T. Mockler, D. F. Garvin, P. Vain, T. Brutnell, R. Sibout, M. Bevan, H. Budak, A. L. Caicedo, C. Gao, Y. Gu, S. P. Hazen, B. F. Holt, 3rd, S. Y. Hong, M. Jordan, A. J. Manzaneda, T. Mitchell-Olds, K. Mochida, L. A. Mur, C. M. Park, J. Sedbrook, M. Watt, S. J. Zheng and J. P. Vogel (2011). "Brachypodium as a model for the grasses: today and the future." Plant Physiol 157(1): 3-13.

Buchsenschutz, K., I. Marten, D. Becker, K. Philippar, P. Ache and R. Hedrich (2005). "Differential expression of K+ channels between guard cells and subsidiary cells within the maize stomatal complex." Planta 222(6): 968-976.

Caine, R. S., X. J. Yin, J. Sloan, E. L. Harrison, U. Mohammed, T. Fulton, A. K. Biswal, J. Dionora, C. C. Chater, R. A. Coe, A. Bandyopadhyay, E. H. Murchie, R. Swarup, W. P. Quick and J. E. Gray (2019). "Rice with reduced stomatal density conserves water and has improved drought tolerance under future climate conditions." New Phytologist 221(1): 371-384.

Camilleri, C., J. Azimzadeh, M. Pastuglia, C. Bellini, O. Grandjean and D. Bouchez (2002). "The Arabidopsis TONNEAU2 gene encodes a putative novel protein phosphatase 2A regulatory subunit essential for the control of the cortical cytoskeleton." Plant Cell 14(4): 833-845.

Cartwright, H. N., J. A. Humphries and L. G. Smith (2009). "PAN1: a receptor-like protein that promotes polarization of an asymmetric cell division in maize." Science 323(5914): 649-651.

Čermák, T., S. J. Curtin, J. Gil-Humanes, R. Čegan, T. J. Y. Kono, E. Konečná, J. J. Belanto, C. G. Starker, J. W. Mathre, R. L. Greenstein and D. F. Voytas (2017). "A Multipurpose Toolkit to Enable Advanced Genome Engineering in Plants." The Plant Cell 29(6): 1196-1217.

Chater, C. C., R. S. Caine, M. Tomek, S. Wallace, Y. Kamisugi, A. C. Cuming, D. Lang, C. A. MacAlister, S. Casson, D. C. Bergmann, E. L. Decker, W. Frank, J. E. Gray, A. Fleming, R. Reski and D. J. Beerling (2016). "Origin and function of stomata in the moss Physcomitrella patens." Nat Plants 2: 16179.

Chen, Z. H., G. Chen, F. Dai, Y. Wang, A. Hills, Y. L. Ruan, G. Zhang, P. J. Franks, E. Nevo and M. R. Blatt (2017). "Molecular Evolution of Grass Stomata." Trends Plant Sci 22(2): 124-139.

Chinnusamy, V., M. Ohta, S. Kanrar, B. H. Lee, X. Hong, M. Agarwal and J. K. Zhu (2003).

"ICE1: a regulator of cold-induced transcriptome and freezing tolerance in Arabidopsis." Genes Dev 17(8): 1043-1054.

Cho, H., H. Ryu, S. Rho, K. Hill, S. Smith, D. Audenaert, J. Park, S. Han, T. Beeckman, M. J. Bennett, D. Hwang, I. De Smet and I. Hwang (2014). "A secreted peptide acts on BIN2-mediated phosphorylation of ARFs to potentiate auxin response during lateral root development." Nat Cell Biol 16(1): 66-76.

Chono, M., I. Honda, H. Zeniya, K. Yoneyama, D. Saisho, K. Takeda, S. Takatsuto, T. Hoshino and Y. Watanabe (2003). "A semidwarf phenotype of barley uzu results from a nucleotide substitution in the gene encoding a putative brassinosteroid receptor." Plant Physiol 133(3): 1209-1219.

Cleary, A. L. and L. G. Smith (1998). "The Tangled1 Gene Is Required for Spatial Control of Cytoskeletal Arrays Associated with Cell Division during Maize Leaf Development." The Plant Cell 10(11): 1875-1888.

Collings, D. A. and G. O. Wasteneys (2005). "Actin microfilament and microtubule distribution patterns in the expanding root ofArabidopsis thaliana." Canadian Journal of Botany 83(6): 579-590.

Cong, L., F. A. Ran, D. Cox, S. Lin, R. Barretto, N. Habib, P. D. Hsu, X. Wu, W. Jiang, L. A. Marraffini and F. Zhang (2013). "Multiplex genome engineering using CRISPR/Cas systems." Science 339(6121): 819-823.

Conlan, B., T. Stoll, J. J. Gorman, I. Saur and J. P. Rathjen (2018). "Development of a Rapid in planta BioID System as a Probe for Plasma Membrane-Associated Immunity Proteins." Front Plant Sci 9: 1882.

Cooper, J. A. (1987). "Effects of Cytochalasin and Phalloidin on Actin." Journal of Cell Biology 105(4): 1473-1478.

Corvalan, C. and S. Choe (2017). "Identification of brassinosteroid genes in Brachypodium distachyon." Bmc Plant Biology 17.

Craddock, C., I. Lavagi and Z. Yang (2012). "New insights into Rho signaling from plant ROP/Rac GTPases." Trends Cell Biol 22(9): 492-501.

de Vries, S. C. (2007). "14-3-3 proteins in plant brassinosteroid signaling." Dev Cell 13(2): 162-164.

Dearruda, M. V., S. Watson, C. S. Lin, J. Leavitt and P. Matsudaira (1990). "Fimbrin Is a Homolog of the Cytoplasmic Phosphoprotein Plastin and Has Domains Homologous with Calmodulin and Actin Gelation Proteins." Journal of Cell Biology 111(3): 1069-1079.

Debernardi, J. M., D. M. Tricoli, M. F. Ercoli, S. Hayta, P. Ronald, J. F. Palatnik and J. Dubcovsky (2020). "A GRF-GIF chimeric protein improves the regeneration efficiency of transgenic plants." Nat Biotechnol 38(11): 1274-1279.

Dong, J. and D. C. Bergmann (2010). "Stomatal patterning and development." Curr Top Dev Biol 91: 267-297.

Dong, J., C. A. MacAlister and D. C. Bergmann (2009). "BASL controls asymmetric cell division in Arabidopsis." Cell 137(7): 1320-1330.

Draper, J., L. A. J. Mur, G. Jenkins, G. C. Ghosh-Biswas, P. Bablak, R. Hasterok and A. P. M. Routledge (2001). "Brachypodium distachyon. A New Model System for Functional

Genomics in Grasses." Plant Physiology 127(4): 1539-1555.

Drewes, G., A. Ebneth and E. M. Mandelkow (1998). "MAPs, MARKs and microtubule dynamics." Trends in Biochemical Sciences 23(8): 307-311.

Dunn, J., L. Hunt, M. Afsharinafar, M. Al Meselmani, A. Mitchell, R. Howells, E. Wallington, A. J. Fleming and J. E. Gray (2019). "Reduced stomatal density in bread wheat leads to increased water-use efficiency." Journal of Experimental Botany 70(18): 4737-4747.

Era, A., M. Tominaga, K. Ebine, C. Awai, C. Saito, K. Ishizaki, K. T. Yamato, T. Kohchi, A. Nakano and T. Ueda (2009). "Application of Lifeact reveals F-actin dynamics in Arabidopsis thaliana and the liverwort, Marchantia polymorpha." Plant Cell Physiol 50(6): 1041-1048.

Facette, M. R., Y. Park, D. Sutimantanapi, A. Luo, H. N. Cartwright, B. Yang, E. J. Bennett, A. W. Sylvester and L. G. Smith (2015). "The SCAR/WAVE complex polarizes PAN receptors and promotes division asymmetry in maize." Nat Plants 1: 14024.

Facette, M. R. and L. G. Smith (2012). "Division polarity in developing stomata." Curr Opin Plant Biol 15(6): 585-592.

Feng, Y., Y. H. Yin and S. Z. Fei (2015). "Down-regulation of BdBRI1, a putative brassinosteroid receptor gene produces a dwarf phenotype with enhanced drought tolerance in Brachypodium distachyon." Plant Science 234: 163-173.

Franks, P. J. and G. D. Farquhar (2007). "The mechanical diversity of stomata and its significance in gas-exchange control." Plant Physiol 143(1): 78-87.

Friml, J., A. Vieten, M. Sauer, D. Weijers, H. Schwarz, T. Hamann, R. Offringa and G. Jurgens (2003). "Efflux-dependent auxin gradients establish the apical-basal axis of Arabidopsis." Nature 426(6963): 147-153.

Fu, Y., H. Li and Z. B. Yang (2002). "The ROP2 GTPase controls the formation of cortical fine F-actin and the early phase of directional cell expansion during Arabidopsis organogenesis." Plant Cell 14(4): 777-794.

Fu, Y. and Z. B. Yang (2001). "Rop GTPase: a master switch of cell polarity development in plants." Trends in Plant Science 6(12): 545-547.

Fujita, M., R. Himmelspach, C. H. Hocart, R. E. Williamson, S. D. Mansfield and G. O. Wasteneys (2011). "Cortical microtubules optimize cell-wall crystallinity to drive unidirectional growth in Arabidopsis." Plant J 66(6): 915-928.

Gallagher, K. and L. G. Smith (1999). "discordia mutations specifically misorient asymmetric cell divisions during development of the maize leaf epidermis." Development 126(20): 4623-4633.

Gallei, M., C. Luschnig and J. Friml (2020). "Auxin signalling in growth: Schrodinger's cat out of the bag." Curr Opin Plant Biol 53: 43-49.

Geisler, M., J. Nadeau and F. D. Sack (2000). "Oriented asymmetric divisions that generate the stomatal spacing pattern in Arabidopsis are disrupted by the too many mouths mutation." Plant Cell 12(11): 2075-2086.

Geisler, M., M. Yang and F. D. Sack (1998). "Divergent regulation of stomatal initiation and patterning in organ and suborgan regions of the Arabidopsis mutants too many mouths and four lips." Planta 205(4): 522-530.

Geitmann, A. and A. Nebenfuhr (2015). "Navigating the plant cell: intracellular transport logistics in the green kingdom." Mol Biol Cell 26(19): 3373-3378.

Giannoutsou, E., P. Apostolakos and B. Galatis (2016). "Spatio-temporal diversification of the cell wall matrix materials in the developing stomatal complexes of Zea mays." Planta 244(5): 1125-1143.

Gibbon, B. C., D. R. Kovar and C. J. Staiger (1999). "Latrunculin B has different effects on pollen germination and tube growth." Plant Cell 11(12): 2349-2363.

Gibson, D. G., L. Young, R.-Y. Chuang, J. C. Venter, C. A. Hutchison and H. O. Smith (2009). "Enzymatic assembly of DNA molecules up to several hundred kilobases." Nature Methods 6(5): 343-345.

Gong, Y., J. Alassimone, R. Varnau, N. Sharma, L. S. Cheung and D. C. Bergmann (2021). "Tuning self-renewal in the Arabidopsis stomatal lineage by hormone and nutrient regulation of asymmetric cell division." Elife 10.

Gong, Y., R. Varnau, E. S. Wallner, R. Acharya, D. C. Bergmann and L. S. Cheung (2020). "Quantitative and dynamic cell polarity tracking in plant cells." New Phytol.

Gonzalez-Garcia, M. P., J. Vilarrasa-Blasi, M. Zhiponova, F. Divol, S. Mora-Garcia, E. Russinova and A. I. Cano-Delgado (2011). "Brassinosteroids control meristem size by promoting cell cycle progression in Arabidopsis roots." Development 138(5): 849-859.

Goodstein, D. M., S. Shu, R. Howson, R. Neupane, R. D. Hayes, J. Fazo, T. Mitros, W. Dirks, U. Hellsten, N. Putnam and D. S. Rokhsar (2012). "Phytozome: a comparative platform for green plant genomics." Nucleic Acids Res 40(Database issue): D1178-1186.

Griffis, A. H., N. R. Groves, X. Zhou and I. Meier (2014). "Nuclei in motion: movement and positioning of plant nuclei in development, signaling, symbiosis, and disease." Front Plant Sci 5: 129.

Guan, Y., J. Guo, H. Li and Z. Yang (2013). "Signaling in pollen tube growth: crosstalk, feedback, and missing links." Mol Plant 6(4): 1053-1064.

Gudesblat, G. E., J. Schneider-Pizon, C. Betti, J. Mayerhofer, I. Vanhoutte, W. van Dongen, S. Boeren, M. Zhiponova, S. de Vries, C. Jonak and E. Russinova (2012). "SPEECHLESS integrates brassinosteroid and stomata signalling pathways." Nature Cell Biology 14(5): 548-U214.

Guo, X., C. H. Park, Z. Y. Wang, B. E. Nickels and J. Dong (2021). "A spatiotemporal molecular switch governs plant asymmetric cell division." Nat Plants 7(5): 667-680.

Guo, X., L. Wang and J. Dong (2021). "Establishing asymmetry: stomatal division and differentiation in plants." New Phytol 232(1): 60-67.

Hamada, T. (2007). "Microtubule-associated proteins in higher plants." J Plant Res 120(1): 79-98.

Han, S., J. Li and A. Y. Ting (2018). "Proximity labeling: spatially resolved proteomic mapping for neurobiology." Current Opinion in Neurobiology 50: 17-23.

Han, S. K., X. Qi, K. Sugihara, J. H. Dang, T. A. Endo, K. L. Miller, E. D. Kim, T. Miura and K. U. Torii (2018). "MUTE Directly Orchestrates Cell-State Switch and the Single Symmetric Division to Create Stomata." Dev Cell 45(3): 303-315 e305.

Hara, K., R. Kajita, K. U. Torii, D. C. Bergmann and T. Kakimoto (2007). "The secretory peptide gene EPF1 enforces the stomatal one-cell-spacing rule." Genes & Development 21(14): 1720-1725.

Hara, K., T. Yokoo, R. Kajita, T. Onishi, S. Yahata, K. M. Peterson, K. U. Torii and T. Kakimoto (2009). "Epidermal Cell Density is Autoregulated via a Secretory Peptide, EPIDERMAL PATTERNING FACTOR 2 in Arabidopsis Leaves." Plant and Cell Physiology 50(6): 1019-1031.

Hashimoto-Sugimoto, M., T. Higaki, T. Yaeno, A. Nagami, M. Irie, M. Fujimi, M. Miyamoto, K. Akita, J. Negi, K. Shirasu, S. Hasezawa and K. Iba (2013). "A Munc13-like protein in Arabidopsis mediates H+-ATPase translocation that is essential for stomatal responses." Nat Commun 4: 2215.

He, J. X., J. M. Gendron, Y. Yang, J. Li and Z. Y. Wang (2002). "The GSK3-like kinase BIN2 phosphorylates and destabilizes BZR1, a positive regulator of the brassinosteroid signaling pathway in Arabidopsis." Proc Natl Acad Sci U S A 99(15): 10185-10190.

Herrmann, A., P. Livanos, E. Lipka, A. Gadeyne, M. T. Hauser, D. Van Damme and S. Müller (2018). "Dual localized kinesin-12 POK2 plays multiple roles during cell division and interacts with MAP65-3." EMBO Rep 19(9).

Hetherington, A. M. and F. I. Woodward (2003). "The role of stomata in sensing and driving environmental change." Nature 424(6951): 901-908.

Higaki, T., M. Hashimoto-Sugimoto, K. Akita, K. Iba and S. Hasezawa (2014). "Dynamics and environmental responses of PATROL1 in Arabidopsis subsidiary cells." Plant Cell Physiol 55(4): 773-780.

Holweg, C. L. (2007). "Living markers for actin block myosin-dependent motility of plant organelles and auxin." Cell Motil Cytoskeleton 64(2): 69-81.

Houbaert, A., C. Zhang, M. Tiwari, K. Wang, A. de Marcos Serrano, D. V. Savatin, M. J. Urs, M. K. Zhiponova, G. E. Gudesblat, I. Vanhoutte, D. Eeckhout, S. Boeren, M. Karimi, C. Betti, T. Jacobs, C. Fenoll, M. Mena, S. de Vries, G. De Jaeger and E. Russinova (2018). "POLAR-guided signalling complex assembly and localization drive asymmetric cell division." Nature 563(7732): 574-578.

Hu, Y. X., F. Bao and J. Y. Li (2000). "Promotive effect of brassinosteroids on cell division involves a distinct CycD3-induction pathway in Arabidopsis." Plant Journal 24(5): 693-701.
Hugdahl, J. D., C. L. Bokros, V. R. Hanesworth, G. R. Aalund and L. C. Morejohn (1993). "Unique Functional-Characteristics of the Polymerization and Map Binding Regulatory Domains of Plant Tubulin." Plant Cell 5(9): 1063-1080.

Hughes, J., C. Hepworth, C. Dutton, J. A. Dunn, L. Hunt, J. Stephens, R. Waugh, D. D. Cameron and J. E. Gray (2017). "Reducing Stomatal Density in Barley Improves Drought Tolerance without Impacting on Yield." Plant Physiology 174(2): 776-787.

Humphries, J. A., Z. Vejlupkova, A. Luo, R. B. Meeley, A. W. Sylvester, J. E. Fowler and L. G. Smith (2011). "ROP GTPases act with the receptor-like protein PAN1 to polarize asymmetric cell division in maize." Plant Cell 23(6): 2273-2284.

Hunt, L., K. J. Bailey and J. E. Gray (2010). "The signalling peptide EPFL9 is a positive regulator of stomatal development." New Phytologist 186(3): 609-614.

Hussey, P. J., T. Ketelaar and M. J. Deeks (2006). "Control of the actin cytoskeleton in plant cell growth." Annu Rev Plant Biol 57: 109-125.

Imkampe, J., T. Halter, S. H. Huang, S. Schulze, S. Mazzotta, N. Schmidt, R. Manstretta, S. Postel, M. Wierzba, Y. Yang, W. M. A. M. van Dongen, M. Stahl, C. Zipfel, M. B. Goshe, S. Clouse, S. C. de Vries, F. Tax, X. F. Wang and B. Kemmerling (2017). "The Arabidopsis Leucine-Rich Repeat Receptor Kinase BIR3 Negatively Regulates BAK1 Receptor Complex Formation and Stabilizes BAK1." Plant Cell 29(9): 2285-2303.

International Brachypodium, I. (2010). "Genome sequencing and analysis of the model grass Brachypodium distachyon." Nature 463(7282): 763-768.

Ito, M., C. MarieClaire, M. Sakabe, T. Ohno, S. Hata, H. Kouchi, J. Hashimoto, H. Fukuda, A. Komamine and A. Watanabe (1997). "Cell-cycle-regulated transcription of A- and B-type plant cyclin genes in synchronous cultures." Plant Journal 11(5): 983-992.

Jasechko, S., Z. D. Sharp, J. J. Gibson, S. J. Birks, Y. Yi and P. J. Fawcett (2013). "Terrestrial water fluxes dominated by transpiration." Nature 496(7445): 347-350.

Jinek, M., K. Chylinski, I. Fonfara, M. Hauer, J. A. Doudna and E. Charpentier (2012). "A Programmable Dual-RNA–Guided DNA Endonuclease in Adaptive Bacterial Immunity." Science 337(6096): 816-821.

Jones, M. A., M. J. Raymond and N. Smirnoff (2006). "Analysis of the root-hair morphogenesis transcriptome reveals the molecular identity of six genes with roles in root-hair development in Arabidopsis." Plant Journal 45(1): 83-100.

Jones, M. A., J. J. Shen, Y. Fu, H. Li, Z. B. Yang and C. S. Grierson (2002). "The Arabidopsis Rop2 GTPase is a positive regulator of both root hair initiation and tip growth." Plant Cell 14(4): 763-776.

Kanaar, R., J. H. Hoeijmakers and D. C. van Gent (1998). "Molecular mechanisms of DNA double strand break repair." Trends Cell Biol 8(12): 483-489.

Kanaoka, M. M., L. J. Pillitteri, H. Fujii, Y. Yoshida, N. L. Bogenschutz, J. Takabayashi, J. K. Zhu and K. U. Torii (2008). "SCREAM/ICE1 and SCREAM2 specify three cell-state transitional steps leading to arabidopsis stomatal differentiation." Plant Cell 20(7): 1775-1785.

Kang, Y. H., A. Breda and C. S. Hardtke (2017). "Brassinosteroid signaling directs formative cell divisions and protophloem differentiation in Arabidopsis root meristems." Development 144(2): 272-280.

Keller, B. and C. Feuillet (2000). "Colinearity and gene density in grass genomes." Trends Plant Sci 5(6): 246-251.

Kerppola, T. K. (2006). "Design and implementation of bimolecular fluorescence complementation (BiFC) assays for the visualization of protein interactions in living cells." Nature Protocols 1(3): 1278-1286.

Khan, M., J.-Y. Youn, A.-C. Gingras, R. Subramaniam and D. Desveaux (2018). "In planta proximity dependent biotin identification (BioID)." Scientific Reports 8(1): 9212.

Kim, D. I. and K. J. Roux (2016). "Filling the Void: Proximity-Based Labeling of Proteins in Living Cells." Trends Cell Biol 26(11): 804-817.

Kim, T.-W., C. H. Park, C.-C. Hsu, J.-Y. Zhu, Y. Hsiao, T. Branon, S.-L. Xu, A. Y. Ting and Z.-Y. Wang (2019). "Application of TurboID-mediated proximity labeling for mapping a GSK3 kinase signaling network in Arabidopsis." bioRxiv: 636324.

Kim, T. H., M. Bohmer, H. Hu, N. Nishimura and J. I. Schroeder (2010). "Guard cell signal transduction network: advances in understanding abscisic acid, CO2, and Ca2+ signaling." Annu Rev Plant Biol 61: 561-591.

Kim, T. W., M. Michniewicz, D. C. Bergmann and Z. Y. Wang (2012). "Brassinosteroid regulates stomatal development by GSK3-mediated inhibition of a MAPK pathway." Nature 482(7385): 419-U1526.

Kimata, Y., T. Higaki, T. Kawashima, D. Kurihara, Y. Sato, T. Yamada, S. Hasezawa, F. Berger, T. Higashiyama and M. Ueda (2016). "Cytoskeleton dynamics control the first asymmetric cell division in Arabidopsis zygote." Proc Natl Acad Sci U S A 113(49): 14157-14162.

Kir, G., H. Ye, H. Nelissen, A. K. Neelakandan, A. S. Kusnandar, A. Luo, D. Inze, A. W. Sylvester, Y. Yin and P. W. Becraft (2015). "RNA Interference Knockdown of BRASSINOSTEROID INSENSITIVE1 in Maize Reveals Novel Functions for Brassinosteroid Signaling in Controlling Plant Architecture." Plant Physiol 169(1): 826-839.

Kirik, A., D. W. Ehrhardt and V. Kirik (2012). "TONNEAU2/FASS Regulates the Geometry of Microtubule Nucleation and Cortical Array Organization in Interphase Arabidopsis Cells." Plant Cell 24(3): 1158-1170.

Kollist, H., M. Nuhkat and M. R. Roelfsema (2014). "Closing gaps: linking elements that control stomatal movement." New Phytol 203(1): 44-62.

Kopczak, S. D., N. A. Haas, P. J. Hussey, C. D. Silflow and D. P. Snustad (1992). "The small genome of Arabidopsis contains at least six expressed alpha-tubulin genes." The Plant cell 4(5): 539-547.

Kost, B., P. Spielhofer and N. H. Chua (1998). "A GFP-mouse talin fusion protein labels plant actin filaments in vivo and visualizes the actin cytoskeleton in growing pollen tubes." Plant Journal 16(3): 393-401.

Lampropoulos, A., Z. Sutikovic, C. Wenzl, I. Maegele, J. U. Lohmann and J. Forner (2013). "GreenGate---a novel, versatile, and efficient cloning system for plant transgenesis." PLoS One 8(12): e83043.

Lauster, T., D. Stockle, K. Gabor, T. Haller, N. Krieger, P. Lotz, R. Mayakrishnan, E. Spath, S. Zimmermann, P. Livanos and S. Muller (2022). "Arabidopsis pavement cell shape formation involves spatially confined ROPGAP regulators." Current Biology 32(3): 532-+.

Lawson, T. and S. Vialet-Chabrand (2019). "Speedy stomata, photosynthesis and plant water use efficiency." New Phytologist 221(1): 93-98.

Lease, K. A., N. Y. Lau, R. A. Schuster, K. U. Torii and J. C. Walker (2001). "Receptor serine/threonine protein kinases in signalling: analysis of the erecta receptor-like kinase of Arabidopsis thaliana." New Phytol 151(1): 133-143.

Li, J.-F., J. E. Norville, J. Aach, M. McCormack, D. Zhang, J. Bush, G. M. Church and J. Sheen (2013). "Multiplex and homologous recombination–mediated genome editing in Arabidopsis and Nicotiana benthamiana using guide RNA and Cas9." Nature Biotechnology 31(8): 688-691.

Li, J., K. H. Nam, D. Vafeados and J. Chory (2001). "BIN2, a new brassinosteroid-insensitive locus in Arabidopsis." Plant Physiol 127(1): 14-22.

Li, J. M. and J. Chory (1997). "A putative leucine-rich repeat receptor kinase involved in

brassinosteroid signal transduction." Cell 90(5): 929-938.

Lijavetzky, D., P. Carbonero and J. Vicente-Carbajosa (2003). "Genome-wide comparative phylogenetic analysis of the rice and Arabidopsis Dof gene families." BMC Evol Biol 3: 17.

Lin, J.-S. and E.-M. Lai (2017). Protein–Protein Interactions: Co-Immunoprecipitation. Bacterial Protein Secretion Systems: Methods and Protocols. L. Journet and E. Cascales. New York, NY, Springer New York: 211-219.

Lin, Q., Z. Zhou, W. Luo, M. Fang, M. Li and H. Li (2017). "Screening of Proximal and Interacting Proteins in Rice Protoplasts by Proximity-Dependent Biotinylation." Front Plant Sci 8: 749.

Lipka, E., A. Gadeyne, D. Stockle, S. Zimmermann, G. De Jaeger, D. W. Ehrhardt, V. Kirik, D. Van Damme and S. Muller (2014). "The Phragmoplast-Orienting Kinesin-12 Class Proteins Translate the Positional Information of the Preprophase Band to Establish the Cortical Division Zone in Arabidopsis thaliana." Plant Cell 26(6): 2617-2632.

Liu, C. M. and D. W. Meinke (1998). "The titan mutants of Arabidopsis are disrupted in mitosis and cell cycle control during seed development." Plant J 16(1): 21-31.

Liu, L. P., L. H. Zhao, P. J. Chen, H. Y. Cai, Z. M. Hou, X. Y. Jin, M. Aslam, M. N. Chai, L. Y. Lai, Q. He, Y. H. Liu, X. Y. Huang, H. H. Chen, Y. Z. Chen and Y. Qin (2020). "ATP binding cassette transporters ABCG1 and ABCG16 affect reproductive development via auxin signalling in Arabidopsis." Plant Journal 102(6): 1172-1186.

Liu, T., K. Ohashi-Ito and D. C. Bergmann (2009). "Orthologs of Arabidopsis thaliana stomatal bHLH genes and regulation of stomatal development in grasses." Development 136(13): 2265-2276.

Livanos, P., B. Galatis and P. Apostolakos (2016). "Deliberate ROS production and auxin synergistically trigger the asymmetrical division generating the subsidiary cells in Zea mays stomatal complexes." Protoplasma 253(4): 1081-1099.

Livanos, P., E. Giannoutsou, P. Apostolakos and B. Galatis (2015). "Auxin as an inducer of asymmetrical division generating the subsidiary cells in stomatal complexes of Zea mays." Plant signaling & behavior 10(3): e984531-e984531.

Livanos, P. and S. Muller (2019). "Division Plane Establishment and Cytokinesis." Annu Rev Plant Biol 70: 239-267.

Lowder, L. G., D. Zhang, N. J. Baltes, J. W. Paul, 3rd, X. Tang, X. Zheng, D. F. Voytas, T. F. Hsieh, Y. Zhang and Y. Qi (2015). "A CRISPR/Cas9 Toolbox for Multiplexed Plant Genome Editing and Transcriptional Regulation." Plant Physiol 169(2): 971-985.

Lu, J. J., J. J. He, X. S. Zhou, J. J. Zhong, J. Li and Y. K. Liang (2019). "Homologous genes of epidermal patterning factor regulate stomatal development in rice." Journal of Plant Physiology 234: 18-27.

Müller, S., S. Han and L. G. Smith (2006). "Two kinesins are involved in the spatial control of cytokinesis in Arabidopsis thaliana." Curr Biol 16(9): 888-894.

MacAlister, C. A. and D. C. Bergmann (2011). "Sequence and function of basic helix-loop-helix proteins required for stomatal development in Arabidopsis are deeply conserved in land plants." Evol Dev 13(2): 182-192.

MacAlister, C. A., K. Ohashi-Ito and D. C. Bergmann (2007). "Transcription factor control

of asymmetric cell divisions that establish the stomatal lineage." Nature 445(7127): 537-540.

Mair, A., S. L. Xu, T. C. Branon, A. Y. Ting and D. C. Bergmann (2019). "Proximity labeling of protein complexes and cell-type-specific organellar proteomes in Arabidopsis enabled by TurboID." Elife 8.

Makarevitch, I., A. Thompson, G. J. Muehlbauer and N. M. Springer (2012). "Brd1 gene in maize encodes a brassinosteroid C-6 oxidase." PLoS One 7(1): e30798.

Manoli, A., S. Trevisan, S. Quaggiotti and S. Varotto (2018). "Identification and characterization of the BZR transcription factor family and its expression in response to abiotic stresses in Zea mays L." Plant Growth Regulation 84(3): 423-436.

Marc, J., C. L. Granger, J. Brincat, D. D. Fisher, T. H. Kao, A. G. McCubbin and R. J. Cyr (1998). "A GFP-MAP4 reporter gene for visualizing cortical microtubule rearrangements in living epidermal cells." Plant Cell 10(11): 1927-1939.

Martinez, P., A. Luo, A. Sylvester and C. G. Rasmussen (2017). "Proper division plane orientation and mitotic progression together allow normal growth of maize." Proc Natl Acad Sci U S A 114(10): 2759-2764.

McCurdy, D. W. and M. Kim (1998). "Molecular cloning of a novel fimbrin-like cDNA from Arabidopsis thaliana." Plant Molecular Biology 36(1): 23-31.

McKown, K. H. and D. C. Bergmann (2020). "Stomatal development in the grasses: lessons from models and crops (and crop models)." New Phytol 227(6): 1636-1648.

Mendrinna, A. and S. Persson (2015). "Root hair growth: it's a one way street." F1000Prime Rep 7: 23.

Miyazawa, Y., N. Nakajima, T. Abe, A. Sakai, S. Fujioka, S. Kawano, T. Kuroiwa and S. Yoshida (2003). "Activation of cell proliferation by brassinolide application in tobacco BY-2 cells: effects of brassinolide on cell multiplication, cell-cycle-related gene expression, and organellar DNA contents." J Exp Bot 54(393): 2669-2678.

Molendijk, A. J., F. Bischoff, C. S. V. Rajendrakumar, J. Friml, M. Braun, S. Gilroy and K. Palme (2001). "Arabidopsis thaliana Rop GTPases are localized to tips of root hairs and control polar growth." Embo Journal 20(11): 2779-2788.

Moscou, M. J. and A. J. Bogdanove (2009). "A Simple Cipher Governs DNA Recognition by TAL Effectors." Science 326(5959): 1501-1501.

Mouchel, C. F., G. C. Briggs and C. S. Hardtke (2004). "Natural genetic variation in Arabidopsis identifies BREVIS RADIX, a novel regulator of cell proliferation and elongation in the root." Genes Dev 18(6): 700-714.

Mouchel, C. F., K. S. Osmont and C. S. Hardtke (2006). "BRX mediates feedback between brassinosteroid levels and auxin signalling in root growth." Nature 443(7110): 458-461.

Muroyama, A. and D. Bergmann (2019). "Plant Cell Polarity: Creating Diversity from Inside the Box." Annu Rev Cell Dev Biol 35: 309-336.

Muroyama, A., Y. Gong and D. C. Bergmann (2020). "Opposing, Polarity-Driven Nuclear Migrations Underpin Asymmetric Divisions to Pattern Arabidopsis Stomata." Curr Biol 30(22): 4549-4552.

Murray, M. G. and W. F. Thompson (1980). "Rapid isolation of high molecular weight plant DNA." Nucleic Acids Res 8(19): 4321-4325.

Nakamura, M., K. Naoi, T. Shoji and T. Hashimoto (2004). "Low concentrations of propyzamide and oryzalin alter microtubule dynamics in Arabidopsis epidermal cells." Plant and Cell Physiology 45(9): 1330-1334.

Nakaya, M., H. Tsukaya, N. Murakami and M. Kato (2002). "Brassinosteroids control the proliferation of leaf cells of Arabidopsis thaliana." Plant and Cell Physiology 43(2): 239-244.

Nalivaeva, N. N. and A. J. Turner (2009). Lipid Anchors to Proteins. Handbook of Neurochemistry and Molecular Neurobiology: Neural Lipids. A. Lajtha, G. Tettamanti and G. Goracci. Boston, MA, Springer US: 353-372.

Nam, K. H. and J. Li (2002). "BRI1/BAK1, a receptor kinase pair mediating brassinosteroid signaling." Cell 110(2): 203-212.

Nan, Q., H. Liang, J. Mendoza, L. Liu, A. Fulzele, A. Wright, E. J. Bennett, C. G. Rasmussen and M. R. Facette (2021). "The OPAQUE1/DISCORDIA2 myosin XI is required for phragmoplast guidance during asymmetric cell divisiEvolution of polarity protein BASLon in maize." bioRxiv: 2021.2008.2029.458084.

Nan, Q., J. Mendoza and M. Facette (2019). "Double Labeling of Microtubules and Actin Filaments in Maize Leaf Division Zone." Bio-protocol 9(12): e3262.

Nance, J. and J. A. Zallen (2011). "Elaborating polarity: PAR proteins and the cytoskeleton." Development 138(5): 799-809.

Nir, I., G. Amador, Y. Gong, N. K. Smoot, L. Cai, H. Shohat and D. C. Bergmann (2022). "Evolution of polarity protein BASL and the capacity for stomatal lineage asymmetric divisions." Curr Biol 32(2): 329-337 e325.

Nunes, T. D. G., M. W. Slawinska, H. Lindner and M. T. Raissig (2022). "Quantitative effects of environmental variation on stomatal anatomy and gas exchange in a grass model." Quantitative Plant Biology 3: e6.

Nunes, T. D. G., D. Zhang and M. T. Raissig (2020). "Form, development and function of grass stomata." Plant J 101(4): 780-799.

Oda, Y. and H. Fukuda (2012). "Initiation of Cell Wall Pattern by a Rho- and Microtubule-Driven Symmetry Breaking." Science 337(6100): 1333-1336.

Oda, Y. and H. Fukuda (2013). "The dynamic interplay of plasma membrane domains and cortical microtubules in secondary cell wall patterning." Front Plant Sci 4: 511.

Ohashi-Ito, K. and D. C. Bergmann (2006). "Arabidopsis FAMA controls the final proliferation/differentiation switch during stomatal development." Plant Cell 18(10): 2493-2505.

Ortega, A., A. de Marcos, J. Illescas-Miranda, M. Mena and C. Fenoll (2019). "The Tomato Genome Encodes SPCH, MUTE, and FAMA Candidates That Can Replace the Endogenous Functions of Their Arabidopsis Orthologs." Frontiers in Plant Science 10.

Panteris, E., T. Achlati, G. Daras and S. Rigas (2018). "Stomatal Complex Development and F-Actin Organization in Maize Leaf Epidermis Depend on Cellulose Synthesis." Molecules 23(6).

Panteris, E., P. Apostolakos and B. Galatis (2006). "Cytoskeletal asymmetry in Zea mays subsidiary cell mother cells: a monopolar prophase microtubule half-spindle anchors the nucleus to its polar position." Cell Motil Cytoskeleton 63(11): 696-709.

Paredez, A. R., C. R. Somerville and D. W. Ehrhardt (2006). "Visualization of cellulose synthase demonstrates functional association with microtubules." Science 312(5779): 1491-1495.

Pavelescu, I., J. Vilarrasa-Blasi, A. Planas-Riverola, M. P. Gonzalez-Garcia, A. I. Cano-Delgado and M. Ibanes (2018). "A Sizer model for cell differentiation in Arabidopsis thaliana root growth." Mol Syst Biol 14(1): e7687.

Pillitteri, L. J., N. L. Bogenschutz and K. U. Torii (2008). "The bHLH protein, MUTE, controls differentiation of stomata and the hydathode pore in Arabidopsis." Plant Cell Physiol 49(6): 934-943.

Pillitteri, L. J., K. M. Peterson, R. J. Horst and K. U. Torii (2011). "Molecular profiling of stomatal meristemoids reveals new component of asymmetric cell division and commonalities among stem cell populations in Arabidopsis." Plant Cell 23(9): 3260-3275.

Pillitteri, L. J., D. B. Sloan, N. L. Bogenschutz and K. U. Torii (2007). "Termination of asymmetric cell division and differentiation of stomata." Nature 445(7127): 501-505.

Pires, N. and L. Dolan (2010). "Origin and diversification of basic-helix-loop-helix proteins in plants." Mol Biol Evol 27(4): 862-874.

Raissig, M. T., E. Abrash, A. Bettadapur, J. P. Vogel and D. C. Bergmann (2016). "Grasses use an alternatively wired bHLH transcription factor network to establish stomatal identity." Proc Natl Acad Sci U S A 113(29): 8326-8331.

Raissig, M. T., J. L. Matos, M. X. Anleu Gil, A. Kornfeld, A. Bettadapur, E. Abrash, H. R. Allison, G. Badgley, J. P. Vogel, J. A. Berry and D. C. Bergmann (2017). "Mobile MUTE specifies subsidiary cells to build physiologically improved grass stomata." Science 355(6330): 1215-1218.

Ramalho, J. J., V. A. S. Jones, S. Mutte and D. Weijers (2022). "Pole position: How plant cells polarize along the axes." Plant Cell 34(1): 174-192.

Rasmussen, C. G., A. J. Wright and S. Muller (2013). "The role of the cytoskeleton and associated proteins in determination of the plant cell division plane." Plant J 75(2): 258-269.

Reichheld, J. P., S. Sonobe, B. Clement, N. Chaubet and C. Gigot (1995). "Cell-Cycle-Regulated Histone Gene-Expression in Synchronized Plant-Cells." Plant Journal 7(2): 245-252.

Reinhardt, B., E. Hanggi, S. Muller, M. Bauch, J. Wyrzykowska, R. Kerstetter, S. Poethig and A. J. Fleming (2007). "Restoration of DWF4 expression to the leaf margin of a dwf4 mutant is sufficient to restore leaf shape but not size: the role of the margin in leaf development." Plant J 52(6): 1094-1104.

Rhodes, S. J. and S. F. Konieczny (1989). "Identification of MRF4: a new member of the muscle regulatory factor gene family." Genes Dev 3(12B): 2050-2061.

Riedl, J., A. H. Crevenna, K. Kessenbrock, J. H. Yu, D. Neukirchen, M. Bista, F. Bradke, D. Jenne, T. A. Holak, Z. Werb, M. Sixt and R. Wedlich-Soldner (2008). "Lifeact: a versatile marker to visualize F-actin." Nat Methods 5(7): 605-607.

Riou-Khamlichi, C., R. Huntley, A. Jacqmard and J. A. H. Murray (1999). "Cytokinin activation of Arabidopsis cell division through a D-type cyclin." Science 283(5407): 1541-1544.

Roux, K. J., D. I. Kim, M. Raida and B. Burke (2012). "A promiscuous biotin ligase fusion protein identifies proximal and interacting proteins in mammalian cells." Journal of Cell Biology 196(6): 801-810.

Rowe, M. H., J. Dong, A. K. Weimer and D. C. Bergmann (2019).

Russinova, E., J. W. Borst, M. Kwaaitaal, A. Cano-Delgado, Y. Yin, J. Chory and S. C. de Vries (2004). "Heterodimerization and endocytosis of Arabidopsis brassinosteroid receptors BRI1 and AtSERK3 (BAK1)." Plant Cell 16(12): 3216-3229.

Sakamoto, T. (2006). "Phytohormones and rice crop yield: strategies and opportunities for genetic improvement." Transgenic Res 15(4): 399-404.

Sano, T., T. Higaki, Y. Oda, T. Hayashi and S. Hasezawa (2005). "Appearance of actin microfilament 'twin peaks' in mitosis and their function in cell plate formation, as visualized in tobacco BY-2 cells expressing GFP-fimbrin." Plant J 44(4): 595-605.

Schroder, F., J. Lisso and C. Mussig (2012). "Expression pattern and putative function of EXL1 and homologous genes in Arabidopsis." Plant Signal Behav 7(1): 22-27.

Sekar, R. B. and A. Periasamy (2003). "Fluorescence resonance energy transfer (FRET) microscopy imaging of live cell protein localizations." The Journal of cell biology 160(5): 629-633.

Sessions, A., J. L. Nemhauser, A. McColl, J. L. Roe, K. A. Feldmann and P. C. Zambryski (1997). "ETTIN patterns the Arabidopsis floral meristem and reproductive organs." Development 124(22): 4481-4491.

Sheahan, M. B., C. J. Staiger, R. J. Rose and D. W. McCurdy (2004). "A green fluorescent protein fusion to actin-binding domain 2 of Arabidopsis fimbrin highlights new features of a dynamic actin cytoskeleton in live plant cells." Plant Physiol 136(4): 3968-3978.

Shpak, E. D., C. T. Berthiaume, E. J. Hill and K. U. Torii (2004). "Synergistic interaction of three ERECTA-family receptor-like kinases controls Arabidopsis organ growth and flower development by promoting cell proliferation." Development 131(7): 1491-1501.

Shpak, E. D., M. B. Lakeman and K. U. Torii (2003). "Dominant-negative receptor uncovers redundancy in the Arabidopsis ERECTA Leucine-rich repeat receptor-like kinase signaling pathway that regulates organ shape." Plant Cell 15(5): 1095-1110.

Shpak, E. D., J. M. McAbee, L. J. Pillitteri and K. U. Torii (2005). "Stomatal patterning and differentiation by synergistic interactions of receptor kinases." Science 309(5732): 290-293.
Smertenko, A. P., M. J. Deeks and P. J. Hussey (2010). "Strategies of actin reorganisation in plant cells." Journal of Cell Science 123(17): 3019-3029.

Smith, L. G., S. M. Gerttula, S. Han and J. Levy (2001). "Tangled1: a microtubule binding protein required for the spatial control of cytokinesis in maize." J Cell Biol 152(1): 231-236.

Smith, L. G., S. Hake and A. W. Sylvester (1996). "The tangled-1 mutation alters cell division orientations throughout maize leaf development without altering leaf shape." Development 122(2): 481-489.

Snustad, D. P., N. A. Haas, S. D. Kopczak and C. D. Silflow (1992). "The small genome of

Arabidopsis contains at least nine expressed beta-tubulin genes." Plant Cell 4(5): 549-556.

Stebbins, G. L. and S. S. Shah (1960). "Developmental Studies of Cell Differentiation in the Epidermis of Monocotyledons .2. Cytological Features of Stomatal Development in the Gramineae." Developmental Biology 2(6): 477-500.

Stoddard, B. L. (2005). "Homing endonuclease structure and function." Q Rev Biophys 38(1): 49-95.

Sugano, S. S., T. Shimada, Y. Imai, K. Okawa, A. Tamai, M. Mori and I. Hara-Nishimura (2010). "Stomagen positively regulates stomatal density in Arabidopsis." Nature 463(7278): 241-U130.

Sun, Y., X. Y. Fan, D. M. Cao, W. Tang, K. He, J. Y. Zhu, J. X. He, M. Y. Bai, S. Zhu, E. Oh, S. Patil, T. W. Kim, H. Ji, W. H. Wong, S. Y. Rhee and Z. Y. Wang (2010). "Integration of brassinosteroid signal transduction with the transcription network for plant growth regulation in Arabidopsis." Dev Cell 19(5): 765-777.

Sutimantanapi, D., D. Pater and L. G. Smith (2014). "Divergent roles for maize PAN1 and PAN2 receptor-like proteins in cytokinesis and cell morphogenesis." Plant Physiol 164(4): 1905-1917.

Takagi, S. (2003). "Actin-based photo-orientation movement of chloroplasts in plant cells." J Exp Biol 206(Pt 12): 1963-1969.

Takemoto, T., M. Uchikawa, M. Yoshida, D. M. Bell, R. Lovell-Badge, V. E. Papaioannou and H. Kondoh (2011). "Tbx6-dependent Sox2 regulation determines neural or mesodermal fate in axial stem cells." Nature 470(7334): 394-398.

Tong, H. N. and C. C. Chu (2012). "Brassinosteroid Signaling and Application in Rice." Journal of Genetics and Genomics 39(1): 3-9.

Truernit, E., H. Bauby, K. Belcram, J. Barthelemy and J. C. Palauqui (2012). "OCTOPUS, a polarly localised membrane-associated protein, regulates phloem differentiation entry in Arabidopsis thaliana." Development 139(7): 1306-1315.

Udenwobele, D. I., R.-C. Su, S. V. Good, T. B. Ball, S. Varma Shrivastav and A. Shrivastav (2017). "Myristoylation: An Important Protein Modification in the Immune Response." Frontiers in immunology 8: 751-751.

Ueda, K., T. Matsuyama and T. Hashimoto (1999). "Visualization of microtubules in living cells of transgenic Arabidopsis thaliana." Protoplasma 206(1-3): 201-206.

Urnov, F. D., E. J. Rebar, M. C. Holmes, H. S. Zhang and P. D. Gregory (2010). "Genome editing with engineered zinc finger nucleases." Nature Reviews Genetics 11(9): 636-646.

Van Damme, D. (2009). "Division plane determination during plant somatic cytokinesis." Curr Opin Plant Biol 12(6): 745-751.

Vidali, L., C. M. Rounds, P. K. Hepler and M. Bezanilla (2009). "Lifeact-mEGFP reveals a dynamic apical F-actin network in tip growing plant cells." PLoS One 4(5): e5744.

Vitha, S., F. Baluska, M. Mews and D. Volkman (1997). "Immunofluorescence detection of F-actin on low melting point wax sections from plant tissues." Journal of Histochemistry & Cytochemistry 45(1): 89-95.

Vukasinovic, N., Y. Wang, I. Vanhoutte, M. Fendrych, B. Guo, M. Kvasnica, P. Jiroutova,

J. Oklestkova, M. Strnad and E. Russinova (2021). "Local brassinosteroid biosynthesis enables optimal root growth." Nat Plants 7(5): 619-632.

Walker, K. L., S. Müller, D. Moss, D. W. Ehrhardt and L. G. Smith (2007). "Arabidopsis TANGLED identifies the division plane throughout mitosis and cytokinesis." Curr Biol 17(21): 1827-1836.

Wang, H., S. Guo, X. Qiao, J. Guo, Z. Li, Y. Zhou, S. Bai, Z. Gao, D. Wang, P. Wang, D. W. Galbraith and C. P. Song (2019). "BZU2/ZmMUTE controls symmetrical division of guard mother cell and specifies neighbor cell fate in maize." PLoS Genet 15(8): e1008377.

Wang, H., S. Yan, H. Xin, W. Huang, H. Zhang, S. Teng, Y. C. Yu, A. R. Fernie, X. Lu, P. Li, S. Li, C. Zhang, Y. L. Ruan, L. Q. Chen and Z. Lang (2019). "A Subsidiary Cell-Localized Glucose Transporter Promotes Stomatal Conductance and Photosynthesis." Plant Cell 31(6): 1328-1343.

Wang, J. H., M. Kucukoglu, L. B. Zhang, P. Chen, D. Decker, O. Nilsson, B. Jones, G. Sandberg and B. Zheng (2013). "The Arabidopsis LRR-RLK, PXC1, is a regulator of secondary wall formation correlated with the TDIF-PXY/TDR-WOX4 signaling pathway." Bmc Plant Biology 13.

Wang, T., L. Liang, Y. Xue, P. F. Jia, W. Chen, M. X. Zhang, Y. C. Wang, H. J. Li and W. C. Yang (2016). "A receptor heteromer mediates the male perception of female attractants in plants (vol 531, pg 241, 2016)." Nature 536(7616): 360-360.

Wang, Z. Y., T. Nakano, J. Gendron, J. He, M. Chen, D. Vafeados, Y. Yang, S. Fujioka, S. Yoshida, T. Asami and J. Chory (2002). "Nuclear-localized BZR1 mediates brassinosteroid-induced growth and feedback suppression of brassinosteroid biosynthesis." Dev Cell 2(4): 505-513.

Weintraub, H., R. Davis, S. Tapscott, M. Thayer, M. Krause, R. Benezra, T. K. Blackwell, D. Turner, R. Rupp, S. Hollenberg and et al. (1991). "The myoD gene family: nodal point during specification of the muscle cell lineage." Science 251(4995): 761-766.

Westphal, M., A. Jungbluth, M. Heidecker, B. Muhlbauer, C. Heizer, J. M. Schwartz, G. Marriott and G. Gerisch (1997). "Microfilament dynamics during cell movement and chemotaxis monitored using a GFP-actin fusion protein." Current Biology 7(3): 176-183.

Wilsen, K. L., A. Lovy-Wheeler, B. Voigt, D. Menzel, J. G. Kunkel and P. K. Hepler (2006). "Imaging the actin cytoskeleton in growing pollen tubes." Sexual Plant Reproduction 19(2): 51-62.

Wong, J. H. and T. Hashimoto (2017). "Novel Arabidopsis microtubule-associated proteins track growing microtubule plus ends." BMC Plant Biol 17(1): 33.

Wong, S. C., I. R. Cowan and G. D. Farquhar (1979). "Stomatal conductance correlates with photosynthetic capacity." Nature 282(5737): 424-426.

Wright, A. J., K. Gallagher and L. G. Smith (2009). "discordia1 and alternative discordia1 function redundantly at the cortical division site to promote preprophase band formation and orient division planes in maize." Plant Cell 21(1): 234-247.

Wright, M. H., W. P. Heal, D. J. Mann and E. W. Tate (2010). "Protein myristoylation in health and disease." Journal of chemical biology 3(1): 19-35.

Wu, G., H. Li and Z. B. Yang (2000). "Arabidopsis RopGAPs are a novel family of Rho GTPase-activating proteins that require the Cdc42/Rac-interactive binding motif for Rop-

specific GTPase stimulation." Plant Physiology 124(4): 1625-1636.

Wu, Z., L. Chen, Q. Yu, W. Zhou, X. Gou, J. Li and S. Hou (2019). "Multiple transcriptional factors control stomata development in rice." New Phytol 223(1): 220-232.

Xu, S. X., L. J. Wang, Z. P. Qiu, Y. J. Ye and X. H. Yu (2002). "Actin visualization in living immature pollen of rice using a GFP-mouse talin fusion protein." Acta Botanica Sinica 44(6): 642-648.

Yamamuro, C., Y. Ihara, X. Wu, T. Noguchi, S. Fujioka, S. Takatsuto, M. Ashikari, H. Kitano and M. Matsuoka (2000). "Loss of function of a rice brassinosteroid insensitive1 homolog prevents internode elongation and bending of the lamina joint." Plant Cell 12(9): 1591-1606.

Yang, H. P., Y. Matsubayashi, K. Nakamura and Y. Sakagami (2001). "Diversity of Arabidopsis genes encoding precursors for phytosulfokine, a peptide growth factor." Plant Physiology 127(3): 842-851.

Yang, W., S. Ren, X. Zhang, M. Gao, S. Ye, Y. Qi, Y. Zheng, J. Wang, L. Zeng, Q. Li, S. Huang and Z. He (2011). "BENT UPPERMOST INTERNODE1 encodes the class II formin FH5 crucial for actin organization and rice development." Plant Cell 23(2): 661-680.

Yin, X. J., A. K. Biswal, J. Dionora, K. M. Perdigon, C. P. Balahadia, S. Mazumdar, C. Chater, H. C. Lin, R. A. Coe, T. Kretzschmar, J. E. Gray, P. W. Quick and A. Bandyopadhyay (2017). "CRISPR-Cas9 and CRISPR-Cpf1 mediated targeting of a stomatal developmental gene EPFL9 in rice." Plant Cell Reports 36(5): 745-757.

Yin, Y., Z. Y. Wang, S. Mora-Garcia, J. Li, S. Yoshida, T. Asami and J. Chory (2002). "BES1 accumulates in the nucleus in response to brassinosteroids to regulate gene expression and promote stem elongation." Cell 109(2): 181-191.

Yoo, S. Y., Y. Kim, S. Y. Kim, J. S. Lee and J. H. Ahn (2007). "Control of Flowering Time and Cold Response by a NAC-Domain Protein in Arabidopsis." Plos One 2(7).

Yoshinari, A. and J. Takano (2017). "Insights into the Mechanisms Underlying Boron Homeostasis in Plants." Front Plant Sci 8: 1951.

Zhang, X., M. Facette, J. A. Humphries, Z. Shen, Y. Park, D. Sutimantanapi, A. W. Sylvester, S. P. Briggs and L. G. Smith (2012). "Identification of PAN2 by quantitative proteomics as a leucine-rich repeat-receptor-like kinase acting upstream of PAN1 to polarize cell division in maize." Plant Cell 24(11): 4577-4589.

Zhang, Y., P. Wang, W. Shao, J. K. Zhu and J. Dong (2015). "The BASL polarity protein controls a MAPK signaling feedback loop in asymmetric cell division." Dev Cell 33(2): 136-149.

Zhang, Z., Y. Zhang, H. Tan, Y. Wang, G. Li, W. Liang, Z. Yuan, J. Hu, H. Ren and D. Zhang (2011). "RICE MORPHOLOGY DETERMINANT encodes the type II formin FH5 and regulates rice morphogenesis." Plant Cell 23(2): 681-700.

Zhiponova, M. K., I. Vanhoutte, V. Boudolf, C. Betti, S. Dhondt, F. Coppens, E. Mylle, S. Maes, M. P. Gonzalez-Garcia, A. I. Cano-Delgado, D. Inze, G. T. S. Beemster, L. De Veylder and E. Russinova (2013). "Brassinosteroid production and signaling differentially control cell division and expansion in the leaf." New Phytol 197(2): 490-502.